Validation of Automotive

Electromagnetic Models

by

Alastair Richmond Ruddle

A Doctoral Thesis submitted in partial fulfilment of the requirements for the award of

Doctor of Philosophy of Loughborough University

September 2002

ABSTRACT

The problems of modelling the electromagnetic characteristics of vehicles and the experimental validation of such models are considered. The validity of the measurement methods that are applied in model validation exercises is of particular concern.

A philosophy for approaching the validation of automotive electromagnetic models of realistic complexity is presented. Mathematical modelling of the key elements of the measurement processes is proposed as the only reliable mechanism for addressing these issues. Areas considered include:

- basic elements of numerical models
- geometrical fidelity requirements for model elements
- calibration and use of experimental transducers
- the inclusion of cables in electromagnetic models
- essential content for vehicle models.

A number of practical measurement processes are also investigated using numerical methods, leading to recommendations for improved practices in:

- calibration of transducers for current measurement at high frequencies
- measurement of radiated emissions from vehicles
- identification of range requirements for simple methods of determining antenna gain and related characteristics in EMC test facilities.

The impact of such measures on the success of model validation studies for automotive applications is demonstrated. It is concluded that experimental results are no less in need of validation than the numerical results that are, more conventionally, judged against them.

ACKNOWLEDGEMENTS

LIST OF SYMBOLS

Symbol	Interpretation
$a, b, d, D, h, H, L, r, R_i, s, x, y, z, \Delta$	Lengths (m)
$A_i(f), B_i(f), C_i(f), \tau_i(f), \xi(f), \Psi_i(f)$	Voltage transmission coefficients
c	Speed of light in vacuum $\approx 2.997925 \times 10^8$ m/s
$F(f), H(f), J(f), K(f), M(f), N(f),$ $Q(f), S(f), T(f), U(f), W(f)$	Network scattering matrices
e	≈ 2.718282
$\mathbf{E}_i(f), E_i(f)$	Electric field strength (V/m)
f	Frequency (Hz)
$G(\theta,\phi,f)$	Antenna gain
$\mathbf{h}_A(f), h_A(f)$	Effective height of antenna
$\mathbf{i}(f)$	Network port current vector (A)
$I_i(f)$	Current (A)
$I_i(s,f)$	Longitudinal wire current distribution (A)
$\mathbf{I}$	Identity matrix
k	Ratio of phase difference to π
$n(E_i), m(P_i), q(v)$	Measured quantities (electric field, current etc.)
$N(f), M(f), Q(f)$	Normalized measurements (electric field, current etc.)
$P_i(f)$	Power (W)
$\mathbf{P}, \mathbf{S}$	Position vectors
(r,θ,ϕ)	Spherical coordinates
$\mathbf{T}$	Network termination impedance vector
u	Relative amplitude
$\mathbf{v}(f)$	Network port voltage vector (V)
$V_i(f), v_i(f)$	Voltage (V)
$V_i(s,f)$	Longitudinal wire voltage distribution (V)
$w(x,y,z,f)$	Spatial field distribution function
(x,y,z)	Cartesian coordinates
$\mathbf{Y}(f)$	Network admittance matrix
$\mathbf{Z}(f)$	Network impedance matrix
$Z_i(f)$	Impedance
$\alpha_i(f)$	Antenna factor
$\beta_i(f), \gamma(f)$	Propagation constants
$\delta\phi$	Phase difference (radians)
$\delta\psi$	Amplitude difference
ε_r	Relative permittivity
$\eta(f)$	Loss factor
$\lambda(f)$	Wavelength (m)
π	Ratio of circle circumference to diameter
$\rho_i(f), \Gamma_i(f), \psi(f)$	Voltage reflection coefficients
$\sigma_{ij}(f)$	Scattering matrix elements
$\Phi(\theta,\phi,f)$	Antenna directivity in direction (θ,ϕ) at frequency f
$\psi(\theta,\phi,f)$	Power radiated per unit solid angle in direction (θ,ϕ) at frequency f (W/steradian)

CONTENTS

Page

CHAPTER 1:   INTRODUCTION

The essence of engineering design processes is that some form of prior knowledge is used to shape the outcome. Success without such knowledge is due to chance and not design, although chance may provide the starting point for knowledge, and hence design, to evolve. The nature of this design knowledge can range from purely practical experience, through simple mathematical models and scaled experiments, to very sophisticated numerical simulations. However, the quality of such knowledge is also dependent on the novelty and complexity of the application, which may be beyond the experience of the designer or the validity of simple models. Consequently, as technologies develop and system complexity increases there is generally a complementary evolution towards more mature engineering processes based on detailed numerical simulation to investigate the design before physical prototyping takes place.

For simulation to be useful in the design process the user must have confidence in the results, as it is of limited benefit if it cannot be used without recourse to physical measurements. This is not to say that limitations are not acceptable, since suitable allowance can be made if the user understands the limitations. However, establishing the limitations and reliability of simulation techniques initially requires extensive validation of computed results against some independent, and trusted, reference. Measurements are generally regarded as the most reliable reference.

This process is already fairly advanced in many automotive engineering disciplines: examples where simulation is already widely used include crashworthiness [1.1], aerodynamics [1.2] and heat transfer [1.3]. However, numerical simulation of the electromagnetic (EM) performance of vehicles, encompassing both electromagnetic compatibility (EMC) and the performance of vehicle-mounted antennas, requires even greater computing resources and is still in its infancy.

1.1   Motivation

The EMC performance of vehicles is of fundamental importance to the reliability and safety of modern vehicles, which are increasingly reliant on sophisticated electronic control systems. In Europe, as in many other parts of the world, vehicle manufacturers are therefore required to demonstrate the compliance of their products with legislative EMC requirements [1.4]. The installed performance characteristics of automotive antennas are also becoming much more important as greater use is made of wireless technologies in order to provide new services.

At present, however, there is only limited design analysis for the EM performance of vehicles, both because of the inherent technical difficulties and because these issues have, until recently, represented a relatively small part of the wider vehicle development process.

Historically, physical measurements have been the only viable approach for the investigation of electromagnetic performance for complex systems such as vehicles. However, recent developments in computing technology [1.5-1.8] are now beginning to make numerical modelling a more feasible alternative. Nonetheless, automotive EM modelling is still regarded with considerable scepticism by many potential users, and the credibility of simulation results must be convincingly demonstrated against measured results before wider acceptance of EM modelling techniques can be achieved.

1.2   Approach

The initial premise in validation against experiment is that the measurements must be correct, almost by definition, particularly if they comply with widely accepted standards (and can therefore be reproduced by another laboratory). This argument, however, is flawed in that almost all measurements of any complexity are subject to some form of interpretation. Simply comparing results based on the same interpretation of the measurement process provides information about their repeatability and precision, but not their absolute accuracy. It is to be expected, therefore, that successful model validation will depend upon a critical appraisal of both numerical models and the measurements that they are compared with.

Mathematical modelling of the key elements of the measurement processes is proposed as the only reliable mechanism for addressing these issues. Such analysis provides the opportunity to refine both the modelling and measurement techniques that are used, bringing benefits to both methods of investigation.

1.3   Objectives

The objectives of this work are to:

- increase confidence in the quality of automotive electromagnetic measurements, in terms of the basic techniques that are applied and the interpretation of results from such measurements
- improve understanding of the required content and practical limitations of automotive electromagnetic models

- develop improved model validation strategies that provide a more accurate picture of the reliability and limitations of numerical techniques.

These objectives support the overall goal of improving the quality of model validation results. The use of modelling techniques to investigate measurement methods also leads to improvements in the accuracy of parameters that are derived from physical measurements.

1.4   Overview

Chapter 2 gives a brief outline of EMC modelling approaches, concentrating on automotive applications in particular. Thereafter, the thesis falls into two parts, both linked by their use of numerical techniques and their pursuit of more successful model validation results. The first part is concerned with the practical problems of validating EM model results against experiments and vehicle level simulation issues.

The importance of model validation is discussed in Chapter 3, which also outlines the philosophy that is adopted in this work. In Chapter 4 the application of microwave network theory to describe the EMC problem is investigated, including some illustrations based on simple wire networks. The problems of building and validating wider vehicle models are considered in Chapter 5, including the content of numerical models, an approach for classifying the model fidelity requirements for different applications and methods for ensuring that simulated results can be presented in a form that can be directly compared with measured data.

In the second part, numerical modelling is applied to the analysis of a number of key measurement processes, in order to assess the theoretical validity of the types of measurements that are used in model validation exercises.

The use of transducers for current measurement is addressed in Chapter 6, in which an improved calibration method is described. The correlation between emissions measurements at different ranges is considered in Chapter 7, including a proposal for relating measurements carried out at 3 m and 10 m ranges. In Chapter 8 the validity of measurements on vehicle-mounted antennas in semi-anechoic environments is investigated using numerical models of simple dipole antennas and of a monopole on a vehicle bodyshell. Experimental validation of vehicle mounted antenna models is presented, and model results are used to investigate range requirements for measuring the characteristics of antennas positioned close to ground as well as mounted on vehicles.

Finally, Chapter 9 summarizes the findings and identifies possible areas for further work, while publications that were derived from the work described in this thesis are listed in Appendix A. The papers listed in Appendix A are referred to in the text using the format "[A.x]", while those relating to chapter "N" are identified using the format "[N.x]".

1.5   References

[1.1]   T.K.S. Murthy and C.A. Brebbia, *Structural design and crashworthiness of automobiles*, Springer-Verlag, 1987

[1.2]   W.-H. Hucho, *Aerodynamics of road vehicles*, Butterworth-Heinemann, 1990

[1.3]   G. Rogers and Y. Mayhew, *Engineering thermodynamics and heat transfer*, Longman Scientific and Technical, 1992

[1.4]   *Commission Directive 95/54/EC of 31 October 1995 adapting to technical progress Council Directive 72/245/EEC on the approximation of the laws of the Member States relating to the suppression of radio interference produced by spark-ignition engines fitted to motor vehicles and amending Directive 70/156/EEC on the approximation of the laws of the Member States relating to the type-approval of motor vehicles and their trailers,* Official Journal of the European Communities, No. L 266, 8 November 1995, pp. 1-66

[1.5]   D.D. Ward and A.R. Ruddle, *Developing a strategy for automotive electromagnetic modelling,* Autotech Congress, Birmingham, November 1997, IMechE Seminar Publication 1997-10

[1.6]   A.R. Ruddle and D.D. Ward, *Evaluation of parallel computing in the analysis of EMC problems,* IEE Colloquium "High frequency simulation: part two", London, November 1997, Digest No. 1997/374, Paper No. 5

[1.7]   D.D. Ward and A.R. Ruddle, *Developments in electromagnetic modelling,* Society of Automotive Engineers Congress, Detroit, February 1998, Paper No. 98-0305

[1.8]   F. Canavero, J.-C. Kedzia, P. Ravier and B. Scholl, *Automotive EMC: Numerical simulation for early EMC design of cars*, Proceedings of 4th European Conference on Electromagnetic Compatibility, Brugge, Belgium, September 2000, Tutorials, pp. 32–39

CHAPTER 2: AUTOMOTIVE EM MODELLING

Historically, vehicles have been predominantly mechanical systems, providing very basic transportation functions. However, the electrical, electronics and software content of modern vehicles represents an increasingly significant part of the cost of a modern vehicle. These newer technologies are being deployed to provide driver support in safety-related transportation applications (eg. anti-lock braking, cruise control), enhanced efficiency measures (eg. engine management) and convenience facilities for the occupants (eg. entertainment and communications). Furthermore, these changes show no sign of deceleration, and vehicles are now beginning to be considered as much as "infotainment portals" as in their traditional role as transportation platforms.

2.1 System characteristics

A typical passenger vehicle is approximately 5 m long, 2 m wide, 1.5 m high, and contains three main cavities (passenger compartment, engine bay and luggage space). The vehicle shell, although generally metallic, is pierced by many apertures, with dimensions ranging from $\sim 10^{-3}$ m up to ~ 1 m. The doors and other closures are also accompanied by slots with widths of $\sim 10^{-3}$ m, depths of $\sim 10^{-2}$ m, and lengths of $\sim 10^0$ m. The doors are of hollow construction, again pierced by apertures, with separations of $\sim 10^{-2}$ m between the inner and outer skins.

Despite recent developments in multiplex bus systems for vehicles, the total length of wire in the vehicle is still likely to be of the order of 2.5 km, with transverse dimensions of $\sim 10^{-3}$ m for individual wires and $\sim 10^{-2}$ m for bundles of wires following a common path. The wiring harness typically contains tens of channels and branches, resulting in hundreds of terminals. The wiring harness is currently the single most expensive component in a typical vehicle.

Modern vehicles are making increasing use of wireless systems, not only for implementing operational functions (eg. radio keyless entry) and driver support systems (eg. GPS for navigation systems), but also to provide a variety of convenience and entertainment facilities (mobile telephone, TV etc.). Thus, a modern luxury vehicle will already have around 20 antennas, and this number continues to climb rapidly as new technologies (Bluetooth, millimetre-wave radar etc.) are deployed in vehicles.

Vehicle styling and security issues lead to requirements for conformal antenna designs, which must provide adequate performance in far from ideal locations. This is radically different to the traditional situation with a single monopole antenna providing radio reception. The move to digital systems also has significant implications for automotive antennas, since they will fail completely if signal levels fall too low (unlike the progressive degradation that occurs for analogue systems). Thus, antenna engineering issues are becoming increasingly significant for successful vehicle development.

Vehicle manufacturers prefer to avoid the use of shielded modules and connecting cables, even simple twisted pairs, on the grounds of their contribution to both cost and weight, as well as the additional difficulties of installation. Shielded components are only used where absolutely necessary, such as between antennas and receivers. To simplify installation, groups of cables are bundled together, thus providing opportunities for intra-system EMC problems by facilitating coupling between cables. The vehicle structure can provide only limited shielding, as all of the cavities have large apertures as well as slots around the periphery of closures that, together with the wiring harness, provide a large number of possible coupling paths.

The frequency band for European legislative vehicle-level EMC measurements currently ranges from 30 MHz to 1 GHz [1.4]. However, these legislative requirements are already falling behind current practices in the automotive industry. As digital clock speeds and wireless transmission frequencies continue to rise the upper frequency limits for EMC requirements will also need to increase [2.1-2.2] in order to provide the intended levels of protection. In practice, most manufacturers carry out more stringent tests than are required by legislation, and some are already beginning to carry out testing at frequencies above 1 GHz.

Thus, the range of physical scales within the structure, which are crucial for electromagnetic simulation considerations, spans some six orders of magnitude. The frequency range of interest (10 kHz to 1 GHz) is similarly wide, spanning 5 orders of magnitude now and probably more in the near future. Electromagnetic simulation on this scale therefore represents a significant technical challenge. Nonetheless, the electromagnetic aspects represent only a fraction of the complete problem that must be addressed in attempting to predict vehicle EMC performance.

2.2   Electromagnetic compatibility

The properties described collectively as "electromagnetic compatibility" are simple to describe in qualitative terms, but quantitative descriptions of these properties are not generally so easy.

The basic phenomena are classified in terms of "emissions" and "immunity" characteristics. Electromagnetic interference may be both "conducted" to or from a system via the associated wiring, as well as "radiated" to or from it. Legislation specifies the emissions and immunity performance criteria that electrical and electronic equipment must satisfy before it may be used. Conducted emissions and immunity are not really a consideration for vehicles, which are not normally directly connected to the external environment via cables except when charging batteries or undergoing diagnostic or maintenance procedures. Nonetheless, sub-system conducted emissions may contribute to the radiated emissions of the vehicle, and incident fields may be coupled into vehicle subsystems via the wiring harness. "Intra-system" EMC issues are also of fundamental importance for the successful operation of the system. Consequently, automotive EMC measurements are carried out [2.3] at both component and vehicle level.

The maximum acceptable radiated emissions levels for a vehicle are specified in terms of the electric field strength as measured using an antenna placed in a particular geometrical configuration relative to the vehicle. Specifying (and measuring) the immunity of a vehicle is rather more difficult, as the essential criterion is continued functional performance rather than a readily measured physical parameter. Moreover, the magnitude of the external "threat" that is actually applied in immunity tests is not easy to quantify.

Vehicle immunity measurements are often conducted in semi-anechoic chambers, with the result that the applied field is actually a complex interference pattern resulting from direct illumination from the source antenna and the effects of ground reflections. Furthermore, the separation between the source antenna and the vehicle under test is normally only of the order of 1 m, so the field structure will also be complicated by the presence of near-field components. As an illustration of the impact of these effects, Fig. 2.1 shows the frequency dependence of the field generated by a vertically polarized wire cage biconical antenna at a height of 1.8 m above a ground plane along a vertical line at a distance of 3 m from the antenna. These results were computed using a numerical model based on the "method of moments" [2.4]. The field is normalized to the value at the calibration point (ie. 1 m high at 3 m from the antenna), as is the case using the single point chamber calibration method that is employed in automotive immunity measurements. The height range (ie. 0.2-2 m) reflects the vertical dimensions of typical passenger and light goods vehicles. For vertical polarization, the field at the sample line deviates from the notional "applied field" by factors of 0.7-1.7 over the operating frequencies of the antenna. For horizontal polarization, the field variations will be greater as the image source is in anti-phase to the real antenna. At higher frequencies, even greater feature densities can be expected, for both polarizations.
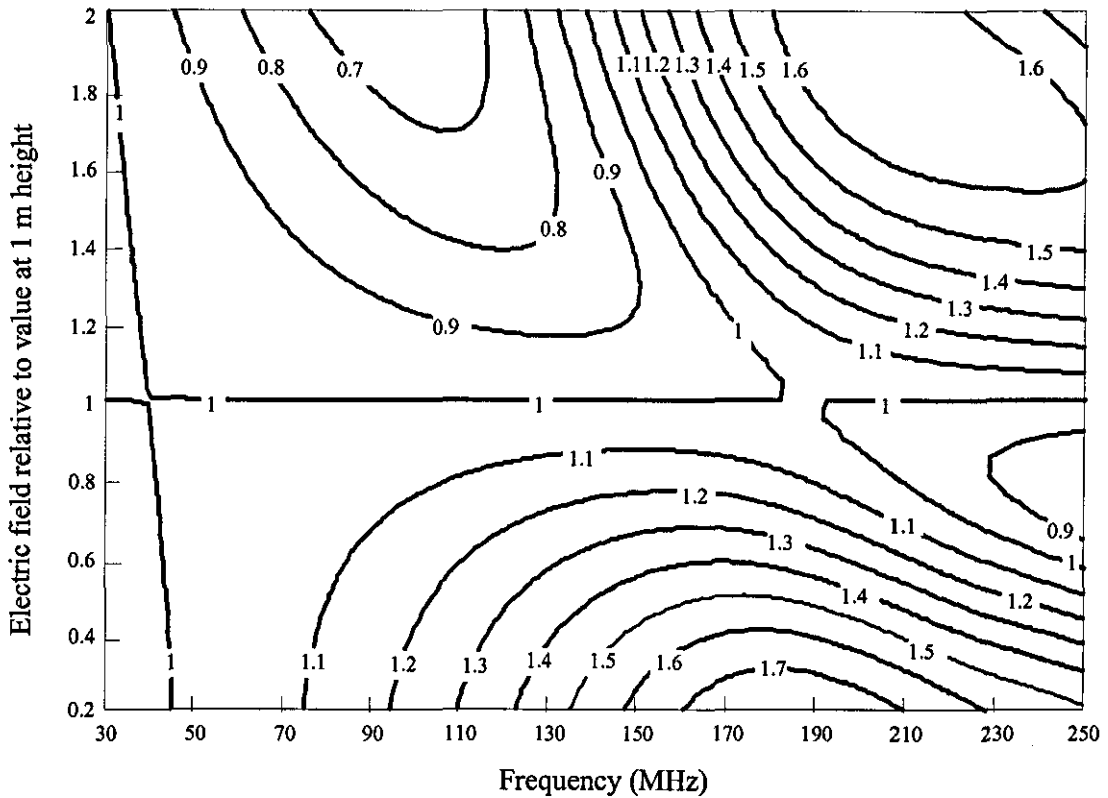
Fig. 2.1   **Contour plot of relative electric field strength as a function frequency along a vertical line through the calibration point for a representative automotive immunity test configuration**

2.3   EMC models

The external emissions of a vehicle could be predicted if the transfer function between the ports of the harness and the emissions measurement point could be determined, assuming that the modules only radiate via their associated cables and that the magnitude of these noise currents are known. The coupling parameters can, in principle, be determined from measurement, as employed in [2.5], although reliable measurements of this type are not easy to achieve and become increasingly difficult as the frequency and the number of cables in the system increase.

Simulation offers a much more efficient source of coupling data for realistic wiring harnesses, since a single simulation can provide any number of coupling coefficients for the same model building and simulation overhead. Information regarding the emissions characteristics of the electronic modules, which could again be derived from either numerical or experimental results, could then be used as inputs to the vehicle level emissions model.

By contrast, the immunity of the vehicle to external fields is not described in terms of the noise levels reaching the electronic modules, but in terms of their functional response to these levels of interference. Measures of the field coupling into particular regions of a vehicle (such as harness terminal currents and local field distribution) are therefore only useful as a measure of relative risk. They are not in themselves sufficient to determine whether the resulting field will have a functional effect. Assessing the implications for functional performance would require either a detailed simulation of the electronic module or a test that replicates the impact of the interference due to the external source. Furthermore, establishing the functional performance characteristics of modern vehicles will increasingly require consideration of the software used in vehicle subsystems, as well as the degree of integration between systems.

Models that aim to predict true "EMC performance" therefore need to accommodate a very wide range of phenomena. A single monolithic simulation for such purposes is not a practicable proposition, so a combination of appropriate techniques represents the most viable approach to developing a functional EMC model. This assumes that the system can be decomposed into more manageable elements, which can be treated separately and their results combined to provide a wider solution. This compositional approach is a well-known and successful technique for managing complexity in a wide range of disciplines, particularly in systems design and specification [2.6]. In an EMC model, even the electromagnetic elements of the system may need to be further decomposed in order to improve the efficiency and viability of the modelling process [2.7]. For example, different techniques could be used for modelling the inside and outside of an enclosure [2.8], rather than using a single method throughout.

For field to cable coupling calculations "separated methods", which combine transmission-line models with 3D field calculations [2.9-2.11], represent a possible alternative to embedding models of wires in a 3D field model. The latter can be achieved either by introducing additional mesh refinement to allow wires to be added to the model, which is very expensive in terms of computational requirements, or by introducing special "thin-wire" models. Thin-wire models provide a more efficient mechanism for including such structures in 3D field models, but require the correct termination conditions to be applied in order to obtain valid results. The separated approach avoids including the cable and its terminations in the 3D model, which then requires minimal simulations to obtain the field exciting the cable. The impact of this excitation on the cable can then be determined using very efficient network-based methods [2.12] for any required cable and termination configurations. The main drawbacks of the separated approach are that the requirement for the wires to be close to ground will not always be met, and this approach is not so easily applied to the analysis of intra-system EMC performance.

Multi-domain models

In attempting to build an EMC model it is useful to consider a range of modelling techniques operating at a number of different levels, as outlined in Table 2.1 below.

Model class	Model order	Model nature	Comments
A	3D + time or frequency	Electromagnetic – volume or surface meshing	3D electromagnetic field distribution and related parameters (eg. antenna characteristics)
B	2D static	Electrostatic – planar or peripheral meshing	Lumped circuit model of transmission line segments (low frequency approximation)
C	1D + time or frequency	Analytical or numerical (linear meshing)	Wave propagation effects on transmission lines (length and load dependent)
D	0D + time	Circuit simulation [2.13] and executable algorithmic models (eg. temporal logic [2.14] descriptions)	Device physics in circuit models, but no account of physical layout
E	0D	Behavioural only	High level systems model

Table 2.1   Classification of model types required in order to predict functional performance of vehicle electrical systems

At present, all of the model types outlined in Table 1 are possible, but to varying degrees. The linking of 3D field calculations to separated cable models [2.7] and then to simple circuit simulation [1.8] has been demonstrated. Nonetheless, the integration of all of the techniques that are indicated in Table 2.1 into a complete system model remains untried.

A possible scheme for modelling true functional radiated immunity performance is illustrated in Fig. 2.2, which outlines the necessary interactions between electromagnetic modelling techniques and other types of simulation that are required to complete the functional EMC model. It is also quite likely that EM simulation at board level [2.15-2.17] will be required to characterize the performance of the sub-systems themselves. In fact the scope of the system model as conceived here goes beyond that of purely EMC performance, as the integration of software models would enable wider issues of functional safety to be simulated, such as the potential impact of software defects.

EXTERNAL EM NOISE

Harness CAD

Transmission line parameters

Vehicle CAD → A → C ← B

Wave propagation between harness terminals

Sub-system software specifications → D ← **Sub-system circuit design**

Sub-system hardware and software performance

D → E ← **System design**

FUNCTIONAL IMMUNITY PERFORMANCE
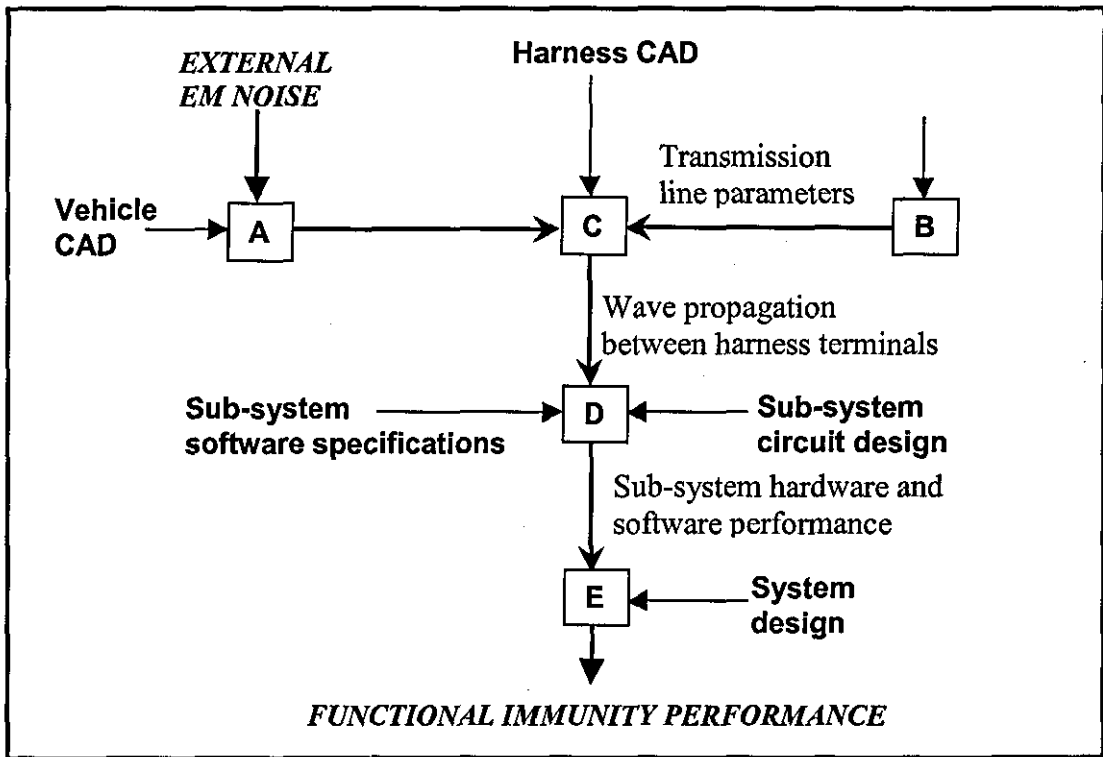
Fig. 2.2   Possible composition of a multi-domain system level model required for predicting functional EMC performance in vehicles and similar systems

A system level model of this nature could equally well draw on measured results to supply part of the information required. Such an approach is particularly suitable for automotive applications, where sub-system modelling for EMC applications is even less well developed than at whole-vehicle level but test data for the vehicle sub-systems is likely to be available before a physical prototype of the vehicle is built. This combination of vehicle level modelling with sub-system testing is perhaps the most viable strategy, in the short to medium term, for introducing simulation techniques into vehicle development processes.

Benefits of a collaborative approach

Partitioning the model as outlined above not only helps to make the problem computationally tractable, but also helps to make simulation "politically" acceptable where a number of commercial organisations may need to collaborate in the development of a system level model of this nature.

This is almost certainly the case in the automotive industry, where vehicle manufacturers typically design the overall packaging (the vehicle structure) and then add systems and equipment provided by their suppliers, who may themselves be obtaining part of their product from secondary suppliers. In this situation it is not entirely clear where the responsibility for carrying out EMC simulation lies, as no single organisation automatically possesses all of the information that is required for such work.

The type of information that is required for EMC simulation, such as vehicle geometry and design details for electronic modules, essentially represents the intellectual property of the organisations involved in the project. As such, there will be considerable reluctance among these organisations to making their design details available to other parties. Furthermore, it is perhaps more equitable to share the burden of simulation amongst the various parties that are involved. Partitioning the EMC modelling task provides a natural mechanism for achieving this, since the parties involved may then exchange simulation results rather than providing the design details of their products for integration into a single, monolithic model.

In terms of Fig. 2.2, tasks in the upper and lower parts of the diagram could be the responsibility of the vehicle manufacturer, or perhaps of a supplier appointed by the manufacturer to act as the "vehicle electrical systems integrator". The latter would need access to vehicle geometry and wiring harness data in order to develop suitable models of the vehicle as an equipment enclosure. The tasks in the central part of the diagram reflect work which could be carried out by a system supplier, and which may also represent a chain of suppliers.

2.4   EM field modelling

Although an electromagnetic model is not the same as an EMC model, it certainly provides the basis for the wider analysis that is needed to investigate functional EMC effects. An electromagnetic model is also required for other applications, such as the prediction of antenna performance.

A wide range of numerical techniques has been developed for electromagnetic modelling applications [2.18]. Although the motivation for the development of these techniques was primarily the analysis and design of antennas, waveguide components, and power generation and distribution equipment, many of these techniques have also been applied to EMC [2.19-2.20]. The most notable of the various techniques are the method of moments (MoM) [2.4], finite differences in the time domain (FDTD, [2.21]), finite elements (FE, [2.22]), and transmission line matrix (TLM, [2.23]).

Issues such as the installed performance of vehicle antennas have been investigated using MoM [2.24], and FDTD has been applied in similar studies of helicopter antennas [2.25]. Both FDTD [2.26] and TLM [2.27] have also been applied in modelling EMC and lightning strike effects in aircraft, while the use of FE for modelling vehicles is described in [2.28]. Although all techniques have their own particular merits, TLM is found to be particularly well suited for large-scale, broadband applications such as vehicle EMC [2.29-2.31], as well as in the investigation of electromagnetic metrology issues [2.32].

2.5   Tools employed in this work

Different tools are required not only to address different modelling problems, but also to allow validation to be carried out between numerical models (for those cases where it may be feasible to apply more than one technique to the same, or very similar, problems). In the course of this work, two commercial electromagnetic modelling tools have been employed in this context. These are a frequency-domain MoM code (AWAS [2.33]) and a time-domain TLM code (Microstripes [2.34]). The motivation for choosing these particular tools is summarized below.

AWAS - MoM

The performance of antennas can be simulated very efficiently using frequency domain integral equation techniques. Although these methods are most commonly applied to thin wire structures or 2D problems where the discretization is in terms of linear elements, it is also possible to include bulk conductors and dielectrics represented using a surface mesh (boundary elements). Thus, these techniques provide a body-fitted mesh through a piece-wise linear approximation. Moreover, it is only necessary to mesh the structure, so the space between elements is essentially unlimited, and there is no potential for corruption due to finite radiation boundary conditions (the environment can be either completely free-space or perfectly semi-anechoic). The main disadvantage, however, is that a dense matrix of self and mutual impedance terms is developed, of order N^2 where N is the number of elements in the model. This impedance matrix must be inverted, for each frequency in the band of interest, leading to significant computing requirements and long run-times for "electrically large" models (where the dimensions of the structure are greater than the wavelength at the frequencies of interest).

The AWAS code is a commercial implementation of MoM for thin wire structures that is particularly convenient in that the current on a wire segment is represented using a polynomial expansion. This avoids the need to model regions where there are likely to be rapid spatial variations in the current using large numbers of small segments, as the use of higher order polynomials allows the length of the segments to be a significant fraction of the wavelength.

The geometry can therefore be entered more intuitively in terms of the physical nodes and segments comprising the structure of interest. Any overly long segments are automatically subdivided to ensure that the constraints for using the polynomial expansion are satisfied at each frequency. However, when the segment lengths approach $\lambda/2$ the polynomial expansion may become of order 9, which can result in oscillatory functions that give rise to spurious features in the frequency response. Care is therefore needed to ensure that the higher order polynomials do not lead to numerical errors.

Microstripes - TLM

Modelling large and complex structures such as vehicles over very wide frequency ranges can lead to very significant computing requirements. The most computationally efficient methods for such large models are time domain volume meshing techniques based on structured Cartesian meshes, such as FDTD and TLM. These methods avoid the need to invert a large matrix, and simple specifications for cell size and location ensure that the memory requirements do not increase as rapidly for electrically large models as is the case with MoM and FEM. In addition, a broadband frequency response can be obtained from a single time-domain simulation. Although this normally takes longer to complete than a single frequency domain simulation, a more realistic comparison of computing time per frequency shows the time domain methods to be much more efficient for large models.

Nonetheless, major limitations of this type of approach include the use of rectangular cells or "nodes" (in TLM), which results in a "sugar-cubed" approximation to curved surfaces, and the need to truncate the model using an artificial radiation boundary. The latter will inevitably be afflicted with finite reflection characteristics that can compromise the reliability of the results if these effects are not given adequate consideration. In TLM the mesh can be truncated with a matched termination in the far-field, where the wave impedance approximates that of free-space, but a more sophisticated technique such as the "perfectly matched layer" (PML) may permit the workspace to be truncated much closer to the radiating structure [2.35].

The Microstripes tool is a commercial implementation of TLM that provides a range of useful modelling facilities, including multigrid meshing [2.36], sub-cell thin wire [2.37], multiconductor [2.38] and slot [2.39] models, and CAD import facilities. The latter are of considerable importance for building models based on both real and synthetic vehicle geometries. For real vehicles, however, the more sophisticated and reliable geometry repair and mesh generation capabilities of a specialized intermediate model building tool (CADfix [2.40] was used in this work) are generally found to be essential.

2.6   Conclusions

The functional EMC performance of automotive systems encompasses and depends upon such a wide range of phenomena that the prediction of these characteristics currently remains a desirable objective rather than a practical reality.   A single monolithic simulation is unlikely to provide a successful solution to this problem, due not only to technical limitations (essentially computing), but also the need to spread the associated cost burden (as currently happens with testing) and to protect the intellectual property of both suppliers and vehicle manufacturers. Consequently, simulation strategies that aim to decompose the system and then combine different types of more restricted models in a compositional manner are perhaps more likely to succeed.

Although an electromagnetic model does not provide the functional EMC performance measures that are ultimately required for more efficient vehicle development, it can provide information that is indirectly useful for EMC analysis. Examples include the investigation of generic issues associated with vehicle structures, and the provision of quantitative and objective data to support vehicle packaging decisions. This can also include automotive antenna engineering, which is an increasingly important issue in the development of modern vehicles. At present, however, even predicting the electromagnetic characteristics of vehicle structures remains extremely challenging, and reliably validating such predictions against physical measurements is far from easy.

2.7   References

[2.1]   I.E. Noble, I.D. Flintoft and L.M. McCormack, *Study on the application of directive 95/54/EC relative to the EMC of road vehicles*, York EMC Services Ltd, Report 5018CR

[2.2]   A.J. Rowell, D.W. Welsh and A.D. Papatsoris, *Practical limits for EEMC emission testing at frequencies above 1 GHz: Final report (AY3601)*, York EMC Services Ltd, Report R/00/261

[2.3]   I. Noble, *Electromagnetic compatibility in the automotive environment*, IEE Proceedings Part A, Science, Measurement and Technology, Vol. 141, No. 4, 1994, pp. 252-258

[2.4]   R.F. Harrington, *Field computation by moment methods*, Macmillan, New York, 1968

[2.5]   C. Chen, *Predicting vehicle-level radiated EMI emissions using module level conducted EMIs and harness radiation efficiencies*, Proceedings of IEEE EMC Symposium, Montreal, Canada, August 2001, Vol. II, pp. 1146-1151

[2.6]   E. Yourdon and L.L. Constantine, *Structured design: fundamentals of a discipline of computer program and systems design*, Yourdon Press Computing Series, Prentice Hall, Eaglewood Cliffs, NJ, 1979

[2.7]   J.-P. Parmantier, *Theory and modeling for EMC in extended systems: current capabilities and requirements*, Proceedings of 13th Zurich EMC Symposium, February 1999, pp. 111-116

[2.8]   B. Archambeault, *EMI/EMC computational modelling handbook*, Kluwer Academic Publishers, 1998, Chapter 9

[2.9]   C.D. Taylor, R.S. Satterwhite and C.W. Harrison, *The response of a terminated two-wire transmission line excited by a non-uniform electromagnetic field*, IEEE Transactions on Antennas and Propagation, Vol. 13, No. 6, November 1986, pp. 987-989

[2.10] A.K. Agrawal, H.J. Price and S.H. Gurbaxani, *Transient response of multiconductor transmission lines excited by a nonuniform electromagnetic field*, IEEE Transactions on EMC, Vol. 22, No. 2, May 1980, pp. 119-129

[2.11] F. Rachidi, *Formulation of field to transmission line coupling equations in terms of magnetic excitation field*, IEEE Transactions on EMC, Vol. 35, No. 3, August 1993, pp. 404-407

[2.12] C.R. Paul, *Analysis of multiconductor transmission lines*, Wiley, New York, 1994

[2.13] J. Carlsson and U. Lundgren, *An approach to the generation of SPICE models feasible for EMC models*, Proceedings of IEEE EMC Symposium, Washington, USA, August 2000, Vol. 1, pp. 71-76

[2.14] B. Moszkowski, *Executing temporal logic programs*, Cambridge University Press, Cambridge, UK, 1986

[2.15] R. Laroussi and G.I. Costache, *Finite-element method applied to EMC problems (PCB environment)*, IEEE Transactions on EMC, Vol. 35, No. 2, May 1993, pp.178-184

[2.16] G. Cerri, R.D. Leo and V.M. Primiani, *A rigorous model for radiated emission predictions from PCB circuits*, IEEE Transactions on EMC, Vol. 35, No. 1, February 1993, pp.102-109

[2.17] A. Nishizawa, G. Kobidze and S. Tanabe, *Hybrid FDTD-SPICE analysis of radiated emission from PCB with integrated circuits*, Proceedings of IEEE EMC Symposium, Montreal, Canada, August 2001, Vol. 1, pp. 559-563

[2.18] E.K. Miller, *A selective survey of computational electromagnetics*, IEEE Transactions on Antennas and Propagation, Vol. 36, No. 9, September 1988, pp.1281-1305

[2.19] S.J. Porter and J.F. Dawson, *Electromagnetic modelling for EMC using finite methods*, IEE Proceedings Part A, Science, Measurement and Technology, Vol. 141, No. 4, 1994, pp.303-309

[2.20] R.F. Milsom, *Electromagnetic computer modelling for EMC (integral methods)*, IEE Proceedings Part A, Science, Measurement and Technology, Vol. 141, No. 4, 1994, pp, 297-302

[2.21] A. Taflove, *Computational electromagnetics: the finite difference time domain method* Artech House, London, 1995

[2.22] P.P. Sylvester and R.L. Ferrari, *Finite elements for electrical engineers*, Cambridge University Press, Cambridge, 1983

[2.23] C. Christopoulos, *The transmission-line modelling method: TLM*, IEEE Press, New York, 1995

[2.24] R. Abou-Jaoude and E.K. Walton, *Numerical modelling of on-glass conformal automobile antennas*, IEEE Transactions on Antennas and Propagation, Vol. 46, No. 6, June 1998, pp. 845-852

[2.25] S.V. Georgakopoulos, C.A. Balanis and C.R. Birtcher, *Cosite interference between wire antennas on helicopter structures and rotor modulation effects: FDTD versus measurements*, IEEE Transactions on EMC, Vol. 41, No. 3, August 1999, pp. 221-233

[2.26] C. Birtcher, C. Balanis, K.J. Moeller and C.C. Quatch, *FDTD predictions of HIRF penetration into a Boeing 757*, Proceedings of IEEE EMC Symposium, Denver, USA, August 1998, pp. 670-672

[2.27] C.C.R. Jones, I.P. MacDiarmid, R.J. Simpson and C.P. Loller, *A review of approaches to the enhancement of performance in computational methods applied to electromagnetic hazards*, Proceedings of 3rd International Conference on Computation in Electromagnetics, University of Bath, UK, April 1996, IEE Conference Publication No. 420, pp. 89-95

[2.28] R. de Leo, G. Cerri, L. Claretti, V. Mariani Primiani, M. Moscariello and M. de Riso, *Theoretical and experimental radiated immunity tests on cars*, Proceedings of the 4th European EMC Conference, Brugge, Belgium, September 2000, Volume 1, pp. 449-452

[2.29] C. Christopoulos, P.B. Johns, A. Mallik and P. Naylor, *The use of numerical modelling techniques for EMC studies in vehicles*, Proceedings of 6th International Conference on Automotive Electronics, London, UK, October 1987, pp.159-163

[2.30] J.L. Herring and C. Christopoulos, *The vehicle body as an electromagnetic shield – numerical simulation for emission and susceptibility studies*, Proceedings of 7th International Conference on EMC, York, UK, August 1990, pp. 125-131

[2.31] D.D. Ward and S. Lawton, *Numerical modelling for automotive EMC*, Proceedings of IEEE EMC Symposium, Atlanta, GA, USA, August 1995, pp. 222-227

[2.32] C. Christopoulos and I. Argyri, *Characterisation of EMC environments using numerical simulation*, Proceedings of IEEE EMC Symposium, Denver, USA, August 1998, pp. 334-338

[2.33] A.R. Djordjevic, M.B. Bazdar, T.K. Sarkar and R.F. Harrington, *AWAS for Windows: analysis of wire antennas and scatterers*, Artech House, Boston, 1995

[2.34] D.P. Johns, R. Scaramuzza, and A.J. Wlodarczyk, *'Micro-Stripes' – microwave design tool based on 3D-TLM*, Proceedings of 1st International Workshop on Transmission Line Matrix (TLM) Modeling – Theory and Applications, Victoria, BC, Canada, August 1995, pp.169-177

[2.35] J.L. Dubard and D. Pomeir, *Simulation of Berenger's perfectly matched layer with a modified TLM node*, IEE Proceedings Part H, Microwaves, Antennas and Propagation, Vol. 144, No. 3, June 1997, pp. 205-207

[2.36] J.L Herring and C. Christopoulos, *Solving electromagnetic field problems using a multiple grid transmission-line modeling method*, IEEE Transactions on Antennas and Propagation, Vol. 42, No. 12, December 1994, pp. 1654-1658

[2.37] A.J. Wlodarczyk and D.P. Johns, *New wire interface for graded 3-D TLM*, Electronics Letters, Vol. 28, No. 8, April 1992, pp. 728-729

[2.38] A.J. Wlodarczyk, V. Trenkic, R.A. Scaramuzza and C. Christopoulos, *A fully integrated multiconductor model for TLM*, IEEE Transactions on Microwave Theory and Techniques, Vol. 46, No. 12, December 1998, pp. 2431-2437

[2.39] V. Trenkic and R.A. Scaramuzza, *Modelling of arbitrary slot structures using transmission line matrix (TLM) method*, Proceedings of 14th Zurich EMC Symposium, February 2001, pp. 393-396

[2.40] G. Butlin and C. Stops, *CAD data repair*, Proceedings of 5th International Meshing Roundtable, Pittsburgh, PA, USA, October 1996, pp. 7-12

CHAPTER 3: MODEL VALIDATION

The modern scientific method has successfully developed on the basis that observations of the real world are used to construct a theory, and that the theory is used to generate predictions that are then tested against further real world observations. The theory, therefore, aims to identify and quantify the links between cause and effect. Such a theory can then be considered successful if the predictions are useful, and this generally implies that the predictions give a good indication of real world behaviour [3.1], irrespective of its inherent truth or falsity.

In the first chapter of Feynman's "Lectures on Physics" [3.2], the introductory remarks include the following statement:

> * The principle of science, the definition almost, is the following: *The test of all knowledge is experiment.* Experiment is the *sole judge* of scientific "truth".

An unfortunate consequence of the successful theory is that it may become regarded as "true" in some fundamental sense. In reality, however, all theories are "models", human constructs with limited domains of validity, and as such will inevitably be refuted as these limits are probed. When this point is reached the theory may be refined or generalized in some way, or perhaps even replaced with a radically different view (Kuhn's "paradigm shift" [3.3]), and the cycle of "predict and test" enters another series of iterations. The process of conjecture and refutation as a means of progressing science, proposed by Popper [3.4], is termed "falsification". This view overcomes many of the limitations of the Carnap's view of progressing science through the acquisition of "gradually increasing confirmation" [3.5].

3.1 Measurements as reference data

The inherent superiority of experimental results is also normally assumed in the assessment of EMC models. For example, Tesche et al [3.6] assert that:

> It is useless for an engineer to develop a model without checking it using real data, or at least with experiments that simulate the real situation.

As an alternative, they are prepared to accept validation against a different computational technique provided that this has been validated against experiment. At first sight this approach may suggest that the measurements that are used to test theoretical models are essentially objective. This, again, is the view espoused by Feynman [3.2] in his description of the scientific method:

> Now, how can an experiment be "wrong"? First, in a trivial way: if something is
> wrong with the apparatus that you did not notice. But these things are easily fixed,
> and checked back and forth. So without snatching at such minor things, how *can*
> the results of an experiment be wrong? Only by being inaccurate.

This seems a reasonable position in principle, but in practice measurements are rarely simple, and accuracy is not the only issue to influence the results. The term "accuracy" refers to the closeness of the measurements to the real value of the physical quantity. The features that limit the accuracy of a measurement are the "errors of observation", which comprise both "accidental" and "systematic" components [3.7]. As noted by Popper [3.8], however:

> observation always presupposes the existence of some system of expectations

Thus, measurements will also generally rely on some theoretical model to support and inform the interpretation of their "measured" parameters from the quantities that are actually observed. This "interpretation model" is likely to comprise the theoretical basis for the design of the measurement equipment and the test method, augmented with some assumptions about the nature of the stimulus, the influence of the transducers and quality of the test environment. It is, however, quite conceivable that there could be some flaw in the interpretation model, although the values generated by the instrumentation will remain independent of this. Thus, it is possible that the same measurement could support a different model as its interpretation shifts. Consequently, the role of measurements as the ultimate gauge of correctness is not always as clear as is often expected.

In modern electromagnetic metrology any such shifts in interpretation are likely to be subtle, as electromagnetic theory is amongst the most successful and widely exploited branches of physics. Any change in the interpretation of electromagnetic measurements in engineering applications are most likely to arise from improved understanding of measurement artefacts, such as environmental effects or shortcomings of the test and calibration methods.

For example, electric field strength can be measured using a calibrated antenna, but the calibration of the antenna can only be sensibly specified in terms of a uniform field with a particular polarization and frequency. Other spatial field distributions and polarizations will not provide a unique value. Thus, when the device is used to sample some unknown field the received voltage is interpreted in terms of a uniform field. However, the sampled field may deviate from this ideal, or the antenna may be used in an environment that causes its characteristics to be modified in some way (eg. near to a conductor). The "measured" field will then be interpreted, incorrectly, as that uniform field strength which the calibration indicates would result in the voltage received at the antenna terminals in the reference environment.

The difficulties in validating models against measurements that may be influenced by unexpected or erroneously neglected effects that may modify the result, as well as establishing which is correct when they are not the same, are recognized by Archambeult [3.9]:

> Creating a model and a test setup which provide results which agree is quite challenging. While the measured results are often assumed to be the "correct" result when the model and measurement disagree, the truth is usually that both results are "correct", just for different problems.

It is important to note, however, that while the features of the model are known in considerable detail, because they have been deliberately introduced, the same may not be true of the measurement. Thus, while the model is likely to be correct within its own limitations, provided that it has been successfully implemented, the significance of practical limitations for the validity of physical measurements is not always easy to identify.

The experiment may well provide an accurate representation of the measured parameter, but this does not guarantee that our interpretation of that parameter is correct. Thus, the measurement may represent a parameter that is different to the one that the model is attempting to predict. The measurement, in fact, is no less in need of validation than the mathematical model.

3.2   Measurements as models

The reality for practical measurements on any realistic system is that numerous assumptions must inevitably be made in the interpretation of the readings provided by the instruments. The most common assumption is that the transducers that are used to monitor the parameters of interest have no influence on the value that is obtained.

Some form of calibration procedure is normally used to correct for such effects, but this relies upon the validity of a further measurement. Other aspects that can be expected to have a bearing on the results include:

- interactions between the transducer and the system under test
- influences due to the test environment
- differences between the artificial test configuration and the real world.

Given these limitations, it is apparent that there is no guarantee that measurements will provide the desired absolute reference. In fact it seems more appropriate to consider a measurement as an "experimental model", providing another imperfect representation of the parameter of interest. However, the fact that such a parameter is physically measured does not in itself guarantee that the result has greater validity than a result obtained from a mathematical model. This view suggests that a more reliable validation strategy would be to compare results obtained from a number of sources, ideally based on a range of theoretical and experimental models exploiting different techniques. The results of such a cross comparison would then provide much greater confidence in the similarities or disparities that are revealed.

3.3   Nature of different models

The most significant difference between the experimental and mathematical models is that it is not possible to access the parameter of interest directly in a physical measurement. A physical interaction is always necessary in order to obtain a quantitative result. Thus, the measurement process, and the assumptions that are used to interpret the result, may well profoundly influence the value obtained from the measurement. In addition, the nature of the excitation in a theoretical model is likely to be unrealistically simplified relative to that of a practical measurement. Consequently, the results from experimental and "conventional" mathematical models, which do not reflect these practical details, cannot be expected to be directly comparable. Striving for higher fidelity models in terms of geometric detail, mesh discretization and material properties will be of no significant benefit if the numerical model does not adequately capture the physical measurement process as well.

In the mathematical model, by contrast, it is more common to compute absolute values for the parameters of interest directly. This is equivalent to carrying out measurements with perfect probes, which can provide values at localized points and do not exert any influence on the system under test. Nonetheless, it is in principle possible to augment the basic model with a representation of the measurement transducer, and perhaps a better model of the excitation.

In this way it is possible to create a sub-set of mathematical models which can be described as "simulated measurements", which aim to bridge the gulf between conventional mathematical models and practical experiments. It then becomes more realistic to expect to achieve a good degree of correlation between the data provided by the experimental model and the results obtained from a simulated measurement. This approach therefore makes the experimental validation of theoretical predictions a much more viable proposition.

3.4 Validation of numerical models

The validation process for any numerical technique can be decomposed into three distinct levels [3.9], which could be classified using the terms "formulation", "implementation" and "application". Firstly, it is necessary to demonstrate that the proposed numerical technique does indeed have the capability to represent the physical phenomena that it aims to model in a consistent manner (ie. that the underlying formulation of the numerical method is correct). Detailed analytical studies and the investigation of spurious or non-physical model features that can arise from numerical solutions form the basic elements of this "formulation level" validation.

Secondly, it is essential to demonstrate that the theoretical techniques have been correctly implemented in any software that is used to carry out practical modelling using these methods. Moreover, as part of this implementation phase it is also necessary to validate the pre-processing and data analysis capabilities that are used to build the model and analyse the results. The "implementation level" validation is normally carried out using models of standard or canonical test cases, by demonstrating correlation with results which have already been obtained using alternative codes or analytical methods, and perhaps even with reliable measurement data.

Finally, it is necessary to establish that models of complex systems can provide credible and useful results. This stage is much more difficult as the potential for errors in model construction becomes much greater as the complexity of systems under investigation also rises. Furthermore, success in the "application validation" phase also becomes increasingly dependent on the understanding and experience of the analyst in developing the skills needed to:

- exploit the strengths of the modelling technique
- mitigate the weaknesses of the modelling technique
- identify the significant elements of the system
- approximate the problem to ensure computational tractability.

The formulation and implementation levels depend essentially upon "direct validation" of results from different sources for success. This is necessary in order to establish that the fundamental method is reliably formulated and implemented. Ideally, the types of test cases to be used in these preliminary stages should be sufficiently simple that there is no uncertainty as to whether the results have been successfully validated or not.

The same type of direct comparison is also the most desirable method for the application level validation, where the aim is generally to demonstrate an acceptable degree of correlation with experimental results for test cases of representative complexity. However, this is at best a difficult option for real world models, because of the complexity of the systems under investigation. Nonetheless, this type of validation data is essential in order to demonstrate the credibility of modelling techniques, and a considerable amount of EMC modelling research effort is devoted to generating a convincing body of results for this purpose.

In some circumstances it may be possible to obtain some form of "indirect" validation evidence, which could be based on measurements that are not directly represented in the model under investigation. This may be achieved by showing that the trends and behaviour that are predicted using a representative model are also observed in similar real systems. Although such qualitative results are not as immediately convincing as a direct comparison, they are nonetheless very useful indicators. Possible examples of indirect validation of electromagnetic models for EMC applications could include measured emissions peaks occurring at frequencies identified as cavity resonances in an immunity model. Other forms of indirect validation providing quantitative results could perhaps be based on statistical correlations.

The ultimate objective of validation at the application level is to establish sufficient confidence in the basic quality of the numerical results for them to be used without reference to experiment. This will allow these techniques to be used to their full effect, but good practice would require some form of basic checking to be applied, even where confidence high.

The investigation of internal consistency in "intermediate" results from numerical simulations has been proposed as an alternative where other sources are not available [3.9]. The nature of such results will vary with the particular method under consideration. Features such as abrupt changes in the values between neighbouring cells or elements and other non-physical behaviour, such as finite currents at the ends of un-terminated wires or mesh-related dispersion effects, may also indicate defects in the formulation, implementation or application of the numerical method.

Furthermore, time series that are truncated too early or frequency steps that are too large would also make the results questionable. In finite element models the presence of highly distorted element shapes can be expected to result in poor results.

3.5   Modelling experimental processes

Effective calibration of measurement transducers is essential to obtain experimental data that is both valid (in terms of the interpretation of the results) and of quantifiable accuracy. The nature of the transducer and the methods used to calibrate the device may therefore have a profound influence on the measurement. Thus, the consideration of transducer calibration issues is also a key feature for the success of attempts to validate numerical models against practical experiments.

The basic transducers used in EMC measurements are current probes, antennas and broadband field probes. Broadband field probes provide amplitude information only, and are not amenable to calibration via scattering matrix measurements. The calibration of field probes therefore depends on indirect methods, based on a previously calibrated antenna or a TEM cell that is assumed to provide calculable field strength. Current probes and antennas may be used as both excitation sources and measurement devices. These transducers may also be calibrated using scattering matrix measurements carried out using vector network analysers, which provide both amplitude and phase information with a good degree of accuracy.

A detailed understanding of the assumptions and limitations associated with the calibration of basic transducers is important since they are used to carry out direct measurements, as well as providing reference points in the calibration of other equipment and larger scale systems, such as EMC test environments. The latter may include open area test sites, anechoic or semi-anechoic chambers and TEM cells.

The ability to perform simulated measurements also raises the possibility investigating the experimental process used in a measurement. This differs from the use of modelling in design studies, where a number of model variants may be used to evaluate a range of options or to optimise the details of a particular design. Although this type of activity emulates physical prototyping, and is therefore often described as "numerical experimentation", it does not normally address the problems of measuring the parameters of interest. Thus, "numerical prototyping" is perhaps a more accurate description for design studies based on such models. The aim in modelling the experiment, however, is to simulate not only the system of interest, but also key elements of the process that is used to make practical measurements on the system.

By harnessing the features of the simple mathematical model and the simulated measurement it becomes possible to investigate the influence of transducers and the wider environment on the "experimental models". Unlike any physical measurement, this theoretical approach provides access to both absolute values and simulated measurements. This additional information makes it possible to quantify the significance of practical measurement issues, thus improving understanding of the measurements and, in particular, their interpretation. Modelling the experimental process therefore offers several unique advantages over measurements, including:

- access to absolute quantities as well as simulated transducer responses
- known and repeatable source characteristics
- precise and repeatable geometric positioning
- a controlled test environment.

The study of such models provides insights into the interpretation of practical experiments that facilitate the development of experimental methods and their associated calibration techniques. The ability to develop simulated measurements that are more appropriate for validation against experimental data also permits the limitations of the theoretical models to be established and addressed more reliably.

3.6   Conclusions

Demonstrating the validity of numerical results against practical experiments is essential for both the development and the promotion of numerical methods in EMC applications. However, closer consideration of typical assumptions concerning the inherent objectivity of measurements suggests that validation by simple comparison of model results against physical measurements is not, in general, as straightforward as is commonly assumed.

Measurements generally depend on some form of "interpretation model", so the results are not necessarily absolute but reflect the expectations of the designer of the experiment. It seems, therefore, more appropriate to consider a measurement as an "experimental model", providing another imperfect representation of the parameter of interest. The measurement, in fact, is no less in need of validation than the mathematical model. Building confidence through the successful comparison of results from a number of differing experimental and numerical methods is probably the best approach in the validation of both measured and computed results for complex systems. However, practical constraints generally limit the availability of data for validation purposes, so numerical models must reflect the key features of the measurement in order to maximize the chances of a successful outcome.

Numerical methods can be used to undertake "simulated measurements", which represent the key elements of the measurement process as well as the system of interest. Consequently, mathematical models are uniquely able to provide both absolute values and simulated measurement results. Such data can be used both to maximize the success of model validation studies and to illuminate the interpretation of experimental results, thus providing significant benefits to both experimental and numerical methods.

3.7   References

[3.1]   L. Laudan, *Progress and its problems,* University of California Press, Berkeley, CA, USA, 1977, p. 13

[3.2]   R.P. Feynman, R.B. Leighton and M. Sands, *Lectures on physics: volume I,* Addison-Wesley, Reading, MA, USA, 1963, p. 1-1

[3.3]   T.S. Kuhn, *The structure of scientific revolutions,* University of Chicago Press, Chicago, IL, USA, 1962

[3.4]   K.R. Popper, *The logic of scientific discovery,* Hutchinson, London, 1959

[3.5]   R. Carnap, *Philosophical foundations of physics,* Basic Books, New York, 1966

[3.6]   F.M. Tesche, M.V. Ianoz and T. Karlson, *EMC analysis methods and computational models,* Wiley, New York, 1987, §1.2

[3.7]   J. Topping, *Errors of observation and their treatment,* Chapman and Hall, London, Fourth Edition, 1972, p. 14

[3.8]   K.R. Popper, *Objective knowledge: an evolutionary approach,* Clarendon Press, Oxford, UK, 1972, p. 344

[3.9]   B. Archambeult, *Modeling and simulation validation for EMC applications,* Proceedings of 1999 IEEE EMC Symposium, Washington, USA, pp. 492-496

CHAPTER 4:   CABLE NETWORK MODELS

The electrical and electronic systems in vehicles are interconnected via a complicated wiring harness. The harness assembly typically contains many individual cables (of various types, but rarely screened or twisted) and is complicated by the presence of many loops, branches and grounding points (see Fig. 4.1).
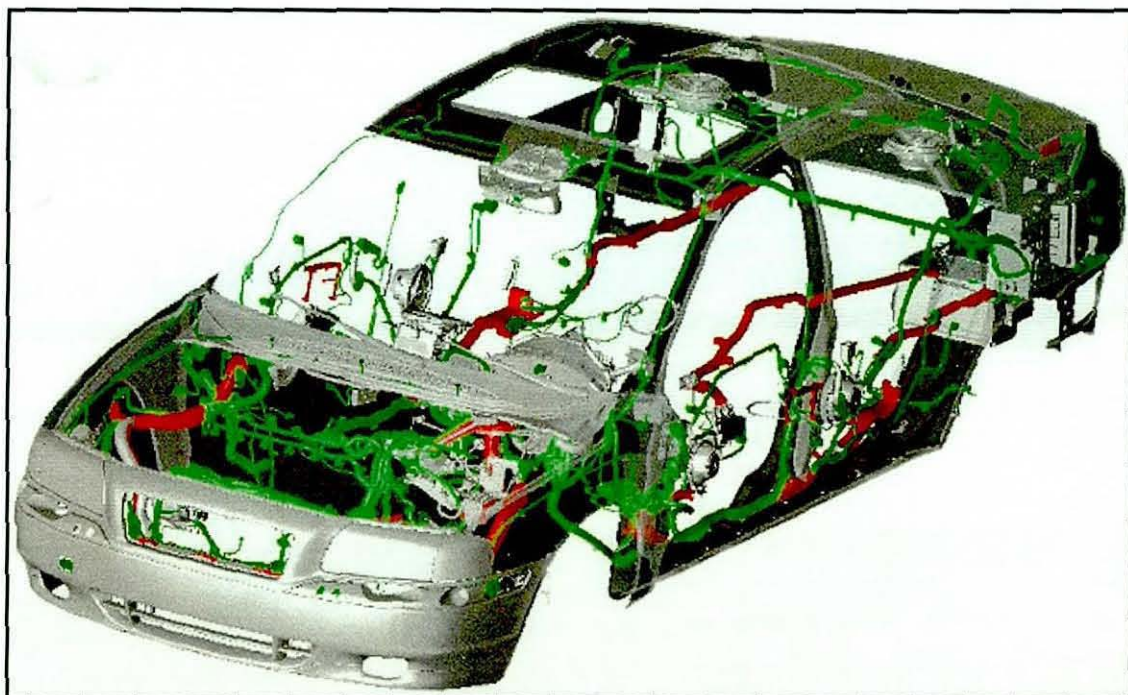

Fig. 4.1   Representative vehicle harness configuration
(courtesy of Volvo Car Corporation, Sweden)

Even for a modern vehicle exploiting multiplex bus technology to link the electrical and electronic systems, the total length of harness in the vehicle is likely to be around 2.5 km and the number of terminals is of the order of 10^3. Since the vehicle structure provides only limited electromagnetic shielding, coupling onto the wiring harness and hence into the electronic systems is a potential threat to the immunity performance of vehicles. The harness therefore represents an extremely significant component for the electromagnetic characteristics of the vehicle.

4.1   Scattering matrix representation

If it is assumed that the electronic modules are well designed then the emissions from these units and their response to radiated electromagnetic fields should be very low.   The most significant factors in promoting the coupling of energy from one system to another are then the vehicle structure and its associated harness.   Under these assumptions, the vehicle installation could be considered in terms of a "microwave junction" [4.1] with many ports.

Since the system also radiates, both intentionally and unintentionally, the vehicle and its harness effectively act as a complex multi-port antenna, with transmitters and receivers located at the harness terminations.   Taking this view of vehicle EMC and antenna issues (ie. as a microwave network problem) the system can be conveniently characterized in terms of the "scattering matrix" [4.2] for the vehicle system, representing the harness terminations and any on-board antenna terminals as the ports.   In studying vehicle electromagnetic metrology issues, this network could also be extended to include the test antennas used to excite or monitor the system under test.

In microwave systems the network is usually assembled from a number of devices and waveguide elements for which the port impedances and coupling paths are well defined.   In general the overall system will only have a few ports, but the paths between them may include many subsystems (although for structures such as phased array antenna systems the number of ports may reach a few hundred).   In considering the vehicle installation, however, the number of ports is always very large, the coupling paths may not be clear, and the termination impedances are likely to vary with frequency and operational mode.   Harness routes are generally in close proximity to the vehicle structure, so transmission line approximations can be applied for "immunity" analysis.   Neglecting scattering and re-radiation, the fields at the location of the wire (with the wire absent) can be used as inputs to a 1D network model, which will give the terminal currents and voltages if the termination impedances are known.

Since a transmission line can receive energy it must also, by reciprocity, be capable of radiating energy.   The analysis of "intra-system" EMC and radiated emissions performance therefore requires knowledge of the current distribution along the excited cables, which could be provided by a 1D network model, and the interaction between the radiated fields and the surrounding structure, for which a 3D model is required.   Any variability or uncertainty in the termination impedances is therefore costly for separated schemes in these applications. Furthermore, some elements of the harness may be a significant distance from the vehicle structure (eg. under the dashboard and in the engine bay), for which 3D modelling will be unavoidable.

4.2   Simple two-port wire network

Attempts to validate 3D models of representative networks have been carried out using simple wire networks adjacent to a ground plane [A.7]. The networks were constructed such that the individual wires could be terminated using coaxial connectors. This ensured that the complexity of the system was controlled, allowing accurate measurements to be carried out using a network analyser. Thus, it was possible to measure both the amplitude and phase of the elements of the scattering matrix for the network between the coaxial ports. In addition, analytical models for these simple networks were developed, in order to provide an additional source of validation data.

Experimental arrangement

The simplest case that can be considered is transmission through a single wire above a ground plane, which is connected between the centre pins of two coaxial connectors. For experimental purposes, a 3 mm thick square aluminium plate with a side of 1 m was drilled to accommodate a number of coaxial connectors providing a female N-type connector and a projecting centre pin and mounting flange of SMA format. The presence of an insulating sheath around the conductor influences both the characteristic impedance and the propagation constant. However, since the properties of the insulation were not known, this material was removed from the conductor for the purposes of these investigations. The dielectric sheath around the projecting centre pin of the connectors was also trimmed back until flush with the surface of the ground plane. This is illustrated in Fig. 4.2, which provides a schematic view of the experimental arrangement.
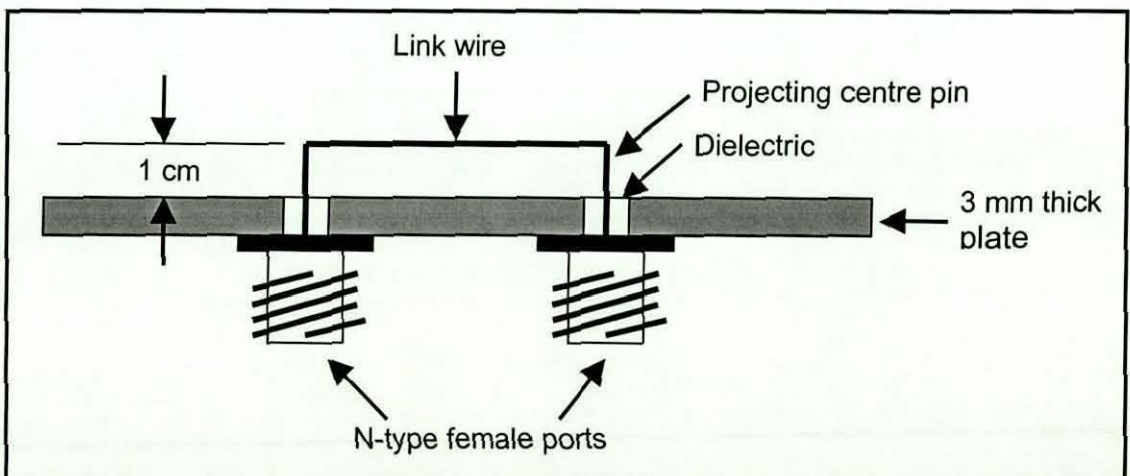

Fig. 4.2   Schematic view of experimental two-port network

The N-type connection was desirable in order to ease the problems of connecting the system under test to a network analyser, as these instruments are typically equipped with N-type ports. The reduced dimensions provided by the SMA format were selected to minimize disparities between idealized models (which do not take any account of the significance of the dielectric material which is present where the test network emerges from the ground plane) and the experimental measurements.

The separation of the projecting centre pins for the two-port network, and hence the length of the link wire at 1 cm above the ground plane, was 0.6 m. Single conductor wires with a diameter of 0.9 mm (2.5 mm^2 domestic wiring cable) were also used in order to obtain mechanical rigidity and thus avoid the need to include supports to maintain the height of the wire above the ground plane. Small pieces of expanded polystyrene foam ($\varepsilon_R \approx 1.03$) were used to counteract any distortion due to sagging.

Although the single wire TLM model [2.37] can accommodate a dielectric sheath, the multi-conductor formalism that has been developed [2.38] does not. None of the TLM wire models work well in close proximity to a ground plane since the formulations assume a symmetrical field distribution around the wire. Nonetheless, it is possible to achieve reasonable results if a few additional cells are inserted between the wire cells and the ground [4.4]. While this may be an acceptable approach for planar networks, it is not practicable for complex 3D geometries, where the need to introduce localized mesh refinement is highly undesirable.

Analytical model for two-port network

The characteristic impedance of the transmission line formed from the wire and the ground can be estimated from the capacitance of an infinitely long wire, provided that the frequency is sufficiently low that the spacing is a small fraction of the wavelength. For a wire of radius a at height h the characteristic impedance Z_0 is [4.5]:

$$Z_0 = 60\cosh^{-1}(h/a) \tag{4.1}$$

Assuming the system to be lossless, and neglecting any possible effects associated with the right angle bends at the connectors, the scattering matrix for the junction between the wire and the coaxial system is:

$$S = \begin{bmatrix} \Gamma & 1-\Gamma \\ 1+\Gamma & -\Gamma \end{bmatrix} \tag{4.2}$$

where the input reflection coefficient (Γ) from the coaxial side of the junction is:

$$\Gamma = \frac{Z_0 - Z_C}{Z_0 + Z_C} \tag{4.3}$$

and Z_C is the characteristic impedance of the coaxial system (usually 50 Ω for practical measurement systems).

The effective input reflection coefficient for the system comprising a pair of such junctions and an intermediate length y of transmission line with propagation constant $\beta(f)$ is then [4.6]:

$$\psi(f) = \Gamma \left[\frac{1 - e^{-2j\beta(f)y}}{1 - \Gamma^2 e^{-2j\beta(f)y}} \right] \tag{4.4}$$

Validation results for two-port network

Comparing the predictions of the models with experimental measurements obtained using a network analyser (HP8753A) it is found that good agreement is achieved if the length of the wire in the analytical model is extended to include the lengths of the two vertical pins at the connectors (see Fig. 4.3). Thus, for frequencies up to 600 MHz, the main effect of the 90° bends seems to be to extend the apparent length of the wire by the length of the vertical parts.
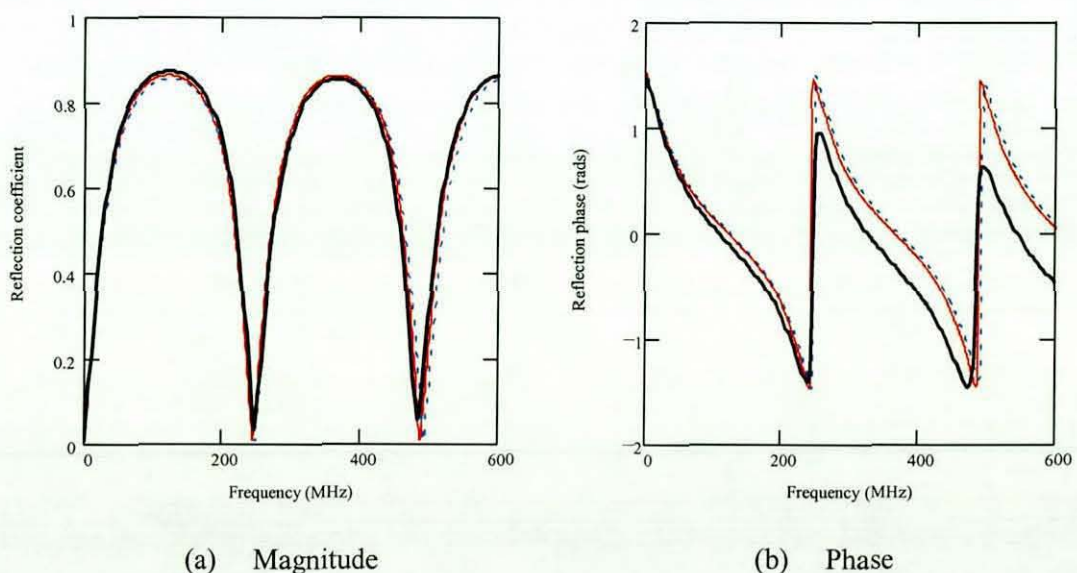

| (a)   Magnitude   (b)   Phase |

Fig. 4.3   Comparison of analytical (solid) and TLM (dotted) models with measured data (heavy line) for single wire 1 cm above ground

The analytical and numerical predictions are in very good agreement, giving confidence in these two results, but the agreement with measured results is markedly poorer for the phase than for the magnitude. The differences may be due to features that are inadequately represented in the models, but limitations in the accuracy of phase measurements are perhaps a more likely cause. The finite lengths of the connectors used to implement the coaxial ports add phase error that is not accounted for in the calibration. In addition, the "through" connection used in the calibration is of finite length and therefore also contributes to the phase errors.

4.3   Simple four-port wire network

The next level of complexity is to consider a pair of wires over ground. The system studied is illustrated in Fig. 4.4 below, comprising a pair of parallel wires that are linked to coaxial connectors via simple wire-over-ground transmission lines. Nonetheless, the analysis of this arrangement represents a very significant increase in analytical complexity, even when the system is configured for maximum symmetry.
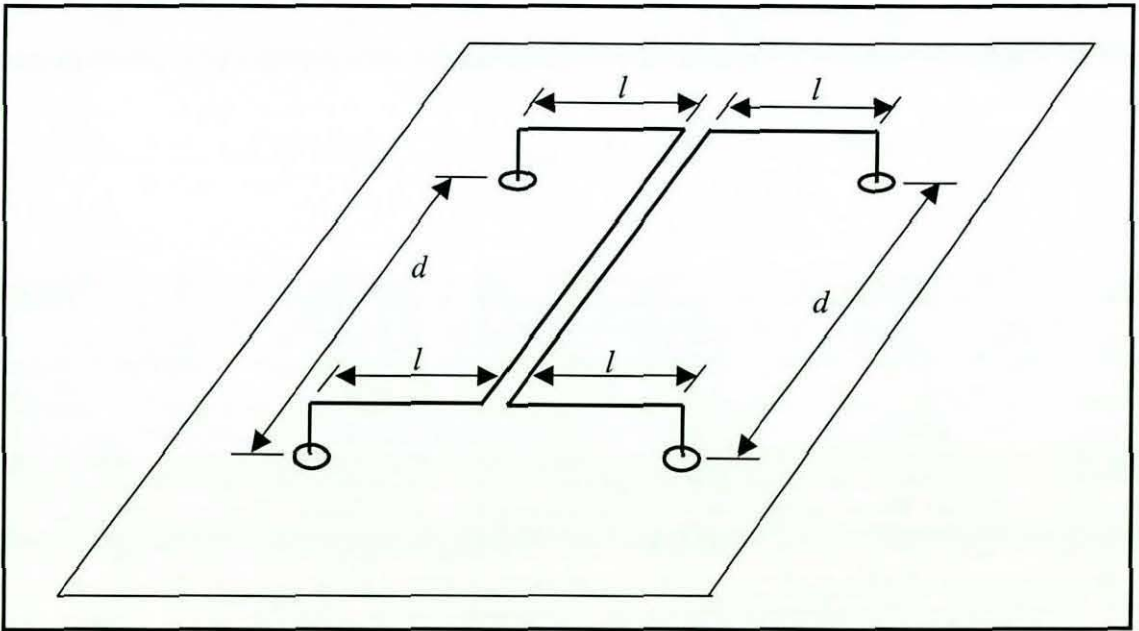

Fig. 4.4   Topology of symmetrical four-port network for validation studies

This kind of topology is used to implement directional couplers at RF and microwave frequencies (but using microstrip networks rather than wires). Careful selection of the length of the parallel conductor section ensures that the outputs have the required directional coupling characteristics over the frequency band of interest.

Properties of parallel wires over ground

The transmission lines linking the four-port network and the coaxial terminations support only a single TEM mode of propagation when the dimensions are small relative to the wavelength. The parallel wire section, however, supports both "odd" and "even" modes of propagation, as illustrated in Fig. 4.5 below.
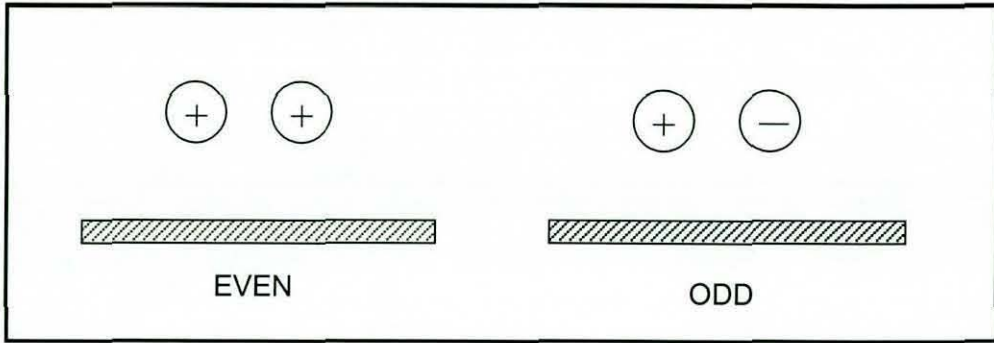

Fig. 4.5   Transmission line modes for pair of wires above ground

Analytical expressions for the characteristic impedances associated with these two modes for wires for wires of radius a at height h and separation s in air [4.5] are:

$$Z_{even} = 30\ln\left\{\frac{2h}{a}\sqrt{1+\left(\frac{2h}{s}\right)^2}\right\} \tag{4.5}$$

$$Z_{odd} = 120\ln\left\{\frac{s}{a}\left[1+\left(\frac{s}{2h}\right)^2\right]^{-\frac{1}{2}}\right\} \tag{4.6}$$

The expression for Z_{even} is based on a wide separation approximation, which breaks down for closely spaced wires as proximity effects distort the charge distribution around the periphery of the conductors. A two-dimensional electrostatic model for the charge distribution, including the proximity effect, was therefore used to obtain more accurate values for the odd and even mode impedance for the geometry used in the experiments. The numerical and analytical values differed by less than 2% for the configuration under investigation here, so the analytical results were considered to be adequate for the transmission line model in this case. As the insulation was removed from the wires used in this work, the propagation constants for the two modes are also identical in this case, and equal to $2\pi/\lambda$, where λ is the wavelength.

Analytical model of four-port network

The analysis of even this simple network is difficult by direct algebraic methods, because of the high level of connectivity. However, signal flow graph techniques [4.7] can be applied to simplify the analysis of such networks. Decomposition of the overall network into more manageable fragments is illustrated in Fig. 4.6, in terms of the scattering matrices for these subsections of the network.
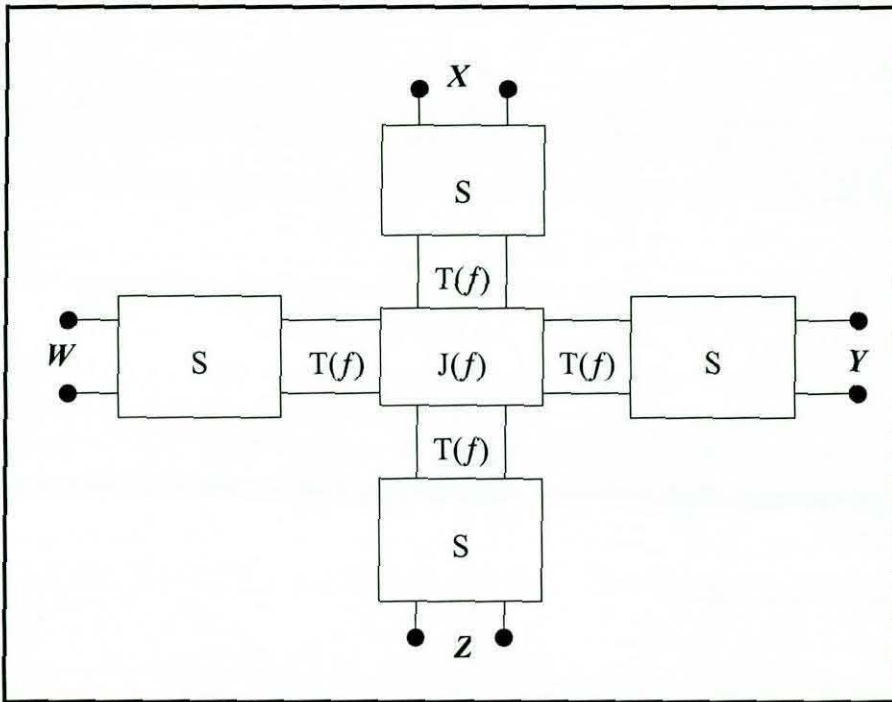

Fig. 4.6   Scattering matrix representation of symmetrical four-port network

The ports W, X, Y and Z refer to the coaxial terminations represented by the scattering matrix S (defined in section 4.2 above), while the central block $J(f)$ represents the length where the wires run in parallel. The scattering matrices $T(f)$ represent the lengths of transmission line linking the coaxial ports to the parallel section.

As all of the ports of this device are assumed to be connected to identical transmission lines, the symmetry of the device can be exploited to determine the scattering parameters of the parallel part of the network under matched conditions. The port numbering scheme is as indicated in Fig. 4.7, which relates the port designations to the physical layout of the network.
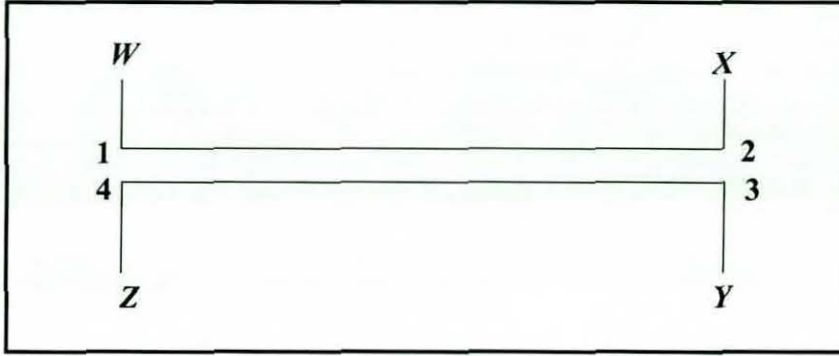
Fig.4.7   Port numbering scheme for overall network

Due to the four-fold symmetry of the network, there are only four independent parameters in the 4x4 scattering matrix $J(f)$ since:

$$J_{11}(f) = J_{22}(f) = J_{33}(f) = J_{44}(f) \tag{4.7}$$

$$J_{12}(f) = J_{21}(f) = J_{34}(f) = J_{43}(f) \tag{4.8}$$

$$J_{13}(f) = J_{31}(f) = J_{24}(f) = J_{42}(f) \tag{4.9}$$

$$J_{14}(f) = J_{41}(f) = J_{23}(f) = J_{32}(f) \tag{4.10}$$

The four scattering parameters describing the parallel conductor section can be determined from the symmetry of the system by superposition of the solutions for the four possible excitation modes, as detailed in [4.8]. The resulting expressions for the four independent elements of the scattering matrix are as follows:

$$J_{11}(f) = \frac{1}{4}\left[\Gamma_a(f) + \Gamma_b(f) + \Gamma_c(f) + \Gamma_d(f)\right] \tag{4.11}$$

$$J_{12}(f) = \frac{1}{4}\left[\Gamma_a(f) - \Gamma_b(f) + \Gamma_c(f) - \Gamma_d(f)\right] \tag{4.12}$$

$$J_{13}(f) = \frac{1}{4}\left[\Gamma_a(\ ) - \Gamma_b(f) - \Gamma_c(f) + \Gamma_d(f)\right] \tag{4.13}$$

$$J_{14}(f) = \frac{1}{4}\left[\Gamma_a(f) + \Gamma_b(f) - \Gamma_c(f) - \Gamma_d(f)\right] \tag{4.14}$$

The reflection coefficients $\Gamma_i(f)$ for each of the four modes are given by:

$$\Gamma_a(f) = \frac{Z_{even} \coth\left\{\beta_{even}(f)\frac{d}{2}\right\} - Z_0}{Z_{even} \coth\left\{\beta_{even}(f)\frac{d}{2}\right\} + Z_0} \qquad (4.15)$$

$$\Gamma_b(f) = \frac{Z_{even} \tanh\left\{\beta_{even}(f)\frac{d}{2}\right\} - Z_0}{Z_{even} \tanh\left\{\beta_{even}(f)\frac{d}{2}\right\} + Z_0} \qquad (4.16)$$

$$\Gamma_c(f) = \frac{Z_{odd} \coth\left\{\beta_{odd}(f)\frac{d}{2}\right\} - Z_0}{Z_{odd} \coth\left\{\beta_{odd}(f)\frac{d}{2}\right\} + Z_0} \qquad (4.17)$$

$$\Gamma_d(f) = \frac{Z_{odd} \tanh\left\{\beta_{odd}(f)\frac{d}{2}\right\} - Z_0}{Z_{odd} \tanh\left\{\beta_{odd}(f)\frac{d}{2}\right\} + Z_0} \qquad (4.18)$$

where d is the length of the parallel region, $\beta_{even}(f)$ is the propagation constant for the even mode, $\beta_{odd}(f)$ is the propagation constant for the odd mode, and Z_0 is the characteristic impedance of the transmission lines at the four inputs.

The signal flow graph for the parallel section can then be represented as shown in Fig. 4.8 below, where the parameter $\rho(f)$ represents the reflections at the terminals of the parallel section (due to the mismatch at the coaxial connectors and the length of transmission line between the connectors and the parallel conductors). Due to the symmetry of this network the terminal reflection coefficients are assumed to be identical for all ports.

In order to predict the scattering parameters of the network as a whole, it is necessary to reduce the complexity of the flow graph for the parallel wire section. This is achieved by systematically eliminating nodes and combining paths in the full flow graph until the reduced form shown in Fig. 4.9 is obtained.
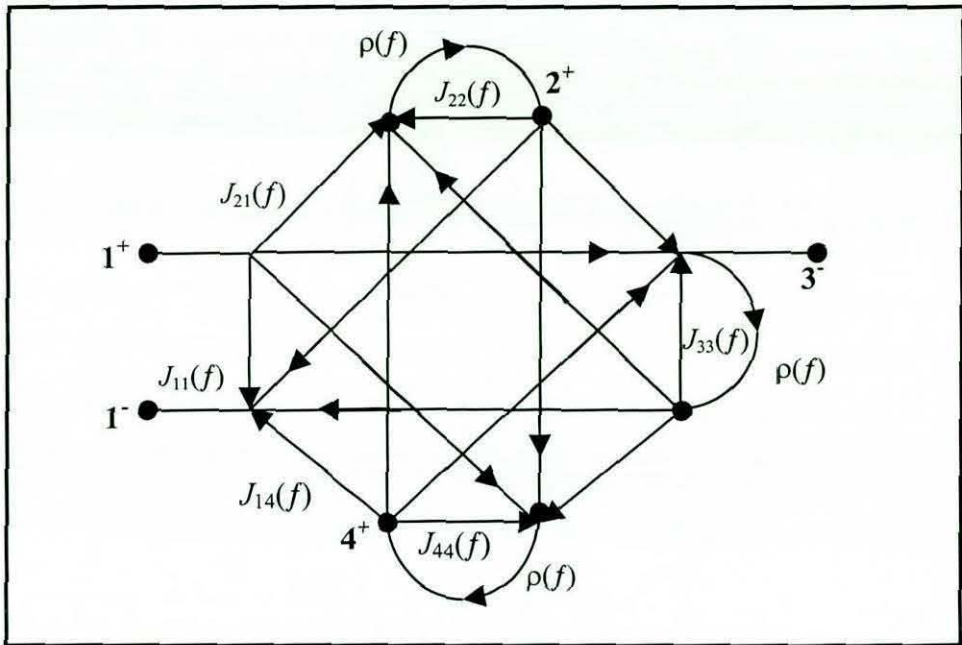
**Fig. 4.8   Signal flow graph for ports 1 and 3 of parallel section
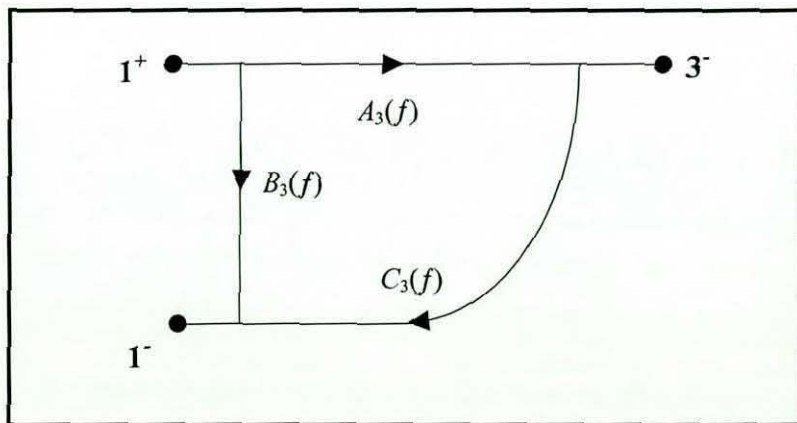with finite termination mismatches**

Fig. 4.9 Reduced signal flow graph for transmission from port 1 to port 3

The parameters $A_3(f)$, $B_3(f)$ and $C_3(f)$ of Fig. 4.9 that are derived from reduction of the flow
graph shown in Fig. 4.8 are as follows:

$$A_3(f) = \cfrac{\left\{ \begin{array}{l} \left[1 - \dfrac{\rho(f)^2 J_{13}(f)^2}{\zeta(f)^2}\right]\left[\dfrac{J_{13}(f)}{\zeta(f)} + \dfrac{\rho(f)J_{12}(f)J_{14}(f)}{\zeta(f)^2}\right] + \ldots \\[3ex] + \left[\dfrac{J_{14}(f)}{\zeta(f)} + \dfrac{\rho(f)J_{12}(f)J_{13}(f)}{\zeta(f)^2}\right]\left[\dfrac{\rho(f)J_{12}(f)}{\zeta(f)} + \dfrac{\rho(f)^2 J_{13}(f)J_{14}(f)}{\zeta(f)^2}\right] \end{array} \right\}}{\left[1 - \dfrac{\rho(f)^2 J_{13}(f)^2}{\zeta(f)^2}\right]\left[1 - \dfrac{\rho(f)^2 J_{14}(f)^2}{\zeta(f)^2}\right] - \left[\dfrac{\rho(f)J_{12}(f)}{\zeta(f)} + \dfrac{\rho(f)^2 J_{13}(f)J_{14}(f)}{\zeta(f)^2}\right]^2} \tag{4.19}$$

$$B_3(f) = J_{11}(f) + \frac{\rho(f)}{\zeta(f)}\left\{ J_{12}(f)^2 + \frac{\left[J_{14}(f) + \dfrac{\rho(f)J_{12}(f)J_{13}(f)}{\zeta(f)^2}\right]^2}{\left[1 - \dfrac{\rho(f)^2 J_{13}(f)^2}{\zeta(f)^2}\right]} \right\} \tag{4.20}$$

$$C_3(f) = \rho(f)J_{13}(f) + \frac{\rho(f)^2}{\zeta(f)}\left\{ \begin{array}{l} J_{12}(f)J_{14}(f) + \ldots \\[2ex] + \dfrac{\left[J_{12}(f) + \dfrac{\rho(f)J_{13}(f)J_{14}(f)}{\zeta(f)}\right]\left[J_{14}(f) + \dfrac{\rho(f)J_{12}(f)J_{13}(f)}{\zeta(f)}\right]}{\left[1 - \dfrac{\rho(f)^2 J_{13}(f)^2}{\zeta(f)^2}\right]} \end{array} \right\} \tag{4.21}$$

where the terms $\rho(f)$ and $\zeta(f)$ represent:

$$\rho(f) = S_{22}(f)e^{-2j\beta(f)x} \tag{4.22}$$

$$\zeta(f) = 1 - \rho(f)J_{11}(f) \tag{4.23}$$

and x is the length of the wires connecting the parallel section to the coaxial connectors.

This analysis assumes that the objective is to determine the reflection at port 1 and the transmission through to port 3 of the parallel wire section. Nonetheless, the four-fold symmetry of the network also allows transmission to the remaining two ports of the system to be obtained by appropriate permutation of the indices in the preceding expressions for the matrix elements J_{1j} (where $j \in \{2,3,4\}$) to provide values for the parameters $A_i(f)$, $B_i(f)$ and $C_i(f)$ (where $i \in \{2,4\}$).

The overall response for the complete system, between any pair of coaxial ports, can then be obtained by reducing the wider network, as illustrated in Fig. 4.10 for ports W and Y.
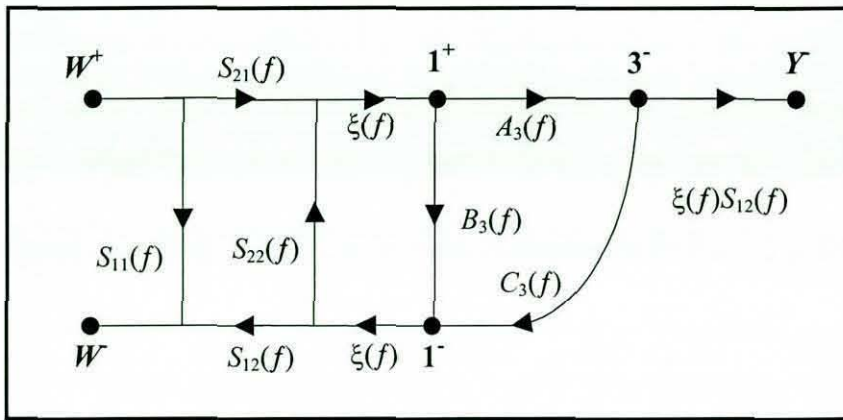
Fig. 4.10   Signal flow graph for transmission from port W to port Y of overall network

Reduction of the flow graph shown in Fig. 4.10 results in an expression for the input reflection coefficient $\psi_P(f)$ at each port of the full network of the form:

$$\psi_P(f) = S_{11}(f) + \frac{S_{12}(f)S_{21}(f)\xi(f)[B_i(f) + A_i(f)C_i(f)]}{1 - S_{22}(f)\xi(f)[B_i(f) + A_i(f)C_i(f)]} \qquad (4.24)$$

The transmission coefficient $\tau_i(f)$, where $i \in \{2,3,4\}$, between any pair of ports is given by:

$$\tau_i(f) = \frac{S_{12}(f)S_{21}(f)\xi(f)A_i(f)}{1 - S_{22}(f)\xi(f)[B_i(f) + A_i(f)C_i(f)]} \qquad (4.25)$$

where the parameter $\xi(f)$ represents transmission through the wires connecting the parallel wires to the coaxial connectors:

$$\xi(f) = e^{-j\beta(f)x} \qquad (4.26)$$

The analytical expressions indicate that the positions of the nulls in the magnitude of the reflection coefficient are determined primarily by the length of the through connections. However, the length of the parallel sections determines the positions of nulls in the transmission coefficients.

Comparison of four-port network results

The measurements were carried out using a metal plate approximately 1 m^2 containing 4 coaxial connectors with projecting centre pins (in SMA format) mounted on a 40 cm grid. Experimental results were obtained for two such symmetrical four-port networks, in which the length of the parallel section and the length and angle of arrival of the feed lines differed (see Fig. 4.11). In both cases the separation of the parallel wires was 8 mm, and all wires were 1 cm above the ground plane. Several measurements of the characteristics of these two networks were obtained, using two different vector network analysers (HP 8753A and Wiltron 37347A).
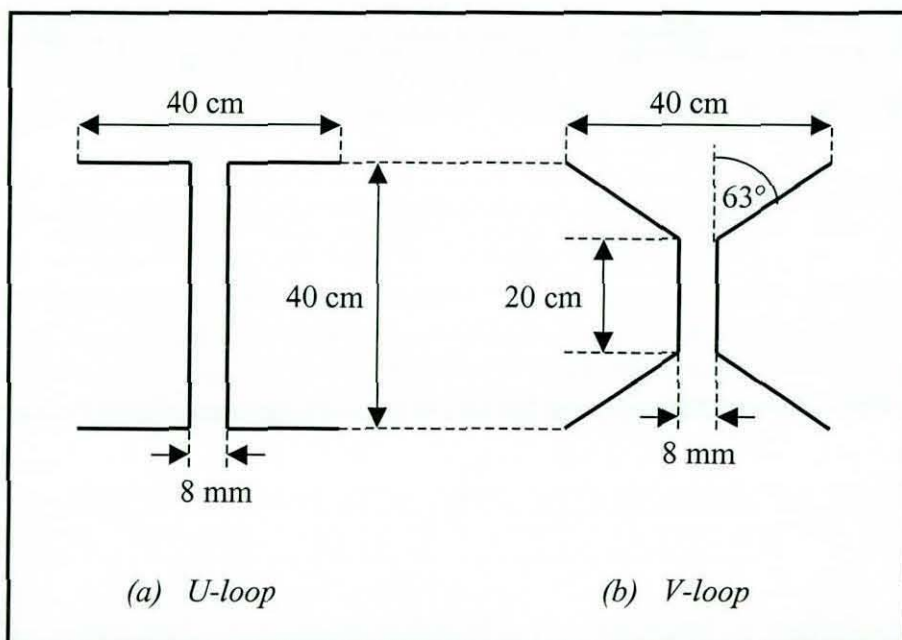

Fig. 4.11   Geometry of 4-port wire networks used for experimental validation

In the first case (designated the "U-loop") the length of the parallel section was nominally 0.4m and the feed lines were 0.196 m long, arriving at 90° to the parallel section. In the second case (the "V-loop") the length of the parallel section was 0.2 m and the feed lines were 0.22 m long, arriving at an angle of almost 63° to the parallel section. Sample results for the V-loop configuration are illustrated in Figs. 4.12, showing the magnitudes of the input reflection coefficient and one of the transmission paths. The results for the input reflection coefficient of the V-loop are reasonable in terms of the positions of the features and the maximum levels that are achieved. For transmission, however, there are larger variations in the amplitudes of the measurements, although the overall topology of the frequency response is very similar for each curve.
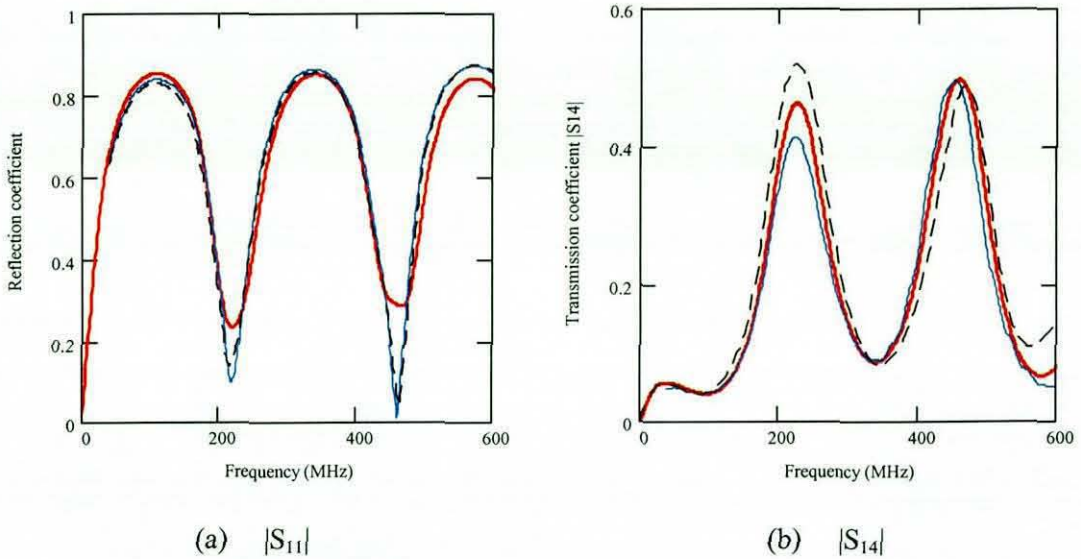
(a) $|S_{11}|$ (b) $|S_{14}|$

**Fig. 4.12   Results for the "V-loop" configuration derived from the analytical model
(heavy line) and measurements (light and dashed lines) with two
different network analysers**

Sample results for the U-loop configuration are illustrated in Figs. 4.12, with a 2 mm adjustment applied to the length x in the analytical models in order to represent the finite bend radius at the ends of the parallel section. The results for the input reflection coefficient of the U-loop configuration are not quite as good as for the V-loop, and the transmission results are much poorer in this case.
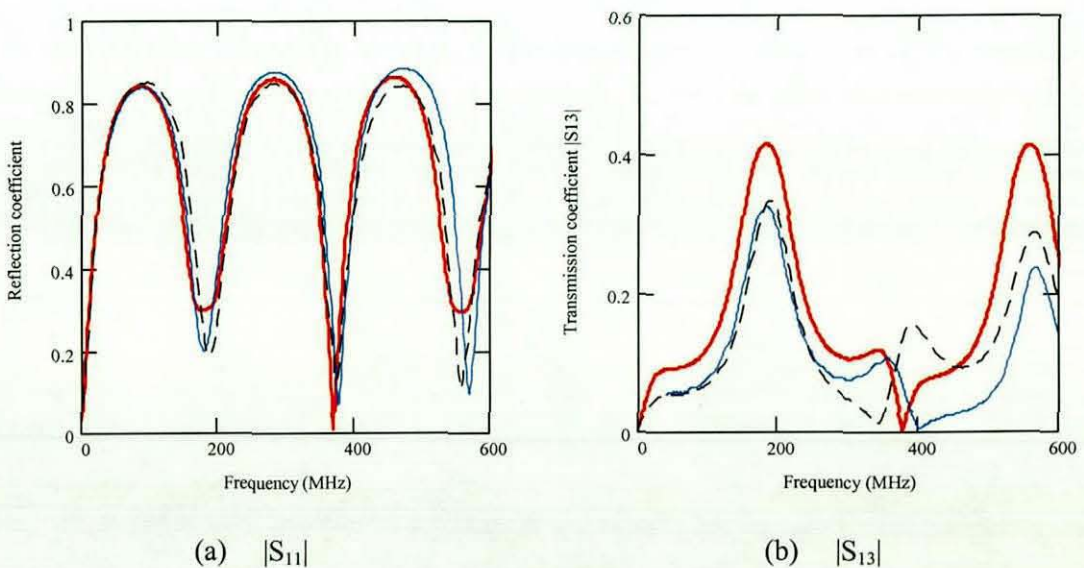

(a) $|S_{11}|$ (b) $|S_{13}|$

**Fig. 4.13   Results for the "U-loop" configuration derived from the analytical model
(heavy line) and measurements (light and dashed lines) with two
different network analysers**

The position of the transmission null in Fig. 4.13(b) varies significantly between measurements, occurring at frequencies above and below that predicted using the analytical model. However, the analytical and TLM models for this configuration, shown in Fig. 4.14, are in very close agreement, including the position of this null.
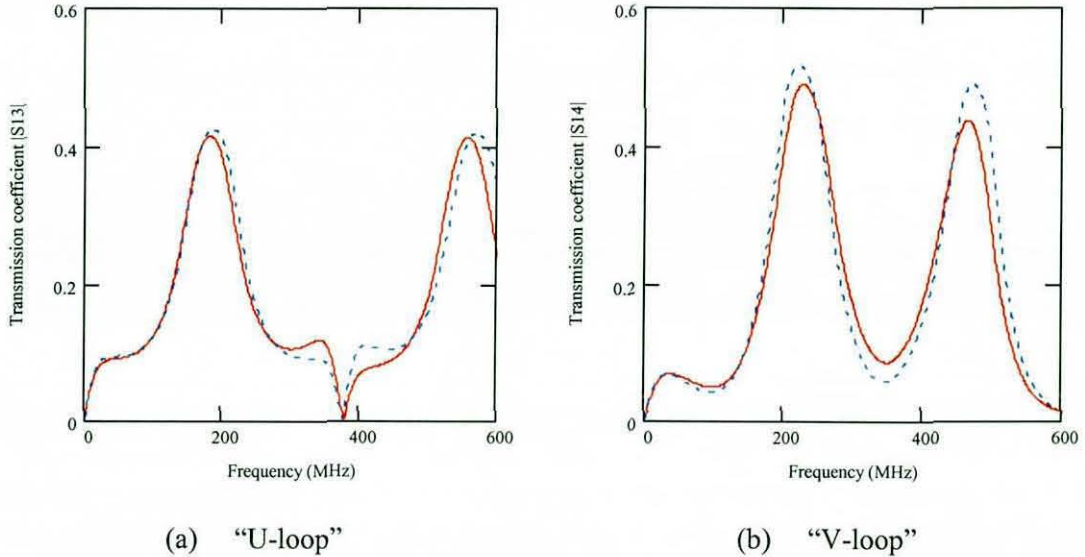

(a)   "U-loop"   (b)   "V-loop"

Fig. 4.14   Results for the "U-loop" and "V-loop" configuration derived from the analytical (solid line) and TLM (dashed lines) models

The level of agreement between the analytical and TLM models for the U-loop configuration gives confidence in the validity of these two theoretical results. The variations in the experimental results are therefore likely to be associated with defects in the experiment. The differences in the measured position of the null in Fig. 4.13(b) probably reflect difficulties in maintaining the height and relative position of the parallel wires.

Although the correlation between measurements and both the analytical and numerical models is good for the single wire case, the results for the two four-port cases are poorer. The analytical model is based on one-dimensional transmission line theory, and therefore takes no account of the angle of arrival of the feed lines at the parallel section of the four-port examples. However, the numerical results were obtained using three-dimensional field solutions and should therefore reflect any effects associated with the angle of arrival if they are significant at the frequencies of interest. The fact that the correlation between the analytical and numerical models is good gives confidence that the models are essentially correct, suggesting that it is more likely that the experiment does not fully represent the model. The repeatability problems encountered in the measurements also confirm this view.

4.4   Complex four-port networks under external illumination

Systems comprising a complex, multi-port cable network and a nearby antenna are of much greater practical interest. A vehicle-scale four-port network illuminated by a biconilog antenna has therefore been investigated, with the network both flat and inside a vehicle bodyshell.

Planar network

The network comprised a loop with four branches each terminated to a 50 Ω coaxial connector mounted in a small vertical plate. The height of the single conductor cable and the centre of the coaxial connectors was 2 cm, relative to a ground plane that was 2 m wide and 5 m in length. The latter was mounted at a height of 18 cm in a large semi-anechoic chamber (based on the height of the floor pan for the vehicle to be used in subsequent measurements). This system was illuminated by a biconilog antenna as illustrated in Fig. 4.15, which shows the TLM model for the simulated measurement.
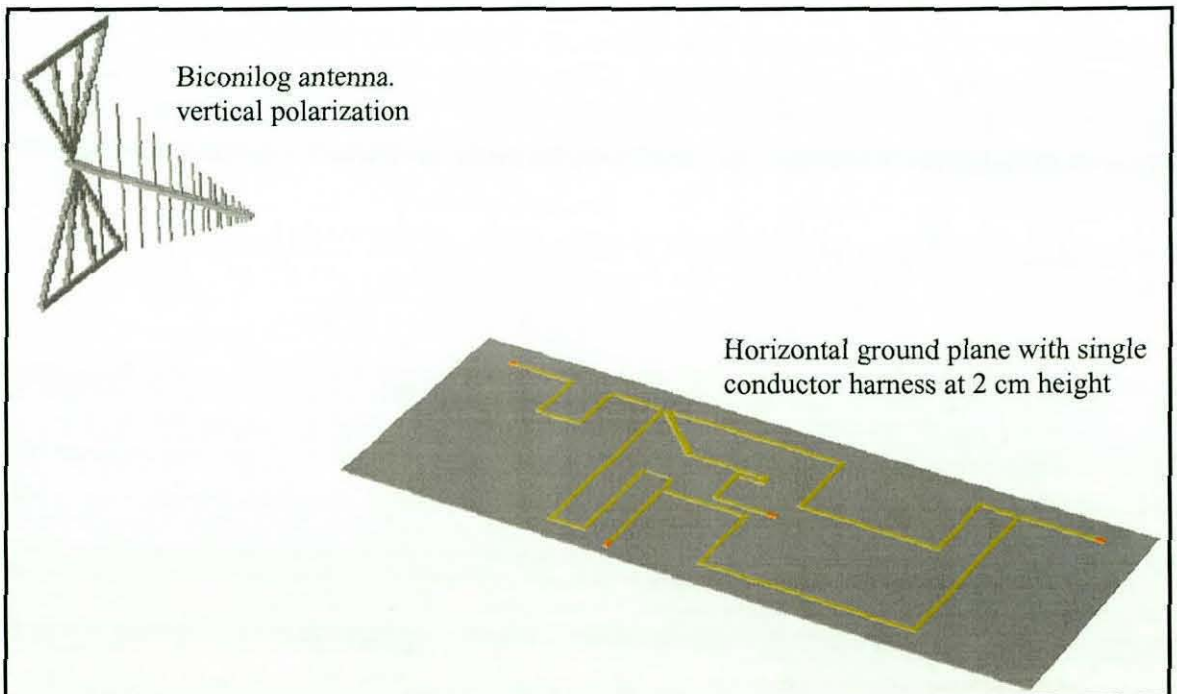

Fig. 4.15   TLM model for harness on ground plane illuminated by biconilog antenna

The antenna structure was represented using solid metal for both the feeder bars and the dipole elements, although many of the smaller elements had to be omitted from the model in order to avoid very small cell sizes. Three cells were placed between the feeder bars and the structure was excited using a thin wire carrying a voltage source with a 50 Ω impedance. This source was placed between the feeder bars near the shortest elements of the antenna.

The antenna model was validated against measurements, as well as against a range of other modelling techniques by other organisations [A.10, A.17]. In using TLM for modelling this type of antenna, careful mesh grading is required in order to ensure that the correct field distribution is obtained, particularly in terms of the cross-polar components in the near field [4.9]. A network analyser was used to measure the coupling between the antenna and the harness ports for comparison with model results (see Fig. 4.16).

In this case it was possible to use mesh grading to improve the performance of the wire model where close to ground. The results show similar levels and similar feature densities, but specific features do not really correlate particularly well between the measurements and the simulations.
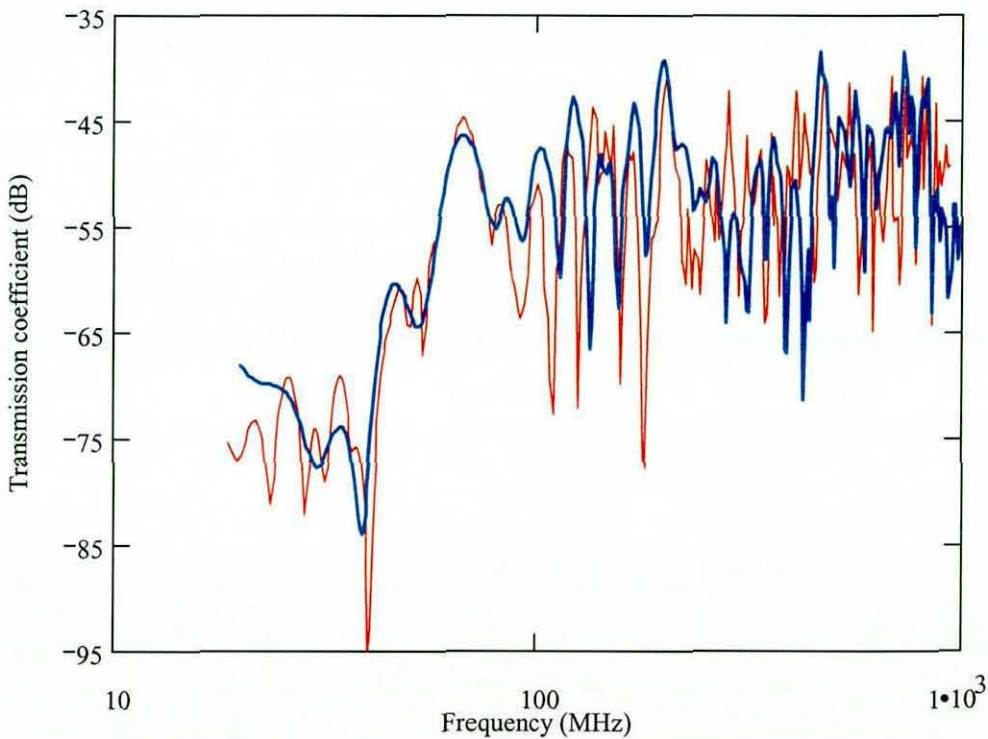

Fig. 4.16   Measured (heavy) and computed (light) coupling between biconilog antenna and port of harness on ground plane

Network in vehicle bodyshell

For a harness in a vehicle bodyshell it is not practicable to introduce the mesh refinement needed to overcome the limitations of the TLM thin wire model. An alternative approach therefore had to be adopted, in which a specific inductance and capacitance per unit length were enforced for the wire.

The required parameters were obtained from a separate 2D boundary element calculation for a dielectric-coated conductor above an infinite ground plane, based on the intended geometry (at 2 cm height) and assumptions about the likely dielectric constant for the cable sheath. The geometry is illustrated in Fig. 4.17, which shows a view of the TLM model.
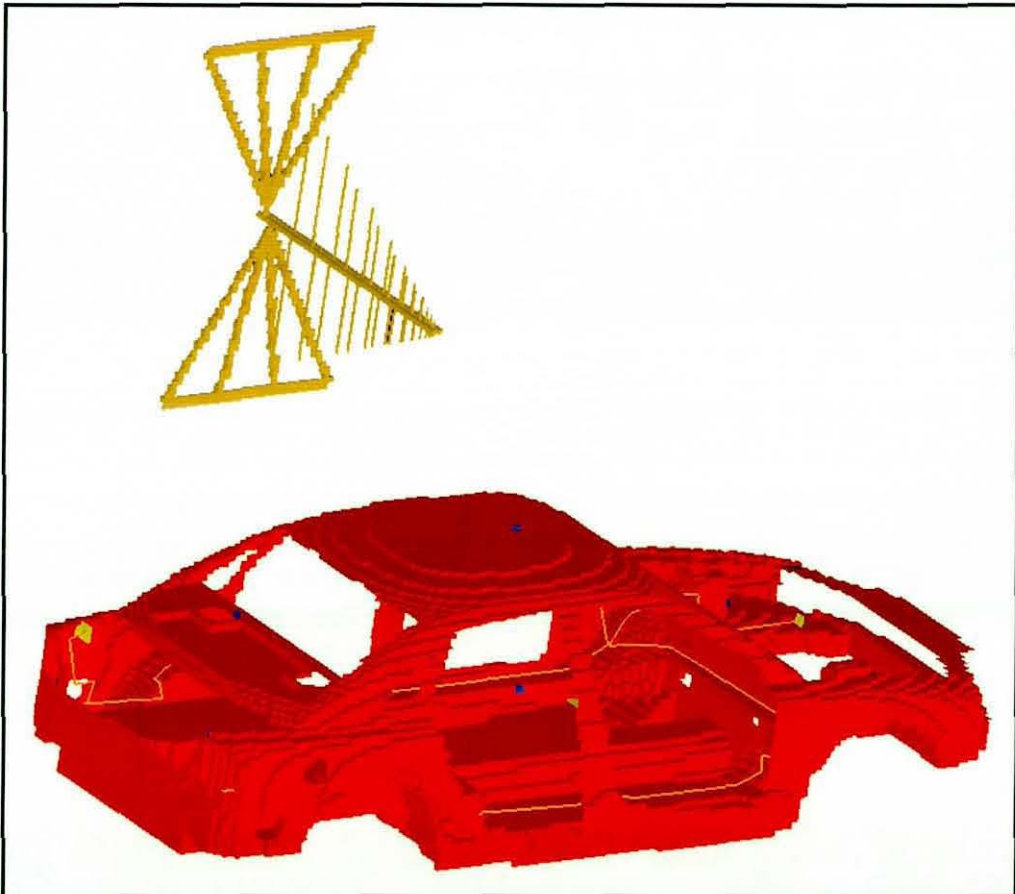

Fig. 4.17   TLM model for vehicle bodyshell with simple harness and vertical biconilog antenna at side

Sample model validation results are illustrated in Fig. 4.18, which shows the comparison between measured and computed results for transmission from the antenna to one of the ports on the network in the vehicle. As with the flat harness configuration the results show similar levels and similar feature densities, but individual features are not correlate well between the measurements and the simulations. In this case, however, the harness geometry is subject to much greater variability in the physical system, and capturing the correct geometry in the model is also much more difficult. Considering these additional problems, and the quality of the results obtained for the flat configuration, the vehicle results are perhaps better than might be expected.
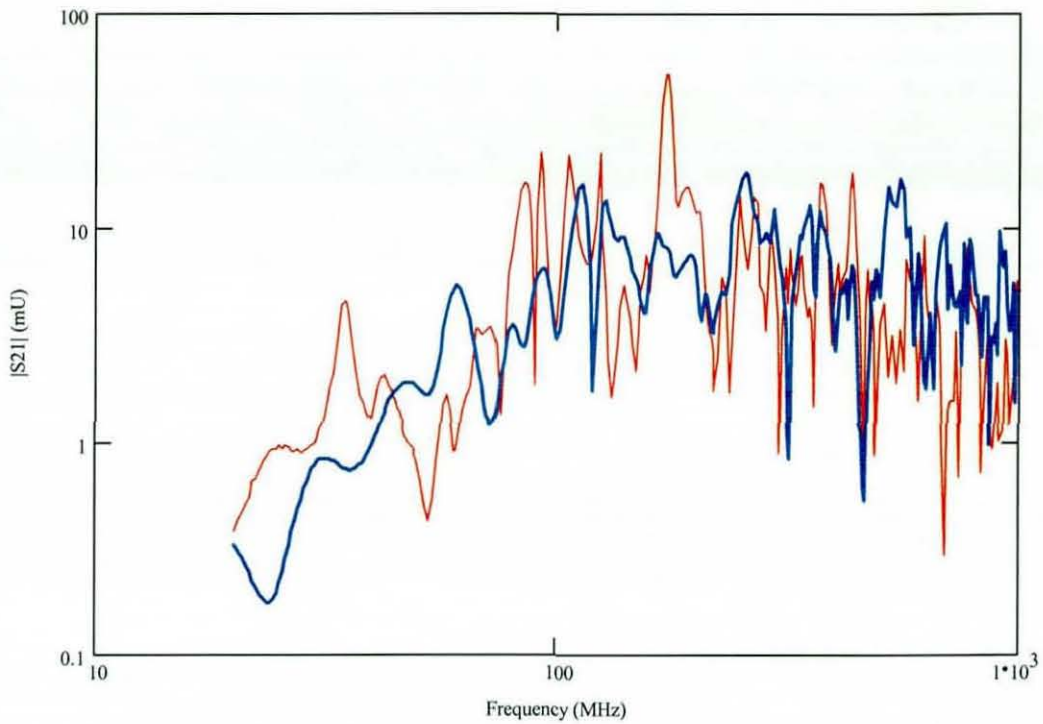
Fig. 4.18   Measured (heavy) and computed (light) transmission coefficient between biconilog antenna and harness port in vehicle

Possible error sources

In the flat configuration the results are increasingly poor at higher frequencies, despite the fact that the geometry is reasonably well controlled. In numerical models errors can be expected to increase with frequency because the mesh density decreases. A further approximation used in the model is to neglect the small wooden blocks ($\sim$6 cm^3) that were used at intervals to support the cables both over the ground plane and in the vehicle. However, it seems unlikely that this would be a major source of error given the relatively small amount of material that is involved. However, there are at least two possible causes for the disparities between the simulated and measurements in both the flat and in-vehicle harness cases that will become more significant as the frequency increases.

Firstly, it is not possible to model the antenna in sufficiently fine detail in such large models (ie. vehicle-scale object with nearby antenna) to be able to predict the input reflection coefficient of the antenna, and errors in S_{11} must inevitably lead to errors in S_{21}. Nonetheless, the predicted field distribution compares favourably with experimental results [A.10]. Secondly, the termination impedances are assumed to be exactly 50 Ω in the model, but measurements of the real termination impedances (N-type network analyser calibration kit loads used with adaptors) reveal significant deviations as the frequency increases (see Fig. 4.19).
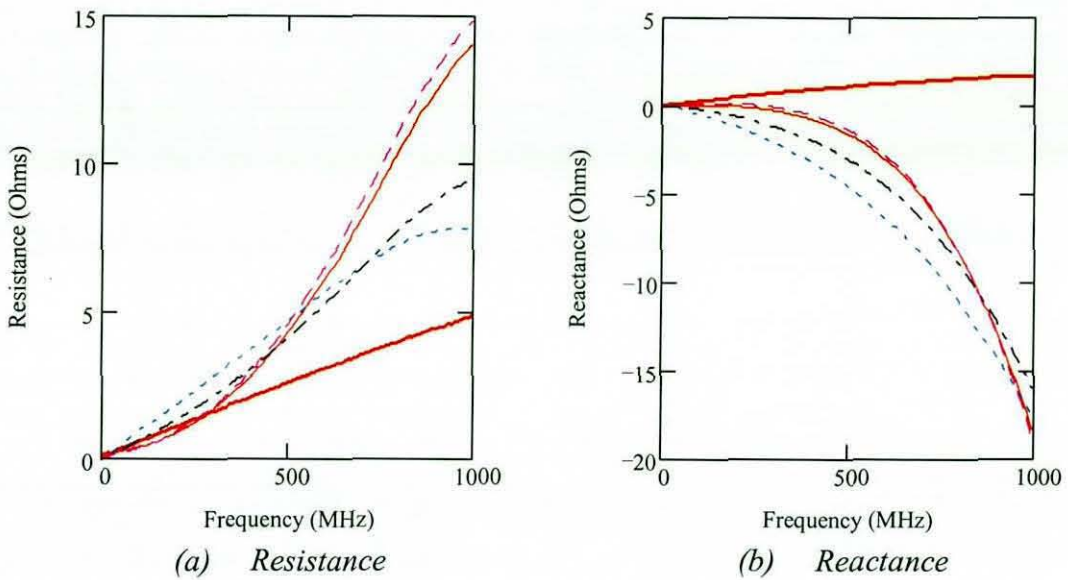
(a)   Resistance   *(b)   Reactance*

Fig. 4.19   Measured resistance and reactance deviation (from 50+*j*0 Ω) for representative calibration kit load (heavy) and loads used to terminate flat and vehicle networks

Measurements also show some clear evidence of variability between the calibration kit loads that are used to provide the reference for the measurements. Further sources of error associated with the vehicle model include:

- the quality of the vehicle geometry, which was heavily simplified and limited to a single surface in this case

- inaccuracies in the harness path definition, which was estimated from sets of measurements from points on the cable path to reference points on the vehicle structure

- the imposition of estimated capacitance and inductance parameters in order to emulate the properties of the wire close to ground without introducing additional mesh grading.

4.5   Computing the scattering matrix for a vehicle

It is necessary to excite each port individually, and with the correct termination impedances, in order to determine the scattering matrix for a network. For a vehicle system, however, the termination impedances are unlikely to be well known, and may vary with frequency and perhaps the mode of operation, making direct calculation of the scattering matrix for the system using 3D field modelling techniques impracticable in general. An approach is therefore required which can accommodate this uncertainty and variability without the need to repeat 3D field simulations.

The scattering matrix $S(f)$ can be expressed in terms of the network impedance matrix $Z(f)$ and the vector of termination impedances $\mathbf{T}(f)$ as:

$$S(f) = [Z(f) - I\mathbf{T}(f)][Z(f) + I\mathbf{T}(f)]^{-1} \tag{4.27}$$

where "I" represents an identity matrix of the same order as $S(f)$ and $Z(f)$. Thus, a scattering matrix may in fact be determined using any suitable set of termination impedances, which could include the correct values for each termination or any arbitrary set. The more fundamental properties of the network are actually characterized by the impedance matrix. In the interests of computational efficiency, therefore, using a uniform arbitrary value probably represents a better strategy. This minimizes the number of simulations that must be carried out since, in the absence of symmetry, the number of simulations required to characterize the junction is equal to the number of ports. However, the resulting scattering matrix will not represent the real system, as the termination impedances are incorrect.

If the scattering matrix $S_R(f)$ for a uniform arbitrary port impedance Z_R is available, then the impedance matrix for the network can be derived from:

$$Z(f) = [I - S_R(f)]^{-1}[I + S_R(f)]I Z_R \tag{4.28}$$

From equations 4.27 and 4.28 the required scattering matrix $S(f)$ for any particular set of termination impedances $\mathbf{T}(f)$ can then be obtained, without recourse to further 3D simulation, using:

$$S(f) = \{[I - S_R(f)]^{-1}[I + S_R(f)]I Z_R - I\mathbf{T}(f)\}\{[I - S_R(f)]^{-1}[I + S_R(f)]I Z_R + I\mathbf{T}(f)\}^{-1} \tag{4.29}$$

This assumes that the correct termination impedances are actually available, or can be bounded in some way so that sensitivity studies can be carried out, and that the matrices can be inverted. The correct termination impedances could be obtained from either measurements or simulations of the modules that are to be connected at the terminations. Furthermore, this approach could equally well be applied in a purely experimental analysis, by measuring the components of $S_R(f)$ with different terminations [4.10].

Alternatively, it may be more convenient to compute the admittance matrix $Y(f)$ directly by short circuiting all of the unexcited ports and recording all of the port currents $\mathbf{i}(f)$ due to the exciting voltages $\mathbf{v}(f)$, since:

$$\mathbf{i}(f) = \mathbf{Y}(f)\mathbf{v}(f) \tag{4.30}$$

The impedance matrix is then obtained from the inverse of the admittance matrix, from which the scattering matrix for any desired set of port impedances can again be determined. This method also requires a separate simulation for each port in order to characterize the network, but eliminates the need to derive $Z(f)$ from $S_R(f)$. However, this approach would be at a disadvantage for time domain techniques, because of the absence of loss at the ports.

Once the scattering matrix has been fully characterized for the arbitrary reference impedance, it may be then be instantiated for any required set of termination impedances, thus avoiding the need for further 3D field modelling. Functional EMC effects could, in principle, then be simulated by connecting circuit models of the source and victim modules via the scattering matrix that represents the coupling resulting from the physical installation. Such an approach would, however, make enormous computational demands for systems with large numbers of ports, such as a vehicle wiring harness, since the number of simulations required to define the scattering matrix equals the number of ports in the system. In vehicles there are no convenient symmetries that can be exploited to reduce the number of simulations required, or the size of the models. Ports which are not of interest for the analysis and which have known and fixed termination impedances need not be considered in the derivation of the scattering matrix.

Nonetheless, the number of ports that would need to be considered is still likely to be very large. Coupling between antennas (including unintentional antennas) and from antennas to harness ports will require 3D field modelling, even for separated methods. However, it may be possible to use more computationally efficient models to derive approximate values for the input reflection coefficients and local coupling coefficients within cable bundles, assuming that the coupling to other bundles is negligible and that cable input reflection coefficients are dominated by contributions from within the bundle and the adjacent conducting structures. The resulting approximate scattering matrix would then be relatively sparse, with the active regions populated using different techniques as indicated in Fig. 4.20 below. In this illustration, two antennas are assumed to be present (ports "1" and "2") together with a number of wiring harness terminals (represented as ports labelled from "3" to "N"). In fact, the first two ports may represent either intentional antennas (eg. a vehicle mounted antenna and a test antenna) or unintentional antennas (ie. one or both of them may be harness elements that are not sufficiently close to the vehicle structure to meet the requirements of the transmission line approximation).

$$
S \cong
\begin{bmatrix}
S_{11} & S_{12} & S_{13} & S_{14} & S_{15} & S_{1i} & S_{1j} & S_{1K} & S_{1M} & S_{1N} \\
S_{21} & S_{22} & S_{23} & S_{24} & S_{25} & S_{2i} & S_{2j} & S_{2K} & S_{2M} & S_{2N} \\
S_{31} & S_{32} & S_{33} & S_{34} & S_{35} & \approx 0 & \approx 0 & \approx 0 & \approx 0 & \approx 0 \\
S_{41} & S_{42} & S_{43} & S_{44} & S_{45} & \approx 0 & \approx 0 & \approx 0 & \approx 0 & \approx 0 \\
S_{51} & S_{52} & S_{53} & S_{54} & S_{55} & \approx 0 & \approx 0 & \approx 0 & \approx 0 & \approx 0 \\
S_{i1} & S_{i2} & \approx 0 & \approx 0 & \approx 0 & S_{ii} & S_{ij} & \approx 0 & \approx 0 & \approx 0 \\
S_{j1} & S_{j2} & \approx 0 & \approx 0 & \approx 0 & S_{ji} & S_{jj} & \approx 0 & \approx 0 & \approx 0 \\
S_{K1} & S_{K2} & \approx 0 & \approx 0 & \approx 0 & \approx 0 & \approx 0 & S_{KK} & S_{KM} & S_{KN} \\
S_{M1} & S_{M2} & \approx 0 & \approx 0 & \approx 0 & \approx 0 & \approx 0 & S_{MK} & S_{MM} & S_{MN} \\
S_{N1} & S_{N2} & \approx 0 & \approx 0 & \approx 0 & \approx 0 & \approx 0 & S_{NK} & S_{NM} & S_{NN}
\end{bmatrix}
$$

Labels around the matrix: 3D models; 3D+1D+2D (top); 3D+1D+2D (bottom-left); 1D+2D (bottom-right)

Fig. 4.20   Approximate scheme for populating vehicle scattering matrix using different numerical techniques

The characteristics of the antennas (elements S_{11}, S_{21}, S_{12} and S_{22}) must be obtained from 3D modelling (the white, non-zero area of the matrix), but the coupling between the antennas and the harness terminations could be approximated using separated methods if the corresponding harness elements can be regarded as transmission lines. Thus, the coupling between the antenna ports and the harness ports could be obtained using a combination of 3D models with the antennas excited, to obtain the field distribution along the harness path, together with 2D static field models plus 1D network models to obtain the currents and voltages resulting at the harness terminations (the light grey areas of the matrix).

Cross-talk terms and cable input reflection coefficients within cable bundles (the dark grey regions of the matrix) are represented by the clusters of terms around the diagonal in Fig. 4.20, which can be estimated using 1D network models supported by 2D static field models provided that there is negligible field coupling between the cable bundles (represented by the elements approximated as zeros in the matrix). Under this condition there is no need for 3D modelling of the harness network.

The computational scheme that is proposed to populate the vehicle scattering matrix is therefore as follows:

- Identify the intentional and unintentional antennas in the system for inclusion in the 3D models.

- Carry out 3D field simulations to determine the scattering parameters for the antennas (using arbitrary impedances where there is uncertainty) and the field distribution along the paths of harness elements that meet the requirements of the transmission line approximation.

- Use network simulations to compute the scattering parameters for closely coupled cable bundles that are treated as transmission lines (using arbitrary termination impedances where there is uncertainty).

- Use the computed field distributions as inputs to network simulations to determine the coupling between the antennas and the ports of cable bundles that are treated as transmission lines (using arbitrary impedances where there is uncertainty).

- Assume zero coupling between cable bundles that are treated as transmission lines.

- Renormalize the resulting scattering matrix to represent any desired set of termination impedances.

The viability of the proposed approach has not yet been investigated. However, comparison of network characteristics measured in a vehicle bodyshell and computed from a topological network model that neglects physical layout (and hence field coupling between the harness branches) suggests that negligible radiated field coupling is a reasonable assumption for many parts of a vehicle harness [A.23]. In addition, the separated approach for computing coupling to cables has already been shown to be very successful for automotive examples [4.11, A.16].

4.6   Conclusions

For many practical systems the impedances terminating cables may be difficult to characterize, frequency dependent and vary with the operating mode (eg. due to device switching). The construction and location of cables in vehicle wiring harnesses is also very variable, and their close proximity to the bodyshell is likely to make these variations significant. This variability presents significant difficulties for time-domain 3D field models containing cables (ie. self-consistent or integrated cable models) since the impact of variations in termination impedance would require many models to be run.

Separated methods can more readily accommodate load variability in immunity scenarios since 1D network calculations do not require significant computing resources. However, these approaches are less viable for emissions and intra-system EMC studies since 3D models would need to be rerun with different current distributions derived from 1D network simulations.

A possible strategy for minimising the number of 3D simulations that are required has been proposed, based on computing the scattering matrix for the system as a whole under an arbitrary set of loads. In principle this would allow the coupling between ports under any combination of desired termination impedances to be computed using matrix calculations without recourse to further 3D simulations. A further benefit of this approach is that the scattering matrix provides a convenient mechanism for describing the coupling characteristics that are the basis of all EMC phenomena, including radiated emissions, radiated immunity and intra-system EMC, for the vehicle structure and wiring harness.

A major practical limitation, however, is that N simulations are required to populate the scattering matrix for a system with N ports, in the absence of degeneracy due to symmetry properties within the network, and N may be very large. Excluding terminations that have fixed impedances and are not of direct interest may yield some computational savings, but neglecting coupling terms that are expected to be very small offers the possibility of replacing large numbers of 3D simulations with much more efficient 1D network simulations.

The experimental validation of 3D scattering matrix results is not easy for simple networks with direct excitation, although analytical models give confidence that the numerical models are essentially correct. However, the validation of more realistic systems in which a large and more complex network is illuminated by a nearby antenna is only possible using measurements. The results obtained for such systems are less convincing than is desirable, although some of the potential pitfalls that limit the success of such validation exercises have been identified.

4.7   References

[4.1]   C.G. Montgomery, R.H. Dicke and E.M. Purcell (eds.), *Principles of microwave circuits*, McGraw-Hill, New York, 1948, § 5.1

[4.2]   C.G. Montgomery, R.H. Dicke and E.M. Purcell (eds.), *Principles of microwave circuits*, McGraw-Hill, New York, 1948, § 5.14

[4.3]   D.W. Kerns and R.W. Beatty, *Basic theory of waveguide junctions and introductory network analysis*, Pergamon Press, New York, 1967, § 1.5(c)

[4.4]   A.R. Ruddle, D.D. Ward, R. Scaramuzza and V. Trenkic, *Development of thin wire models in TLM*, Proceedings of 1998 IEEE EMC Symposium, Denver, CO, USA, Vol. 1, pp. 196-201

[4.5] S.A. Schelkunoff and H.T. Friis, *Antennas: theory and practice,* Wiley, New York, 1952, Appendix I

[4.6] R.E. Collin, *Foundations for microwave engineering,* McGraw Hill, 1992, § 5.10

[4.7] L.P.A. Robichaud, M. Boisvert and J. Robert, *Signal flow graphs and applications,* Prentice Hall, 1962

[4.8] R.E. Collin, *Foundations for microwave engineering,* McGraw Hill, 1992, pp. 427-429

[4.9] A.R. Ruddle and D.D. Ward, *Modelling wire antennas in wider simulations,* IEE Colloquium on "High frequency simulation in practice", London, May 1997, Digest 1997-010, Paper No. 10

[4.10] J. van der Merwe, H.C. Reader and J.H. Cloete, *S-parameter measurements yielding the characteristic matrices of multiconductor transmission lines,* IEEE Transactions on EMC, Vol. 40, No. 3, August 1998, pp. 249-256

[4.11] L. Paletta, J.-P. Parmantier, F. Isaac, P. Dumas and J.-C. Alliot, *Susceptibility analysis of wiring in a complex system combining a 3-D solver and a transmission-line network simulation,* IEEE Transactions on EMC, Vol. 44, No. 2, May 2002, pp. 309-317

CHAPTER 5: PRACTICAL VEHICLE MODELS

In order to make the modelling of real-world equipment and test configurations practicable it is inevitably necessary to introduce a degree of approximation. The aim of this process is to minimize the computational requirements, but this would be of no value if the resulting model becomes so poor that the results are unusable. The nature of the required results is likely to be very varied, ranging from order of magnitude estimates through to precise predictions. Moreover, the quality of the geometry that is made available when the results are required is also likely to be very variable. The objective of the analyst, therefore, should be to reduce the model to the simplest representation that can achieve the required results.

5.1 Potential users and applications

Modelling techniques can be used in a wide range of roles in automotive EMC and antenna engineering, including:

- design and specification
- supporting better targeted testing
- analysis and mitigation of problems
- developing basic understanding of EMC phenomena
- investigating and validating measurement techniques.

The exact nature of the associated model, as well as the requirements in terms of the input data and the accuracy of the output, will depend on the user and the application. The vehicle development process can be considered in terms of five main user groups with an interest in electromagnetic issues:

- vehicle manufacturers/integrators
- system suppliers
- test houses
- standards bodies
- certification authorities.

Vehicle integrators

The "vehicle integrator" is responsible for the overall vehicle system, including defining the requirements for systems that are to be provided by the "system suppliers". Although the vehicle integrator has traditionally been the manufacturer of the chassis and major mechanical components, it is possible that this may change as the electronic and software content of the vehicle increases, with the body-shell perhaps becoming a less significant component.

System suppliers

As EMC is considered at both the vehicle and system levels there are requirements for analysis and testing at both of these levels.

Test houses

Modelling can also be applied in the design and development of test facilities and equipment, as well as supporting better targeted testing by reducing reliance on physical testing. Modelling could, for example, be used to identify a "worst-case" illumination configuration, or to select a subset of vehicles for test from a larger number of product variants.

Standards bodies

The requirements for immunity and emissions performance are defined in international standards. These documents also specify the nature of the tests that are to be performed in order to demonstrate compliance with the performance requirements. Modelling techniques are potentially of benefit for the standards community in applications such as the investigation of measurement methods or the definition of emissions and immunity limits.

Certification authorities

Finally, the evidence to support manufacturers' claims that their products conform to the relevant legislation is reviewed by certification authorities. The latter will therefore become indirect users of modelling results when the other user groups begin to exploit electromagnetic modelling techniques and use the results to support claims for compliance with legislative requirements.

Links between user groups

In order to be successfully integrated into vehicle development processes, and automotive EMC engineering in particular, numerical modelling techniques will need to be embraced by all of these user groups. The links between the various user groups and their activities are illustrated in Fig. 5.1, which also outlines a number of potential applications of modelling in activities that are associated with each group.
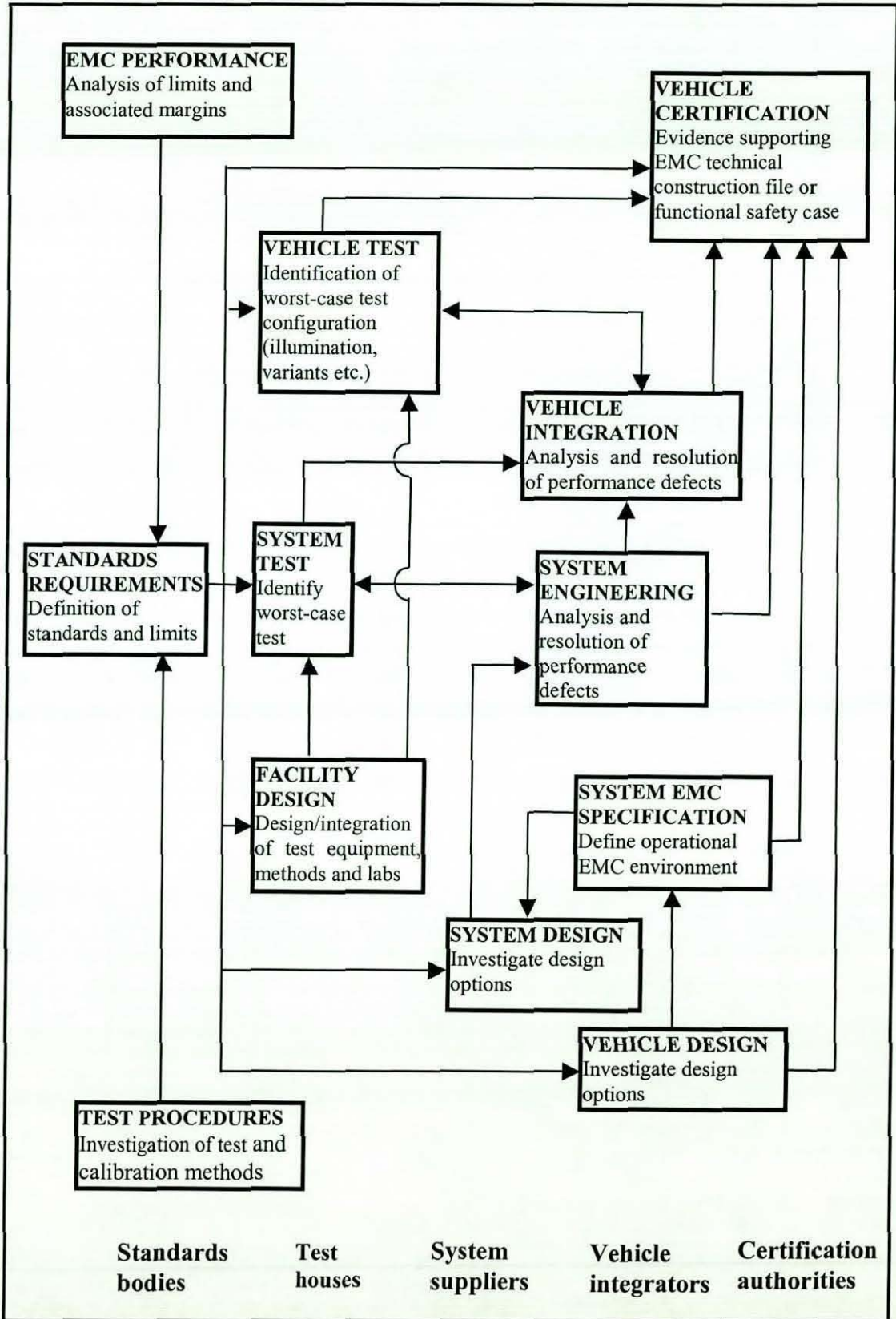
Fig. 5.1   Potential users and applications of electromagnetic modelling

5.2   Quality and accuracy of results

Given the inherent uncertainty and repeatability problems of EMC measurements, as well as the wide variations in model fidelity and modelling tasks that can be expected, it is not easy to quantify the accuracy of simulation results. Presupposing that the basic numerical analysis techniques are sound, and that they are correctly implemented in the simulation software, the factors that determine the "quality" of the results, in terms of how well they represent the real world, are:

- the fidelity of the geometry used to build the model
- the accuracy of the electrical properties that are assigned to different materials
- the representation of real world measurement features (eg. transducer effects)
- the nature of the discretization that is applied when the geometry is meshed (ie. how well it captures the physical geometry and spatial field variations).

An immunity model that is based on plane wave excitation cannot be expected to produce identical results to a measurement carried out using a finite source antenna. Similarly, results generated using "intermediate" vehicle geometry may not be identical to models or measurements based on the final product. Nonetheless, even imperfect results may be of sufficient quality to make decisions about design options or "worst case" test configurations. In some cases, information regarding relative performance may be sufficient, while in others confidence that the absolute values are likely to be within a few dB of actual levels may be required.

Accuracy is commonly considered in terms of the amplitude difference between the model and a reference, which is usually a measurement. However, in EMC the frequency range of interest is very large, with the result that the feature density in the results is very high. In practice, it is commonly the case that there are frequency shifts in features that are present in the two data sets. A large and sharp peak with a small frequency shift between the two data sources would therefore suggest a very large amplitude error, although in practice it may be sufficient to know that such a feature can be expected rather than exactly where it occurs in frequency.

Thus, it is perhaps more useful to take a broader view of the correlation between a pair of data sets, which takes account of both amplitude and frequency differences, and can be weighted in favour of either of these elements if so desired [5.1]. This "feature selective validation" approach (FSV) provides a useful mechanism for quantifying the accuracy of model results against measurements, or against other models.

It is perhaps even more difficult to define the "quality requirements" for model results. The natural inclination is to demand that models should duplicate the results of practical measurements exactly. Measurements, however, are not entirely reliable and often represent rather artificial conditions. In EMC measurements the uncertainties are relatively large, and repeatability is often a significant problem. It is unreasonable, therefore, to expect a better correlation between measured and computed results than can be obtained between repeated experiments. However, levels of correlation between measured and computed field coupling into a vehicle bodyshell that approach those of experimental repeatability for this type of measurement have been demonstrated [5.2, A.3].

5.3   Essential model elements

A common device for providing a simple source in computational electromagnetics is the ideal plane wave. This approach is attractive for its simplicity, since the source is characterized solely by its propagation direction, polarization and magnitude. In the analysis of microwave antennas this is not an unreasonable approximation for the excitation of the device due to a distant source. In radiated immunity measurements, however, far-field conditions are unlikely to be achieved in general. Furthermore, the test environment is often semi-anechoic, with the result that the illuminating field may in fact be a complex interference pattern. Given that a finite source will produce a quite different field distribution from the plane wave, it can be expected that the parameters of interest, such as the coupling into the interior cavities and wiring of the vehicle under test, will also be quite different. Plane wave illumination, therefore, is a poor choice when validating immunity model performance against practical experiments.

Conversely, the prediction of electromagnetic emissions is commonly approached by computing the fields at some point of interest due to a source. Again, this provides for a simpler model, but at the expense of adequately representing the spatial averaging and filtering effects of the receiving antenna. Broadband antennas of significant physical size are normally used in practical measurements, in the interests of test efficiency. Consequently, it is also necessary to represent such structures in the model in order to validate predicted performance against measured values. Thus, radiated emissions and immunity measurements can be considered as comprising of two key elements: the "system under test" and the "test antenna" (which may be either transmitting or receiving). In this context, the system under test may in fact be a controlled environment, such as a semi-anechoic chamber or a reverberant room, or another antenna.

Any model that is to be validated against emissions of immunity measurements must therefore adequately reflect both of these features in order to be sufficiently representative of the practical measurement process to ensure success. More detailed refinement of the model of the system under test will not improve the quality of the validation data if the model does not also take sufficient account of the antenna that is used in the measurements.

The "test antenna" may also include abstract representations such as plane wave or point sources, provided that these abstractions are representative of the measurements. For example, EMC test sites are generally characterized in terms of the "normalized site attenuation" (NSA [5.3]) for a specified antenna configuration. The theory for this parameter is based on ideal "point" antennas, and is derived from the coupling between a pair of antennas in the test environment. In practice this parameter is measured with a set of tuned dipoles, or perhaps using broadband antennas such as biconicals. Simulations for wire cage biconicals with total lengths of 1.273 m and 0.323 m indicate that there is significant error in the interpretation of NSA as determined from the coupling between a pair of the larger biconicals. The results for the smaller devices, however, are extremely good except at low frequencies (see. Fig. 5.2). The feature just below 1 GHz is almost certainly a numerical artefact, due to the use of high order polynomials to represent the current distribution on wire segments with lengths of order $\lambda/2$.
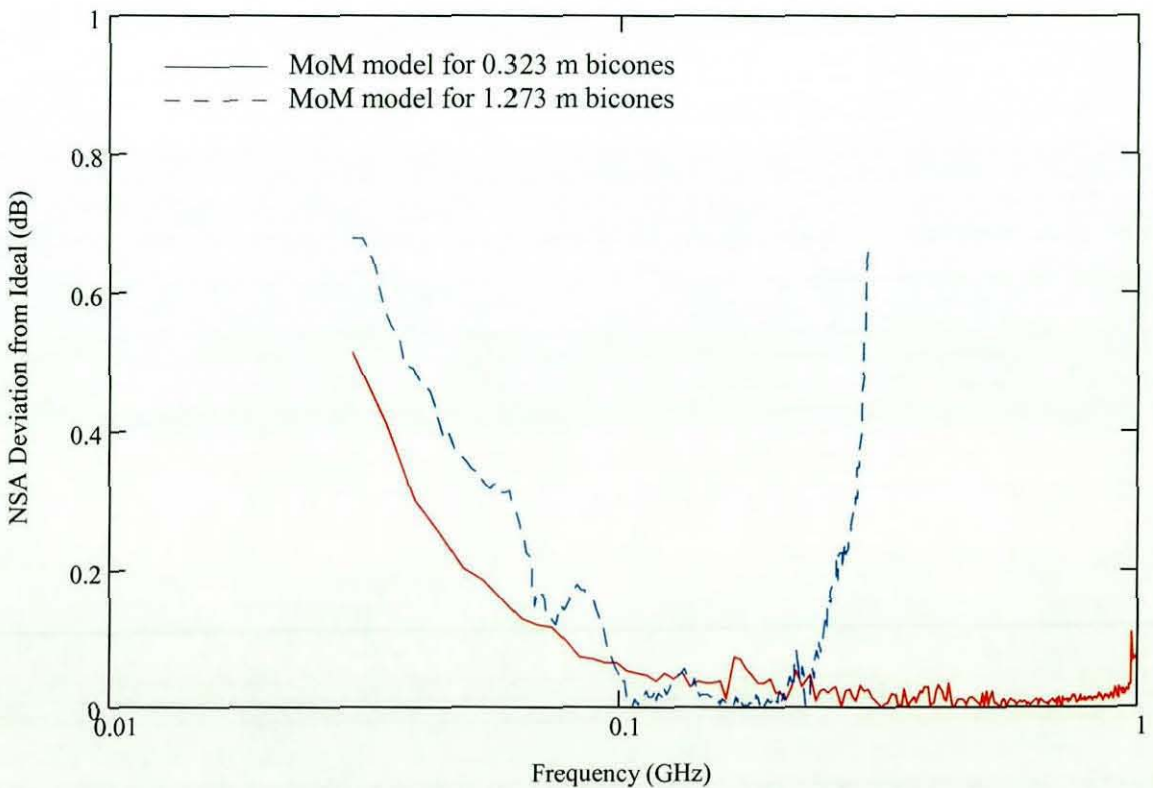
Fig. 5.2   Theoretical error in free space NSA measurements for pairs of bicones [A.6]

Measurements carried out with the smaller biconicals therefore provide a good representation of the ideal point antennas, thus allowing extremely good correlations to be achieved with model results extracted from TLM simulations (see Fig. 5.3).
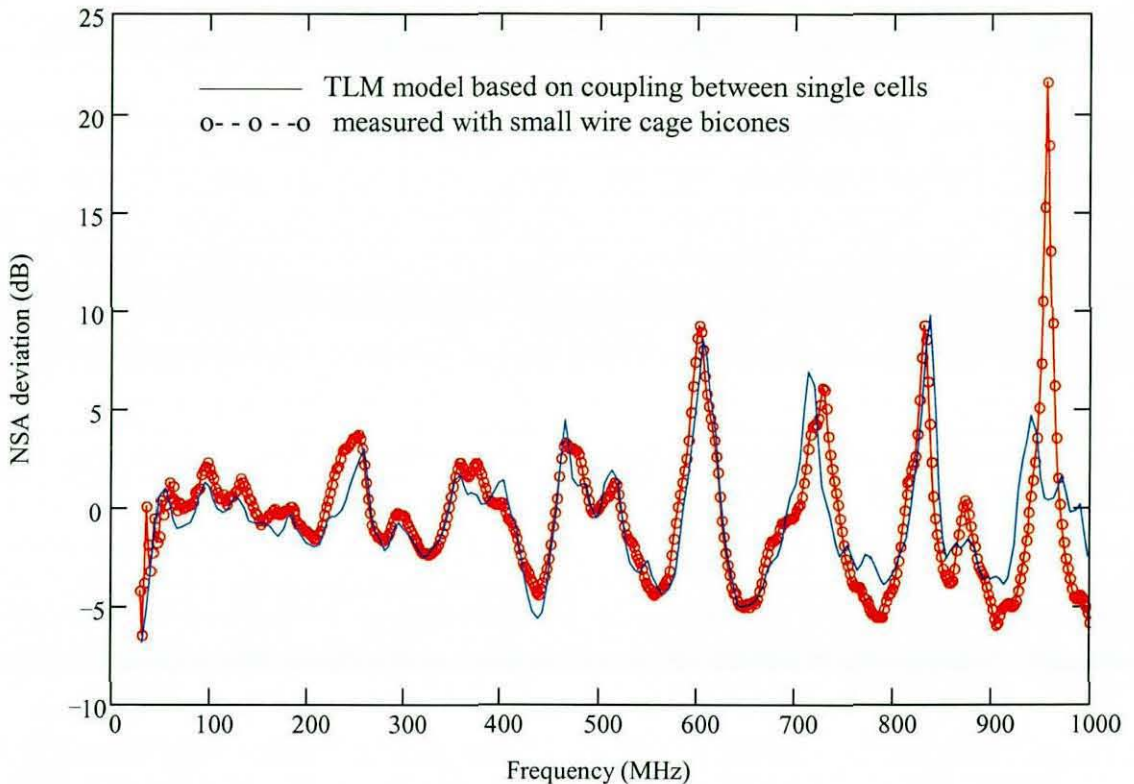

Fig. 5.3   NSA for horizontal polarization in chamber with complex partial lining [A.6]

The object under test in this case was a conducting cavity with 80% of the surface lined with ferrite tiles (as described in [5.4]). The ferrite tiles were modelled using a digital filter [5.5] implemented in a TLM code developed from that used in [5.6]. The NSA was derived from the time domain coupling between a single excited cell (at the transmit antenna location) and another cell (placed at the required receive antenna positions) using a method described in [5.7]. This approach avoids the need to model detailed antenna structures and allows the NSA for any number of receive points to be computed in a single simulation for one transmitter location, thus providing considerable savings in model size and the number of models that need to be constructed and simulated.

The fact that these chamber models with abstract antenna representations correlate so well with measurements can be attributed to two key factors:

- the properties of the ferrite material used to line the real chamber are fairly well controlled, and therefore very similar at all points around the room

- the use of small antennas to make the experimental measurements provides a very good emulation of the point antennas assumed in the theoretical definition of NSA.

This example demonstrates that it is possible to obtain excellent validation from simulations that do not reflect the details of the "antenna" element of the model, provided that the approximation is justifiable. In this case, the preliminary MoM simulations demonstrated that the test antennas were very close to the idealized points used in the model.

5.4   Model requirements

Validation against experiment is not the primary goal of modelling, but provides a means to obtain confidence in the simulated results and assists in promoting the adoption of such techniques in practical engineering. Thus, the requirements for models to be used for validation are somewhat different to those of more mainstream engineering applications. Nonetheless, it is useful to consider all electromagnetic models as comprised of the same two elements as the validation model. The requirements for different modelling applications can then be categorized in terms of the nature of these two essential model elements of the model.

In considering model requirements for wider applications, it is useful to consider the two basic elements in terms of a number of relatively broad and loosely defined "fidelity classifications". This is an attempt to represent a continuum in a form that is amenable to natural language description, and the number of classes is therefore somewhat arbitrary. For this application, however, four basic classifications are proposed, as defined in Table 5.1 below.

Model fidelity class	Interpretation
Abstract	Highly idealized, such as plane wave or point sources
Representative	Synthetic geometry capturing the key features of the real object
Intermediate	Approximate representations of the real object, or similar geometry
Detailed	Accurate representations of the real object

Table 5.1   Model fidelity classifications for key features

The "abstract" and "detailed" cases are more readily defined than "representative" and "intermediate", as the latter must accommodate a very wide spectrum of fidelity levels.

The fidelity requirements for any particular model will depend on the nature of the modelling task that is to be carried out and various practical issues, such as the availability of geometrical data and material properties. Using the proposed four levels to describe the fidelity of each of the two model elements then allows a wider spectrum of overall model fidelity classifications to be defined, which can indicate the nature of models required for different tasks. Based on these classifications, typical model fidelity requirements are presented in Table 5.2, for a number of possible modelling applications associated with test houses as model users.

Modelling task	Objectives	Antenna model fidelity	Test object model fidelity	Comments
Evaluation of worst case model variant in immunity tests	Reduce number of options to be tested, saving test time and costs. Objective basis for test sample selection.	Abstract	Detailed	Selection based on relative performance of model variants under plane wave illumination is feasible and probably adequate.
Identification of 'worst case' test condition	Reduce total configurations to be tested, saving test time and costs.	Abstract	Intermediate or detailed	Relative performance measures are sufficient, so plane wave illumination is adequate.
Design of low frequency test antennas	Design and /or optimisation to meet field strength and uniformity requirements	Detailed	Intermediate	Chamber size and lining properties need to be adequately represented, antenna model must be detailed.
Design and optimisation of anechoic chambers	Optimise cost and performance of chambers.	Abstract or representative	Intermediate	Antenna models can be avoided in TLM/FDTD, but chamber size and lining properties need to be adequately represented.
Design and optimisation of reverberant rooms	Evaluate stirrer design and placement options, determine working volume and assess sparking risk.	Representative	Intermediate	Chamber and stirrer geometry need to be adequately represented, but source characteristics are probably less critical.
Analysis and design of open area test sites	Evaluate suitability and design of site (eg. effect of local structures and all weather housing).	Abstract or representative	Intermediate	Antenna models can be avoided in TLM/FDTD, but environmental features need to be adequately represented.

Table 5.2   Model fidelity requirements for possible applications by EMC test houses

For the vehicle manufacturer role the anticipated applications for modelling are quite different, but again the nature of the application has a bearing on the fidelity that is required of the model elements.

The requirements for a number of possible applications associated with vehicle manufacturers are presented in Table 5.3 below.

Modelling task	Objectives	Antenna model fidelity	Test object model fidelity	Comments
Evaluation of harness and module placement options	Early identification of possible problems	Abstract	Intermediate	Final, detailed geometry will not be available, plane wave source is probably adequate
Specification of system immunity requirements	Realistic system EMC specifications	Abstract	Intermediate	Final, detailed geometry will not be available, plane wave source is probably adequate
Design studies for vehicle antennas	Evaluation of antenna placement options	Intermediate or detailed	Intermediate	General trend assessment is probably feasible without detailed geometry
Prediction of intra-system EMC and/or antenna coupling	Identification of performance defects and EMC protection requirements	Detailed	Detailed	Accurate prediction of coupling is likely to be highly dependent on geometry, placement and termination characteristics
Prediction of emissions from installed systems	Identification of performance defects and EMC protection requirements	Abstract or representative	Detailed	Antenna effect may be significant, and therefore needed in model if the aim is to indicate measured performance

Table 5.3   Model fidelity requirements for possible applications by vehicle manufacturers

5.5   Calibration of models and measurements

In order obtain numerical results that are directly comparable with measured values it would be necessary to include an enormous amount of detail. For example, in an immunity test an antenna is typically excited using a signal source that is amplified, and the transmission path may include couplers, switches and significant lengths of cable.   In addition, such measurements are often made in a semi-anechoic chamber, where issues such as finite ground conductivity and wall reflections may influence the field distribution that is achieved. Moreover, the presence of the system under test will also modify the field distribution, and perhaps even the input impedance of the antenna. The latter could also modify the power radiated by the antenna.

In modelling such measurements it is desirable to minimize the number of real-world elements that must be included in the model, in order to avoid making the model too large. Certainly the system under test must be present, and for comparison with measurement it is also necessary to introduce a suitable representation of the antenna. If the room is a very poor approximation to the semi-anechoic ideal it may be necessary to model the limitations of the test environment. However, features such as cables and couplers can be characterized and their effects removed from the measurements. Thus, the inclusion of such features in a model is not necessary provided that the measured values can be adjusted to account for their contributions.

Calibration of immunity measurements

The comparison of measured results between different laboratories, or between tests on different test objects, presents similar difficulties. In order to ensure that measurements are directly comparable in automotive immunity testing an initial calibration of the empty chamber is used to provide a reference. In this "substitution method", a transfer function is determined that relates the power required to produce a given field strength at some reference point (which is related to the geometry of the test object) with the antenna in the test configuration. The desired test level is then obtained by linearly scaling the source in accordance with the transfer function.

In automotive immunity testing the reference point (and hence the antenna position) are related to the mid-point of the axis of the front axle. Consequently, the substitution method of calibration provides a standardized test configuration for all vehicles under test, although the way in which vehicles of different sizes and shapes interact with the field will inevitably differ. Thus, the local field distribution will be unique to each vehicle, despite the fact that the excitation that is applied in each case is the same. Nonetheless, provided that the same antenna is used in the same environment then the results will be directly comparable for a given vehicle. If either of these is different, however, matching the field at the reference point will not ensure that the spatial field distributions for the two measurements are identical. Thus, it is possible that the two tests may result in different outcomes.

Despite the limitations of this calibration method, it provides a useful model for producing computed and measured results in formats that are directly comparable. During a physical immunity test the aim is to apply the power that would result in a particular field level at the reference point for all frequencies with the empty chamber. In a numerical model, however, it is much more convenient to apply a fixed excitation, with the result that the field will vary across the frequency band. Consequently, it is also highly desirable to remove the need to predict exactly the same levels in the model as those of the physical test. The field at the reference point is therefore ideally suited for normalising the computed and measured results.

Although this presupposes that the system is entirely linear, this condition is not expected to be a limitation for the anticipated applications.

Normalization of measured and computed results

It is assumed that the field $E(x,y,z,f)$ generated by an antenna at a point (x,y,z) and frequency f is linearly related to the incident voltage $V_0(f)$ such that:

$$E(x, y, z, f) = V_0(f)\eta(f)w(x, y, z, f) \tag{5.1}$$

where the function $w(x,y,z,f)$ describes the spatial distribution as a function of frequency and $\eta(f)$ represents losses associated with features such as antenna input impedance mismatch, transmission through the matching network, and cable losses. In the calibration process, measurements of the electric field at a reference point (x_0,y_0,z_0) and the corresponding forward power are recorded at each frequency. These values are used essentially to determine the product $\eta(f)w(x_0,y_0,z_0,f)$, which allows the power needed to establish the required empty chamber test level to be determined. This power is then applied to the antenna terminals during the test to produce the required field strength. The vehicle inevitably modifies the field distribution during the test, but the substitution method at least provides (in theory) a test condition that is reproducible for any vehicle and any test site. In practice, however, differences between the environment and antennas used at different test sites will limit the degree of correlation between them.

For the purpose of model validation, the details of the source can be eliminated by normalizing the field at each point of interest using the value at some reference point. The relative field strength is then merely the ratio of the parameters $w(x_i,y_i,z_i,f)$ for the two points. If the measured electric field data is presented in the same way, the computed and measured results should then be identical if the model is representing the spatial field distribution correctly. A further benefit of this approach is that systematic errors in the values provided by the field probe are also eliminated through the normalization, provided that the response is linear with the applied field strength. This will further improve the correlation between measured and computed values if the probe is not characterized in detail, or has been calibrated against a reference that is imperfect. A preliminary calibration model is required for this purpose, comprising the workspace and the illuminating antenna. A simulation providing electric field at the reference point is then analogous to the chamber calibration method, and provides a mapping between the excitation applied to the antenna terminals, which is likely to be a voltage $v(f)$, and the reference field $E_R(v)$.

In the simulated test the same excitation $v(f)$ is applied and quantities of interest $q_k(v)$ are recorded. These quantities may be of any required type, such as wire currents or spatial fields. However, since the excitation is the same as in the calibration model they can all be normalized to the reference field $E_R(v)$. Thus, the normalized quantities are:

$$Q_k(f) = \frac{q_k(v)}{E_R(v)}$$ (5.2)

The physical measurement can be carried out in any manner that is convenient, such as constant power or constant equivalent substitution field. The results of the chamber calibration ensure that it is possible to map the power used during the measurement to the field at the reference point. Hence the parameters measured with the test object in place can be normalized to this field in the same manner as has been proposed for the treatment of model results.

The calibration yields the power $P(f)$ that is required to achieve the calibration field $E_R(P)$. If a fixed equivalent empty chamber field $E_F(f)$ is applied during the measurements then the measurements $n_k(E_F)$ can be normalized using this field:

$$N_k(f) = \frac{n_k(E_F)}{E_F(f)}$$ (5.3)

In practice it is unlikely to be feasible to achieve a constant equivalent field, primarily because of destructive interference effects associated with the conducting ground, but also because of variations in the antenna characteristics.

If a known power $P_P(f)$ is applied (which could equally well be a constant power), the equivalent field $E_P(P_P)$ is given by:

$$E_P(P_P) = \sqrt{\frac{P_P(f)}{P(f)}} E_R(P)$$ (5.4)

since the electric field is proportional to the square root of the power. Thus the measured quantities $m_k(P_P)$ can be normalized using:

$$M_k(f) = \frac{m_k(P_P)}{E_P(P_P)} = \frac{m_k(P_P)}{E_R(P)} \sqrt{\frac{P(f)}{P_P(f)}}$$ (5.5)

In the simulated test the same excitation $v(f)$ is applied and quantities of interest $q_k(v)$ are recorded. These quantities may be of any required type, such as wire currents or spatial fields. However, since the excitation is the same as in the calibration model they can all be normalized to the reference field $E_R(v)$. Thus, the normalised quantities are:

$$Q_k(f) = \frac{q_k(v)}{E_R(v)}$$
(5.2)

The physical measurement can be carried out in any manner that is convenient, such as constant power or constant equivalent substitution field. The results of the chamber calibration ensure that it is possible to map the power used during the measurement to the field at the reference point. Hence the parameters measured with the test object in place can be normalized to this field in the same manner as has been proposed for the treatment of model results.

The calibration yields the power $P(f)$ that is required to achieve the calibration field $E_R(P)$. If a fixed equivalent empty chamber field $E_F(f)$ is applied during the measurements then the measurements $n_k(E_F)$ can be normalized using this field:

$$N_k(f) = \frac{n_k(E_F)}{E_F(f)}$$
(5.3)

In practice it is unlikely to be feasible to achieve a constant equivalent field, primarily because of destructive interference effects associated with the conducting ground, but also because of variations in the antenna characteristics.

If a known power $P_P(f)$ is applied (which could equally well be a constant power), the equivalent field $E_P(P_P)$ is given by:

$$E_P(P_P) = \sqrt{\frac{P_P(f)}{P(f)}} E_R(P)$$
(5.4)

since the electric field is proportional to the square root of the power. Thus the measured quantities $m_k(P_P)$ can be normalized using:

$$M_k(f) = \frac{m_k(P_P)}{E_P(P_P)} = \frac{m_k(P_P)}{E_R(P)} \sqrt{\frac{P(f)}{P_P(f)}}$$
(5.5)

The normalized quantities obtained from the measurements and the computations are thus referenced to unit field strength at the reference point in the absence of the object under test, and are therefore directly comparable values. Nonetheless, this calibration approach eliminates the need to duplicate the excitation of the physical measurement in the simulation, thus avoiding considerable additional complexity that would not add anything of material interest to the theoretical model.

Application example

The proposed calibration approach will only be completely successful when the radiation patterns of the real and model antennas are identical, as well as the characteristics of the environment for the real and simulated tests. Although it is not practicable to satisfy both of these conditions in detail, a reasonable approximation to both can provide very satisfactory results.

(a)   Test object

A common validation test case, which is representative of typical EMC scenarios, comprises a cavity containing a wire with an aperture that provides coupling to the outside world. A rectangular cavity with internal length of 2 m and a cross-section of 1 m x 0.8 m was studied for this purpose, constructed as illustrated in Fig. 5.4 below.
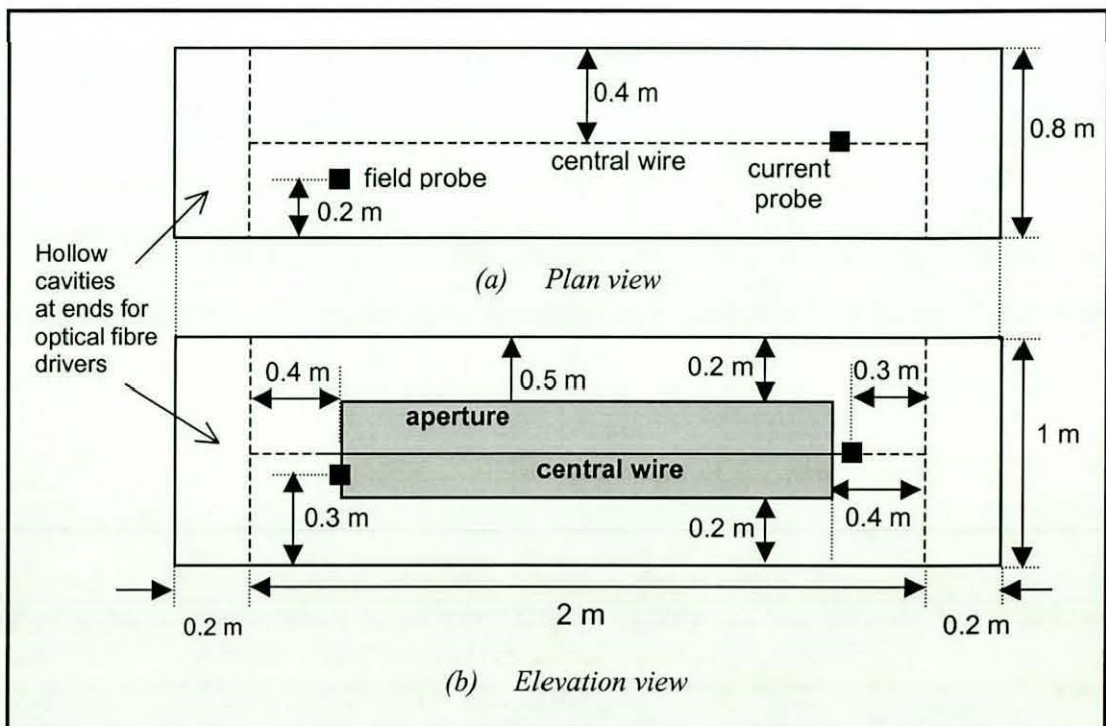
Fig. 5.4   Geometry of rectangular test object and probe positions

This test object was positioned in a MIRA's large semi-anechoic chamber, and illuminated using a log-periodic antenna with relative positioning as indicated in Fig. 5.5 below. The antenna axis was aligned with the centre of the test object.
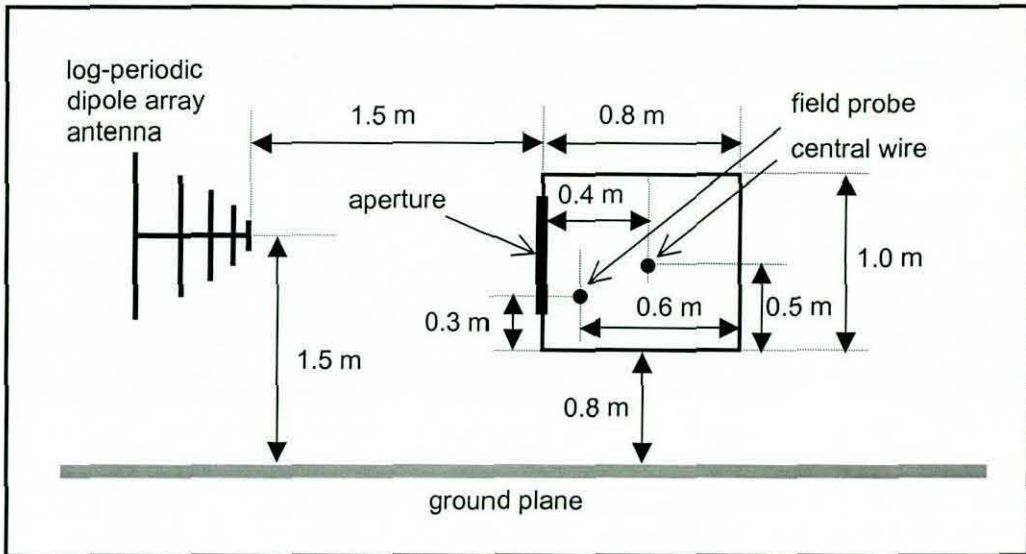
Fig. 5.5   Relative geometry of rectangular test object and antenna for measurements

The characteristics of the aperture could be modified using removable panels. This allowed alternative coupling paths to be investigated, such as those provided by a long thin slot and a carbon fibre window. Experiments with the latter resulted in internal field levels that were too small to measure reliably, but results are presented here for both the large aperture and a thin slot.

The cavities at the ends of the test object (shown in Fig. 5.4) were equipped with a number of coaxial (SMA) connectors on the walls adjacent to the interior cavity. These allowed the current probe signals to be fed to an optical fibre transmitter system located in one of the end cavities, and permitted the internal wire to be located at a number of different positions within the box (ie. displaced from the central position) and terminated with different impedances (eg. short circuit, open circuit and 50 Ω load). The field probes used in this work were equipped with integral optical fibre transmitters. The optical fibres were connected to the measurement systems via "attenuvents" through the walls of the chamber.

(b)   Measured results

A comparison between measured and computed fields coupled into the interior of a rectangular
cavity via a 1 cm wide, 1.2 m long slot is illustrated in Fig. 5.6, indicating that very good
correlations can be obtained using the normalisation approach described above. Although the
model antenna used in this case is a solid metal biconical, the measured results are almost
identical for a real wire cage structure. The predictions also provide a fairly good indication of
the fields measured with a log-periodic dipole array as the source, despite the fact that the
simulation uses a solid biconical antenna.
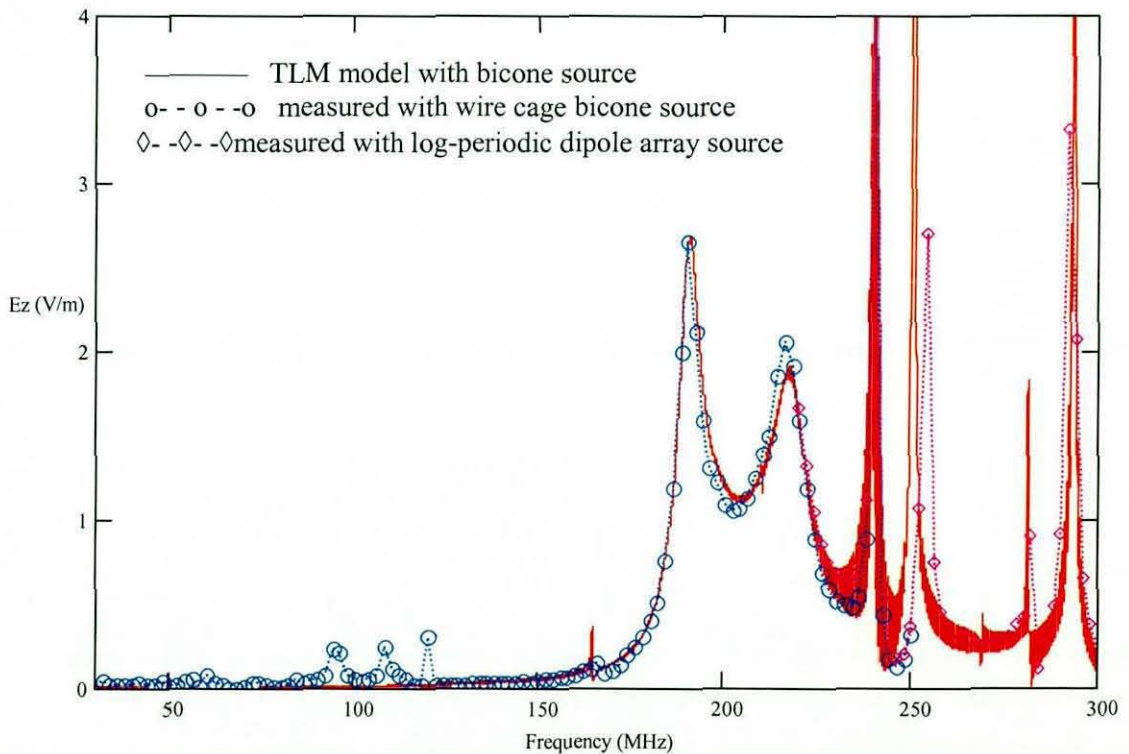
Fig. 5.6   Vertical electric field inside rectangular test box due to vertical source:
coupled through thin slot

Corresponding results for field coupling into the cavity via a large aperture (ie. 1.2 m long and
0.6 m wide, see Fig. 5.4) demonstrate that similar performance can also be obtained (see Fig.
5.7) when differences in the illuminating field distribution are more significant than is the case
for the thin slot. It is concluded, therefore, that this approach provides a sound basis for the
validation of numerical results against measurements, as well as for the comparison of
numerical results from different techniques and experimental results from different laboratories.
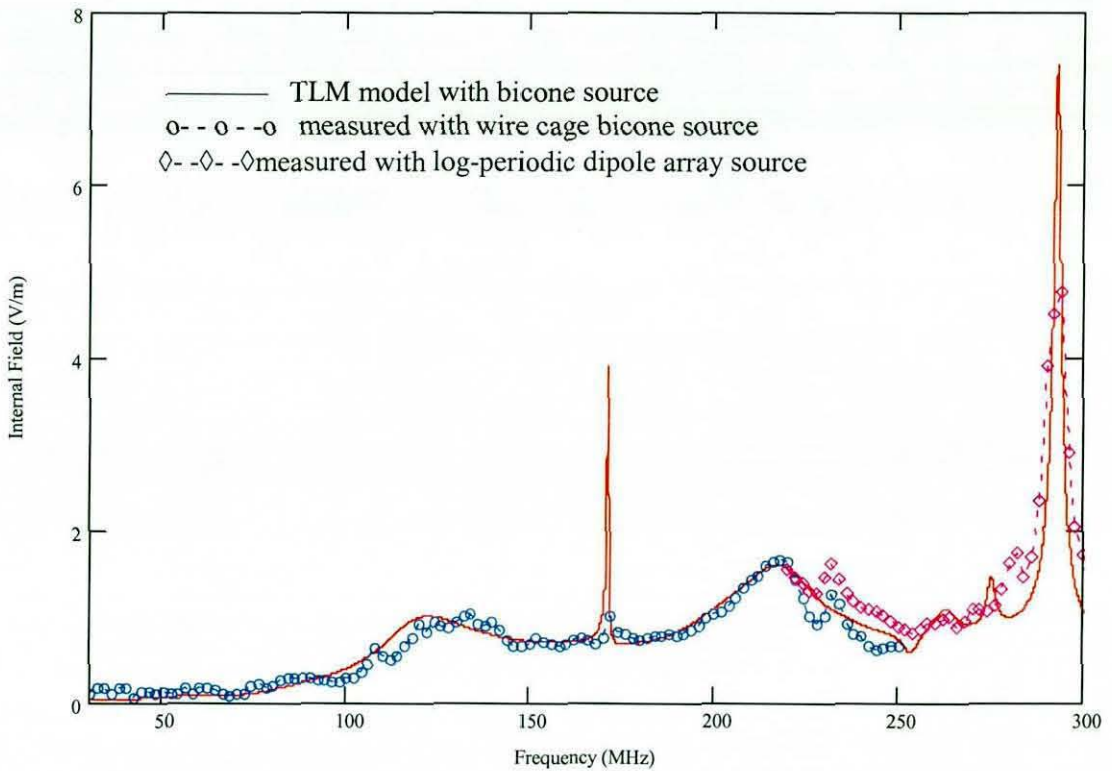
**Fig. 5.7   Vertical electric field inside rectangular test box due to vertical source:
coupled through large aperture**

5.6   Vehicle model content

A complete model containing all parts of a vehicle is unlikely to be practicable for the foreseeable future due to the resulting model complexity and computing requirements. It may also not be feasible because detailed geometry may not be available when the model is required. Consequently, it is necessary to establish which parts of the vehicle must be present in the model in order to ensure that an adequate representation of the characteristics of the real vehicle can be obtained.

A complete vehicle can be decomposed into the following major groups of components:

- bodyshell (ie. chassis and metallic body panels)
- window glazing
- seats (largely metal frames with foam mouldings and leather or textile coverings)
- interior trim (carpets, instrument housing, plastic, leather and textile coverings)
- composite elements (eg. bumpers, body panels for some vehicles)

- mechanical components (engine, powertrain, suspension, brakes, tyres, exhaust etc.)
- electrical components (ie. wiring harness, electronic modules and antennas).

The likely significance of these types of components for CEM models is discussed below.

Bodyshell

The main bulk of the body shell is the most fundamental element of the model. The apertures provide the most significant path for field coupling between the exterior and interior regions. The outer surfaces will determine the scattering characteristics of the vehicle under external illumination, but the interior surfaces, which can be significantly displaced from the outer surfaces (with separations ~ 0.1 m for vehicle doors), will determine the internal resonances of the structure. Both the inner and outer surfaces are required in areas where their separation is significant. For doors, in particular, the internal cavities are of considerable importance as electrical components and elements of the wiring harness are now routinely present in these regions.

Many small details, such as fixings, small apertures and brackets, can probably be neglected without adversely affecting the accuracy of an electromagnetic model.

Windows

Vehicle windows have the potential to be significant electromagnetic features, due to the use of exotic materials, as well as heating elements and antennas that are integrated into the glazing. These issues are discussed in more detail below.

(a) Glass

Although glazing materials have a relatively high dielectric constant ($\varepsilon_r \sim 7$ for typical glasses), the thickness of vehicle windows is sufficiently small to suggest that their effects will be minimal at frequencies up to 1 GHz.

Comparative field measurements [A.14] carried out with the side windows up and down show little difference between these two conditions (see Figs. 5.8-5.9), except in the upper part of the band (where positioning errors are likely to be more significant). In general, therefore, it seems reasonable to ignore the vehicle glazing where simple glass panels (including laminated structures, which are essentially transparent when the thickness is a small fraction of the wavelength) are present.

(a)   On axis in front   (b)   Above right-hand front seat
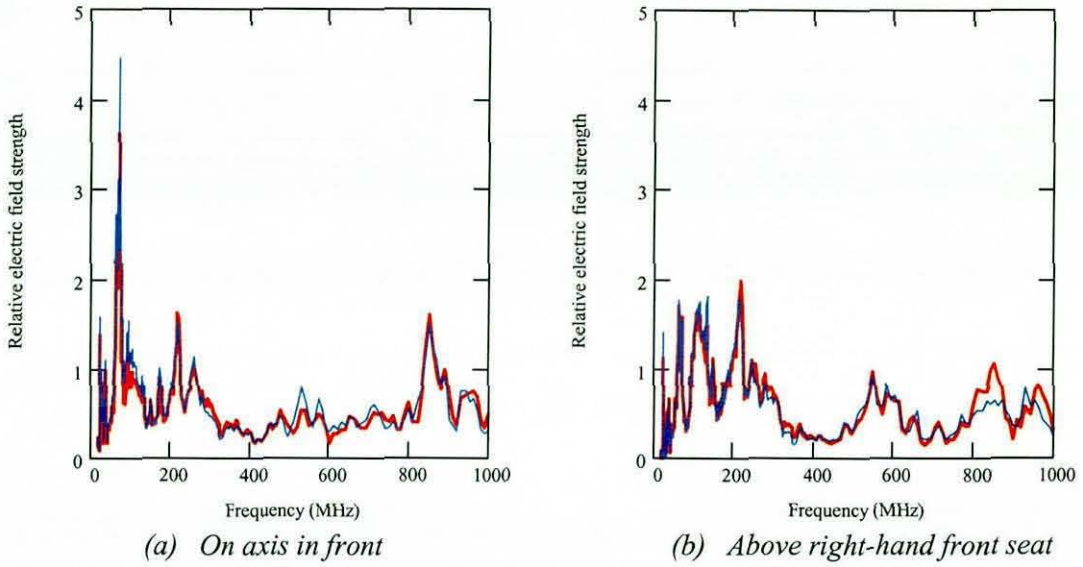
Fig. 5.8   Measured electric fields in front of passenger compartment for vertical illumination from front: with (red, heavy) and without (blue, light) side windows up

(a)   On axis in rear   (b)   Above right-hand rear seat
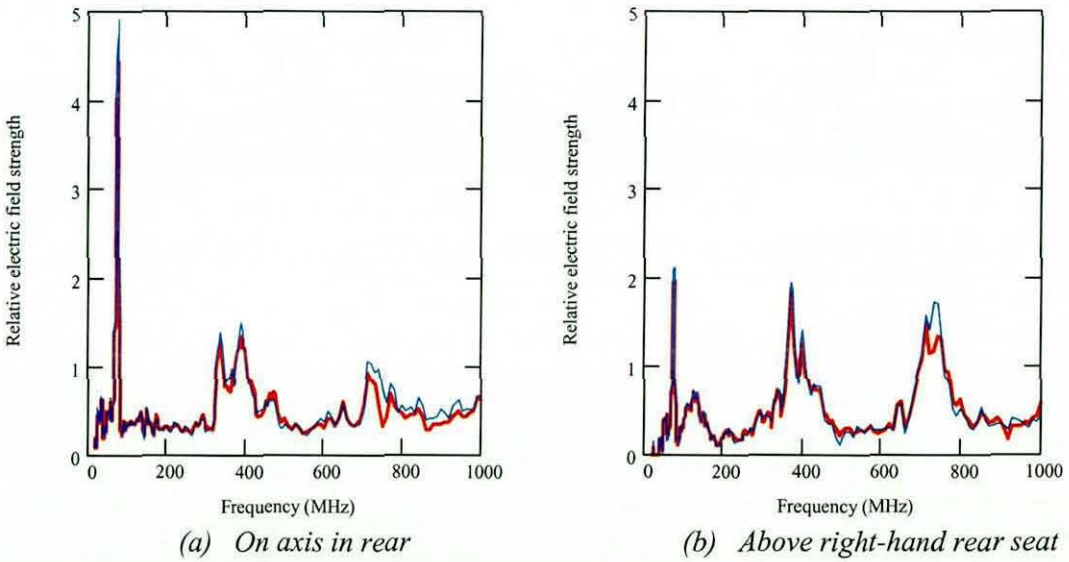
Fig. 5.9   Measured electric fields in rear of passenger compartment for horizontal illumination from side: with (red, heavy) and without (blue, light) side windows up

However, not all windows are of such simple construction, as conductive materials and structures are commonly embedded in the vehicle glazing. In some cases conductive material is added to the glass in order to reduce the transmission of solar radiation (infra-red and ultra-violet) into the vehicle interior. Such schemes are implemented by doping the glass, by adding surface or embedded coatings, or by including a meshed structure. The latter is commonly used in sunroof glazing, while some laminated windscreens also contain an embedded metallic layer.

There is some anecdotal evidence to suggest that this type of solar screening may also influence the transmission properties of the glass at the lower frequencies of interest for EMC performance. In future, therefore, it may become necessary to represent glazing materials in electromagnetic models of vehicles.

(b) Window heaters

Embedded heating elements are commonly used in vehicle windows, usually in the form of simple arrays of conductors, to provide a de-misting or de-icing function. Almost all vehicles are equipped with a heater for the rear window, usually in the form of an array of horizontal conductors, although more complex arrangements can also be found. A more recent development is the introduction of heating elements into the front windscreens of some vehicles, where a much denser array of fine vertical conductors are often used. The polarization and frequency dependent properties of arrays of parallel conductors are well known in microwave engineering, where they are used to modify the polarization characteristics of antennas [5.8]. Meander-line arrays are also used in a similar way [5.9]. Consequently, heater arrays can also be expected to modify vehicle EMC characteristics.

A quantitative indication of the likely effects of heater arrays can be obtained using approximate closed form expressions for the equivalent circuits presented to plane waves by infinite planar arrays of parallel conductors [5.10]. The key parameters influencing the results are:

- array spacing and conductor geometry (ie. cross-sectional form and dimensions) relative to the frequency
- orientation of the conductors relative to the polarization of the incident field
- angle of incidence of the incident field relative to the plane of the array
- presence of dielectric material.

Simple calculations for a representative windscreen heater geometry (ie. vertical wires with a separation of about 5 mm) suggest that such an array would be essentially opaque to vertical polarization for frequencies up to around 1 GHz, and transparent to horizontal polarization. For the more widely spaced (~3 cm) horizontal arrays that are commonly used to implement rear window heaters, the reflection coefficient for a horizontal plane wave for normal incidence falls to around 0.81 at 1 GHz, while for 45° incidence the reflection coefficient falls to around 0.89 at 1 GHz. However the influence of such structures on the electromagnetic characteristics of a vehicle cannot be predicted using such simple methods, because of the geometrical complexity.

Measuring such effects is also not easy, because of the need to remove fixed glazing or to obtain a pair of vehicles that differ only in this respect. However, a TLM model of a vehicle can be augmented with representative models of such structures relatively easily, thus allowing the potential impact of such structures on vehicle emissions and immunity performance to be assessed [A.13].

A dense array of vertical wires (with a spacing of around 5 mm, filling the windscreen aperture) was added to the geometry for a vehicle in order to represent a typical windscreen heater. In order to make this practicable the wires were represented as multiconductors, thus allowing five wires to be placed in the same TLM cell. The rear heater was represented using 21 horizontal wires. The resulting geometrical model is illustrated in Fig. 5.10 below.
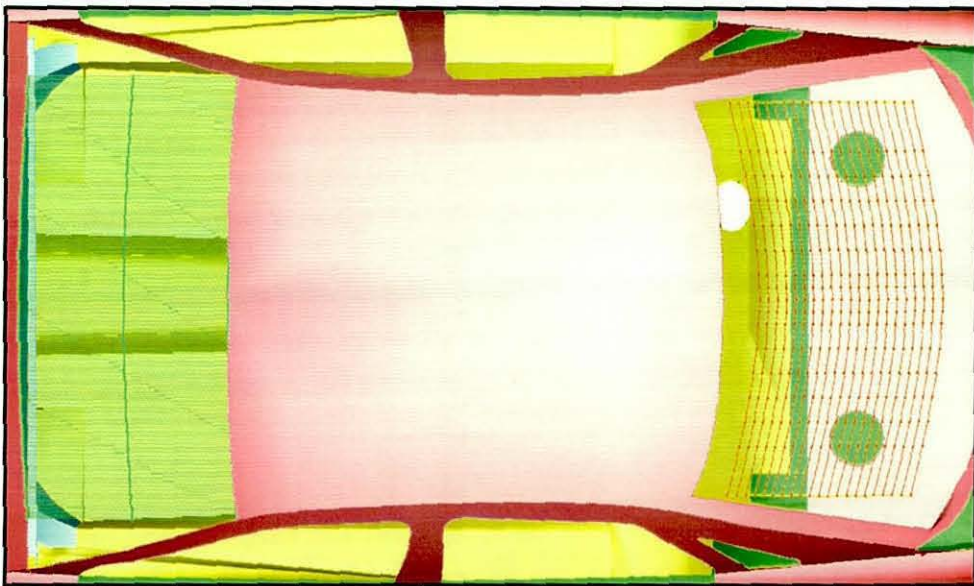
Fig. 5.10   Geometrical model for vehicle with representative heater arrays in front and rear windows

In the interests of computational efficiency, the "immunity" characteristics were investigated using simple plane wave excitations under free-space conditions. Simulations were carried out for both horizontally and vertically polarized plane waves, which were incident from the front (relative to the vehicle). In order to provide some indication of the "emissions" performance, a simple localised field source (with x, y and z field components) was excited inside the vehicle. In both the emissions and immunity scenarios, the resulting electric field was recorded at a number of points in and around the vehicle. In the emissions models, field values were also collected at a point placed 3 m from the vehicle and 1.8 m above the ground plane, on a line through the front axle of the vehicle.

Simulations of the field in and around the vehicle were carried out with no heaters (simplest model, but extremely unlikely in modern vehicles), with the rear heater only (the most common case for current vehicles) and with both front and rear heaters (not yet universal, but increasingly popular).

The results shown in Figs. 5.11 illustrate the computed impact of the heaters on the net field at an internal point under plane wave illumination from the front of the vehicle. This shows the expected behaviour for vertical illumination, in that the windscreen heater generally reduces the internal field strength. For horizontal illumination, the effect of the rear heater is greater and the effect of the front heater is smaller than for the vertical case, as expected from arguments based on the behaviour of planar arrays. However, the impact of the rear heater is negligible up to about 200 MHz for both source polarizations, where simple arguments suggest that the impact of the heater should be most significant for horizontal illumination.

(a) Vertical source   (b) Horizontal source
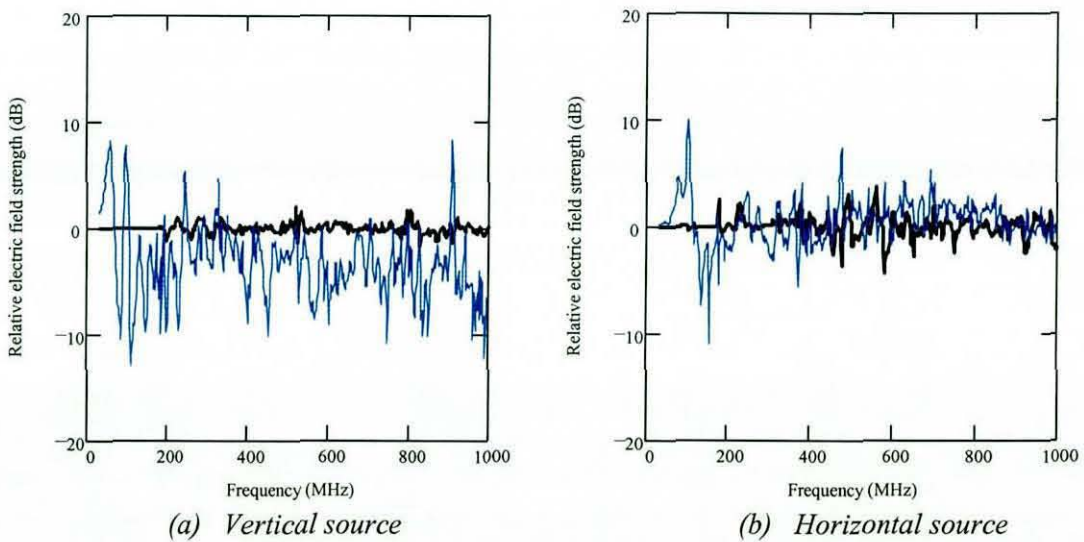
Fig. 5.11 Change in net field at interior point under plane wave illumination from front: from no heater to rear heater (heavy) and from rear only to both heaters (light)

In order to investigate this, the polarization of the field reaching the rear window area under illumination from the front of the vehicle was investigated for both horizontal and vertical incident fields. The results of Fig. 5.12 show that, in the absence of heater arrays, the vertical electric field is larger than the horizontal component in the vicinity of the rear window for vertical plane wave illumination from the front of the vehicle. However, this is also the case at low frequencies for horizontal illumination. This suggests that the impact of the screen heater on immunity characteristics will be small at low frequencies for both polarizations and smaller over the full band for the vertical case than for horizontal, as is seen in the models with heaters.
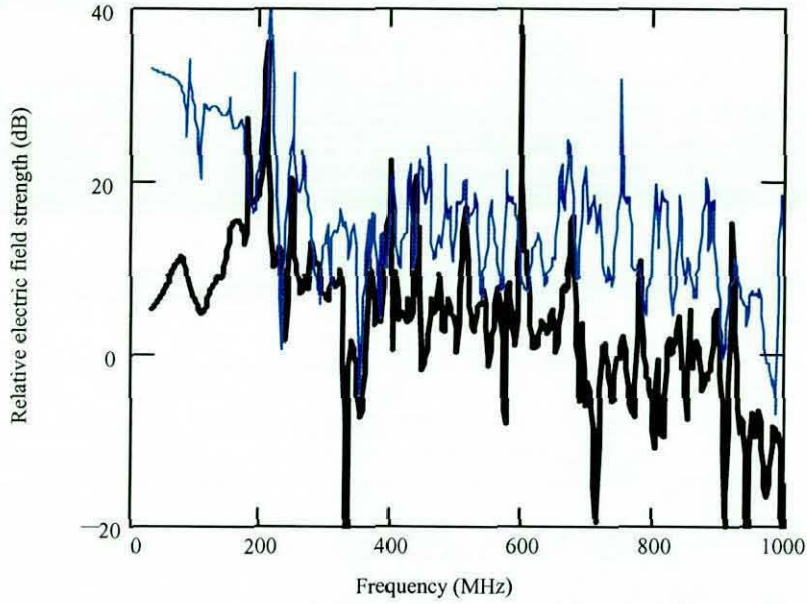
Fig. 5.12   Vertical electric field relative to horizontal component at an interior point adjacent to rear window: for horizontal (heavy) and vertical (light) illumination

For models with a localized internal source the vertical field is found to be the dominant component at the emissions measurement point (located at 3 m from the vehicle). The results of Fig. 5.13, which show changes in the field for both vertical and horizontal fields, illustrate the likely impact of the heaters on the emissions due to such a source.

(a)   Vertical component   *(b)   Horizontal component*
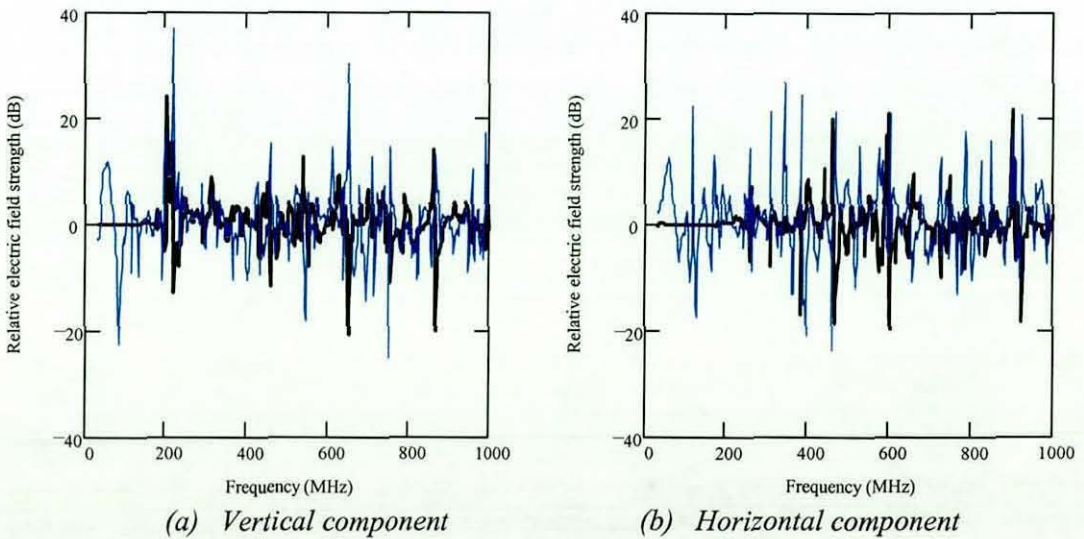
Fig. 5.13   Change in radiated electric field strength at 3 m due to interior source: from no heater to rear heater (heavy) and from rear heater to both heaters (light)

It can be seen from Fig. 5.13 that variations in the emissions of order ±10 dB are associated with the introduction of a rear screen heater, while adding a windscreen heater may introduce further variations of order ±15 dB. The rear heater again has little impact at frequencies below about 200 MHz, since the vertical field is also the dominant component at the rear window in this case.

(c) Antennas integrated with glazing

Security and styling considerations, as well as the increasing numbers of antennas deployed on vehicles, make conformal antennas increasingly attractive for automotive applications. These are often embedded in the window glazing, and are commonly integrated with the rear window heater array. Another possibility is that such antennas are sometimes used behind composite bumpers. At high frequencies the local dielectric material be significant for the performance of such antennas, but even at low frequencies ($f \sim 100$ MHz) where the material is electrically thin the effective dielectric constant is sufficient to modify the electrical length, and hence the performance characteristics, of the antenna.

A TLM model [A.11] of a meanderline monopole mounted in the aperture of a window with a conducting boundary (see Fig. 5.14) illustrates the influence of even an electrically thin layer of glazing material for both embedded and surface mounted configurations (see Fig. 5.15). This effect has also been demonstrated by experimental methods [5.11] at VHF frequencies.
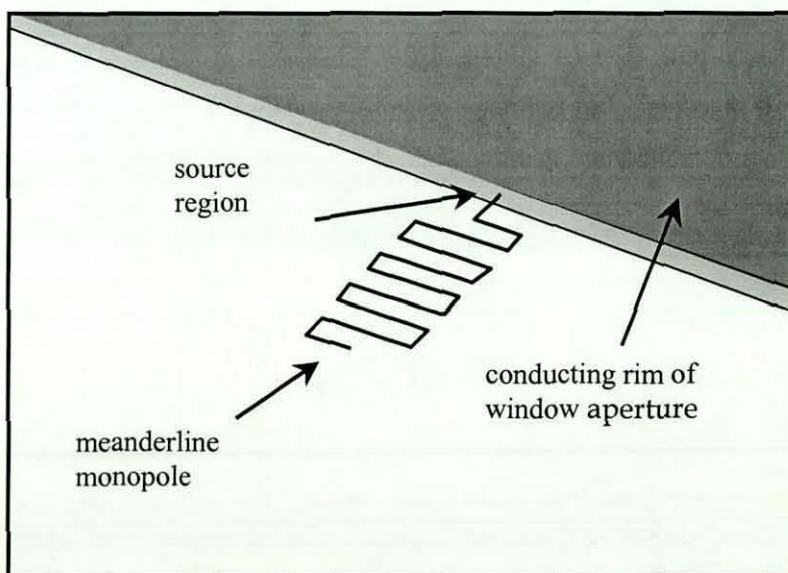
Fig. 5.14   Geometry for meanderline antenna at window edge

(a) Impact of glass   (b) Impact of location relative to glass
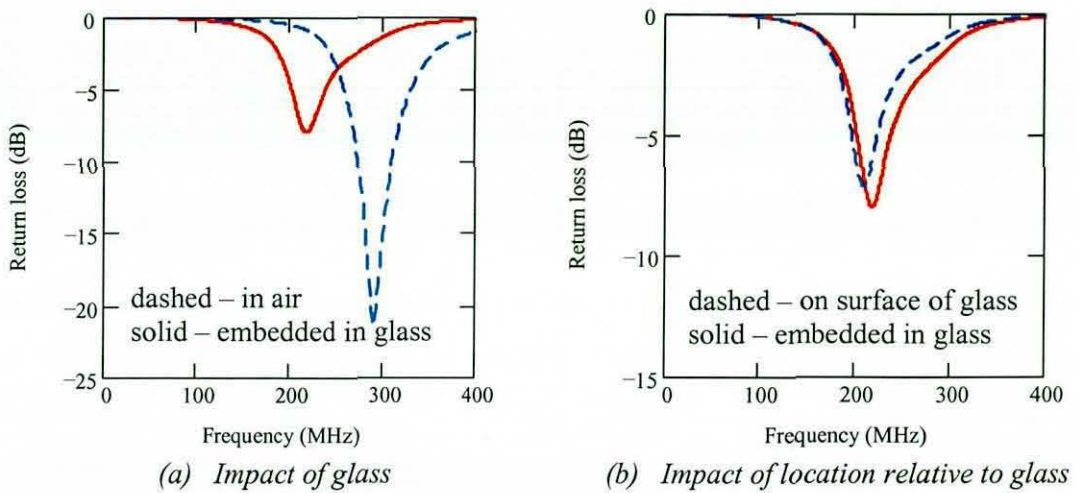
Fig. 5.15   Computed input mismatch for meanderline antenna in air, embedded in laminated glass and mounted on the surface of laminated glass (50 Ω source impedance)

Thus, the presence of the dielectric cannot be simply neglected when attempting to predict the installed performance characteristics of such antennas.

Vehicle seats

Vehicle seats are normally constructed from a metal supporting frame, stiff plastic parts, shaped foam and a thin covering of some type of textile or leather. The rear seats are generally of much simpler geometry than the front seats. The rear seats generally obtain their rigidity from the floor pan and a simple metal panel between the passenger cavity and the rear luggage space. The cushions are therefore largely shaped foam with very little metallic content (perhaps some wire stiffening adjacent to the metal panels). Their electromagnetic significance is therefore likely to be smaller than that of the front seats.

The front seats, by contrast, are much more complicated. The seat itself must provide rigidity for the user, including headrests, and numerous adjustment mechanisms are provided to maximize comfort. In addition, the seat may be fitted with heaters, motors, and even systems for assessing the mass and position of the user. Airbag modules are also found embedded in seat structures. The back of the seat is often constructed from a stiff but open frame, with thick wires running across the open central area to provide support. It would seem likely, therefore, that the front seats would have a very significant impact on the electromagnetic characteristics of a vehicle.

(a) Rear seats

Measurements of the field above a traditional (ie. bench type) rear seat with and without the lower rear seat cushion present (Fig. 5.16) indicate that this structure makes very little difference. This suggests that all such foam and fabric structures within the vehicle can probably be neglected.

(a)   On axis in rear   *(b)   Above right-hand rear seat*
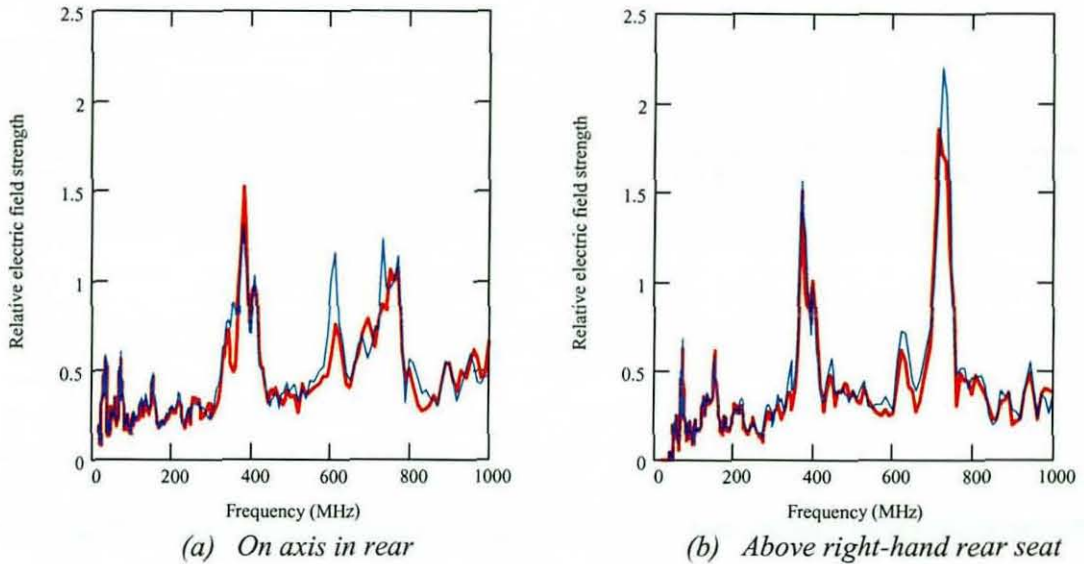
Fig. 5.16   Measured electric fields in rear of passenger compartment for horizontal illumination from side: with (red, heavy) and without (blue, light) lower rear seat cushion

However, an increasing number of vehicles are now being fitted with separate seats, which are very similar to traditional front seats, in order to provide greater flexibility and comfort for users. Thus, in some vehicles, all of the seats are of the more complex construction that has traditionally been used for front seats.

(b) Front seats

In an attempt to quantify the impact of front seats, measurements of the field above the front seats have been made with and without the seats present (see Fig. 5.17). A very significant difference is found in the low frequency resonance on the axis of the vehicle, where the effect of the seats is to reduce the magnitude of the local field by a factor ~4.5. Nonetheless, over much of the frequency range of interest the fields with and without the seats are remarkably similar. The differences are even smaller for the off-axis measurement point.

(a)   On axis in front   (b)   Above right-hand front seat
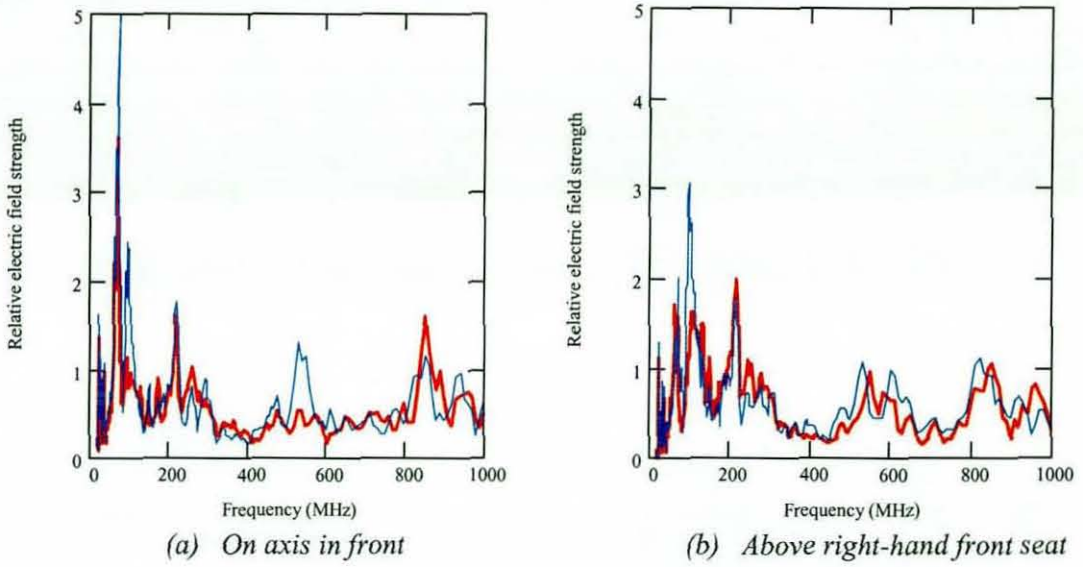
Fig. 5.17   Measured electric fields in front of passenger compartment for vertical illumination from front: with (heavy) and without (light) front seats

In addition, the coupling from an illuminating antenna to coaxial ports on a single conductor harness (added to the vehicle harness in the passenger cavity) has also been measured both with and without the seats present (see Fig. 5.18-5.19). Although there are clear differences between the two responses, the overall level of coupling is generally quite similar.
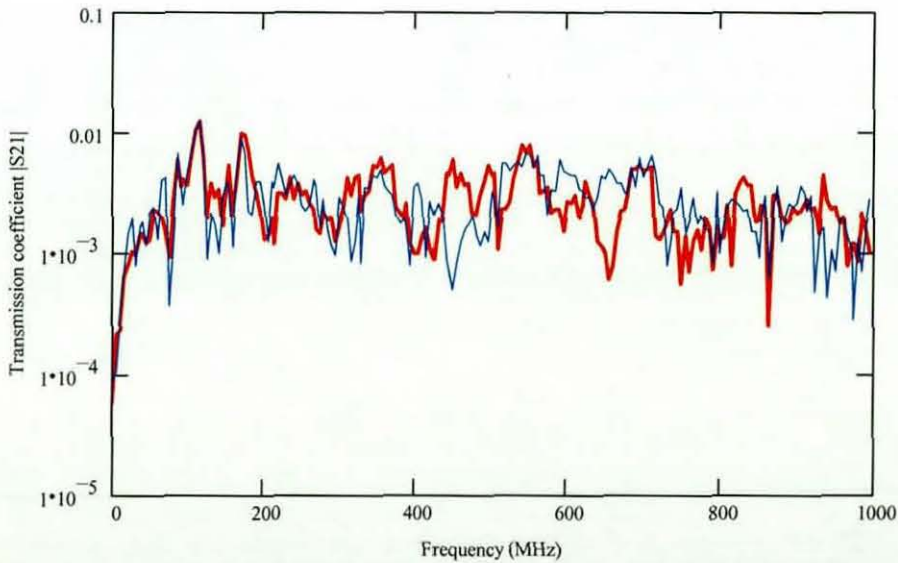
Fig. 5.18   Measured $|S_{21}|$ for harness in passenger compartment for horizontal illumination from side: with (red, heavy) and without (blue, light) front seats
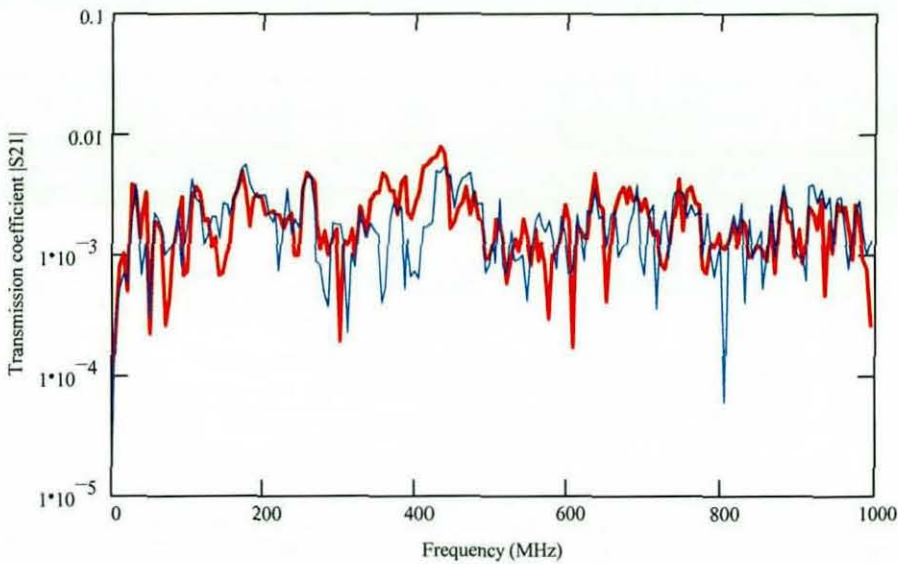
Fig. 5.19   Measured |S$_{21}$| for harness in passenger compartment for horizontal illumination from side: with (red, heavy) and without (blue, light) front seats

Although there are differences between the field and wire coupling results obtained with and without the seats, the impact of these structures is generally much smaller than expected. It appears that a model without the seats would give a good guide to the fields that would be seen above the seats and current levels that would be induced on harness elements running along the floor pan adjacent to the doors. This suggests that even the front seats could be neglected in automotive CEM models for many applications. Nonetheless, they will be essential in models that aim to predict effects in areas that are either within, or at least in very close proximity to, the frames of the front seats.

Interior trim and composite panels

The observations noted above concerning the impact of seat cushions and window glass suggests that most of the interior trim of a vehicle can probably be neglected in vehicle models. Much of the plastic used inside vehicles is thinner than the window glass and is likely to have a smaller dielectric constant (typically $\varepsilon_r \sim 3$ for many such materials). Similar arguments probably apply composite body panels and bumpers, provided that antennas are not associated with such parts.

Mechanical components

Many mechanical components represent large conductors, but their locations are generally such that their influence is likely to be rather limited in many EM and EMC modelling applications.

The majority of the wiring harness and the electronic modules are located around the periphery of the passenger compartment, with some in the engine bay and rear luggage space.

There are often sensors and actuators, and therefore harness elements, associated with the braking system, and perhaps with the suspension elements if an active suspension system is present. Nonetheless, this represents a relatively small proportion of the total and the bodyshell and closures will provide some degree of isolation between the interior cavities and these under-body components. For models where the focus of interest is in the passenger compartment, most major mechanical components are probably of little importance except those associated with the steering column, which is inside the passenger cavity.

The engine bay is packed with mechanical components of many kinds, including metal pipes, and also houses some key electrical components. The latter may include engine management systems in internal combustion vehicles, or electric motors and their associated power conditioning electronics in electric vehicles, together their associated wiring harness elements.

Electrical components

The electrical components of the vehicle include the harness, electronic modules, antennas and electromechanical devices such as motors and actuators.

Vehicle antennas certainly need to be included in models in order to assess their installed performance characteristics, including potential EMC issues relating to these components. Modules that are contained within metallic enclosures that are large compared to the discretization level may also be significant in some areas. Small modules and those harness elements that satisfy the criteria of the transmission line approximation can probably be omitted from models without incurring too much error. However, harness elements that are far from the body panels (such as may occur in the dashboard area and in the engine bay) may act as significant parasitic antennas and ought, therefore, to be included in an electromagnetic model.

5.7   Conclusions

Potential applications of electromagnetic models in automotive EMC and antenna engineering activities are numerous and widespread. However, the requirements for such models are highly dependent on the details of particular applications. A simple classification scheme has therefore been proposed for assessing the geometrical requirements for models intended for different applications.

The complexity of typical results (both measured and computed) and the inherently large uncertainties of EMC measurements are such that the accuracy of such models is not easy to quantify, or even define, in a straightforward manner. It is unreasonable to expect a level of correlation between models and measurements that is better than that obtained for repeated experiments, and a "high fidelity" model (a "simulated measurement", in fact) will generally be required in order to achieve this level of agreement. For model validation purposes it is also necessary to take account of features of the test method that need to be represented in the model, such as calibration practices. The use of normalized field data has been proposed as a means of both taking account of practical chamber calibration methods and mitigating the possible effects of systematic errors in electric field measurement transducers. The success of this approach in providing good quality model validation results has also been demonstrated.

The components that need to be included in vehicle level electromagnetic models are not always obvious. Measurements indicate that significant components such as the seats can have surprisingly little impact, while models suggest that structures that may not be of immediately apparent importance (such as heating arrays in windows, or dielectric materials surrounding conformal antennas) can have a profound effect on the characteristics of the system. Moreover, simple models of the behaviour of individual parts can be misleading when assessing their impact in complex systems such as vehicles. Nonetheless, progress has been made in establishing the necessary content of vehicle models.

5.8   References

[5.1]   A.J.M. Martin, *Quantitative data validation (automated visual evaluations)*, Ph.D. Thesis, De Montfort University, Leicester, UK, September 1999

[5.2]   A.R. Ruddle, D.D. Ward, A.J.M. Williams and A.P. Duffy, *Objective validation of automotive EMC models,* Proceedings of IEEE EMC Symposium, Denver, USA, August 1998, pp. 475-479

[5.3]   A.A. Smith, R.F. German and J.B. Pate, *Calculation of site attenuation from antenna factors,* IEEE Transactions on EMC, Vol. 24, No. 3, August 1982, pp.301-316

[5.4]   J. Clegg, M. Alexander, L. Dawson, J.F. Dawson, J. Jee, A.C. Marvin, B. Loader and S.J. Porter, *A method of reducing the total number of ferrite tiles in an absorber lined chamber*, Proceedings of EMC York 1999, University of York, York, UK, July 1999, IEE Conference Publication No. 464, pp. 59-64

[5.5] J.F. Dawson, *Representing ferrite absorbing tiles as frequency dependent boundaries in TLM,* Electronics Letters, Vol. 29, No.9, pp.791-792, April 1993

[5.6] D.D. Ward, *A three-dimensional model of the lightning return stroke,* Ph.D. Thesis, University of Nottingham, May 1991

[5.7] J.D. Paul, *Modelling of general electromagnetic material properties in TLM,* Ph.D. Thesis, University of Nottingham, October 1999

[5.8] S. Cornbleet, *Microwave optics: the optics of microwave antenna design,* Academic Press, London, 1976, Chapter 5

[5.9] R.-S. Chu and K.-M. Lee, *Analytical model of a multilayered meander-line polarizer plate with normal and oblique plane-wave incidence,* IEEE Transactions on Antennas and Propagation, Vol. 35, No. 6, June 1987, pp. 652-661

[5.10] N. Marcuvitz, *Waveguide handbook,* Peter Peregrinus, London, 1986, Chapter 5

[5.11] B.A. Austin, and R.K. Najm, *Conformal on-glass antennas at VHF,* Proceedings of 8th International Symposium on Antennas and Propagation, 1993, pp. 900-903

CHAPTER 6:   **MEASUREMENT OF CURRENTS**

Toroidal current transducers are commonly used for monitoring currents flowing on single cables or wire bundles, as well as for injecting currents onto such cables. The latter forms the basis of a well-established approach to susceptibility testing (bulk current injection) that is used in the automotive and aerospace industries [6.1-6.2]. Induced currents are also monitored in certain immunity tests, such as those used in the aerospace industry [6.3], as well as in other applications such as the validation of numerical electromagnetic models. These devices are calibrated to determine their transfer impedances, which relate the current on the cable to the voltage at the transducer terminals.

The calibration of these devices is normally carried out using a special calibration fixture, which is essentially a conducting enclosure with coaxial connectors fixed to two opposing faces. A wire connects the centre conductors of the coaxial ports and the enclosure is often an open-sided box, thus providing access to the central wire. The current in the wire (with the remaining coaxial port correctly terminated) and the associated voltage at the transducer terminals are then used to determine the transfer impedance of the device for current measurement purposes.

6.1   Standard calibration techniques

A common approach used to obtain the transfer impedance assumes that the current on the central wire of the calibration fixture is the same as the current flowing in the coaxial ports [6.1]. A network analyser provides a convenient and accurate tool for determining the transfer impedance based on this low frequency model. The current I_0 in the coaxial input, and hence that assumed to flow in the centre conductor of the calibration fixture, is related to the applied voltage V_0 by the characteristic impedance Z_C of the coaxial line:

$$I_0 = V_0 / Z_C \tag{6.1}$$

The transducer output voltage $V_1(f)$ is related to the current $I_W(f)$ flowing through the central wire via the transfer impedance $Z_T(f)$:

$$V_1(f) = I_W(f) Z_T(f) \tag{6.2}$$

Assuming that $I_W(f) = I_0$, the transmission coefficient $\tau(f)$ between the calibration fixture input and the transducer terminals is then:

$$\tau(f) = V_1(f)/V_0 = Z_T(f)/Z_C \qquad (6.3)$$

Hence, the transfer impedance relative to the input can be derived from a simple measurement of $\tau(f)$:

$$Z_{T1}(f) = \tau(f)Z_C \qquad (6.4)$$

This approximation is valid at low frequencies since the electrical separation of the mismatches between the calibration fixture and the coaxial transmission lines will not be sufficiently large for interference effects to become significant. At higher frequencies, however, the effects associated with these mismatches can become increasingly significant, with the result that the current on the wire may be different from that suggested by the low frequency approximation.

A better alternative is to reference the transducer output to the current $I_C(f)$ flowing out of the calibration fixture. This current can be obtained from the transmission coefficient $J_{21}(f)$ between the ports of the calibration fixture, since:

$$J_{21} = I_C Z_C / V_0 \qquad (6.5)$$

Assuming that $I_W(f) = I_C(f)$, an improved estimate for the transfer impedance can be obtained from:

$$Z_{T2}(f) = \tau(f)Z_C / J_{21}(f) \qquad (6.6)$$

In order to minimize the effects of finite mismatch at the ports of the calibration fixture it is desirable to keep the length of the central wire as short as possible, and impedance matching structures are sometimes included at the coaxial inputs in order to reduce the mismatch at the ports.

Thus, the calibration fixture may need to be tailored to the requirements of a particular device. However, it would be desirable to make the design of calibration fixtures as simple as possible, and also to promote the reuse of such equipment with a wide range of devices. This requires a more accurate model of the characteristics of the calibration fixture.

6.2   Including junction reflections

For this analysis [A.8] it is assumed that the calibration fixture may be considered as a section of uniform transmission line with characteristic impedance Z_0 that is terminated at each end with coaxial ports of characteristic impedance Z_C as illustrated in Fig. 6.1 below.
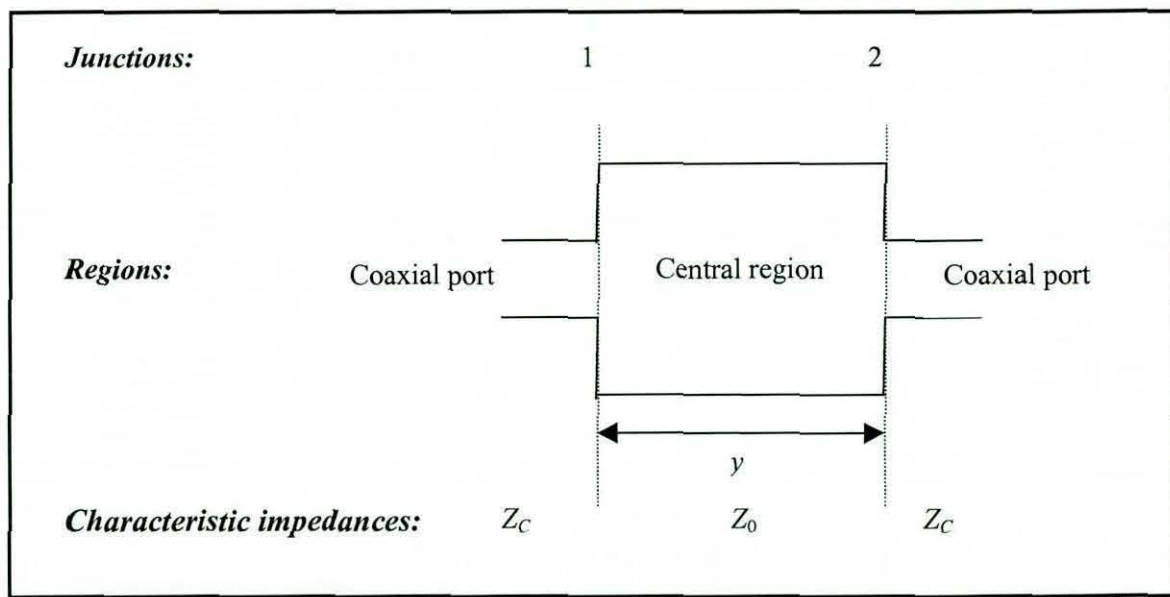
Fig. 6.1   Schematic of transmission line model for calibration fixture

The junctions between the two types of transmission line will give rise to finite reflection coefficients and the resulting reflections will then interfere in a manner that depends on their electrical separation. This model assumes that the junction reflection coefficients take account of the additional path lengths that are introduced between the outer conductors of the coaxial ports as a consequence of the geometry of the calibration fixture.

If the reflection coefficient at junction 1 is $\rho_1(f)$, then assuming symmetry and no returned signal from the output port, it can be shown that the effective reflection coefficient $J_{11}(f)$ at the input port is given by:

$$J_{11}(f) = \rho_1(f) \left[\frac{1 - e^{-2j\beta(f)y}}{1 - \rho_1(f)^2 e^{-2j(f)\beta y}} \right] \tag{6.7}$$

where $\beta(f)$ is the propagation constant and y is the distance between the two junctions. Similarly, the transmission coefficient for the system is given by:

$$J_{21}(f) = \left[\frac{1 - \rho_1(f)^2}{1 - \rho_1(f)^2 e^{-2j(f)\beta y}} \right] e^{-j\beta(f)y} \qquad (6.8)$$

Thus, it is possible to estimate the parameter $\rho_1(f)$ from the measured transmission coefficient for the empty calibration fixture since:

$$\rho_1(f) = \sqrt{ \frac{1 - J_{21}(f)e^{j\beta(f)y}}{1 - J_{21}(f)e^{-j\beta(f)y}} } \qquad (6.9)$$

The only remaining unknown in this expression is $\beta(f)$, which can be determined by substituting for $\rho_1(f)$ in the equation for $J_{11}(f)$, yielding the result:

$$\beta(f) = \frac{1}{y} \cos^{-1} \left\{ \frac{1 - J_{11}(f)^2 + J_{21}(f)^2}{2 J_{21}(f)} \right\} \qquad (6.10)$$

Neglecting any losses, the scattering matrices $U(f)$ and $W(f)$, associated with junctions 1 and 2 (respectively) of the calibration fixture, are then:

$$U(f) = \begin{bmatrix} \rho_1(f) & 1 - \rho_1(f) \\ 1 + \rho_1(f) & -\rho_1(f) \end{bmatrix} \qquad (6.11)$$

$$W(f) = \begin{bmatrix} -\rho_1(f) & 1 + \rho_1(f) \\ 1 - \rho_1(f) & \rho_1(f) \end{bmatrix} \qquad (6.12)$$

The transmission coefficient across junction 1 is given by:

$$\Psi(f) = \frac{U_{21}(f)}{1 - U_{22}(f)W_{11}(f)e^{-2j\beta(f)y}} \qquad (6.13)$$

The voltage at a distance s from junction 1 due to excitation V_0 is then determined from:

$$V_1(s,f) = \Psi(f)V_0 \left[e^{-j\beta(f)s} + W_{11}(f)e^{-2j\beta(f)y}e^{-j\beta(f)s} \right] \qquad (6.14)$$

Hence, the voltage at a distance s, relative to the incident voltage, is:

$$\frac{V_1(s,f)}{V_0} = \left[1 + \rho_1(f) \right] \left[\frac{e^{-j\beta(f)s} - \rho_1(f)e^{-2j\beta(f)y}e^{j\beta(f)s}}{1 - \rho_1(f)^2 e^{-2j(f)\beta y}} \right] \qquad (6.15)$$

The corresponding expression for the relative current may be obtained by negating the reflection coefficients in the voltage expression:

$$\frac{I_1(s,f)}{I_0} = \left[1 - \rho_1(f)\right]\left[\frac{e^{-j\beta(f)s} + \rho_1(f)e^{-2j\beta(f)y}e^{j\beta(f)s}}{1 - \rho_1(f)^2 e^{-2j(f)\beta y}}\right] \tag{6.16}$$

Using the current at the centre of the calibration fixture as the reference, the transmission coefficient between the calibration fixture input port and the current transducer output is:

$$\tau(f) = \frac{Z_{T3}(f)}{I_0 Z_C} I_1(y/2, f) \tag{6.17}$$

The transfer impedance of the current transducer is therefore more accurately given by:

$$Z_{T3}(f) = \frac{\tau(f)Z_C}{\left[1 - \rho_1(f)\right]}\left[\frac{1 - \rho_1(f)^2 e^{-2j\beta(f)y}}{e^{-j\beta(f)\frac{y}{2}} + \rho_1(f)e^{-2j\beta(f)y}e^{j\beta(f)\frac{y}{2}}}\right] \tag{6.18}$$

Both of the approximations that are conventionally used (ie. for the limiting cases with either $\rho_1(f)=0$ or $\rho_1(f)\neq0$ and $s=y$) can be derived from this more general expression. The scattering parameters for the calibration fixture can therefore be used to determine the propagation constant for this structure, and hence the reflection coefficients at the coaxial ports. These two quantities are then sufficient to correct the transfer impedance for the mismatch effects.

6.3   Numerical validation of current estimate

A numerical (TLM) model of a simple calibration fixture has been used to assess the validity and limitations of the approach described above. The internal dimensions for the real device that has been investigated are illustrated in Fig. 6.2 below. The inputs of this device had no special matching structures: the dielectric of the coaxial connectors was flush with the interior surfaces and the centre conductors projected through to meet the central wire. In the model, the central wire (modelled using a thin wire) is terminated with 50 Ω loads (representing the coaxial ports) and excited with a voltage source at one end. The metal panels (3 mm thick) and the central wire (2 mm in diameter) are assumed to be perfect conductors. The real calibration fixture also has thin layers of insulating material (~1 mm thick) bonded to the inner faces of structure, while an insulating sheath surrounds the central wire. However, the electrical properties of these materials are unknown and therefore difficult to model with any certainty.
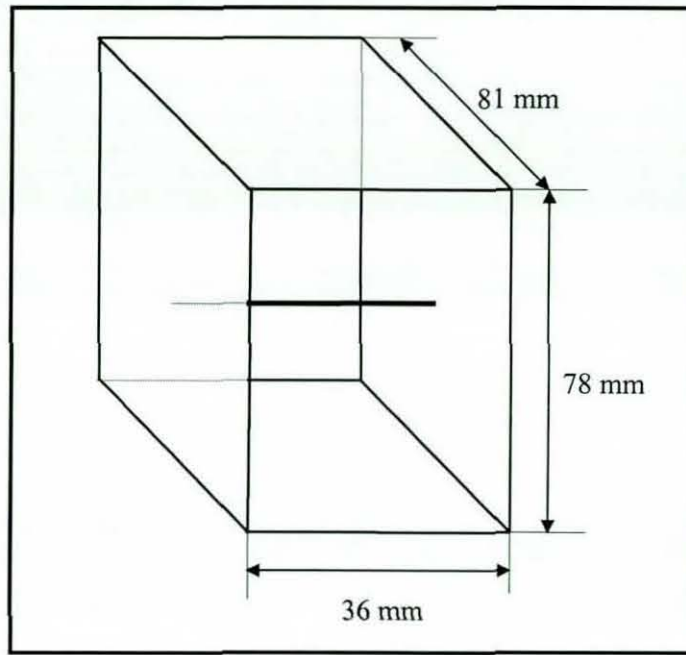
Fig. 6.2   Internal dimensions of calibration fixture

The scattering matrix for the model can be determined from the currents in the loads at the ends of the wire. The sum of the power reflected at the input and transmitted to the output can then be used to establish where the device ceases to be lossless. Measurements can similarly be used to determine the frequency range over which a real structure can be regarded as lossless. It can be seen from Fig. 6.3 that, for this structure, this is a reasonable assumption for frequencies up to about 1 GHz (where the loss is only about 0.5%). For this structure the wire length corresponds to $\lambda/10$ at this frequency, while the dimensions of the larger plates are approaching $\lambda/4$. At higher frequencies the power lost through radiation becomes increasingly significant.

The current at the centre of the wire can be computed directly from the TLM model for comparison with an estimate derived from the computed scattering matrix for the system (as described in section 6.2 above). Results for the propagation constant, also estimated from the scattering matrix, are illustrated in Fig. 6.4, for simulations both with and without dielectric materials present. The latter were represented using a 1 mm thick layer of material with a relative permittivity of 3 added to the inner surfaces of the calibration fixture together with a coating with a relative permittivity of 2.5 and a thickness of 0.6 mm added to the central wire. Both of these dielectrics were assumed to be lossless. In the absence of any detailed information, the relative permittivities that were used were selected as plausible possibilities at best.
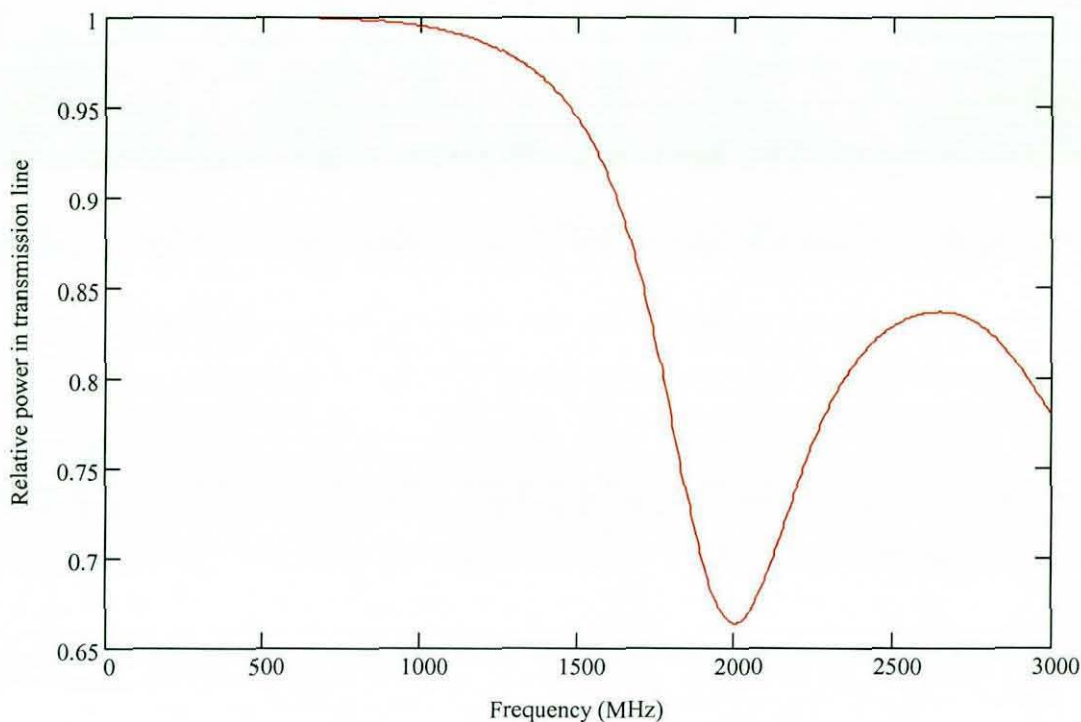
Fig. 6.3 $|S_{11}|^2 + |S_{21}|^2$ **from TLM model of calibration fixture**
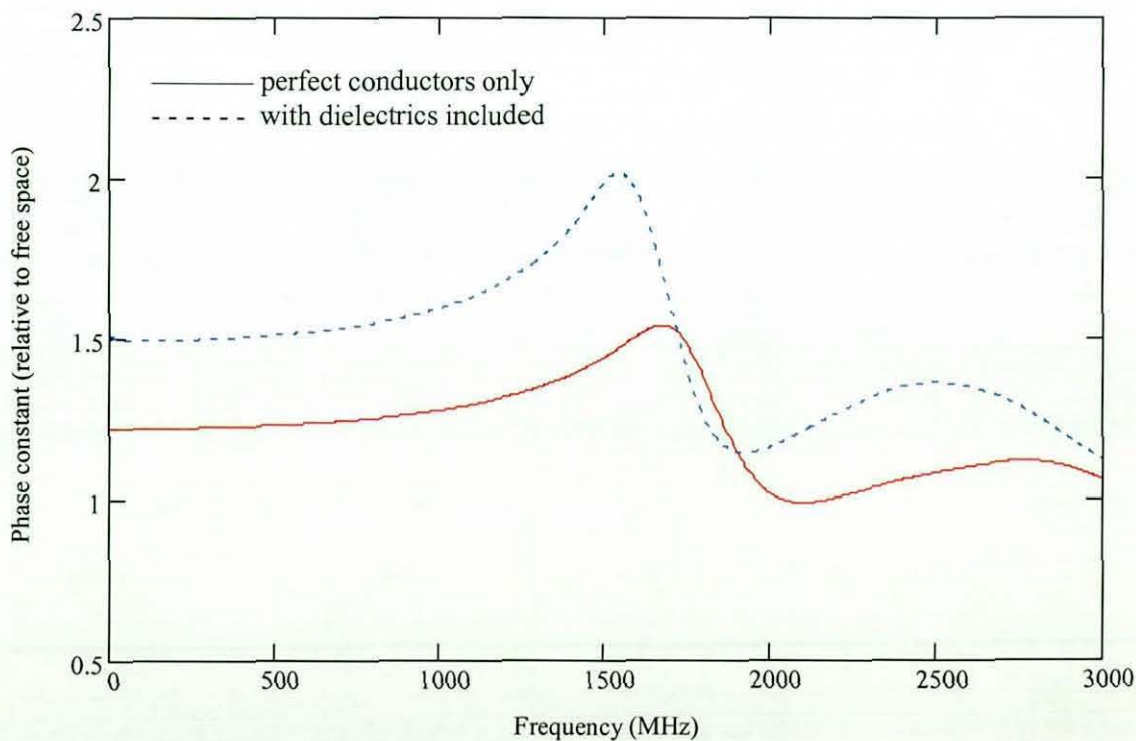
**Fig. 6.4   Phase constant estimated from TLM model of calibration fixture,
with and without dielectrics**

The values for the real component of $\beta(f)$ are greater than $2\pi/\lambda$ for the purely metallic case, and the effect of the dielectric material is to further increase this parameter. The imaginary components are zero up to about 1 GHz, where the behaviour of the device is becoming more complicated.

The results of Fig. 6.5 illustrate that, although the current at the output provides a reasonable estimate for the current at the centre of the wire for low frequencies, the value obtained from the scattering matrix for the device provides a much better estimate. Moreover, this method continues to provide a very good indication of the current at the centre of the wire, even at much higher frequencies where losses become more significant.
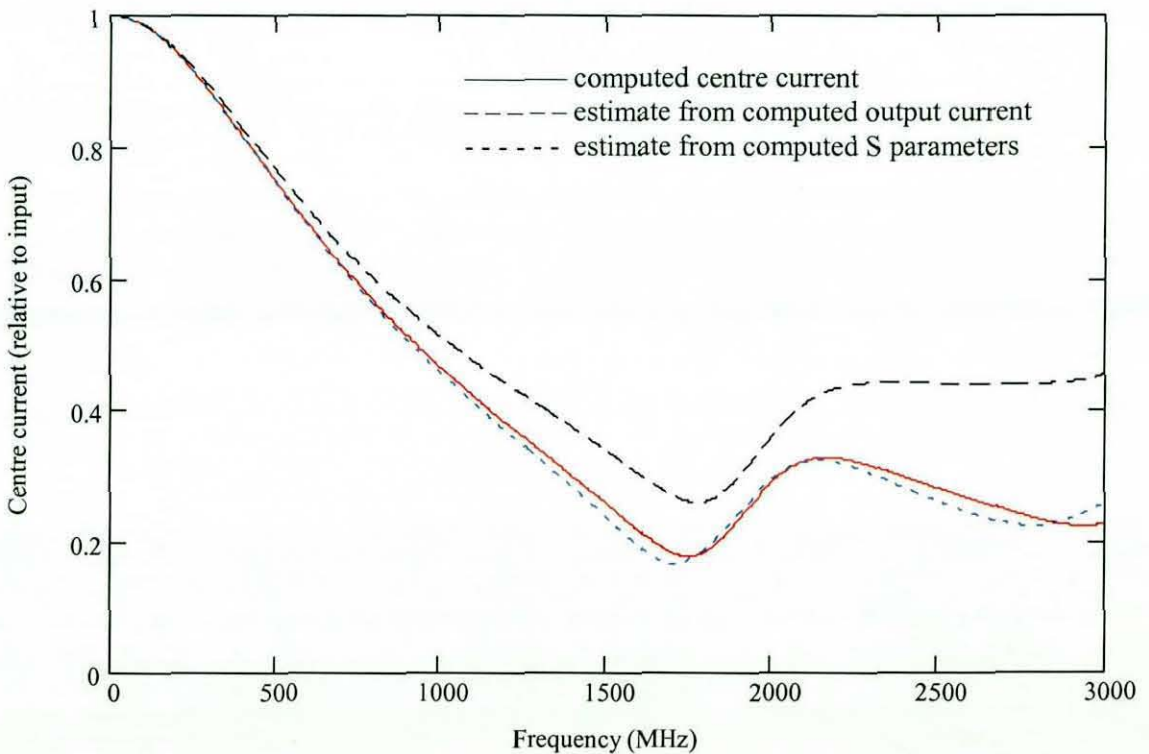
Fig. 6.5   Centre current and estimates derived from TLM model of calibration fixture

Although the structure begins to radiate at the higher frequencies, the junctions remain lossless and the transmission line model still provides a good estimate for the current at the centre of the wire. The errors resulting from estimating the current by different methods are compared in Fig. 6.6, showing errors at 1 GHz of little more than 1% for the proposed method, compared with around 10% for estimates based on the output current.
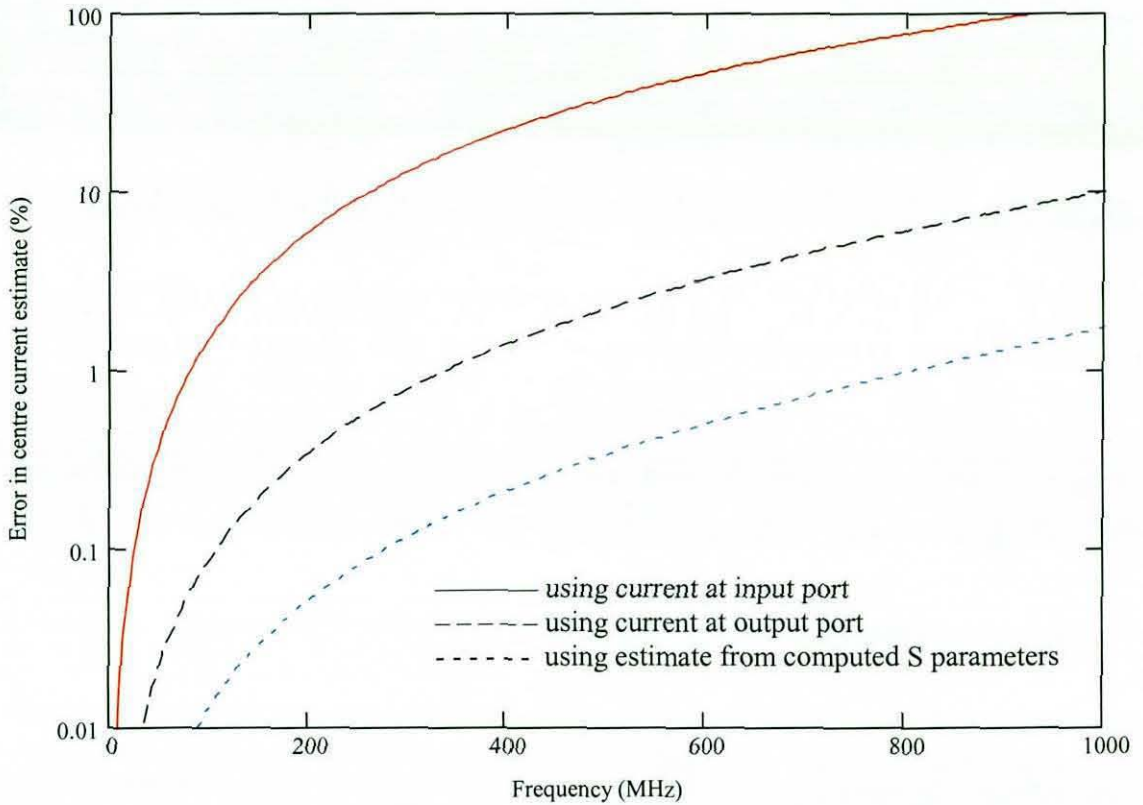
Fig. 6 .6   Error in centre current estimates for TLM model of calibration fixture

6.4   Calibration of model validation test case results

In general, no independent corroboration is available for wire currents measured with a transducer that has been calibrated in the manner described above. However, the experimental validation of numerical models does provide a useful opportunity to assess the success of the proposed calibration technique.

A common test case used in the validation of numerical techniques for EMC applications comprises a cavity containing a wire and an aperture that permits coupling with an external field. In such an experiment, the field at a point inside the cavity and the current at a point on the cable (which was terminated at each end with a 50 Ω load) were recorded under external illumination from a log-periodic dipole array in a large semi-anechoic chamber. The cavity (see section 5.5 and Figs. 5.4-5.5) was 2 m long with a cross-section of 1 m x 0.8 m, and the wire was 2 m long and placed along the longitudinal axis of the cavity. A similar numerical model was also constructed using TLM. Although it was not practicable to model the full details of the real antenna, a simpler version of the log-periodic structure was used to simulate the real antenna over the lower part of its operating band.

In this case the current transducer (25 mm in diameter and 16 mm thick) did not fill the calibration fixture, in which the central wire was 36 mm long. The measurements carried out included the scattering matrices for the calibration fixture in isolation and with the transducer centrally positioned, as well as the transmission between the transducer and calibration fixture ports. The measured return loss for the calibration fixture is illustrated in Fig. 6.7, both in isolation and with the current transducer centrally positioned.
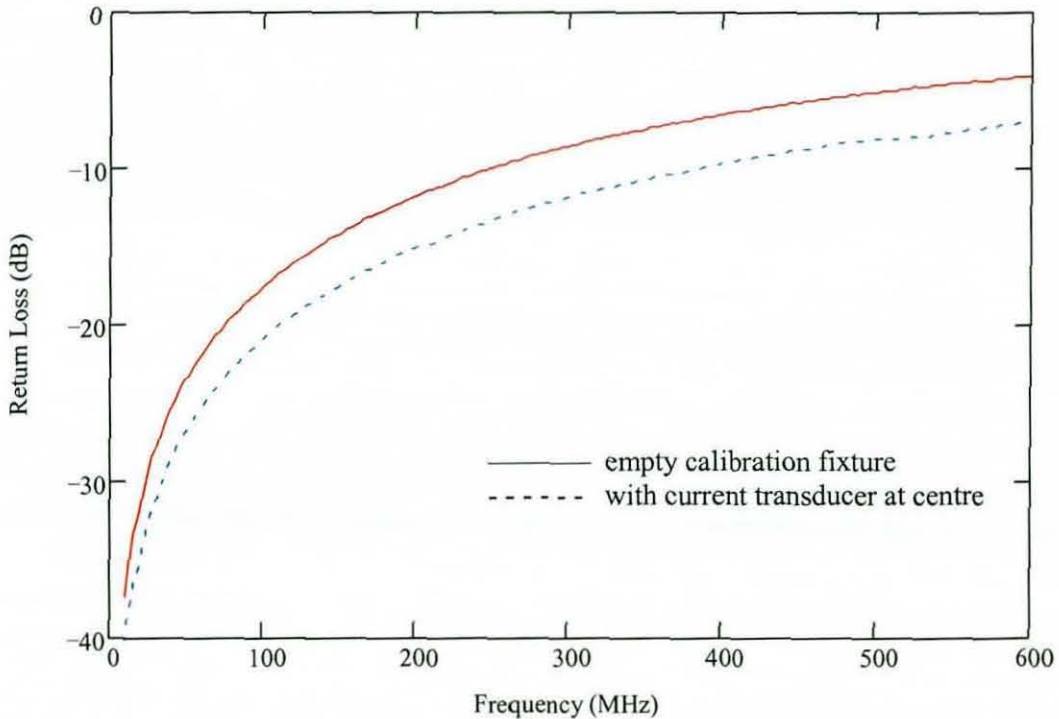
Fig. 6.7   Measured return loss for calibration fixture

The differences between these two cases indicate that the transducer is also a source of additional reflections in the system, which can be expected to further modify the current on the central wire. Nonetheless, the centre current for the empty fixture has been used as the reference, since the calibration then takes some account of the effect of the transducer on the measured currents.

The phase constant that is estimated from the measured characteristics of the empty calibration fixture is shown in Fig. 6.8, while Fig. 6.9 shows the estimated reflection coefficient for the coaxial ports. The phase constant estimated from the measurements is both larger and increases more rapidly than that suggested by the TLM model. However, the dielectric properties used to generate the model results were illustrative only, and the model results can therefore only be expected to indicate general trends.
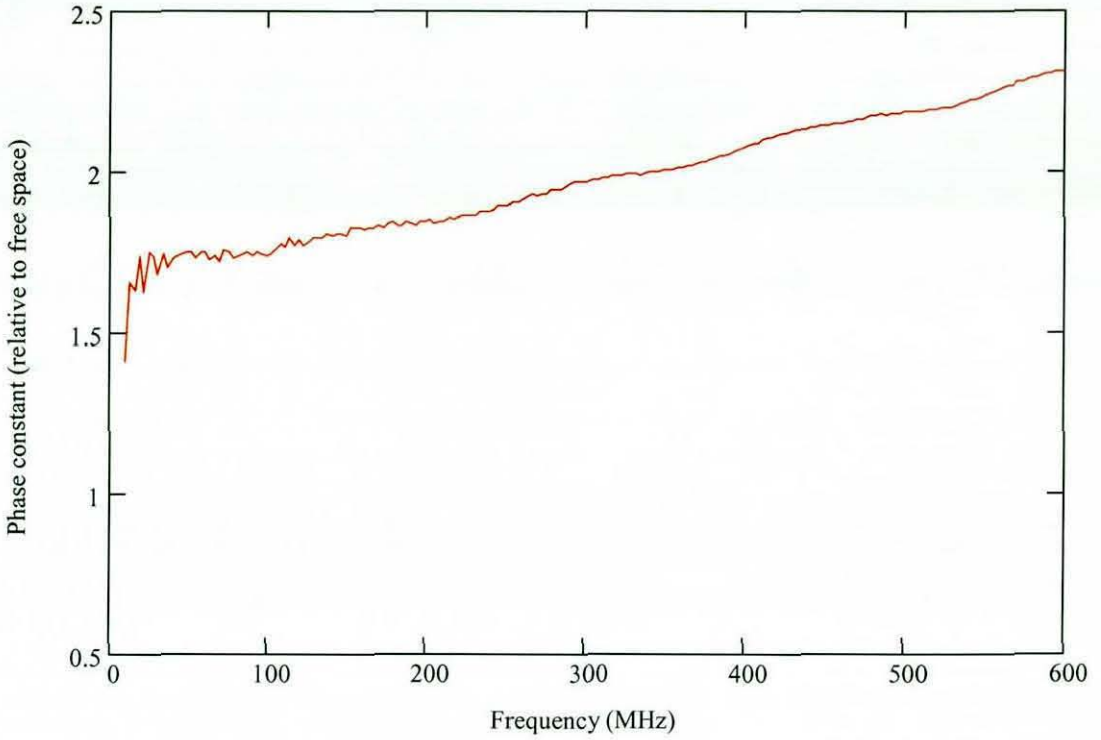
Fig. 6.8   Phase constant estimated from measurements on calibration fixture
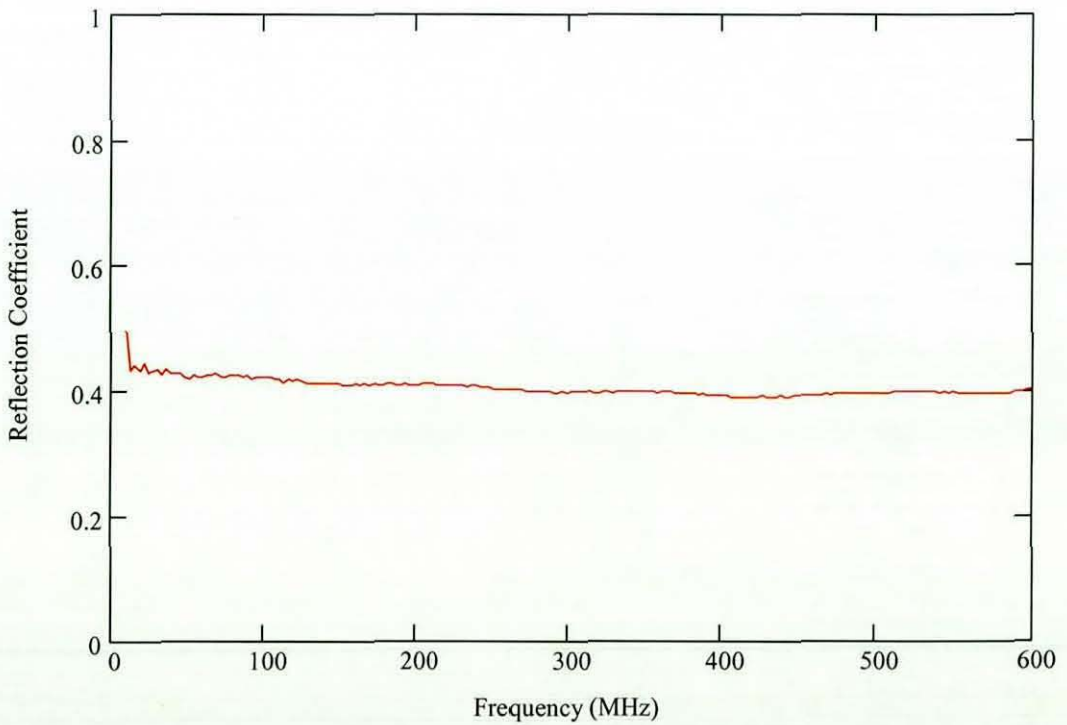
Fig. 6.9   Reflection coefficient for coaxial ports estimated from measurements

The transfer impedance estimates are all of similar form, but the results are increasingly divergent at the higher frequencies (see Fig. 6.10). The differences start to become noticeable for frequencies above 200 MHz, which corresponds to a return loss of around 12 dB for the empty fixture and 15 dB with the current transducer at the centre. Resonant features are also present at the higher frequencies, but as the corrections are individually computed and applied for each measured frequency these effects can be tolerated provided that they are consistent.
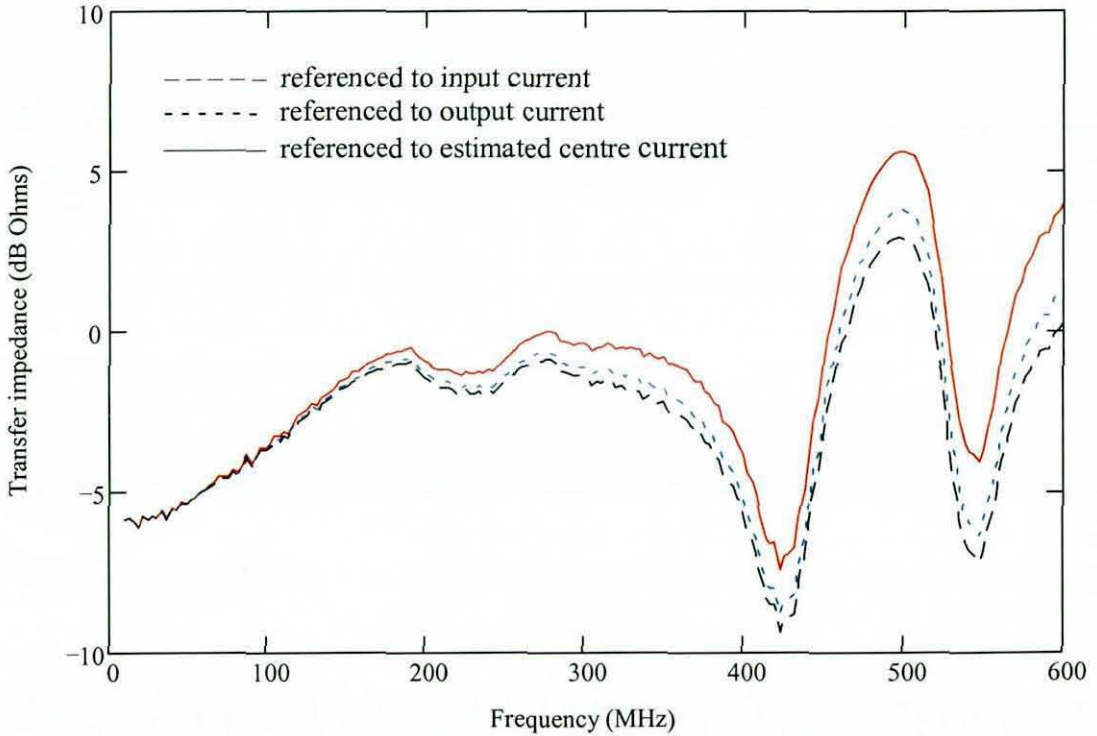
Fig. 6.10   Transfer impedance estimates for a real calibration fixture

It can be seen from Fig. 6.11 that the measured current levels are much closer to the predicted values when the estimated centre current for the calibration fixture is used as the reference. The residual differences and frequency shifts in the features of the modelled and measured results can probably be attributed to differences between the real geometry of the test case and the approximate representation used in the numerical model.
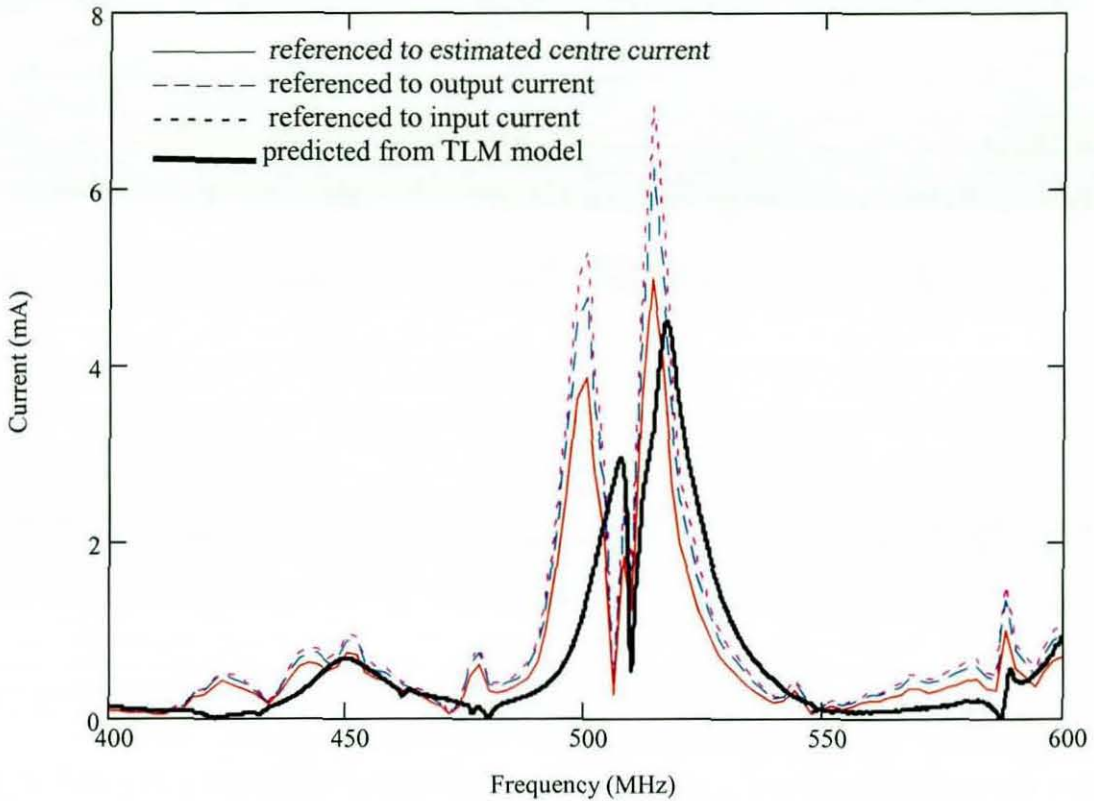
Fig. 6.11   Measured and computed current on wire inside test box

The TLM model of the calibration fixture indicates a significant improvement in accuracy from using the output current, and a further modest improvement from using the estimated current at the centre of the wire. Nonetheless, this does not appear to be the case for the real device. Referencing the real calibration to the current flowing out of the fixture rather than the incident current results in a difference of only around 1.1 dB at 600 MHz. However, using the current estimated for the centre of the real fixture adds a further 2.6 dB at 600 MHz. There are significant differences between the propagation constants and reflection coefficients extracted from measurements on the real device and from the TLM model, but more detailed TLM models and further experimental studies are required to investigate these differences.

6.5   Transducer only partially filling calibration fixture

Referencing the calibration to the current at the centre of the empty calibration fixture provides significant improvements in the correlation between measured and computed currents. Moreover, this approach also takes some account of the effect of the transducer on the measurement, which is important since the parameter that is actually of interest is the current that would flow without the transducer present.

In simulations, it is also highly desirable to avoid the need to include a representation of the transducer in the model.   However, the measured properties of the calibration fixture are modified when the transducer is introduced, and these effects may need more careful treatment in order to obtain an accurate calibration of the current transducer.

In cases where the transducer does not completely fill the calibration fixture the significance of the additional mismatches could be estimated for the symmetrical arrangement as indicated in Fig. 6.12 below.
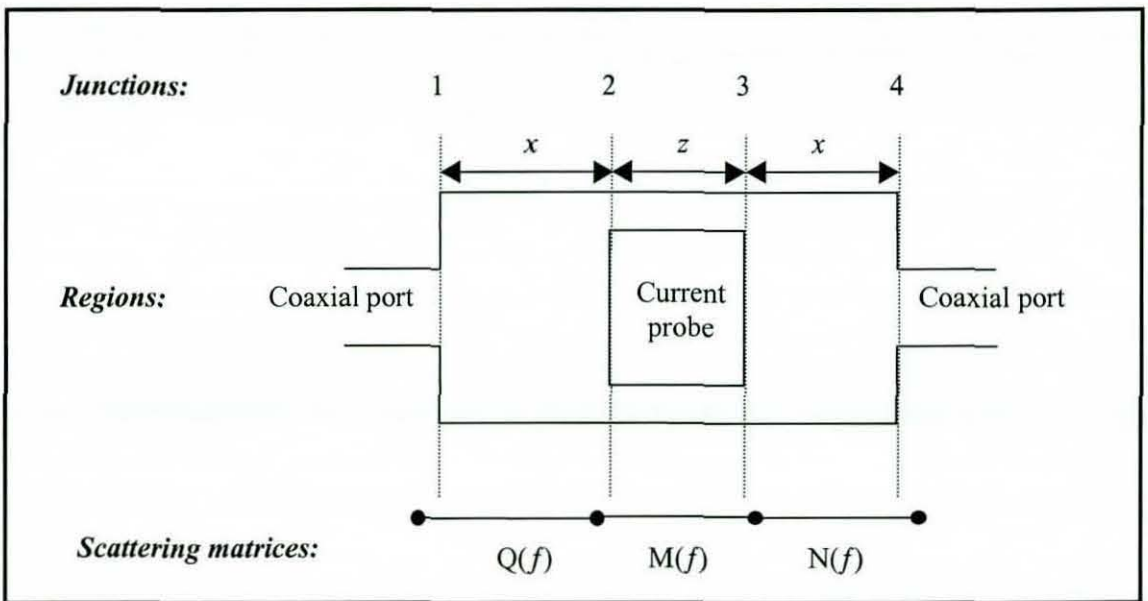
Fig. 6.12   Transmission line model for partially filled calibration fixture

An initial measurement of the calibration fixture without the transducer in place will again provide the reflections at the coaxial ports. With the transducer positioned at the centre of the calibration fixture, the region between the coaxial ports may be considered in terms of three sections with scattering matrices $Q(f)$, $M(f)$ and $N(f)$. The region occupied by the current transducer, represented by the matrix $M(f)$, is approximated as a symmetrical pair of lossless junctions separated by a length z of transmission line with propagation constant $\gamma(f)$.

The, matrices $Q(f)$ and $N(f)$ comprise the coaxial junctions and transmission lines representing the lengths (x) of empty calibration fixture on either side of the current probe. Hence, the associated scattering matrices are:

$$Q(f) = \begin{bmatrix} \rho_1(f) & \{1-\rho_1(f)\}e^{-j\beta(f)x} \\ \{1+\rho_1(f)\}e^{-j\beta(f)x} & -\rho_1(f)e^{-2j\beta(f)x} \end{bmatrix} \tag{6.19}$$

$$N(f) = \begin{bmatrix} -\rho_1(f)e^{-2j\beta(f)x} & \{1+\rho_1(f)\}e^{-j\beta(f)x} \\ \{1-\rho_1(f)\}e^{-j\beta(f)x} & \rho_1(f) \end{bmatrix} \tag{6.20}$$

If T(f) is the measured scattering matrix (referenced to the coaxial ports) for the calibration fixture with the current transducer located at its centre then the effective reflection coefficient of this network, at junction 1, is:

$$T_{11}(f) = Q_{11}(f) + \frac{Q_{12}(f)Q_{21}(f)\Gamma(f)}{1-Q_{22}(f)\Gamma(f)} \tag{6.21}$$

where the effective reflection coefficient of the transducer and the remaining part of the calibration fixture is given by:

$$\Gamma(f) = M_{11}(f) + \frac{M_{12}(f)M_{21}(f)N_{11}(f)}{1-M_{22}(f)N_{11}(f)} \tag{6.22}$$

However, $\Gamma(f)$ may be obtained from (6.21):

$$\Gamma(f) = \frac{T_{11}(f) - Q_{11}(f)}{Q_{21}(f)Q_{12}(f) + Q_{22}(f)[T_{11}(f) - Q_{11}(f)]} \tag{6.23}$$

Transmission from the junction 1 to junction 2 of the network is given by:

$$\Psi_1(f) = \frac{Q_{21}(f)}{1-Q_{22}(f)\Gamma(f)} \tag{6.24}$$

while transmission from junction 2 to junction 4 is given by:

$$\Psi_2(f) = \frac{M_{21}(f)N_{21}(f)}{1-N_{11}(f)M_{22}(f)} \tag{6.25}$$

However, the product of $\Psi_1(f)$ and $\Psi_2(f)$ gives the transmission across the device:

$$T_{21}(f) = \Psi_1(f)\Psi_2(f) \tag{6.26}$$

Consequently, $\Psi_2(f)$ can be found from known parameters since:

$$\Psi_2(f) = \frac{T_{21}(f)}{Q_{21}(f)}\left[1 - Q_{22}(f)\Gamma(f)\right] \tag{6.27}$$

Since the matrix M(f) is symmetrical, it can be shown, from (6.21) and (6.24), that:

$$M_{11}(f) = \frac{N_{21}(f)^2\Gamma(f) - N_{11}(f)\Psi_2(f)^2}{N_{21}(f)^2 - N_{11}(f)^2\Psi_2(f)^2} \tag{6.28}$$

$$M_{21}(f) = \frac{\Psi_2(f)}{N_{21}(f)}\left[1 - N_{11}(f)M_{11}(f)\right] \tag{6.29}$$

Thus, the scattering matrix M(f) for the transducer at the centre of the calibration fixture can be derived from the measured scattering matrix T(f) for the overall system if the junctions of the calibration fixture have already been characterized from the measured scattering matrix J(f) for the empty calibration fixture.

The same analysis method used to analyse the calibration fixture can then be applied to M(f) to extract the reflection coefficient $\rho_2(f)$ associated with the faces of the transducer and the propagation constant $\gamma(f)$ in the transducer region. Thus, from (6.9) the propagation constant $\gamma(f)$ in the transducer region is found to be:

$$\gamma(f) = \frac{1}{z}\cos^{-1}\left\{\frac{1 - M_{11}(f)^2 + M_{21}(f)^2}{2M_{21}f}\right\} \tag{6.30}$$

From (6.10) the reflection coefficient $\rho_2(f)$ associated with the faces of the transducer is:

$$\rho_2(f) = \sqrt{\frac{1 - M_{21}(f)e^{j\gamma(f)x}}{1 - M_{21}(f)e^{-j\gamma(f)x}}} \tag{6.31}$$

Results obtained from measurements for the phase constants $\beta(f)$ and $\gamma(f)$ for the regions outside and inside the transducer are shown in Fig. 6.13, while Fig. 6.14 compares the magnitudes of the reflection coefficients $\rho_1(f)$ and $\rho_2(f)$, which are found to be of similar magnitudes.
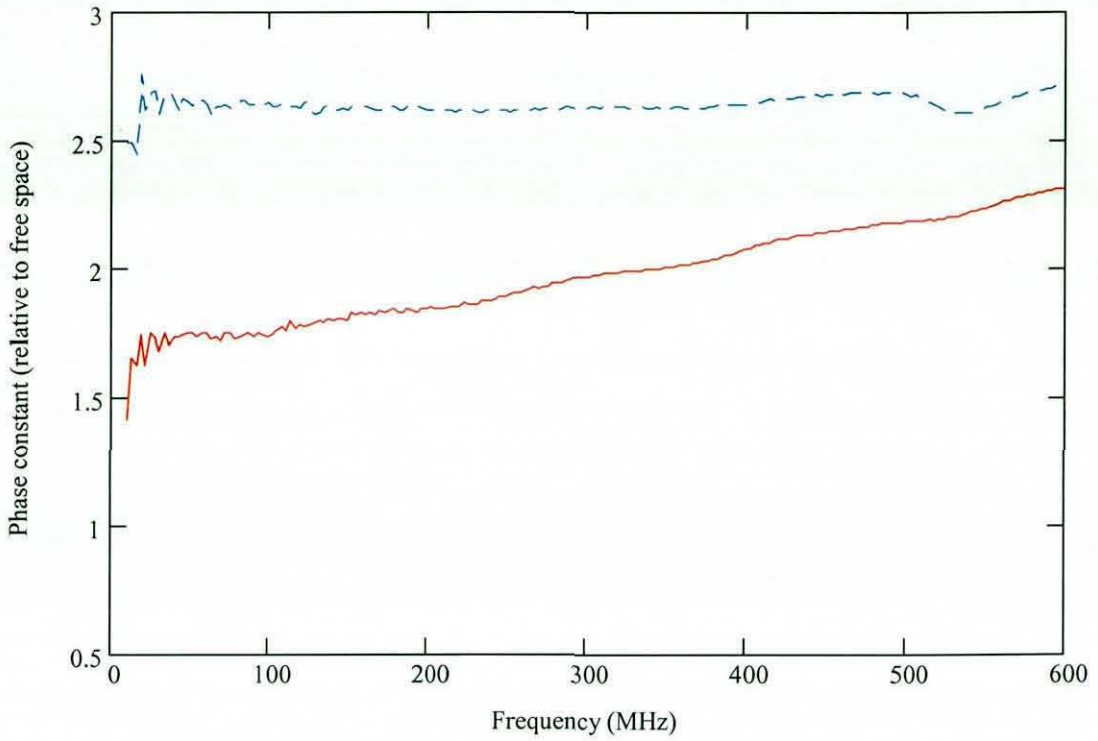
Fig. 6.13   Phase constants estimated from measurements: for empty calibration fixture (solid) and for region occupied by transducer (dashed)
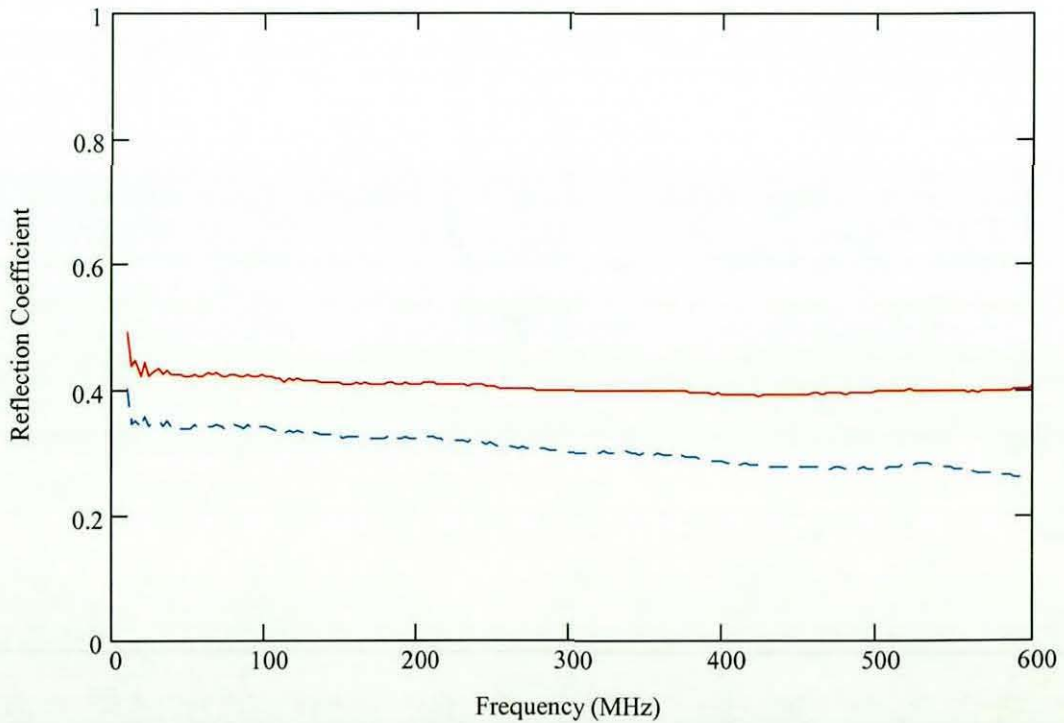
Fig. 6.14   Reflection coefficients estimated from measurements: at coaxial junction (solid) and at face of transducer (dashed)

An alternative view of the network representing the partially filled calibration fixture is shown in Fig. 15 below.
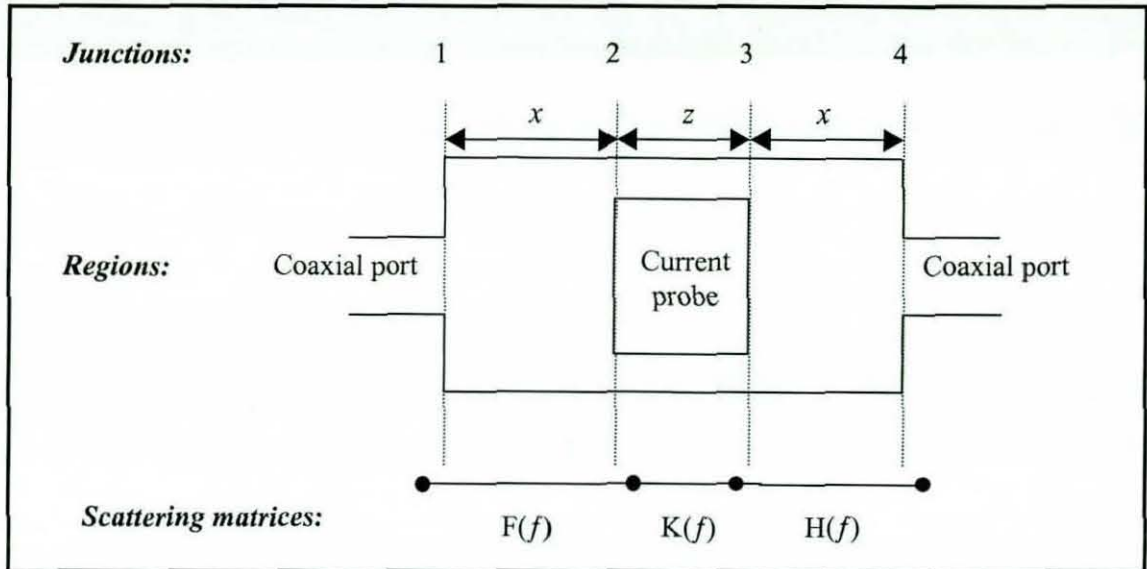

Fig. 6.15   Alternative transmission line model for partially filled calibration fixture

The sub-networks between the coaxial ports and the interior of the transducer can be represented using a pair of matrices of the form:

$$F(f) = \begin{bmatrix} \sigma_{11}(f) & \sigma_{21}(f) \\ \sigma_{12}(f) & \sigma_{22}(f) \end{bmatrix}$$

(6.32)

$$H(f) = \begin{bmatrix} \sigma_{22}(f) & \sigma_{12}(f) \\ \sigma_{21}(f) & \sigma_{11}(f) \end{bmatrix}$$

(6.33)

while the region occupied by the probe is represented as a length of transmission line:

$$K(f) = \begin{bmatrix} 0 & e^{-j\gamma(f)z} \\ e^{-j\gamma(f)z} & 0 \end{bmatrix}$$

(6.34)

The networks represented by $F(f)$ and $H(f)$ are assumed to be composed of a pair of abrupt transitions separated by a length x of transmission line. The reflection coefficients at these interfaces are again $\pm\rho_1(f)$ at the coaxial ports, and $\pm\rho_2(f)$ at the faces of the current transducer. Neglecting losses, the scattering matrices $S_i(f)$ for the individual junctions are assumed to be of the form:

$$S_i(f) = \begin{bmatrix} \Gamma_i(f) & 1-\Gamma_i(f) \\ 1+\Gamma_i(f) & -\Gamma_i(f) \end{bmatrix} \tag{6.35}$$

where $\Gamma_1(f) = \rho_1(f)$, $\Gamma_2(f) = \rho_2(f)$, $\Gamma_3(f) = -\rho_2(f)$, and $\Gamma_4(f) = -\rho_1(f)$. It can be shown that the elements of the matrices $F(f)$ and $H(f)$ are given by:

$$\sigma_{11}(f) = \frac{\rho_1(f) + \rho_2(f)e^{-2j\beta(f)x}}{1 + \rho_1(f)\rho_2(f)e^{-2j\beta(f)x}} \tag{6.36}$$

$$\sigma_{12}(f) = \frac{[1 - \rho_1(f)][1 - \rho_2(f)]e^{-j\beta(f)x}}{1 + \rho_1(f)\rho_2(f)e^{-2j\beta(f)x}} \tag{6.37}$$

$$\sigma_{12}(f) = \frac{[1 - +\rho_1(f)][1 + \rho_2(f)]e^{-j\beta(f)x}}{1 + \rho_1(f)\rho_2(f)e^{-2j\beta(f)x}} \tag{6.38}$$

$$\sigma_{22}(f) = -\frac{[\rho_1(f) + \rho_2(f)e^{-2j\beta(f)x}]}{1 + \rho_1(f)\rho_2(f)e^{-2j\beta(f)x}} \tag{6.39}$$

The transmission coefficient $\Psi_T(f)$ between the coaxial input and the region occupied by the transducer is given by:

$$\Psi_T(f) = \frac{F_{21}(f)}{1 - F_{22}(f)H_{11}(f)e^{-2j\gamma(f)z}} \tag{6.40}$$

The voltage at a point s in the transducer region (where $0 \leq s \leq z$) is then given by:

$$\frac{V_2(s,f)}{V_0} = \Psi_T(f)\left[e^{-js(f)z} + H_{11}(f)e^{-2j\gamma(f)z}e^{j\gamma(f)s}\right] \tag{6.41}$$

From symmetry considerations, $N_{11}(f)=Q_{22}(f)$, $Q_{22}(f)=\sigma_{22}(f)$ and $Q_{21}(f)=\sigma_{21}(f)$. Hence:

$$\frac{V_2(s,f)}{V_0} = \frac{[1+\rho_1(f)][1+\rho_2(f)]e^{-j\beta(f)x}\left\{ \begin{array}{l}[1+\rho_1(f)\rho_2(f)e^{-2j\beta(f)x}]e^{-j(f)s} +... \\ -[\rho_2(f)+\rho_1(f)e^{-2j\beta(f)x}]e^{-2j\gamma(f)z}e^{j\gamma(f)s} \end{array} \right\}}{[1+\rho(f)_1\rho_2(f)e^{-2j\beta(f)x}]^2 - [\rho_2(f)+\rho_1(f)e^{-2j\beta x}]^2 e^{-2j\gamma(f)z}} \tag{6.42}$$

The relative current distribution is obtained by negating the reflection coefficients in (6.41):

$$\frac{I_2(s,f)}{I_0} = \frac{[1-\rho_1(f)][1-\rho_2(f)]e^{-j\beta(f)x}\left[\begin{array}{l}\left\{1+\rho_1(f)\rho_2(f)e^{-2j\beta(f)x}\right\}e^{-j(f)\gamma s}+...\\+\left\{\rho_2(f)+\rho_1(f)e^{-2j\beta(f)x}\right\}e^{-2j\gamma(f)z}e^{j(f)\gamma s}\end{array}\right]}{\left[1+\rho(f)_1\rho_2(f)e^{-2j\beta(f)x}\right]^2-\left[\rho_2(f)+\rho_1(f)e^{-2j\beta x}\right]^2 e^{-2j\gamma(f)z}} \quad (6.43)$$

If the current at the centre of the transducer is used as the reference, the transfer impedance in cases where the device does not entirely fill the calibration fixture is then:

$$Z_{T4}(f) = \frac{\tau(f)Z_C\left|\left\{1+\rho(f)_1\rho_2(f)e^{-2j\beta(f)x}\right\}^2-\left\{\rho_2(f)+\rho_1(f)e^{-2j\beta x}\right\}^2 e^{-2j\gamma(f)z}\right|}{[1-\rho_1(f)][1-\rho_2(f)]e^{-j\beta(f)x}\left[\begin{array}{l}\left\{1+\rho_1(f)\rho_2(f)e^{-2j\beta(f)x}\right\}e^{-j(f)\gamma s}+...\\+\left\{\rho_2(f)+\rho_1(f)e^{-2j\beta(f)x}\right\}e^{-2j\gamma(f)z}e^{j(f)\gamma s}\end{array}\right]} \quad (6.44)$$

where $\tau(f)$ is again the transmission coefficient between the ports of the calibration fixture and the transducer output. The relative current magnitude derived from measurements is shown in Fig. 6.16 for four possible reference currents, including the measured output currents and estimated centre currents, both with and without the transducer at the centre of the calibration fixture.
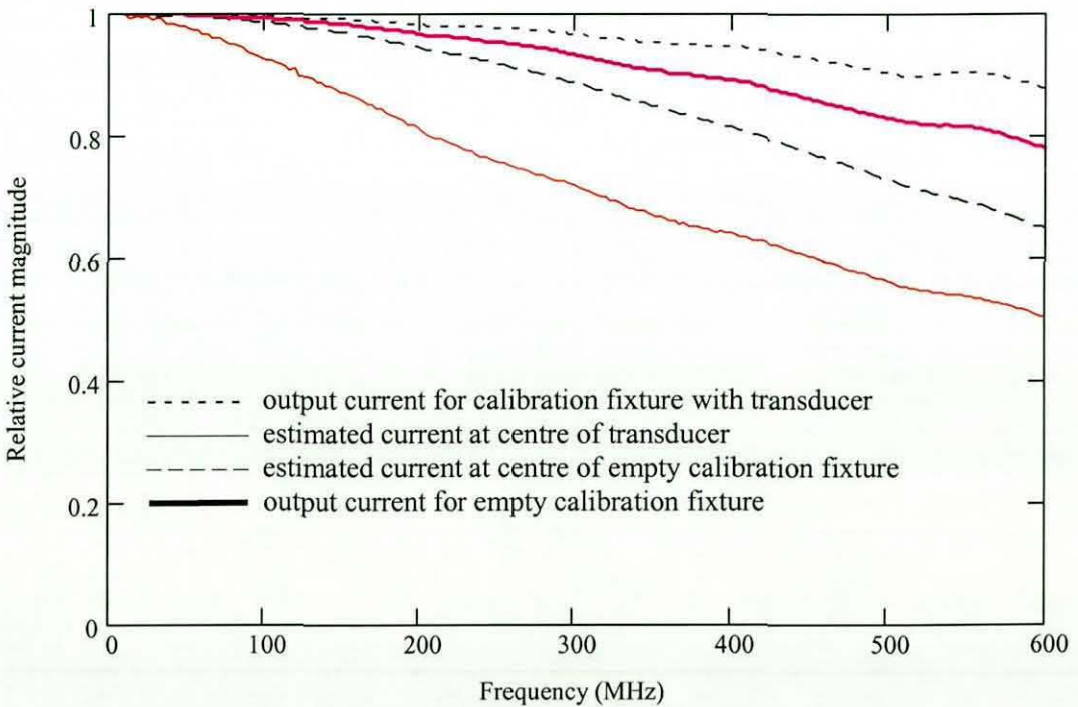
Fig. 6.16   Relative magnitude of currents estimated from measurements on calibration fixture with and without transducer at centre

Applying this analysis to the measured results for the current transducer located at the centre of an incompletely filled calibration fixture results in a larger transfer impedance (see Fig. 6.17) when the calibration is referenced to the estimated current at the centre of the current transducer.
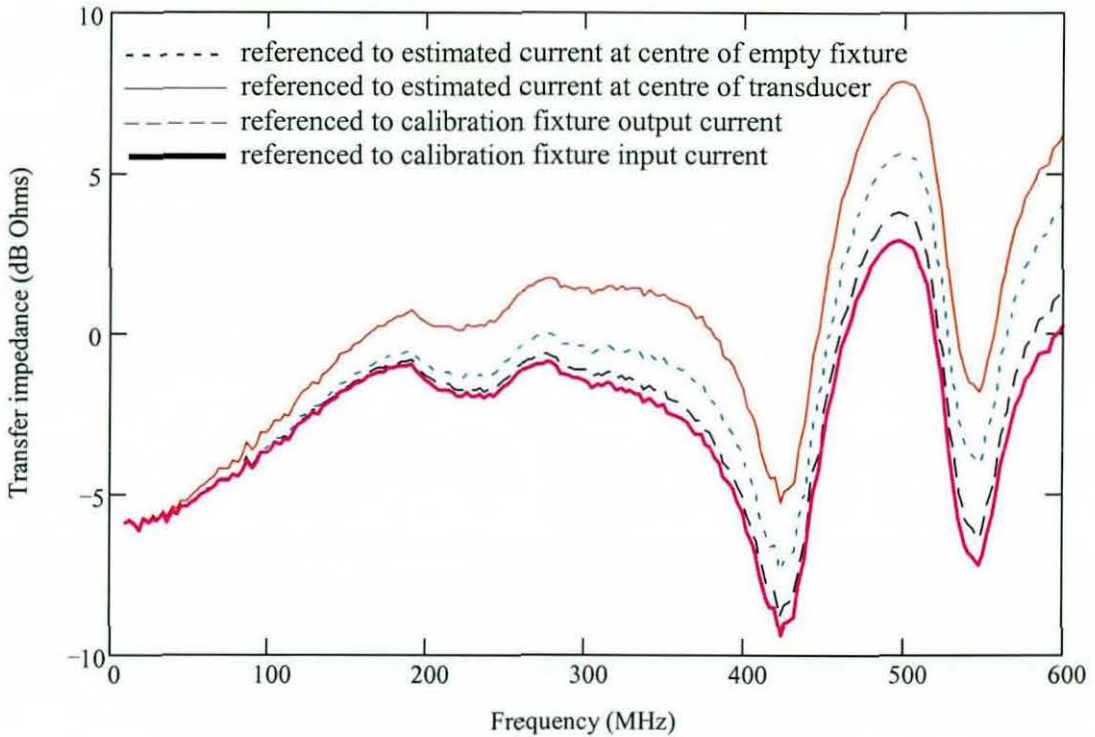

Fig. 6.17   **Transfer impedance estimates for a real calibration fixture**

The differences in this case are much larger at the lower end of the frequency band than is the case for the other alternatives that have been considered. The impact on the measured currents for the model validation experiment (see Fig. 6.18) show a much better result for the feature around 500 MHz, in that the amplitudes are almost identical. The amplitude of the feature at 520 MHz, which was larger than the predicted value for the first three calibration schemes, is smaller than the prediction for this case.

It is not obvious whether it is better to reference the measured current to the current at the centre of the empty calibration fixture or that when the transducer is present, since the impact of the transducer in the calibration will be different from that in the measured system. However, the results of Fig. 6.18 suggest that the current at the centre of the transducer is the better reference in this example.
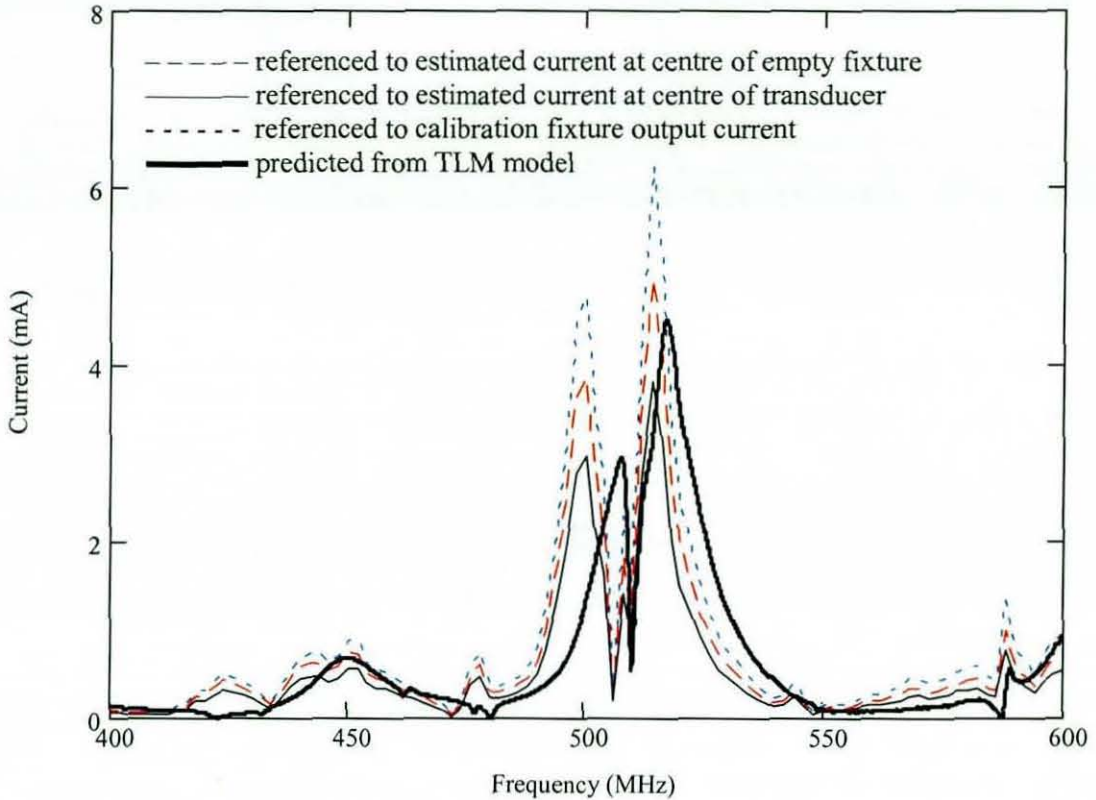
Applying this analysis to the measured results for the current transducer located at the centre of an incompletely filled calibration fixture results in a larger transfer impedance (see Fig. 6.17) when the calibration is referenced to the estimated current at the centre of the current transducer.

Fig. 6.17   Transfer impedance estimates for a real calibration fixture

The differences in this case are much larger at the lower end of the frequency band than is the case for the other alternatives that have been considered. The impact on the measured currents for the model validation experiment (see Fig. 6.18) show a much better result for the feature around 500 MHz, in that the amplitudes are almost identical. The amplitude of the feature at 520 MHz, which was larger than the predicted value for the first three calibration schemes, is smaller than the prediction for this case.

It is not obvious whether it is better to reference the measured current to the current at the centre of the empty calibration fixture or that when the transducer is present, since the impact of the transducer in the calibration will be different from that in the measured system. However, the results of Fig. 6.18 suggest that the current at the centre of the transducer is the better reference in this example.

Fig. 6.18   Measured and computed current on wire inside test box

6.6   Conclusions

Current measurements are commonly employed in EMC investigations, as well as in model validation exercises. However, the calibration methods that are normally applied to current measurement transducers often neglect the properties of the calibration devices. A transmission line model of a typical calibration fixture has therefore been used to investigate the interpretation of high frequency cable currents.

An alternative calibration procedure, based on measuring the scattering matrix of the calibration fixture, has been proposed and tested up to 3 GHz using a numerical model of the device [A.8]. This analysis has also been extended to accommodate transducers that do not completely fill the calibration fixture. In addition the success of this method has been demonstrated for frequencies up to 600 MHz using measured and computed results for the current induced on a wire inside a cavity backed aperture illuminated by a log-periodic antenna.

6.7   References

[6.1]   International Organisation for Standardisation, ISO 11451-4:1995(E), *Road vehicles - electrical disturbance by narrow-band radiated electromagnetic energy - vehicle test methods, Part 4: Bulk current injection (BCI)*

[6.2]   N.J. Carter, *The development of a revised susceptibility test for avionic equipment,* Proceedings of IERE EMC Conference, University of Surrey, UK, September 1982

[6.3]   Radio Technical Commission for Aeronautics, RTCA/DO-160C, *Environmental conditions and test procedures for airborne equipment*, Washington, DC, USA, 1993

CHAPTER 7: EMISSIONS MEASUREMENTS

The EMC test requirements that are applied in many industries (eg. [7.1]) require the "worst case" electromagnetic emissions to be found, usually by rotating the device under test and varying the height of the receive antenna. However, automotive emissions measurements are based on a much more restricted "snapshot" of the emissions as measured at a fixed point relative to the vehicle. These measurements are normally carried out using an antenna positioned 3 m high at a distance of 10 m from the vehicle on an open area test site. Nonetheless, some standards [1.4] permit 3 m measurements to be used, with the antenna height reduced by 1.2 m. Such measurements may also be carried out in both anechoic and semi-anechoic environments, and the acceptability criterion is based on a 10 dB increase on the limits that are applied to 10 m measurements.

During type approval testing a 3 m distance is preferred to permit emissions testing to be carried out alongside the immunity work, thus achieving a more cost-effective procedure. The 3 m measurement configuration also represents a much better option for numerical modelling since the size of the model is considerably smaller than for a 10 m measurement range. This is not only because of the reduced distance between the antenna and the vehicle, but also because the antenna height is only 1.8 m for the 3 m configuration, rather than the 3 m height used in the 10 m case. Further savings would also be obtained if the need to model the structure of the antenna in detail could be eliminated. However, 3 m measurements are considered to be somewhat contentious and measurements at 10 m are generally regarded as superior to those carried out at 3 m. There is a concern that the 3 m test distance is not realistic in terms of the "real world" environment due to interactions between the vehicle and the antenna. Thus, the validation of modelled emissions characteristics is potentially very difficult, particularly at the 3 m range.

7.1 Measurement issues

In the "radiating far-field" of a source the form of the field distribution is stable and the field levels are inversely proportional to the range. In moving from a distance of 3 m to 10 m the separation distance changes by a factor of 3.33, which corresponds to an amplitude difference of 10.45 dB. This factor is reflected in existing standards [1.1], which specify a 10 dB increase on the 10 m limits for measurements that are carried out at the 3 m distance.

However, emissions measurements obtained at different distances from a vehicle are not influenced solely by space attenuation effects. Other phenomena that may have an influence on the correlations between such measurements include the nature of the field distribution around the vehicle (which is influenced by the surrounding environment, the frequency, the distance of the observation point from the vehicle and the physical distribution of equipment) and the influence of the vehicle on the receiving antenna.

Field distribution

The extent of the "reactive near-field region" (where $1/r^3$ and $1/r^2$ field components are significant) is commonly quoted as $2\pi/\lambda$, where λ is the wavelength. Although this definition only really applies to an ideal point source, this simple model is usually adequate for many practical antennas (which normally have dimensions $D<\lambda$). However, for larger structures (with dimensions $D\sim\lambda$) a more appropriate definition [7.2] is:

$$R_A(\lambda) \leq 0.62\sqrt{\frac{D^3}{\lambda}} \qquad (7.1)$$

For more extended sources ($D>\lambda$) Polk's criterion [7.3] is a less restrictive alternative:

$$R_P(\lambda) \leq 0.397\left[\frac{D^4}{\lambda}\right]^{3/2} \qquad (7.2)$$

An emissions source within a vehicle can potentially excite a wide range of structures (wiring, cavities and apertures), and therefore behaves as a complex transmitting antenna system. Since vehicle emissions standards cover an extremely wide bandwidth, the radiating vehicle may well have the characteristics of a more extended source. For vehicle emissions measurements, which are carried out relatively close to the vehicle, the receiving antenna is therefore unlikely to be in the far-field region (which is commonly taken to be at distances in excess of $2D^2/\lambda$ [7.4]). The relative extent of these various boundaries are illustrated in Fig. 7.1, for a structure with a representative dimension $D=2$ m.

Thus, most automotive EMC measurements will actually be carried out in the "radiating-near field" region, sometimes called the "Fresnel zone", which lies between the true far-field and reactive near-field regions. In this region the radiation pattern changes with distance from the source. As a result of this, the radiated field that is sampled is unlikely to be very similar for different measurement distances.
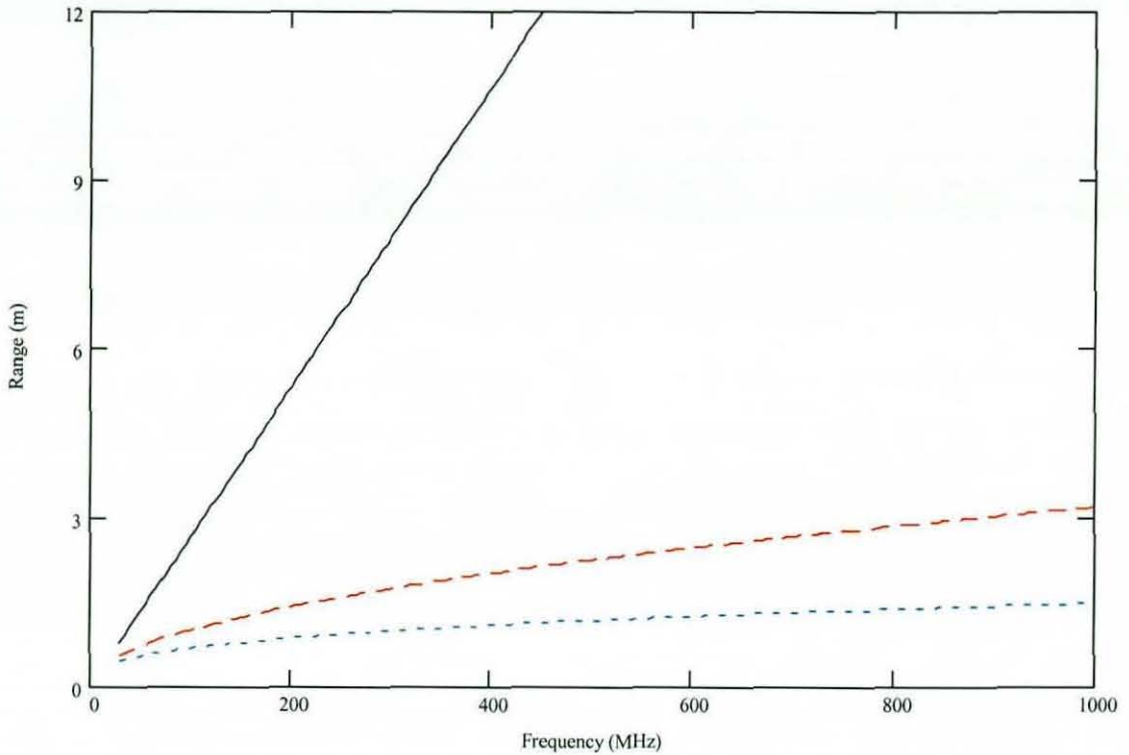
**Fig. 7.1   Field region boundaries for *D*=2 m: radiating far-field (solid),
near-field of antennas (dotted) and Polk's near-field criterion (dashed)**

The near-field problems are further exacerbated by the presence of a ground plane, which introduces significant interference effects.   In antenna engineering, techniques have been developed which use near-field measurements to estimate the far-field characteristics [7.5], thus avoiding the need for very large antenna ranges.   These methods are beginning to attract attention for EMC testing, and have already been suggested for automotive applications [7.6].

Equipment distribution

Given the extended nature of the vehicle as a source, and the fact that the receiving antenna is not in the far-field, radiated emissions measurements will inevitably be sensitive to the relative geometry of the vehicle and the receiving antenna. In addition, differences in the positioning of emissions sources relative to the structure may alter the emissions characteristics of the system as a whole. Thus, the layout of equipment in the vehicle can be expected to be significant.

Ground plane effects

The presence of a conducting ground seems likely to be significant for the 10 m measurement distance, since the relative phase of ground reflections will be quite different from that at 3 m.

However, the differences between the results at the 3 m range with and without a ground plane may be less significant, as the height is smaller than that used at 10 m and the separation between the source and observation point is also reduced.

7.2 Antenna effects

In emissions measurements it is necessary to use an antenna to sample the field at the test location. The measurement antenna will be calibrated in a manner that allows the amplitude of an incident plane wave to be estimated from the voltage generated at the antenna terminals. In practice, however, the incident field is unlikely to be a simple plane wave, and may well exhibit significant spatial variations over the region sampled by the antenna. Thus, the measurement can only provide an "equivalent" plane wave field strength, averaged over the volume sampled by the antenna. In addition, properties such as the impedance of the antenna may be influenced by the presence of the vehicle under test, particularly at small separations. This parameter is captured in the calibration process [7.7], and any disturbances due to the measurement set-up would result in an error in the estimated field.

Broadband devices are commonly used for this purpose, in the interests of efficiency, and the log-periodic dipole array (LPDA) is probably the most widely used design. This introduces a further problem, in that the effective phase centre of the device varies significantly with frequency. Standard LPDAs are normally referenced to the feed point of the device, and this is located at the specified measurement location. However, many laboratories now use a modified design (the "bilog"), which is augmented with a "bow-tie" dipole for enhanced low-frequency performance. These devices are commonly calibrated using a reference point near to the mid-point of the structure, with the result that the high frequency elements of the device are ~0.5 m closer to the structure in use. The significance of vehicle proximity effects may therefore be more significant for antennas of this type when used at the 3 m range.

Measured impact on antenna mismatch

The antenna mismatch recorded in the anechoic chamber without the car is virtually identical for both polarizations as expected, but even the OATS results are quite similar for the 3 m height (see Figs. 7.2-7.3). With the car present, the mismatches for the 3 m and 10 m positions on the OATS (see Figs. 7.4-7.5) are very similar for vertical polarization, although there are more significant differences for the horizontal case. Results obtained from the anechoic chamber are affected by the vehicle at 3 m range, as, but the effect is small (see Figs. 7.6-7.7). Measurements on the OATS show similar effects (see Figs. 7.8-7.9), but the disturbance is more pronounced at high frequency.
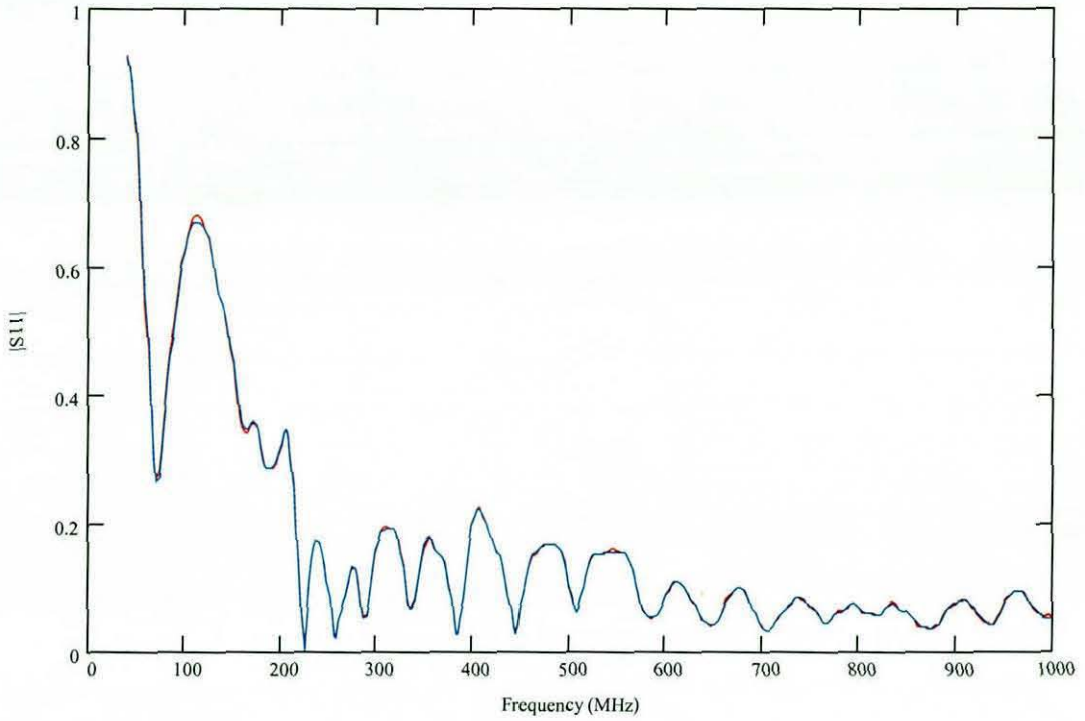
Fig. 7.2   Antenna mismatch for vertical polarization (red) and horizontal polarization (blue) in anechoic chamber without car
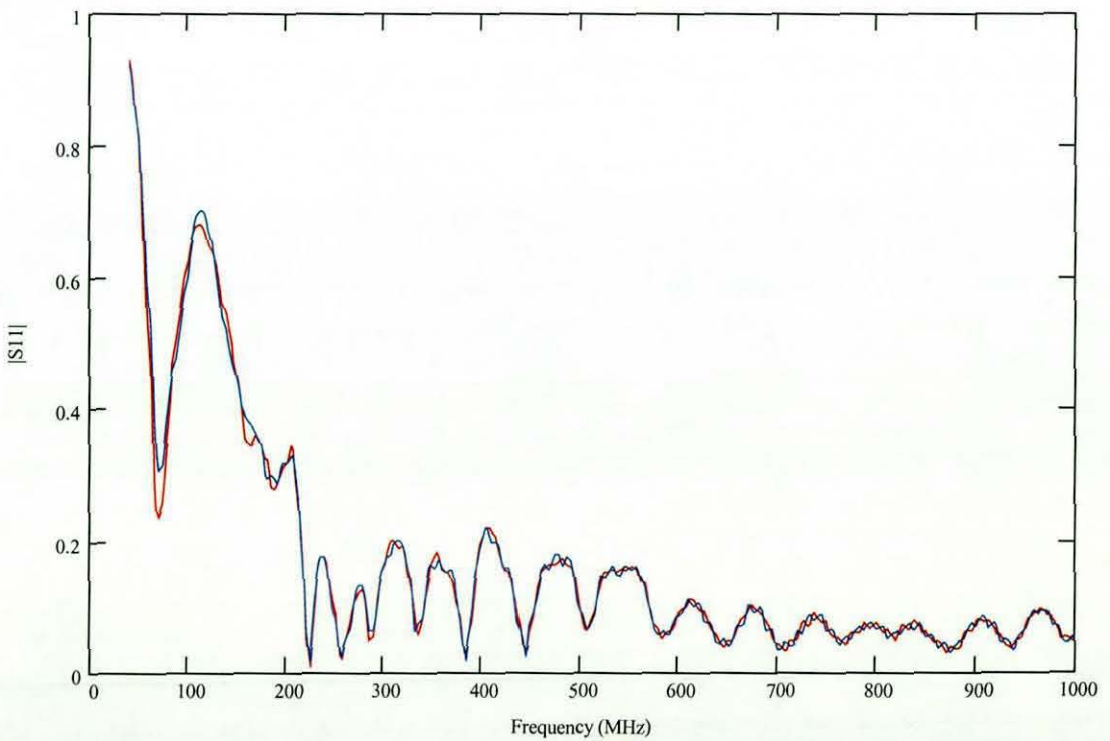

Fig. 7.3   Antenna mismatch at 3 m height for vertical polarization (red) and horizontal polarization (blue) on OATS without car
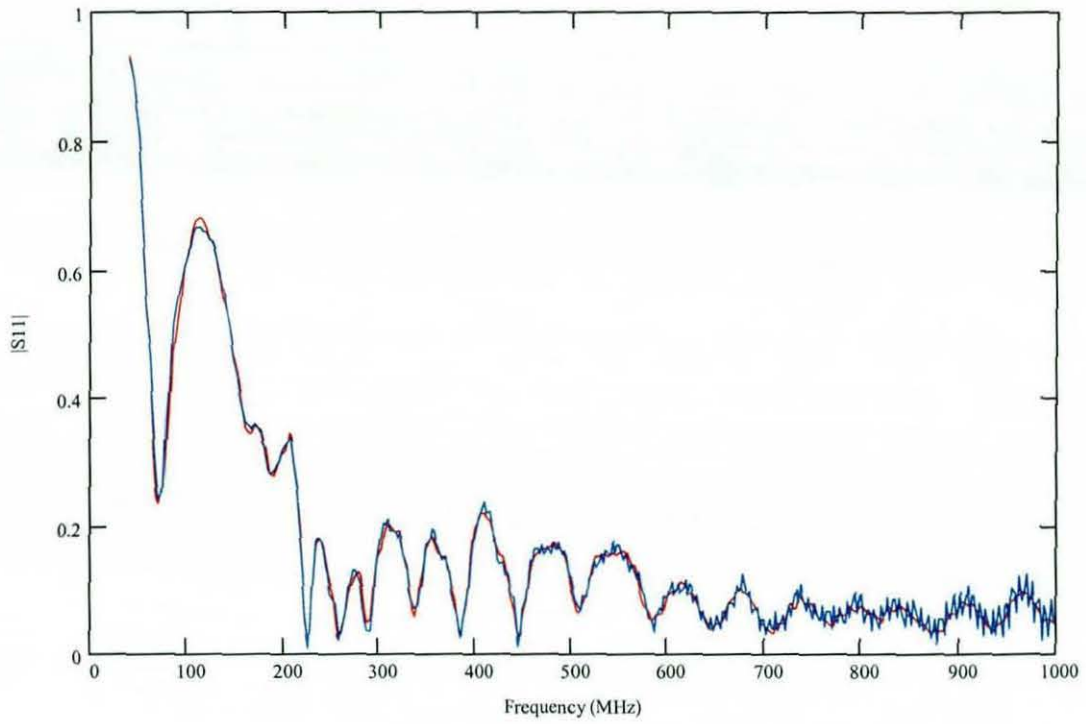
Fig. 7.4   Antenna mismatch on OATS at 10 m range (red) and 3 m range (blue) for
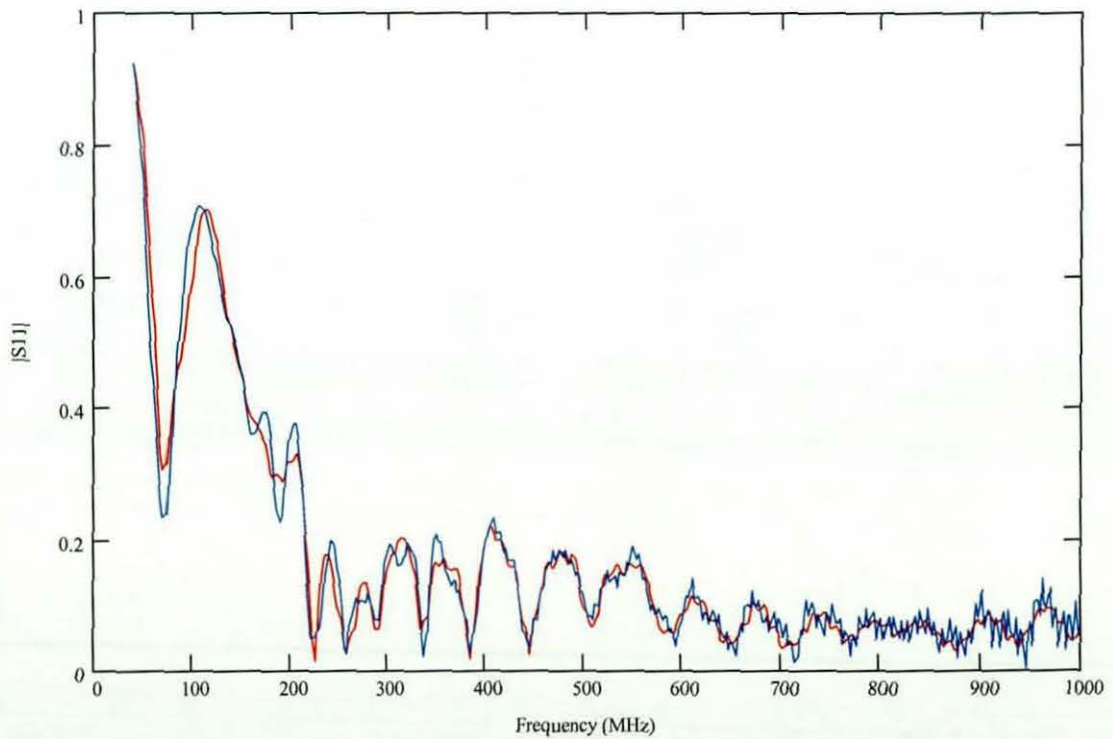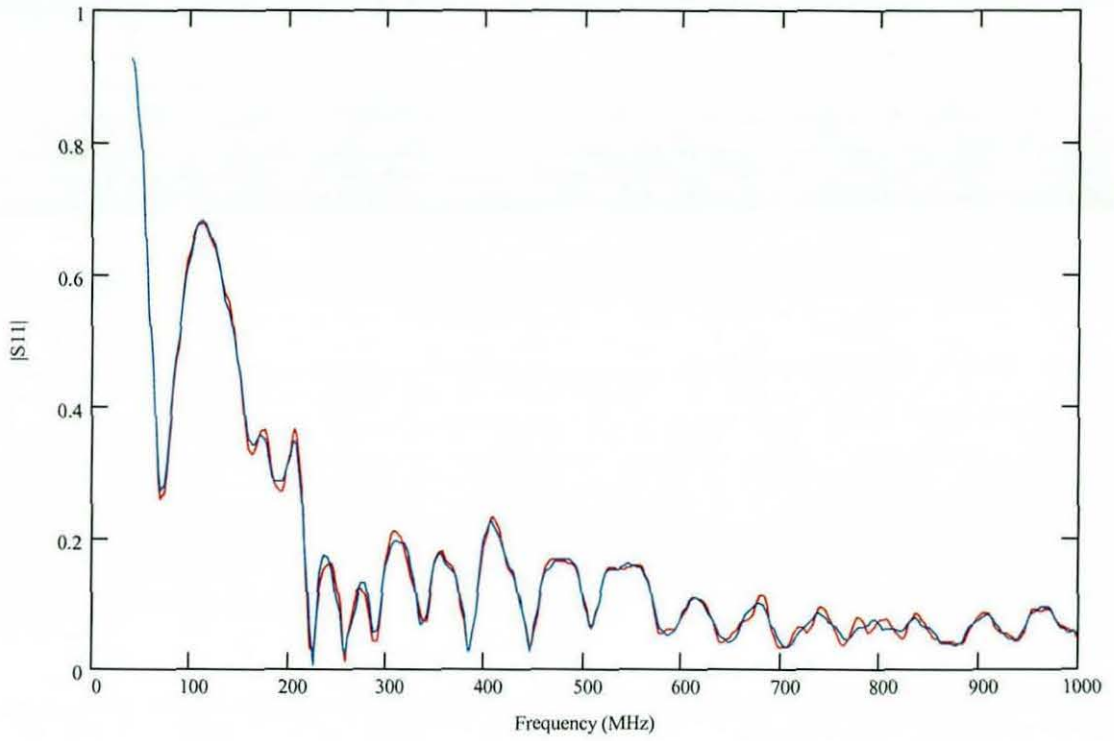vertical polarization with car

Fig. 7.5   Antenna mismatch on OATS at 10 m range (red) and 3 m range (blue) for
horizontal polarization with car

Fig. 7.6   Antenna mismatch in anechoic chamber for vertical polarization with car (red) and without car (blue) at 3 m range
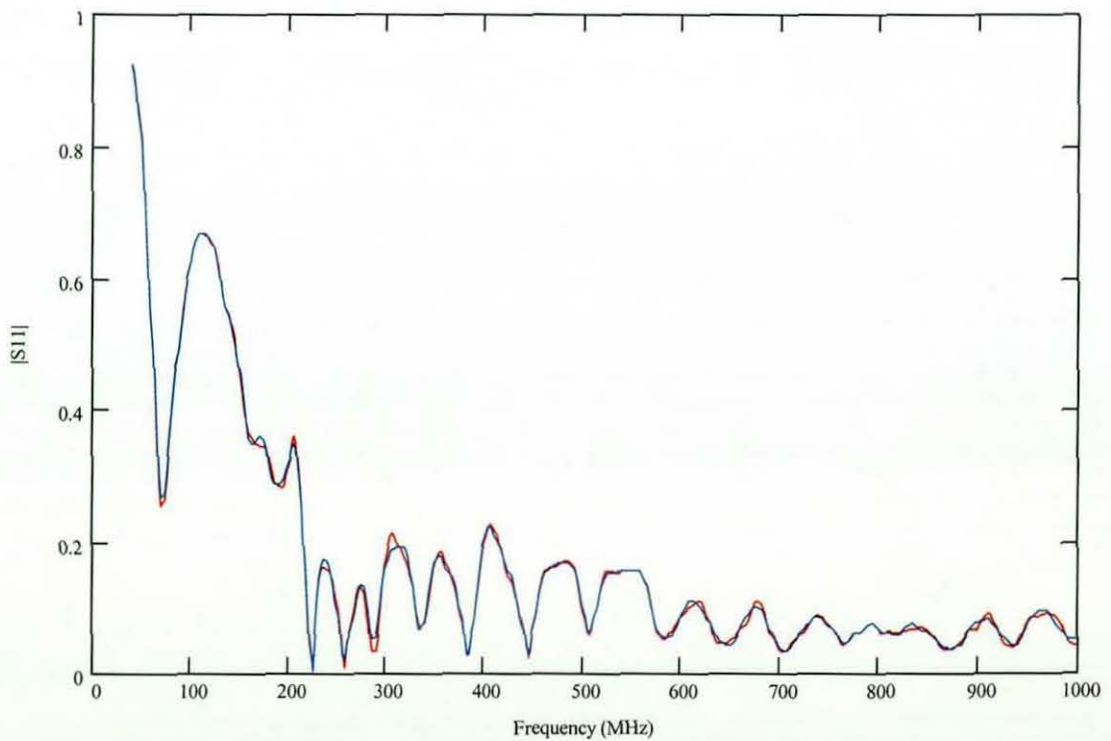
Fig.7.7   Antenna mismatch in anechoic chamber for horizontal polarization with car (red) and without car (blue) at 3 m range
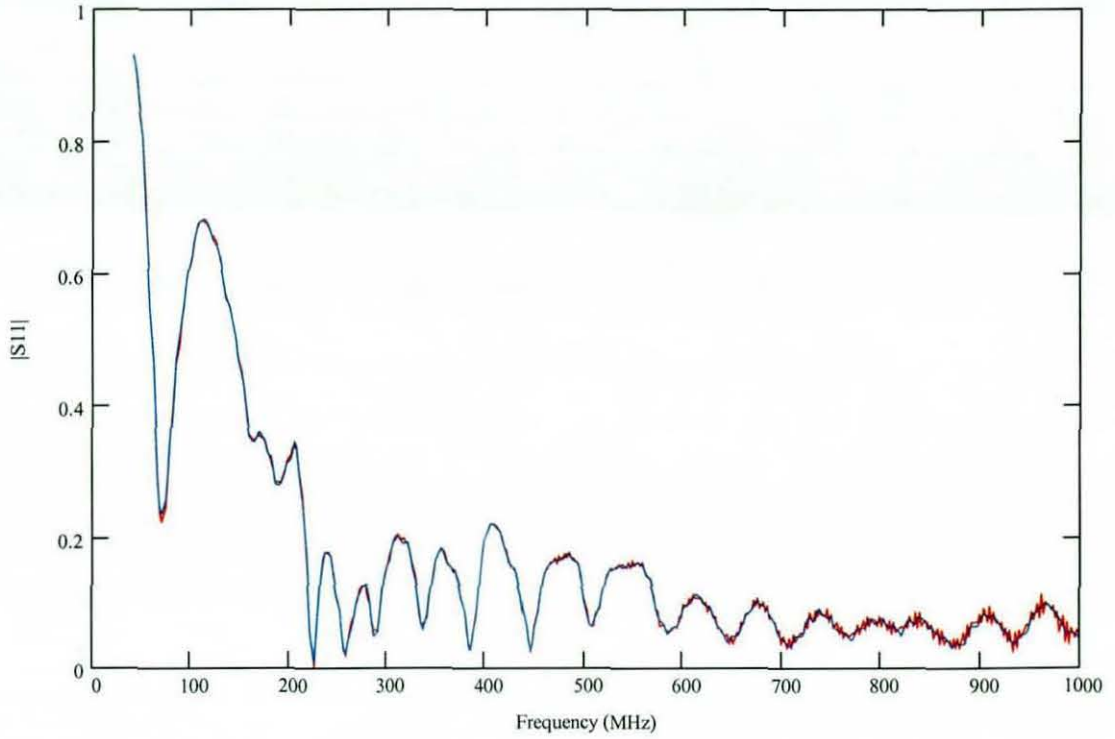
Fig. 7.8   Antenna mismatch on OATS for vertical polarization with car (red) and without car (blue) at 10 m range
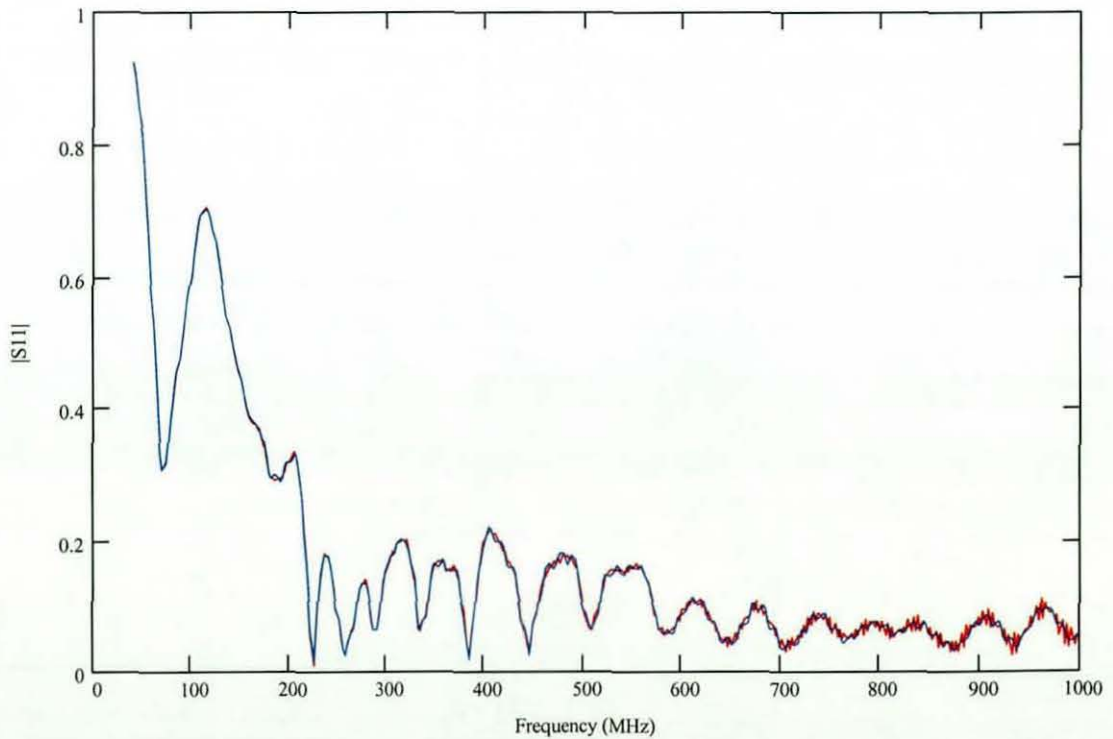
Fig. 7.9   Antenna mismatch on OATS for horizontal polarization with car (red) and without car (blue) at 10 m range

Estimated error due to changes in antenna match

The effect of any change in antenna mismatch is to introduce an error in the calibration factors that are used to interpret a field measurement from the signal provided by the antenna and measured using the EMI receiver. The "antenna factor" $\alpha_A(f)$ [5.3] at frequency f relates the received voltage $V_R(f)$ to the incident field $E_I(f)$ from:

$$E_I(f) = V_R(f)/\alpha_A(f) \tag{7.3}$$

The behaviour of a receiving antenna can also be described in terms of an "effective height" vector $\mathbf{h}_A(f)$ [7.8], which relates the equivalent open circuit voltage $V_0(f)$ at the antenna terminals due to the incident electric field $\mathbf{E}_I(f)$ (see equivalent circuit of Fig. 7.10), where:

$$V_0(f) = \mathbf{h}_A(f) \bullet \mathbf{E}_I(f) \tag{7.4}$$
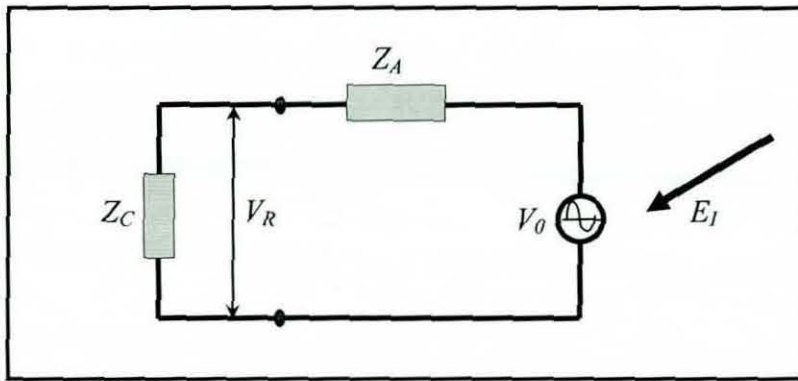
Fig. 7.10   Equivalent circuit for receiving antenna

The magnitude of the effective height can also be related [5.3] to the gain G_A (r,θ,ϕ,f) and the resistive component the antenna impedance $Z_A(f)$ as follows:

$$h_A(f) = \frac{c}{\pi f} \sqrt{\frac{G_A(r,\theta,\phi,f)\mathrm{Re}\{Z_A(f)\}}{120}} \tag{7.5}$$

where c is the speed of light. Hence it can be shown that the antenna factor is related to the gain and resistance of the device according to:

$$\alpha_A(f) = \frac{\pi f [Z_A(f) + Z_C]}{c Z_C} \sqrt{\frac{120}{G_A(r,\theta,\phi,f)\mathrm{Re}\{Z_A(f)\}}} \tag{7.6}$$

The "directivity" $\Phi(\theta,\phi,f)$ of an antenna, which is a function of its geometry, is given by [7.9]:

$$\Phi(\theta,\phi,f) = \frac{4\pi\psi(\theta,\phi,f)}{\int_{-\pi}^{\pi}\int_{0}^{2\pi}\psi(\theta',\phi',f)\sin(\theta')d\theta'd\phi'} \tag{7.7}$$

where $\psi(\theta,\phi,f)$ is the power radiated per unit solid angle in the direction (θ,ϕ) at frequency f.

The gain of an antenna depends on its inherent directivity, together with various losses that include the mismatch between the antenna and its transmission line. Assuming that only the antenna impedance is changed by the presence of a nearby object, the gain in a given direction can be described by:

$$G_i(r,\theta,\phi,f) = \left[1 - |\rho_i(f)|^2\right]\Gamma(r,\theta,\phi,f) \tag{7.8}$$

where the parameter $\Gamma(r,\theta,\phi,f)$ (comprising the antenna directivity and other losses, such as polarization mismatch) is assumed to remain unchanged and the reflection coefficient $\rho_i(f)$ at the antenna terminals is given by:

$$\rho_i(f) = \frac{Z_C - Z_i(f)}{Z_C + Z_i(f)} \tag{7.9}$$

where $Z_i(f)$ is the antenna impedance and Z_C is the characteristic impedance of the transmission line.

Thus, if the antenna impedance changes from $Z_A(f)$ to $Z_B(f)$, with a corresponding change in the mismatch at the antenna terminals from $\rho_A(f)$ to $\rho_B(f)$, then the antenna factor is modified to $\alpha_B(f)$ where:

$$\alpha_B(f) = \alpha_A(f)\left[\frac{Z_B(f)+Z_C}{Z_A(f)+Z_C}\right]\sqrt{\frac{\mathrm{Re}\{Z_A(f)\}}{\mathrm{Re}\{Z_B(f)\}}\left[\frac{1-|\rho_A(f)|^2}{1-|\rho_B(f)|^2}\right]} \tag{7.10}$$

The resulting changes in antenna factor are illustrated in Fig. 7.11, using the worst-case changes observed in the measurements. Above 250 MHz the errors are below 0.1 dB, but at some frequencies below 150 MHz the error is in excess of 1 dB.
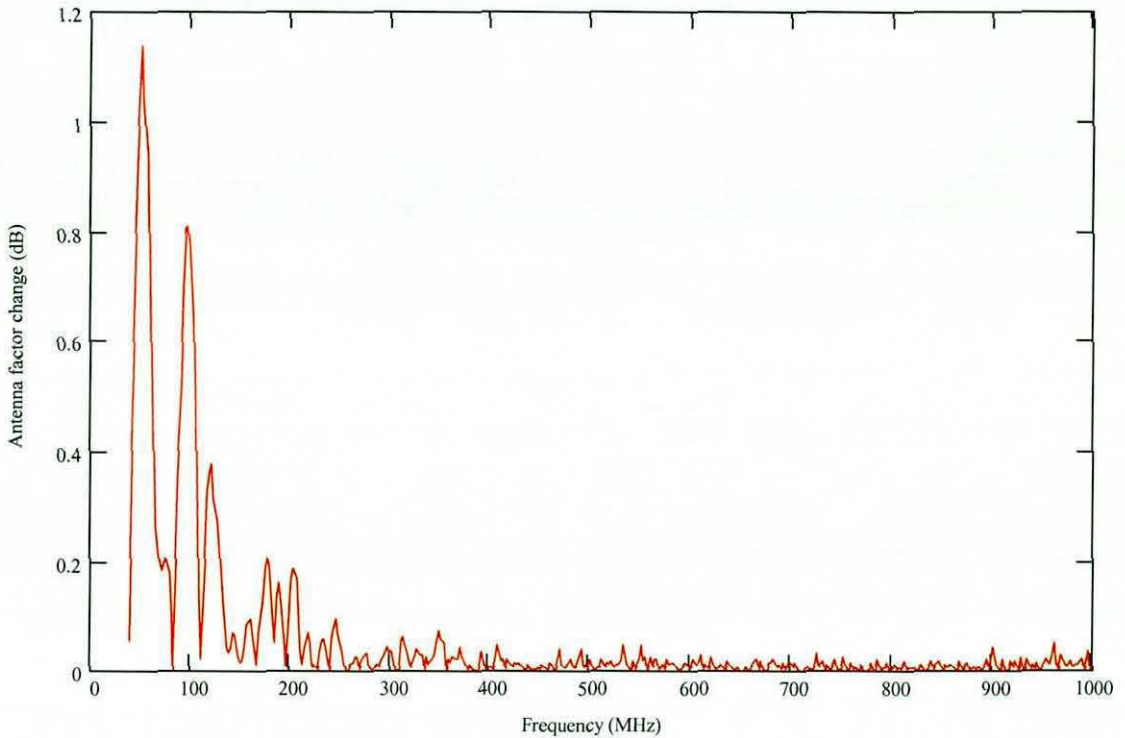
**Fig. 7.11   Change in antenna factor estimated from changes in antenna mismatch for
10 m and 3 m horizontal configurations on OATS with car**

7.3   Emissions models

Simulation techniques permit the field at the measurement reference points to be determined
without the need to use a measurement device. Thus, the "absolute" field values can be
compared for the three environments (fully anechoic at 3 m range, and semi-anechoic at 3 m
and 10 m). A model of a representative antenna structure may then be added to the vehicle
model, thus permitting the key elements of the measurement process to be simulated. The
antenna model may also be used to determine the antenna factors needed to interpret the results
of the simulated emissions measurements. This allows the significance of potential error
sources and the influence of the antenna on "measured" results to be assessed.

The numerical investigations [A.1] were carried out using TLM. Limitations of the available
computer hardware restricted the maximum frequency of these models to 600 MHz
(corresponding to a maximum cell size of 5 cm), and the model was restricted to purely metallic
structures in order to avoid further reducing the bandwidth of the simulation. A representative
"vehicle-like" model was constructed, which provided a radiating system with similar
dimensions and features without the need to obtain geometrical data for a real vehicle.

Model geometry

The model for a vehicle-like object was assembled by combining simple geometric entities. This structure included a central cavity with a simple stepped floor, and apertures representing windows (thus permitting field coupling between the interior and the exterior in a realistic manner). The outer surfaces were planar, but included sloping panels and mitred corners to make the structure more realistic than an assembly of simple rectangular boxes (see Fig. 7.12). This vehicle-like structure was excited using a simple electric field pulse in a single cell, oriented at 45° to the mesh axes, at a point that would roughly correspond with the position of the base of the gear stick in a real vehicle.
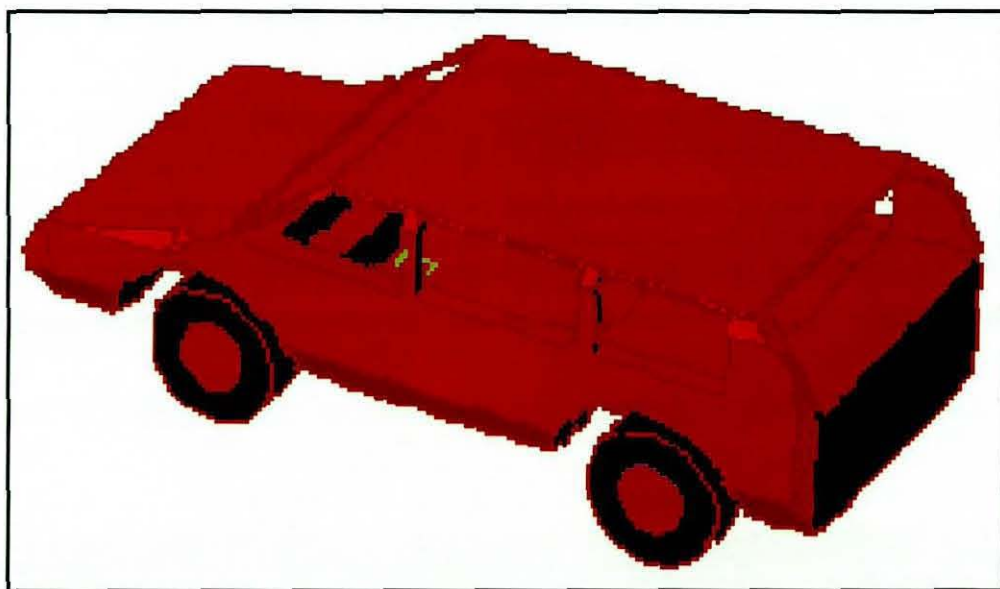
Fig. 7.12   View of model vehicle, with source cell near floor shown in yellow

The antenna model was based on a simple log-periodic structure with 9 pairs of dipole elements. The latter were represented using thin wire models, while the parallel-line feeders were represented by solid metallic bars (see Fig. 7.13). The antennas used in the practical measurements included many more elements, providing a maximum frequency of 1 GHz. However, since the bandwidth of the model was limited to a maximum frequency of 600 MHz (by the available computer hardware) the model antenna was also truncated in order to maximize computational efficiency. In this work the output port was used as the reference point for the antenna model. The output port of the antenna was represented using a thin wire with a central 50 Ω load. This feature was located between the feeder bars close to the smallest elements of the antenna.
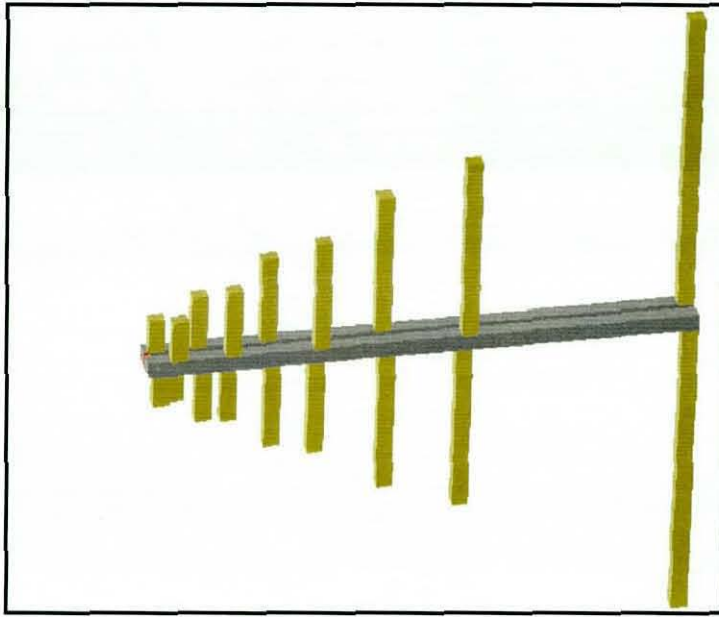
Fig. 7.13   View of TLM model for simplified log-periodic dipole array

Careful mesh grading was applied in the vicinity of this structure to ensure that the details of the geometry could be captured with sufficient accuracy and that the mesh density was adequate in regions with very high spatial field gradients. The very small cells resulting from this mesh refinement resulted in extremely long simulation times, with the result that it was necessary to limit the modelling work to a single antenna polarization.

Field predictions

The baseline for the theoretical studies was a calculation of the electric field generated at selected points around the vehicle in isolation. This field data was therefore not corrupted by any field components scattered from antennas in the vicinity. A single simulation of the semi-anechoic environment provided field data for the antenna reference point at the 10 m range (3 m high), and for a range of reference points along a line parallel to the vehicle at the 3 m distance (1.8 m high). This allowed comparison of the results for the standard 10 m position with data obtained for a range of locations at the 3 m range. A similar simulation was carried out for a fully anechoic environment, again for several points alongside the vehicle at the 3 m distance.

The results for the vertical field component in the three standard positions (ie. in line with the front axle) are shown in Fig. 7.14. The essential characteristics of these results are common for all positions, although the details vary with position and frequency.
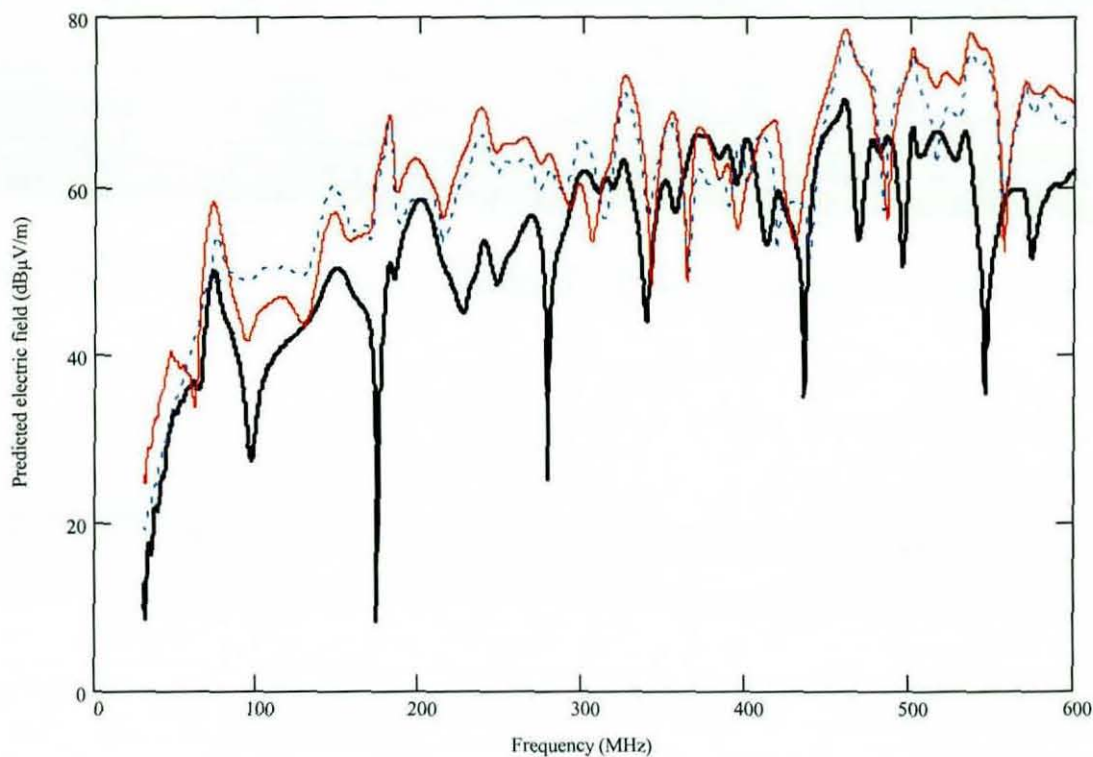
Fig. 7.14   Predicted vertical field in front axle plane: 10 m semi-anechoic (heavy), 3 m semi-anechoic (light), 3 m anechoic (dotted)

It can be seen that the vertical levels are generally lower for the 10 m range than for 3 m, and that the 3 m results under anechoic and semi-anechoic conditions are similar. Around 400 MHz, however, the levels are similar for all three regimes. This effect can probably be ascribed to constructive interference, arising from the relative phasing of the direct radiation and ground reflections. A further general feature is the presence of more prominent nulls in the 10 m data, which also probably results from interference effects.

The nature of the horizontal results (see Fig. 7.15) is much the same as for the vertical case, although the 10 m nulls are not quite so deep and the 3 m semi-anechoic results appear to be more strongly influenced by the presence of a ground plane in this case.
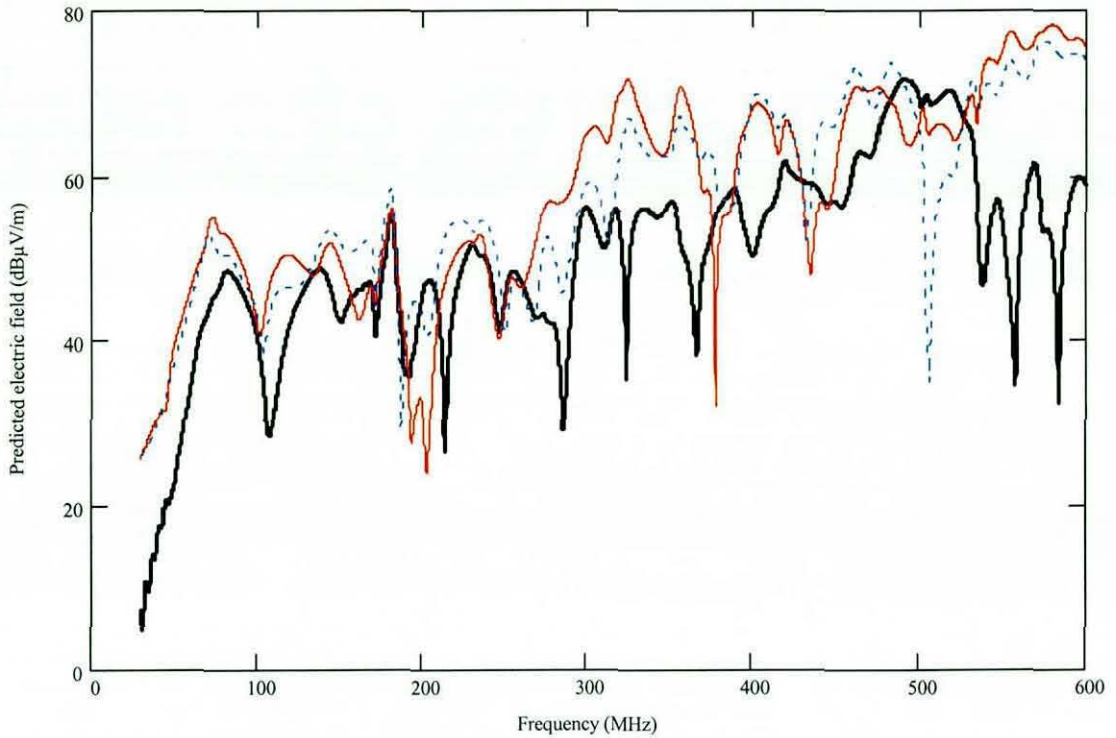
Fig. 7.15   Predicted horizontal field in front axle plane: 10 m semi-anechoic (heavy),
3 m semi-anechoic (light), 3 m anechoic (dotted)

Simulated measurements

Further simulations were carried out to obtain the signal induced at the antenna terminals by the radiating vehicle for 8 antenna configurations. These included the 3 standard configurations, together with two additional positions for the 3 m anechoic and semi-anechoic regimes and one additional position at the 10 m range. The latter was included to provide some indication of the significance of source distribution, since the position of the source was unchanged. Details of the eight antenna configurations that were investigated are summarized in Table 7.1 below:

Antenna range	Antenna height	Antenna position	Environment
10 m	3 m	in line with front axle	semi-anechoic
10 m	3 m	3 m back from axle	semi-anechoic
3 m	1.8 m	in line with front axle	semi-anechoic
3 m	1.8 m	in line with front axle	anechoic
3 m	1.8 m	1.5 m back from axle	semi-anechoic
3 m	1.8 m	1.5 m back from axle	anechoic
3 m	1.8 m	3 m back from axle	semi-anechoic
3 m	1.8 m	3 m back from axle	anechoic

Table 7.1   Simulated measurement configurations

In order to interpret the coupling calculations as simulated measurements, it was necessary to determine the antenna factors for the isolated antenna under the relevant anechoic and semi-anechoic conditions. This parameter captures properties such as the gain and impedance of the antenna, and was determined for the antenna models by monitoring the output of the device for each of the three antenna configurations under plane wave illumination.

The antenna factor data was used to obtain simulated "measurements" of the electric field from the results of the coupling calculations. The results from the three standard configurations are shown in Fig. 7.16. The similarities between the three results are essentially the same as those observed in the raw coupling results.
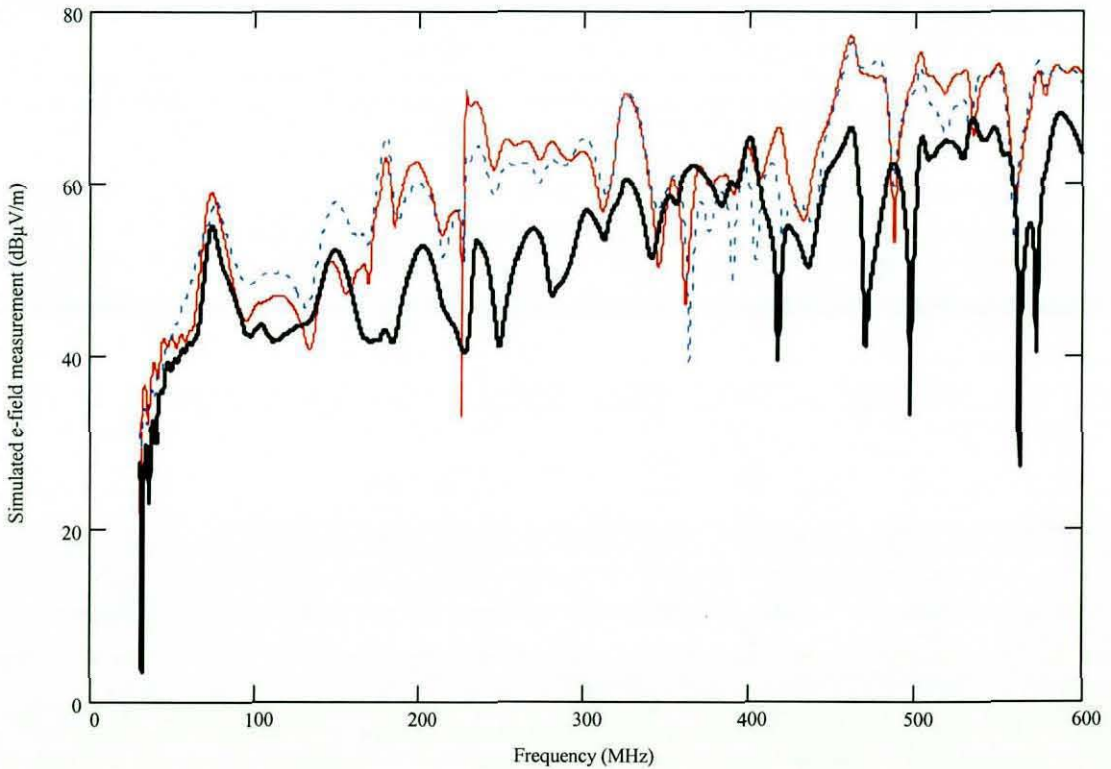

**Fig. 7.16   Simulated measurements in front axle plane: 10 m semi-anechoic (heavy),
3 m semi-anechoic (light), 3 m anechoic (dotted)**

Comparing these estimates with the direct field predictions, however, it can be seen that the accuracy of the estimate for the 10 m case is poorer than that for the 3 m cases (see Figs. 7.17-7.19). This is probably indicative of a more complex field structure at the 10 m range, again due to interference effects associated with ground reflections.
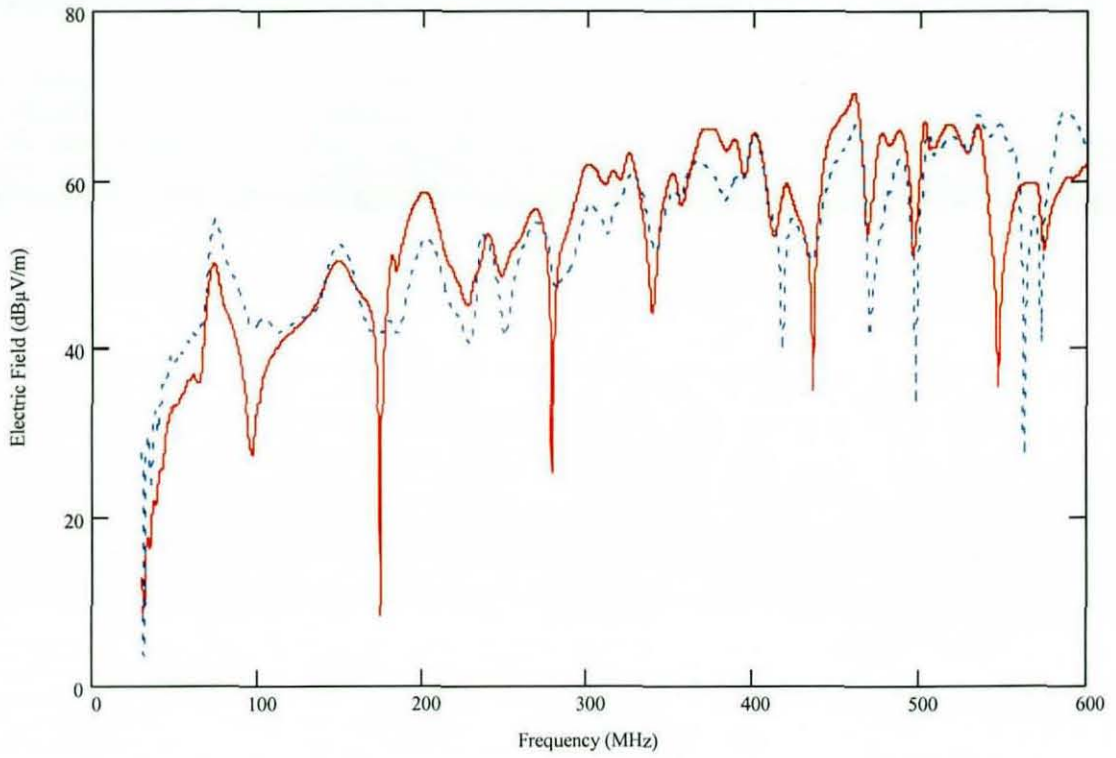
Fig. 7.17   **Vertical electric field at 10 m range on wheel axis for semi-anechoic case:
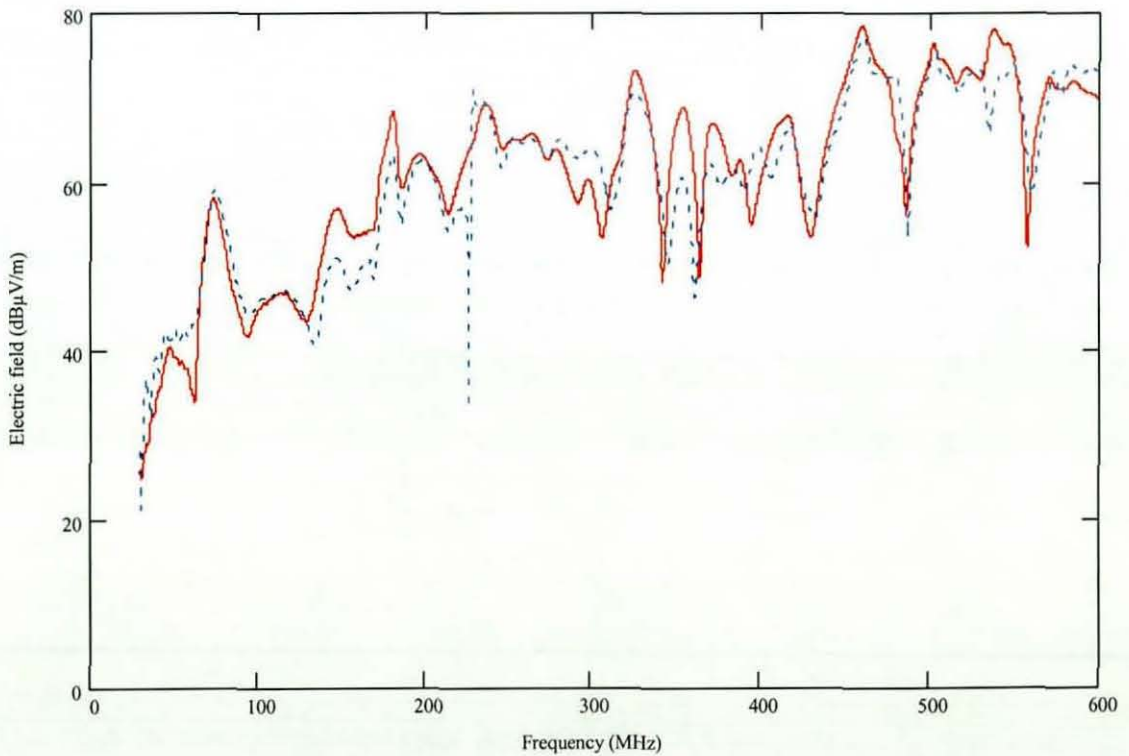predicted field (solid) and simulated measurement (dotted)**

Fig. 7.18   **Vertical electric field at 3 m range on wheel axis for semi-anechoic case:
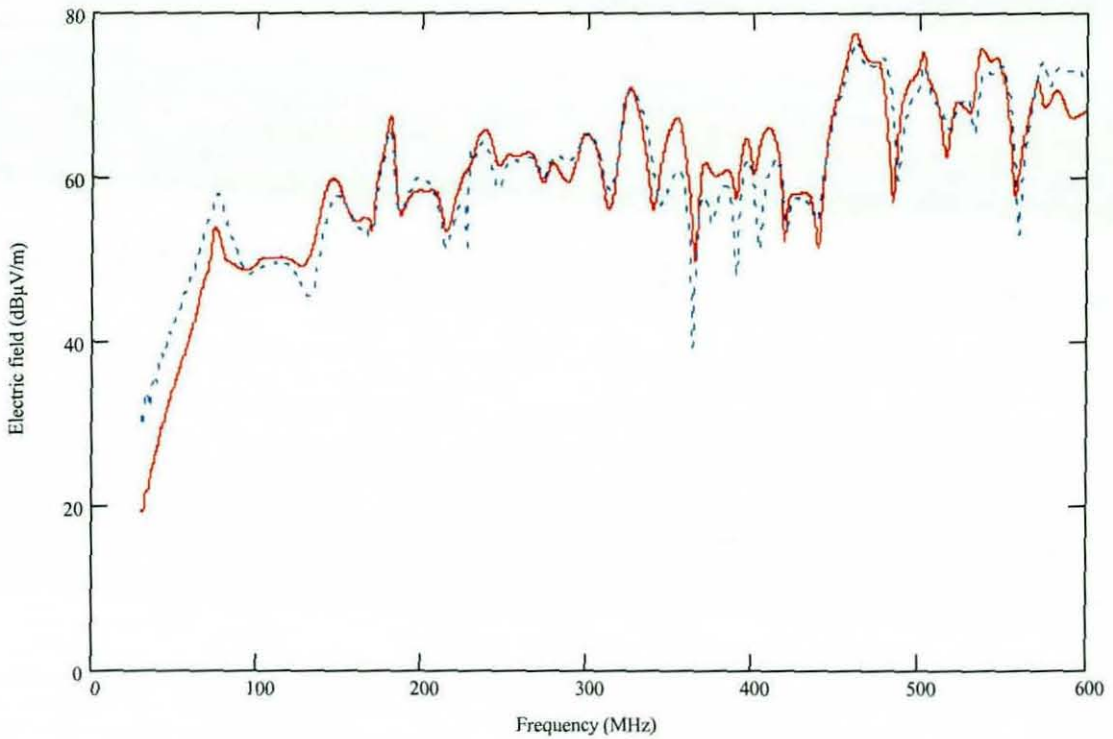predicted field (solid) and simulated measurement (dotted)**

Fig. 7.19   Vertical electric field at 3 m range on wheel axis for fully anechoic case: predicted field (solid) and simulated measurement (dotted)

Model antenna characteristics

Changes in the antenna impedance due to the proximity of a large conducting object represent a further potential error source. Thus the impedance of the antenna was determined for each of the 3 m range configurations both with and without the antenna present. At 10 m the influence of the vehicle would not be expected to be significant, but the duration of the simulation would be extremely long. It was decided, therefore, that there would be insufficient merit in carrying out the impedance calculation with the vehicle present at 10 m range.

The input reflection coefficient (and hence the impedance) of the antenna in isolation was found to be virtually identical for the three environments. Even the results obtained with the antenna at 3 m from the model vehicle were only slightly perturbed, as found in the practical measurements, although the model antenna was clearly not as well matched as the device used in the measurements. However, it was not possible, with the available computing resources, to refine the design of the model antenna to the same degree as the commercial device.

The mismatches at 3 m under fully and semi-anechoic conditions are compared with the result for the isolated antenna in Fig. 7.20, where it can be seen that the disparities are greater for the semi-anechoic case.
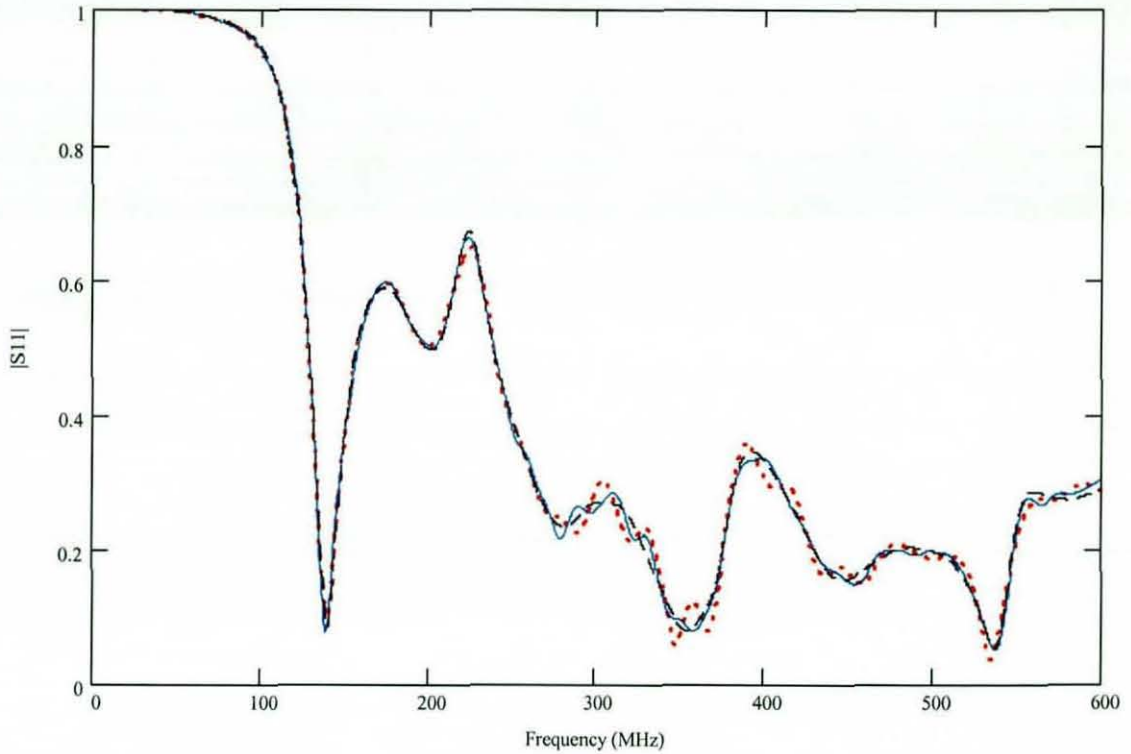
Fig. 7.20   Predicted input reflection coefficient for model LPDA: isolated antenna in free space (solid), antenna at 3 m from vehicle model in free space (dashed) and antenna at 3 m from vehicle model under semi-anechoic conditions (dotted)

The effect of the vehicle structure only becomes noticeable at very high frequencies for the anechoic environment. These observations also correspond to the findings of the experimental investigations (section 7.2).

7.4   Similarity between 10 m and 3 m measurements

Simple approximations would suggest that fields measured at a range of 10 m should be about 10 dB lower than those measured at only 3 m range. However, numerical results for the field distribution around the model vehicle indicate that the relationship between two such results is rather more complex than this, with notable differences in the details of the frequency characteristics as well as the amplitudes of the fields. Thus, although the field at 10 m is generally lower than at 3 m, at some frequencies the field at 10 m exceeds that generated at 3 m, while at others the levels are very similar. Nonetheless, the 10 dB adjustment proves to provide a reasonable guide to the overall differences between the fields at the two different distances. This is illustrated in Fig. 7.21, where a 10 dB reduction has been applied to the 3 m field predictions.
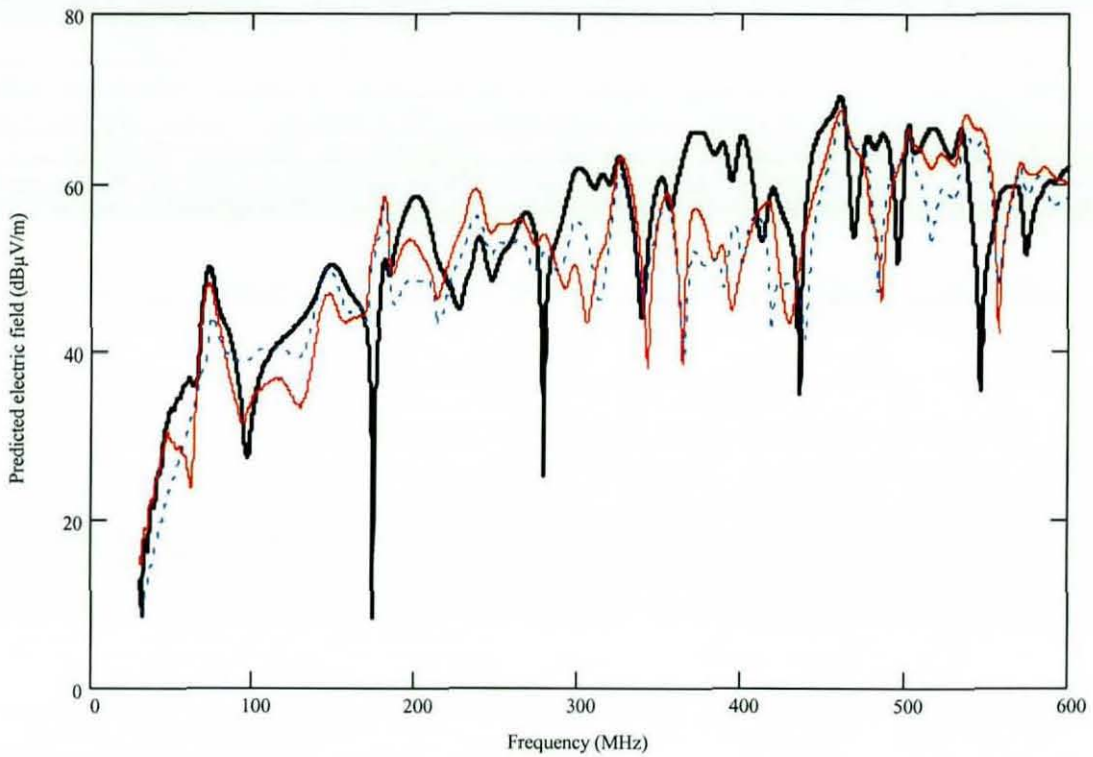
Fig. 7.21   Predicted vertical field in front axle plane: 10 m semi-anechoic (heavy), 3 m semi-anechoic (light) and 3 m anechoic (dotted) with 10 dB adjustments

Simulated antenna measurements

Marked differences in the accuracy of simulated antenna measurements were found between the 3 m and 10 m ranges. Thus, the 10 dB adjustment, which works surprisingly well for the calculated fields, does not appear to be the most appropriate mechanism for estimating the field at 10 m from simulated antenna measurements. It can be seen from Figs. 7.22-7.23, which show simulated measurements in both the front and rear axle planes, that an adjustment of 5 dB to the 3 m data perhaps provides a more realistic guide to the 10 m levels. Nonetheless, significant discrepancies remain between these results.

It is clearly not possible to obtain a simple mapping from the levels measured at 3 m distance to those that would be measured at 10 m. Nonetheless, it is still possible to use data recorded at a distance of 3 m to assess whether the 10 m emissions limit would be exceeded if the measurements were to be carried out at that range. The proposed 5 dB reduction results in a prediction for the 10 m range which is generally higher than the corresponding 10 m measurement. Thus, if the adjusted 3 m data meets the 10 m limit, there are reasonable grounds for confidence that the vehicle would pass the 10 m test. The disadvantage, however, is that the 10 m levels may be over-predicted by quite large margins over some parts of the frequency band, while at other frequencies the levels at 10 m are likely to be under predicted.
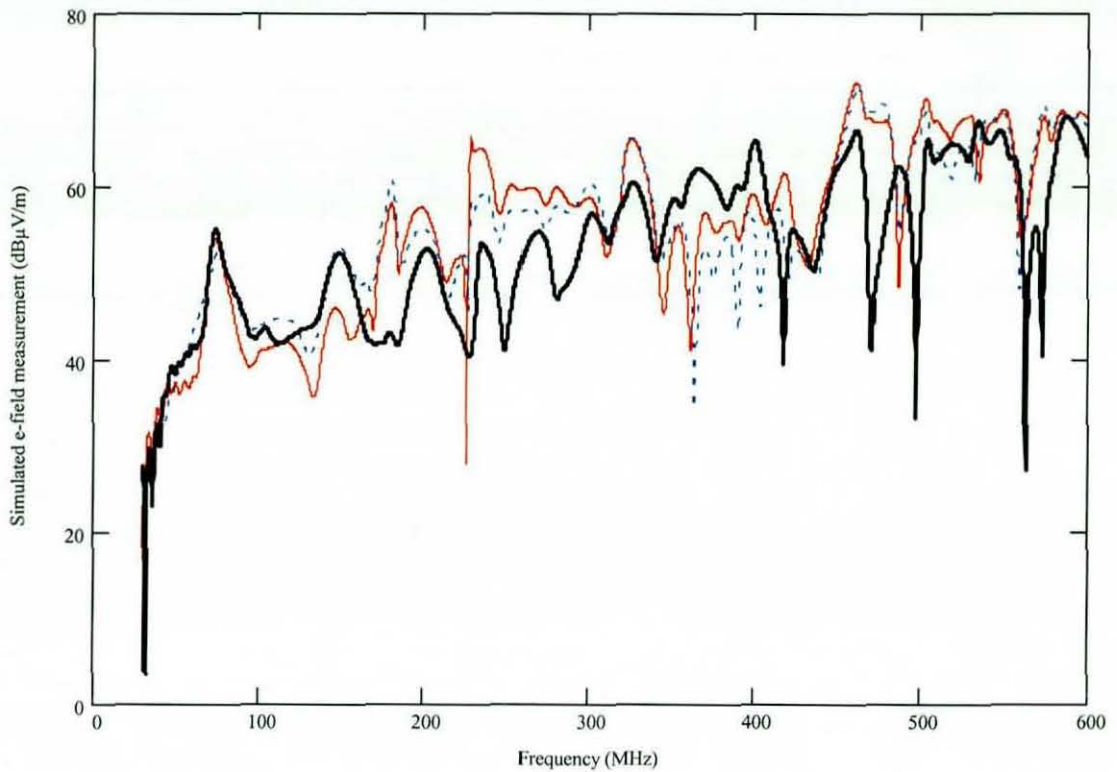
**Fig. 7.22   Simulated measurements for front axle plane: 10 m anechoic (heavy),
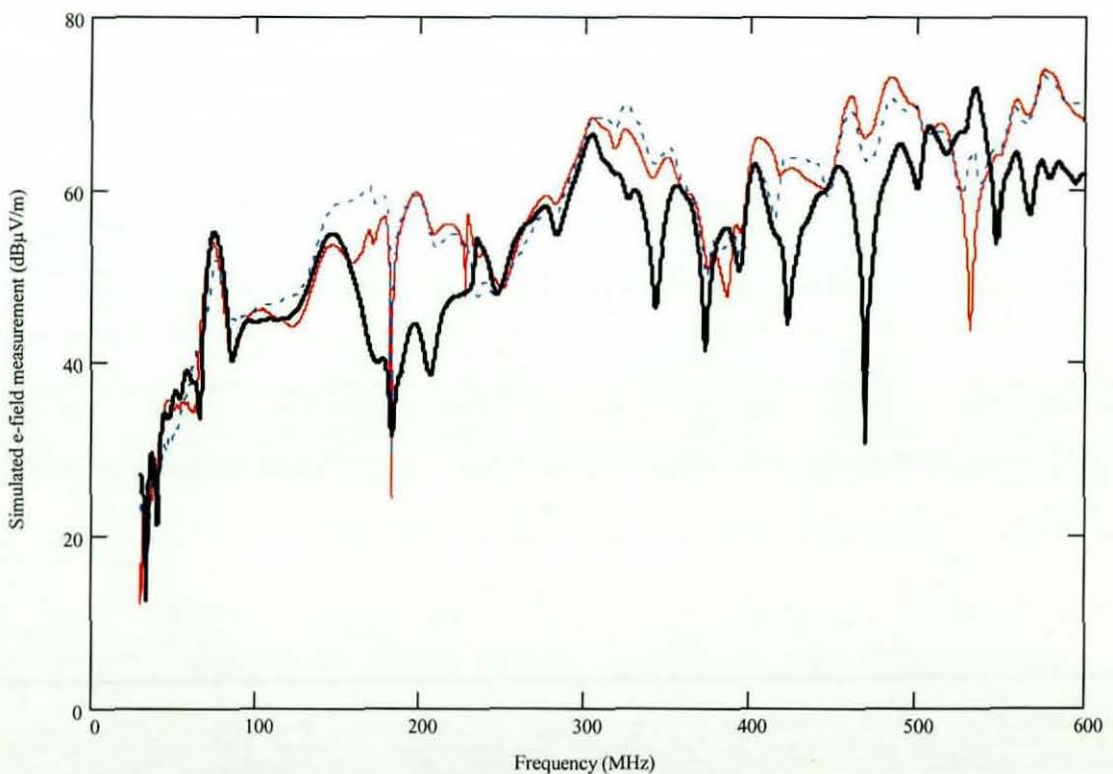3 m semi-anechoic (light) and 3 m anechoic (dotted) with 5 dB adjustments**

**Fig. 7.23   Simulated measurements for back axle plane: 10 m semi- anechoic (heavy),
3 m semi-anechoic (light) and 3 m anechoic (dotted) with 5 dB adjustments**

Experimental measurements

Although these conclusions are based on theoretical models that were limited to vertical polarization and a maximum frequency of 600 MHz, they are generally supported by experimental results [A.2], which were obtained for both horizontal and vertical polarization. These results were obtained using a laboratory noise source coupled into the vehicle wiring harness, which has the following benefits for comparative measurements between different test configurations:

- ensuring that high emissions were present over the full frequency band
- avoiding the need for any cables between the vehicle and the control room
- maximising the repeatability of the measurements.

The results of applying the proposed 5 dB adjustment to the measured data are illustrated in Figs. 7.24-7.27, for 10 m semi-anechoic, 3 m semi-anechoic and 3 m anechoic cases. The 3 m anechoic data also appears to provide a much poorer basis for estimating the levels at 10 m in the semi-anechoic environment for frequencies in the upper half of the band. For frequencies above about 800 MHz, however, the measurements indicate that applying no adjustment is perhaps a more appropriate.
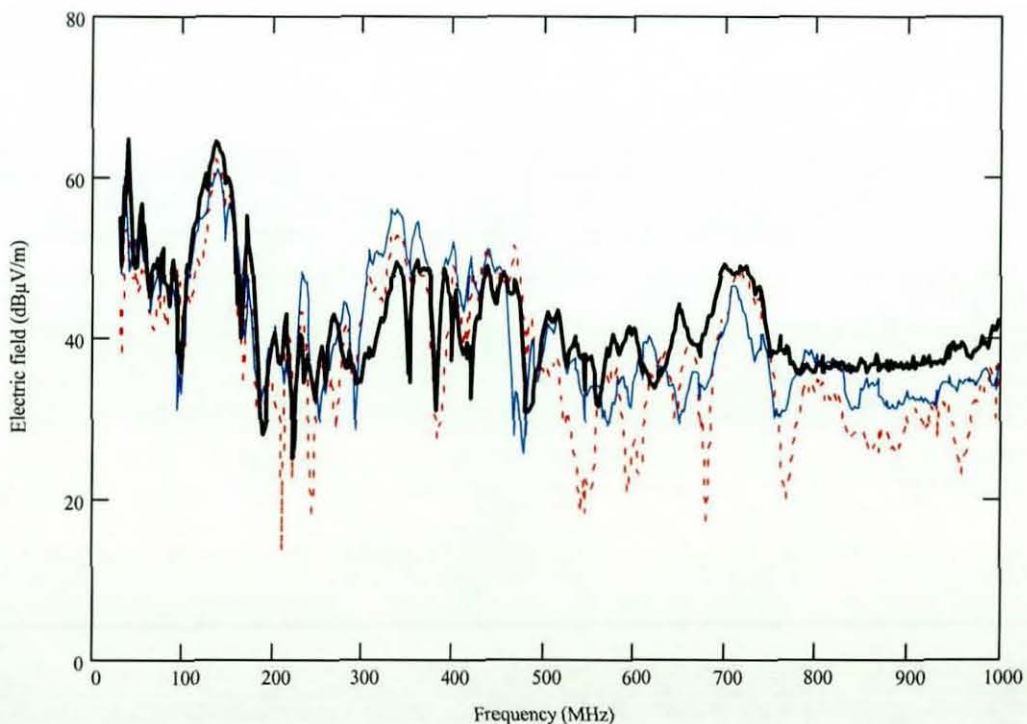

**Fig. 7.24   Chamber results for vertical polarization with wiring excited by noise source:
3 m semi-anechoic (light) and 3 m anechoic (dotted) with 5 dB adjustments,
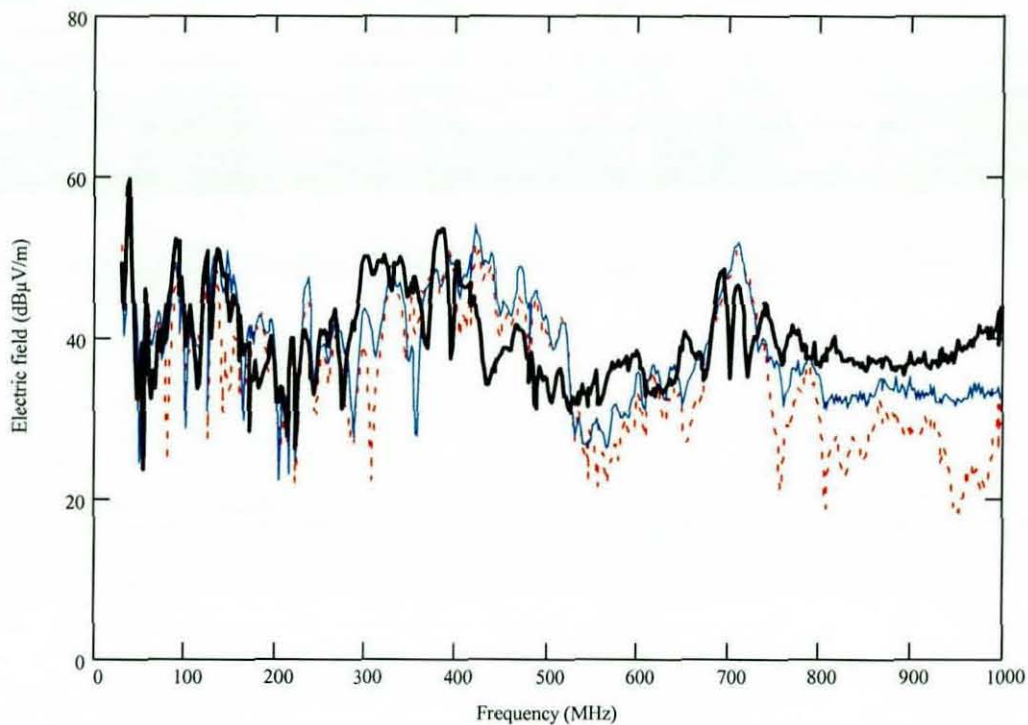10 m semi-anechoic (heavy)**

Fig. 7.25   Chamber results for horizontal polarization with wiring excited by source:
3 m semi-anechoic (light) and 3 m anechoic (dotted) with 5 dB adjustments,
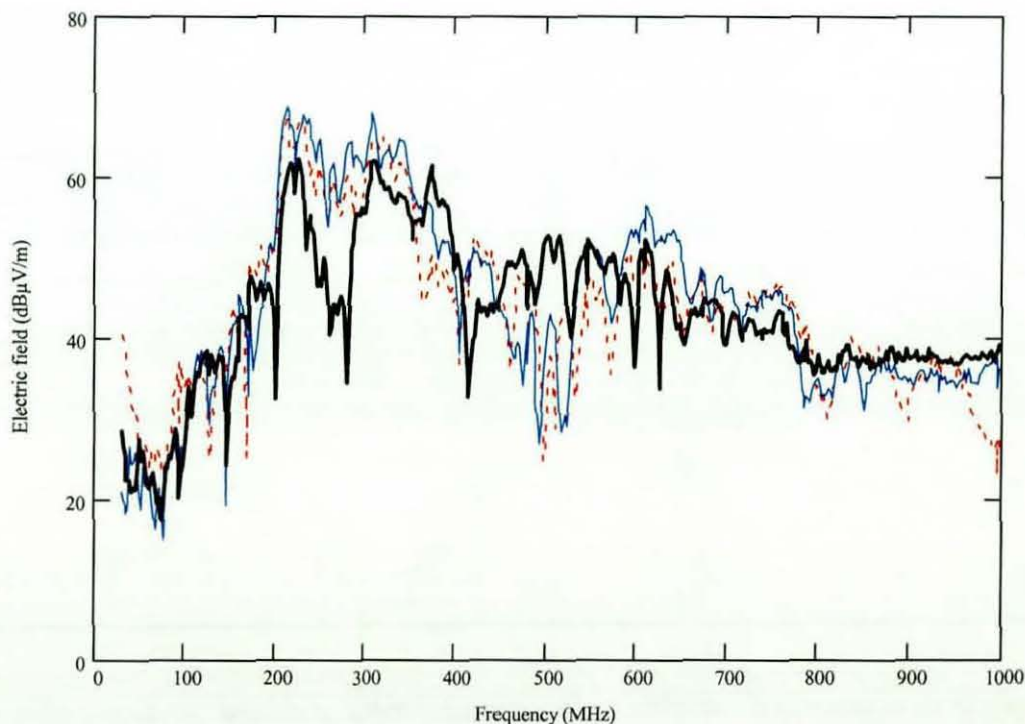10 m semi-anechoic (heavy)

Fig. 7.26   Chamber results for vertical polarization excited by noise source antenna:
3 m semi-anechoic (light) and 3 m anechoic (dotted) with 5 dB adjustments,
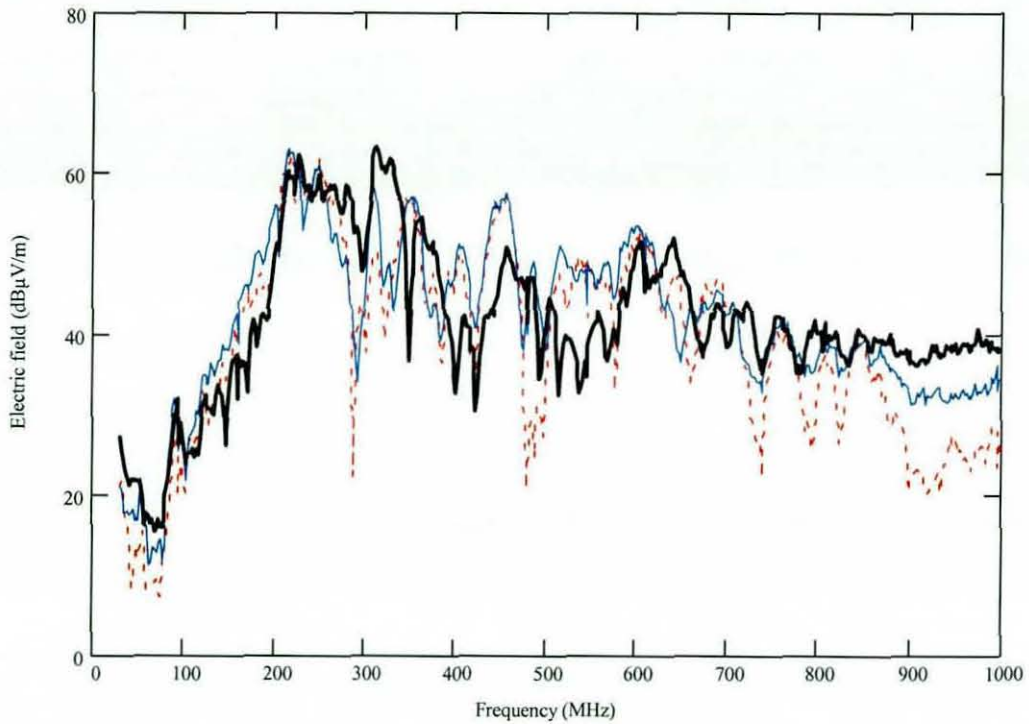10 m semi-anechoic (heavy)

Fig. 7.27   Chamber results for horizontal polarization excited by noise source antenna:
3 m semi-anechoic (light) and 3 m anechoic (dotted) with 5 dB adjustments,
10 m semi-anechoic (heavy)

7.5   Conclusions

Comparing single point field predictions with simulated emissions measurements allows the error due to interpreting the field from the antenna signal to be estimated. It is found that simulated antenna measurements at the 3 m distance for both anechoic and semi-anechoic environments are more accurate, in terms of their representation of the field at the antenna reference point, than simulated measurements carried out at the 10 m distance. This is a very surprising result, as greater field gradients would normally be expected close to the structure, which would make the interpretation of the antenna signal in terms of an equivalent plane wave highly questionable. Moreover, interactions between the antenna and the vehicle would also be expected to be much greater at the 3 m distance.

Both measurements and simulations show that the effect of the test object on the antenna input impedance is relatively small, even the 3 m distance. Both the single point field calculations and the simulated measurements also show that the results at 3 m are similar for both anechoic and semi-anechoic environments. This suggests that the ground plane does not have a very strong effect at close range, but at 10 m the effects of interference between the direct and ground reflected field components are evident from the deeper nulls in the 10 m spectral response.

These observations permit considerable reductions in the size and complexity of models aimed at experimental validation of electromagnetic emissions. For volume-meshing methods, such as TLM, the model size can be reduced because of the smaller distance to the antenna and the reduced height above ground. In addition, simulating a semi-anechoic environment, which at the 3 m distance is not significantly different to the anechoic case, can further reduce the size of the model. Furthermore, avoiding the need to model the receiving antenna provides significant savings in both memory requirements and runtime for all numerical methods.

Both the numerical and measured results demonstrate that there is no simple relationship between the fields at 3 m and 10 m distances, although for computed fields the widely used adjustment 10 dB provides a reasonable guide in an average sense. The numerical results suggest that a 5 dB adjustment provides a better guide for comparing field interpreted from antenna measurements at 3 m and 10 m up to about 600 MHz. The results of measurements suggest that at higher frequencies the fields are not much different at the two distances.

7.6   References

[7.1]   CISPR 22, *Limits and methods of measurement of electromagnetic disturbance characteristics of information technology equipment*, 1993

[7.2]   C.H. Walter, *Travelling wave antennas*, McGraw-Hill, 1965, p. 38

[7.3]   C. Polk, *Optical Fresnel-zone gain of a rectangular aperture*, IRE Transactions on Antennas and Propagation, Vol. 4, January 1956, pp.65-69

[7.4]   S. Silver (ed.), *Microwave antenna theory and design*, McGraw-Hill, 1949, §15.14

[7.5]   E.S. Gillespie (guest ed.), *Special issue on near-field scanning techniques*, IEEE Transactions on Antennas and Propagation, Vol. 36, June 1988

[7.6]   J.-C. Bolomey, *Introduction to near-field techniques for EMC applications: state of the art and prospectives*, Proceedings of IEEE EMC Symposium, Montreal, August 2001, Vol. 1, p. 356

[7.7]   A.A. Smith, *Standard site method for antenna calibration*, IEEE Transactions on EMC, Vol. 24, No. 3, August 1982, pp.316-322

[7.8]   R.S. Elliott, *Antenna theory and design*, Prentice-Hall, 1981, p. 47

[7.9]   R.E. Collin and F.J. Zucker (eds.), *Antenna theory*, McGraw-Hill, 1969, Vol. 1, p.105

CHAPTER 8:   ANTENNA MEASUREMENTS

In addition to radio reception for entertainment, vehicles are now required to provide a much wider range of wireless services resulting in rising demand for antennas on vehicles [8.1]. These include DAB, TV, GPS, mobile telephony and, in future, a variety of telematics applications. The simple monopole antenna that has traditionally been used for vehicle applications is therefore becoming increasingly undesirable as the number of antennas that are used on vehicles rises. Conformal designs are the preferred alternative [8.2], from both styling and security considerations, with the result that there is now considerable interest in integrating vehicle antenna structures into non-conducting structures such as the vehicle glazing, polycarbonate bumpers and non-metallic body panels. However, the performance and location of such antennas are often poorer than could be achieved with the traditional monopole.

The behaviour of antennas installed on real structures is inevitably modified from that which is expected from the device in isolation [A.5]. However, it is the installed performance that ultimately determines whether the required system functionality can be achieved. Access to services operating at a wider range of frequencies, with a very high degree of reliability, is now required. Furthermore, digital systems can suffer complete service loss if the signal level falls below a certain threshold, unlike the steady degradation in reception quality that is encountered with analogue systems. Thus, greater engineering effort will be needed to ensure that the required performance can be achieved. Ideally, it would be possible to predict these properties before the system is built, so that the design and location of the antenna can be optimised early in the development programme [8.3-8.4, A.4]. As a minimum, it is essential to be able to make reliable measurements of the installed performance of vehicle antennas. However, even measurement of these parameters is not straightforward, and numerical modelling has therefore been used to investigate the validity of such measurements and their use in model validation .

The electrical properties of the earth on which vehicles travel may have a significant impact on the behaviour of on-board antennas. These properties, however, depend on the frequency of the electromagnetic field and the nature of the underlying earth. For the purposes of this study, therefore, a perfectly conducting planar ground was assumed in order to provide a standard reference environment. The selected frequency range (up to 200 MHz) is lower than that of many systems that are beginning to be utilized for communications and telematics applications.

This frequency range was selected on the basis of computational requirements for vehicle scale models. Nonetheless, these frequencies do encompass the LW, AM and FM radio bands, which currently represent the most widespread use of vehicle mounted antennas, as well as digital audio broadcasting (DAB).

8.1   Simulated gain measurement

Antenna gain measurements are more usually carried out for isolated devices, often using an anechoic chamber or an open range that is many wavelengths above ground. The simplest methods for determining antenna gain are from coupling measurements, which may be carried out between a pair of identical antennas, relative to a reference antenna of known gain, or between three unknown antennas. All of these techniques are based on the "Friis transmission equation", which assumes that far-field conditions prevail and can be stated in the form [8.5]:

$$\frac{P_R(f,d)}{P_T(f)} = G_R(\theta,\phi,f)G_T(\theta',\phi',f)\left[\frac{c}{4\pi df}\right]^2 \tag{8.1}$$

where c is the speed of light and $P_R(f,d)$ is the power received by an antenna of gain $G_R(\theta,\phi,f)$ at frequency f due to an antenna of gain $G_T(\theta',\phi',f)$ transmitting power $P_T(f)$ at a distance d. As the gain parameters are functions of the spherical co-ordinates, the received power also depends on the relative orientation of the transmit and receive antennas as well as their separation and the frequency. Thus, polarization mismatch and system losses will also contribute to the power transmission, resulting in an effective gain that differs from the inherent directivity of the structure.

Far-field approximation

Gain measurements with antennas at finite separations are inevitably associated with some intrinsic error, since true far-field conditions can never be achieved. In practice, however, a distance of $2D^2/\lambda$ is normally assumed to be sufficient to ensure that range related errors are tolerable (where λ is the wavelength and D represents a characteristic dimension of the antenna), although more and less stringent criteria are sometimes used.

The $2D^2/\lambda$ criterion for gain measurements is based on the assumption of a point source illuminating the antenna under test (in free space) and a maximum acceptable phase error of $\pi/8$ radians across the aperture, while for measurements using a transmit antenna of finite extent a range of $2D_R D_T/\lambda$ is estimated to limit power differences to about 10% [7.4], where D_T and D_R are the dimensions for the source and receive antennas, respectively.

Greater distances of $2(D_T+D_R)^2/\lambda$ [8.6] or $2(D_T^2+D_R^2)/\lambda$ are sometimes proposed where both antennas are of finite extent. Nonetheless, for antennas with large apertures $(D>\lambda)$ numerical results have been used [8.7] to establish that the transmitter extent has no significant influence on the phase error and that a distance of $2D_R^2/\lambda$ is sufficient to limit the effects of phase errors, while a separation of $2.6D_RD_T/\lambda$ is proposed to ensure that amplitude errors are limited to about 1 dB. The difficulty for a complex structure such as a vehicle-mounted antenna is to determine the appropriate dimension for D, particularly when the vehicle is on a conducting ground.

Finite load impedance

In order to carry out both practical and simulated measurements it is necessary to introduce a finite impedance at the antenna terminals. As this effect is not strictly a feature of the antenna itself, it is not included in the theoretical evaluation of far-field directivity from near-field quantities. However, this is a feature of both real and simulated gain measurements, which must therefore be corrected in order to obtain values that are comparable with those computed using a near-far field transformation.

For an incident voltage V_0, the power $P_0(f)$ in the input line of characteristic impedance Z_0 is:

$$P_0(f) = \frac{|V_0|^2}{2}\text{Re}\left\{\frac{1}{Z_0}\right\} \tag{8.2}$$

while the power $P_A(f)$ delivered to the antenna of characteristic impedance $Z_A(f)$ is:

$$P_A(f) = \frac{|V_0|^2|1+\rho(f)|^2}{2}\text{Re}\left\{\frac{1}{Z_A(f)}\right\} \tag{8.3}$$

where $\rho(f)$ represents the input reflection coefficient at the antenna terminals:

$$\rho(f) = \frac{Z_A(f)-Z_0}{Z_A(f)+Z_0} \tag{8.4}$$

Assuming the antenna itself to be lossless, and that Z_0 is entirely real, the ratio of the transmitted power to the applied power is given by:

$$\eta(f) = |1+\rho(f)|^2 Z_0(f)\text{Re}\left\{\frac{1}{Z_a(f)}\right\} \tag{8.5}$$

Substituting for $Z_A(f)$ in terms of the input reflection coefficient then gives:

$$\eta(f) = \left|1 + \rho(f)\right|^2 Z_0 \, \text{Re}\left\{\frac{1 - \rho(f)}{Z_0[1 + \rho(f)]}\right\} \tag{8.6}$$

Thus, gain estimates that include mismatch at the antenna terminals should be divided by the parameter $\eta(f)$ in order to correct for the influence of the finite reflection coefficient. In the absence of any other loss, the modified gain estimate can then be equated with the directivity.

8.2   Simple dipoles in free space

The gain of simple dipole antennas has been computed as a function of range using MoM (AWAS). The length of the dipole was 1.5 m, which simple theory suggests should have a primary resonance at 100 MHz. However, this antenna also has a finite radius of 1.5 mm, reducing the resonant frequency to about 96 MHz, and a load impedance of 50Ω. The azimuthal far-field gain (computed for a separation of 16 km) was 2.018 dB, which increases to 2.157 dB when the effect of finite termination impedance is eliminated by introducing the parameter $\eta(f)$. This result is extremely close to the theoretical ideal of 2.15 dB [8.8] for an infinitely thin dipole at its primary resonance.

The results at resonance are presented in Fig. 8.1, in terms of the error relative to a reference value computed for a separation of 16 km, since there should be no question that this is in the far field. A reasonable target for the gain levels that are anticipated is perhaps an intrinsic error of 0.1 dB, which in this case is achieved at a range of 4 m. The $2D^2/\lambda$ criterion would suggest a range of 1.44 m, indicating that this approximation is not appropriate for this case. The results for the same device at other frequencies are shown in Fig. 8.2, showing that the error generally increases with frequency and that the ripple seen in Fig. 8.1 only becomes significant close to resonance. This is illustrated more clearly in Fig. 8.3, which shows the error in the gain estimate as a function of frequency at various ranges. The ripple near to resonance is due to multiple reflections between the antennas arising from finite mismatch at the terminals, which are terminated using 50 Ω impedances.

Applying the $2D^2/\lambda$ criterion at 200 MHz (ie. 3 m separation) would provide gain values with errors ranging from 0.25 dB to 0.6 dB over the band 50-200 MHz (see Fig. 8.2). Aiming to provide an error of no more than 0.1 dB would increase the required measurement range by a factor of 3, to almost 9 m. The results also suggest that the range requirement would increase further at higher frequencies, for a given antenna.
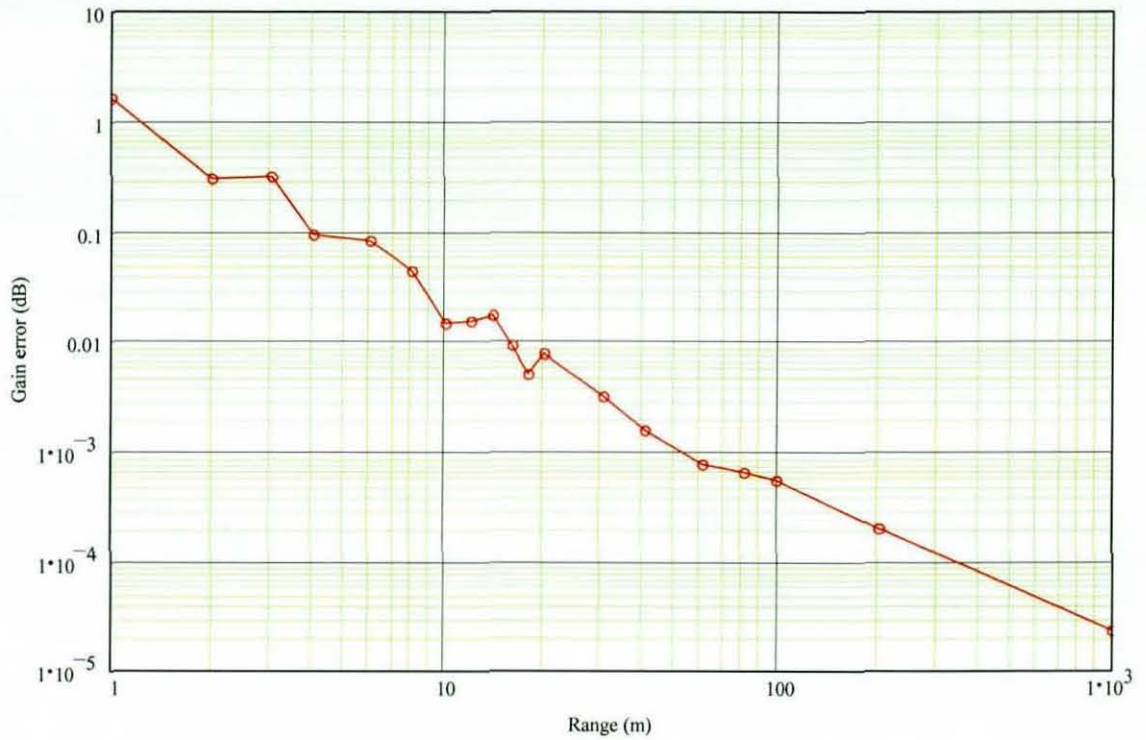
Fig. 8.1   Gain error as a function of range for pair of 1.5 m dipoles in free space at the first resonant frequency (95 MHz)
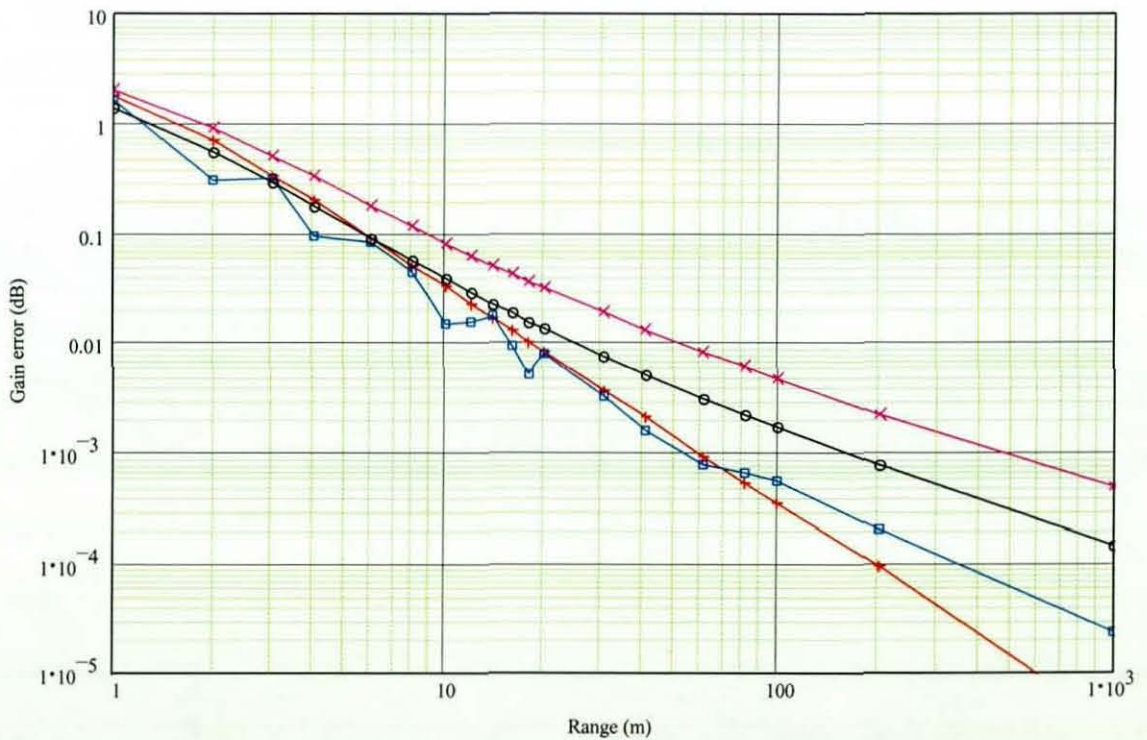

Fig. 8.2   Gain error as a function of range for pair of 1.5 m dipoles in free space for frequencies of 50 MHz (+), 95 MHz (□), 150 MHz(o) and 200 MHz (x)
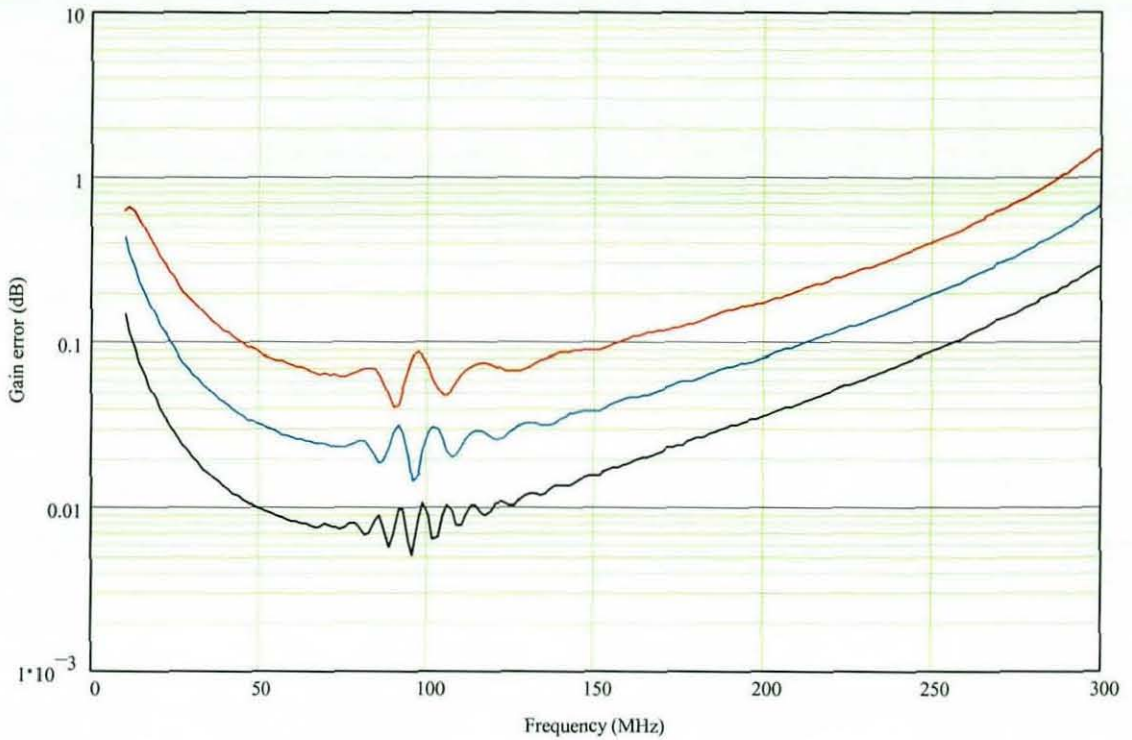
Fig. 8.3   Error in gain estimate with frequency for 95 MHz dipoles in free space, based on measurements at ranges of 6 m (red), 10 m (blue) and 18 m (black)

These observations suggest that the phase error criterion that is commonly assumed to result in acceptable accuracy for gain measurements of this type may not be sufficient in this case.

Analysis of dipole fields

The phase and amplitude errors that can be expected over the length of the receiving dipole can be estimated using the analytical expression for the co-linear field component due to a thin dipole supporting a sinusoidal current distribution [8.9]:

$$E_z(R, f, D_T) = -30jI_0 \left[\frac{e^{\left\{-j\frac{2\pi f}{c}R_1\right\}}}{R_1} + \frac{e^{\left\{-j\frac{2\pi f}{c}R_2\right\}}}{R_2} - 2\cos\left\{\frac{\pi f}{c}D_T\right\}\frac{e^{\left\{-j\frac{2\pi f}{c}R\right\}}}{R} \right] \tag{8.7}$$

where $I_0(f)$ represents the current at the antenna terminals and for a z-directed dipole of length D_T located at **P** with an observation point located at **S** the distances R, R_1 and R_2 are:

$$R = |S - P|, \quad R_1 = \left|S - \left[P + \left(0,0,\frac{D_T}{2}\right)\right]\right| \text{ and } R_2 = \left|S - \left[P - \left(0,0,\frac{D_T}{2}\right)\right]\right| \tag{8.8}$$

This analytical result can therefore be used to determine the maximum amplitude and phase deviations in the field generated by a dipole antenna across the region where a receiving dipole would be placed for gain measurements.

In order to obtain the target accuracy of 0.1 dB for gain measurements for frequencies over the band 50-200 MHz a separation of 9 m was required in the numerical simulations (see Fig. 8.2). Reducing the maximum frequency to 150 MHz allows the separation requirement to be relaxed to around 6 m, while at resonance only 4 m is required. For a 1.5 m long dipole, however, equation (8.8) suggests amplitude and phase errors over the length of an identical second dipole as shown in Figs. 8.4-8.5 at these separation distances.

At resonance, the 4 m separation corresponds to amplitude variations approaching 10%, but the amplitude error becomes progressively smaller as the separation increases (see Fig. 8.4). However, from Fig. 8.5 it appears that the maximum phase error that can be tolerated is around $\pi/24$ radians to achieve the 0.1 dB gain error target. These values are considerably lower than those normally assumed for such measurements. Reducing the length of the transmitter influences both the amplitude and phase errors over the receiver length. Reducing the length of the receiver generally reduces the magnitude of both the phase and amplitude errors.
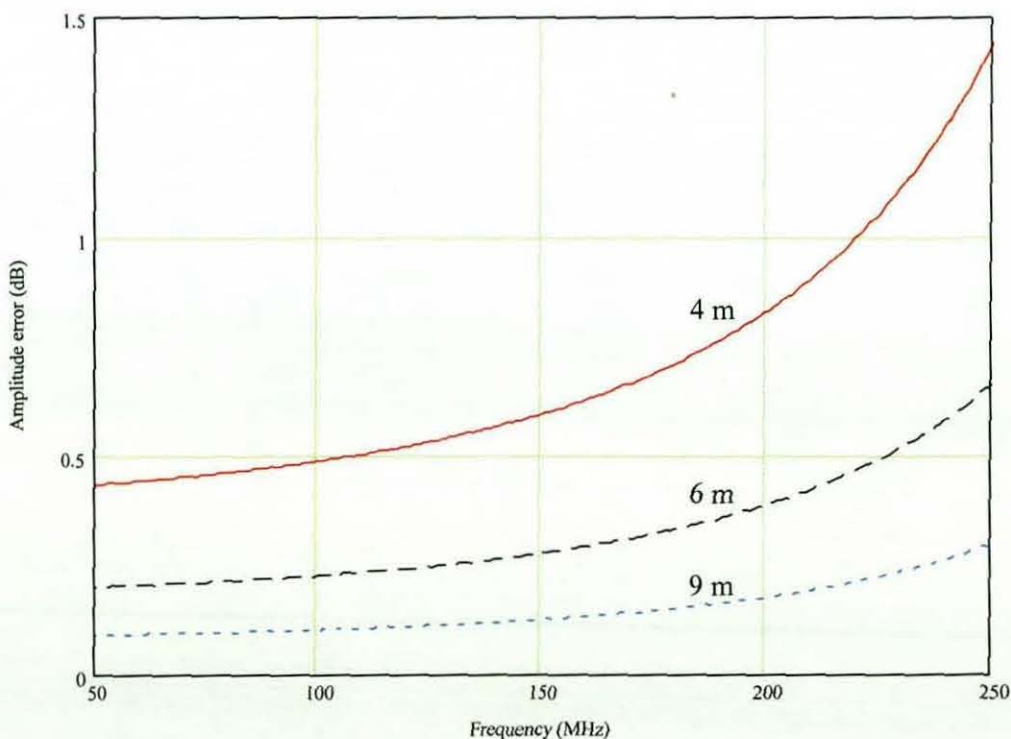

Fig. 8.4   Amplitude error over 1.5 m receiving "aperture" due to a 1.5 m dipole in free space
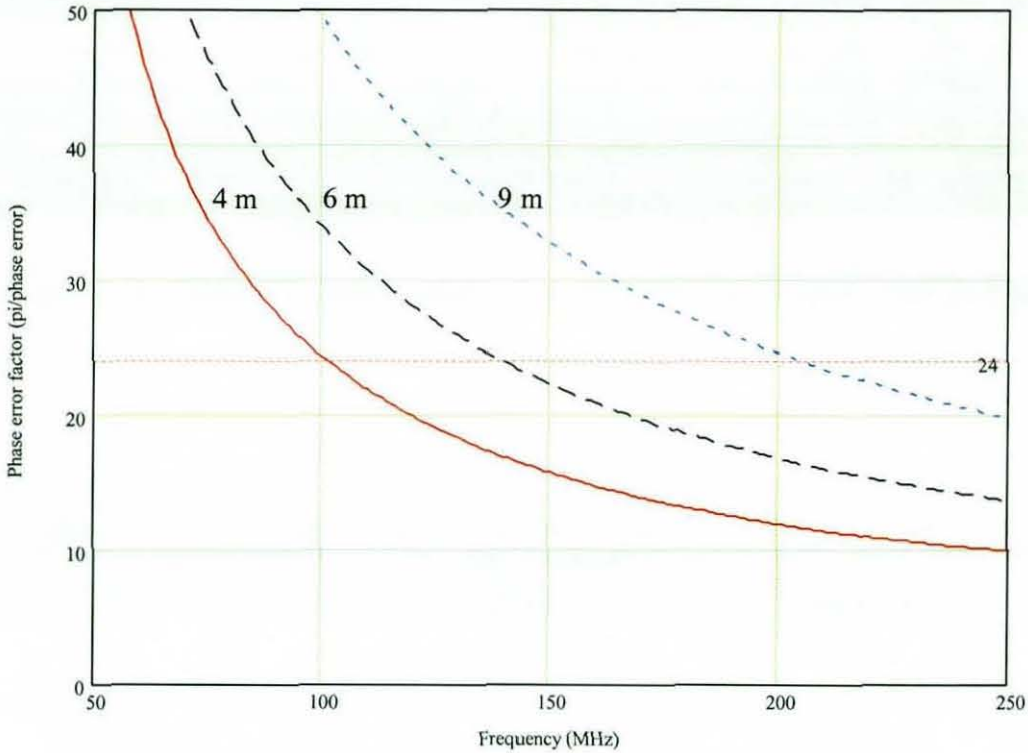
Fig. 8.5   Phase error over 1.5 m receiving "aperture" due to a 1.5 m dipole in free space

Thus, achieving the target gain error of 0.1 dB for dipoles in free space requires the phase error to be limited to no more than $\pi/24$ radians, which is much more stringent than the value of $\pi/8$ which is normally assumed.

8.3   Simple dipoles above a ground plane

For vehicle antenna measurements using EMC test facilities a conducting ground plane is in close proximity. For antennas close to a ground plane, the device can be considered as a two-element array, due to the ground image. Thus, it should be possible to use the same gain measurement techniques, provided that the field over the receiver is sufficient close to a plane wave. When vertical dipoles are placed at a representative vehicle roof height above a ground plane, the logarithmic gain error plots obtained from simulated measurements are found to become linear (see Figs. 8.6-8.7), with the error at any given range increasing with frequency.

The azimuthal far-field gains (as computed at 16 km) at resonance are 5.263 dB for a 1.5 m dipole and 5.185 dB for a 1.2 m dipole. These values correspond well with the 3 dB increase over the gain of the isolated dipole that would be expected based on results for a short current element (which has very similar gain to a half-wave dipole) above a ground plane [8.8].

**Fig. 8.6   Gain error as a function of range for pair of 1.5 m dipoles at 1.725 m
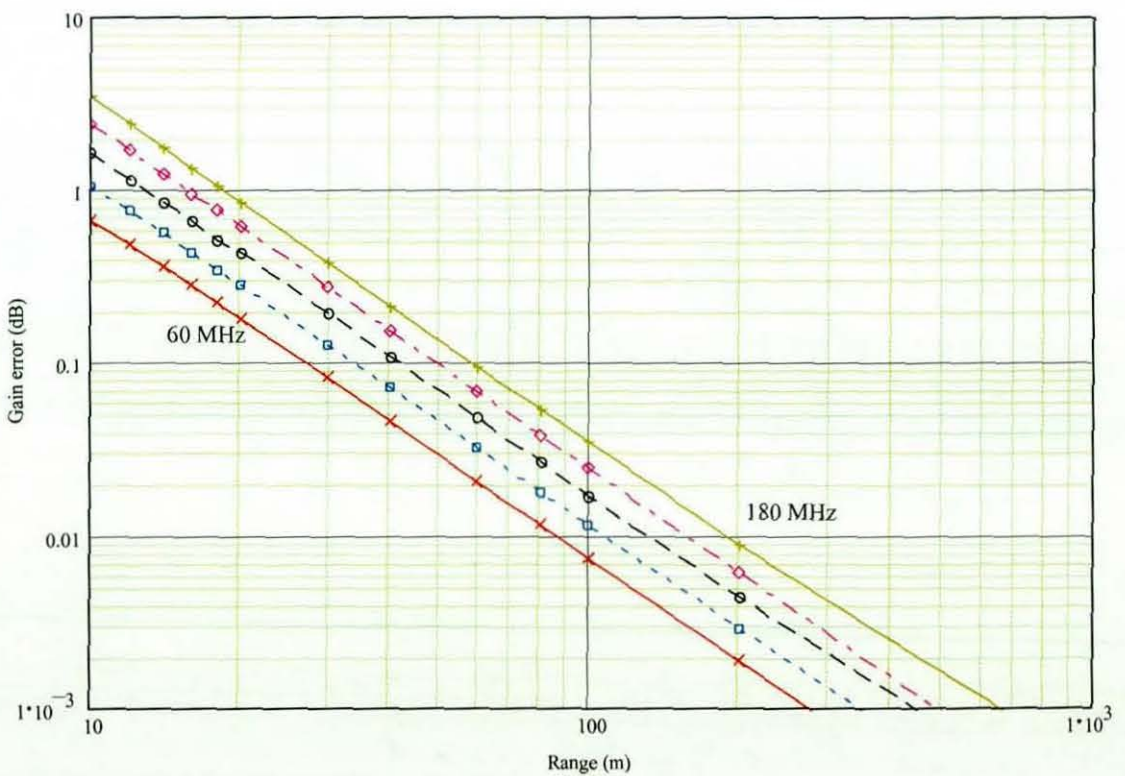above a perfect ground, for frequencies in the range 30-150 MHz**

**Fig. 8.7   Gain error as a function of range for pair of 1.2 m dipoles at 1.725 m
above a perfect ground, for frequencies in the range 60-180 MHz**

Using the antenna height of 1.725 m as $D/2$ suggests range requirements of 30 m at 95 MHz, and 38 m at 120 MHz. However, the models indicate that the ranges required to obtain 0.1 dB error are a little higher than these values, suggesting some underestimation of D. Nonetheless, adding lengths that are representative of the dipole dimensions does not provide any better predictions. As with the isolated dipoles, achieving an accuracy of 0.1 dB at frequencies above resonance requires a significant increase in the measurement range.

Plots of the frequency dependence of the gain estimates for dipoles above a ground plane also show a rather different behaviour to the free space configuration. Not only is the ripple close to resonance absent in this case, but the frequency at which the minimum error is obtained is shifted significantly below the resonant frequency (see Figs. 8.8-8.9). Consequently, it seems that a much greater range is required for dipoles over ground in order to obtain the desired accuracy of 0.1 dB at frequencies close to resonance.
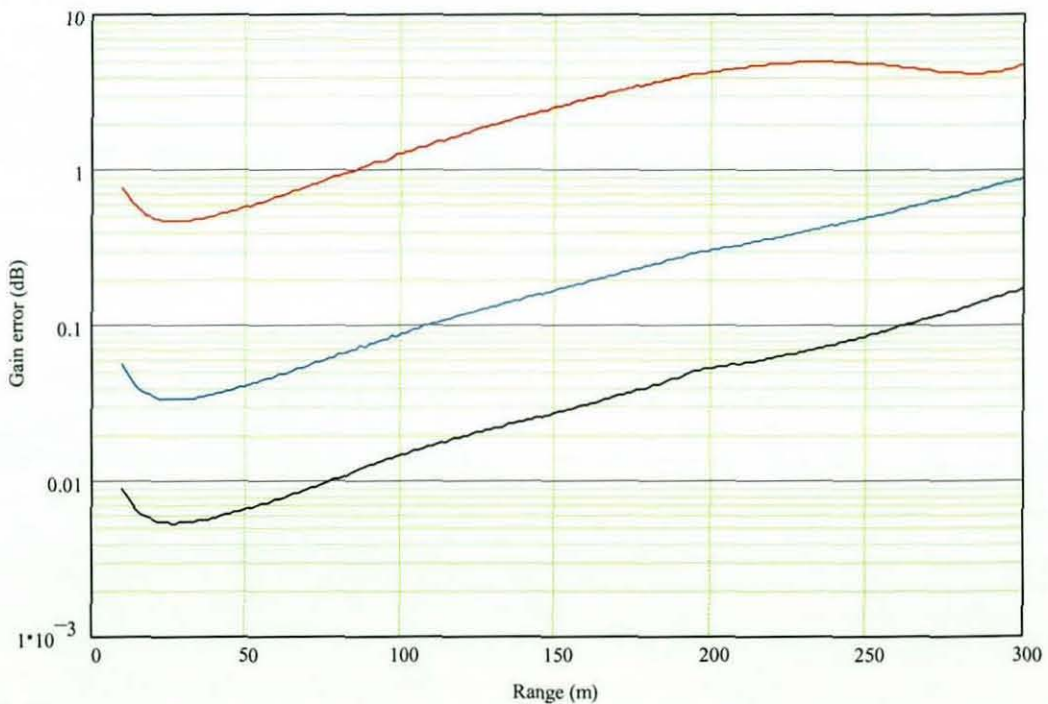

Fig. 8.8   Error in gain estimate with frequency for 95 MHz dipoles over ground, based on measurements at ranges of 10 m (red), 40 m (blue) and 100 m (black)
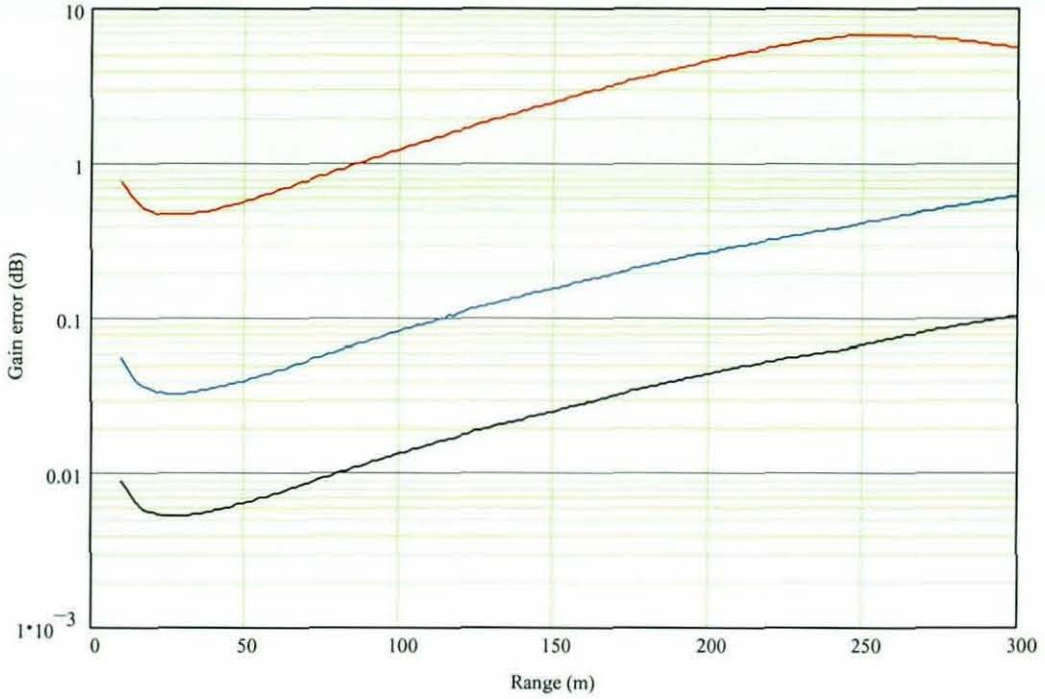
Fig. 8.9   Error in gain estimate with frequency for 120 MHz dipoles over ground, based on measurements at ranges of 10 m (red), 40 m (blue) and 100 m (black)

8.4   Far-field for an antenna over a ground plane

For the geometrical configuration shown in Fig. 8.10, the field at a distance R from a simple array of two in-phase point sources is of the form:

$$E_z(R,h,y,\lambda) = \frac{e^{\left\{-j\frac{2\pi}{\lambda}R_1(R,h,y)\right\}}}{R_1(R,h,y)} + \frac{e^{\left\{-j\frac{2\pi}{\lambda}R_2(R,h,y)\right\}}}{R_2(R,h,y)} \tag{8.9}$$

for a source of unit intensity and:

$$R_1(R,h,y) = \sqrt{R^2 + [h-y]^2} \quad \text{and} \quad R_2(R,h,y) = \sqrt{R^2 + [h+y]^2} \tag{8.10}$$

The lengths $R_1(R, h, y)$ and $R_2(R, h, y)$ can also be written in the form:

$$R_1(R,h,y) = R\sqrt{1 + \left[\frac{h-y}{R}\right]^2} \quad \text{and} \quad R_2(R,h,y) = R\sqrt{1 + \left[\frac{h+y}{R}\right]^2} \tag{8.11}$$
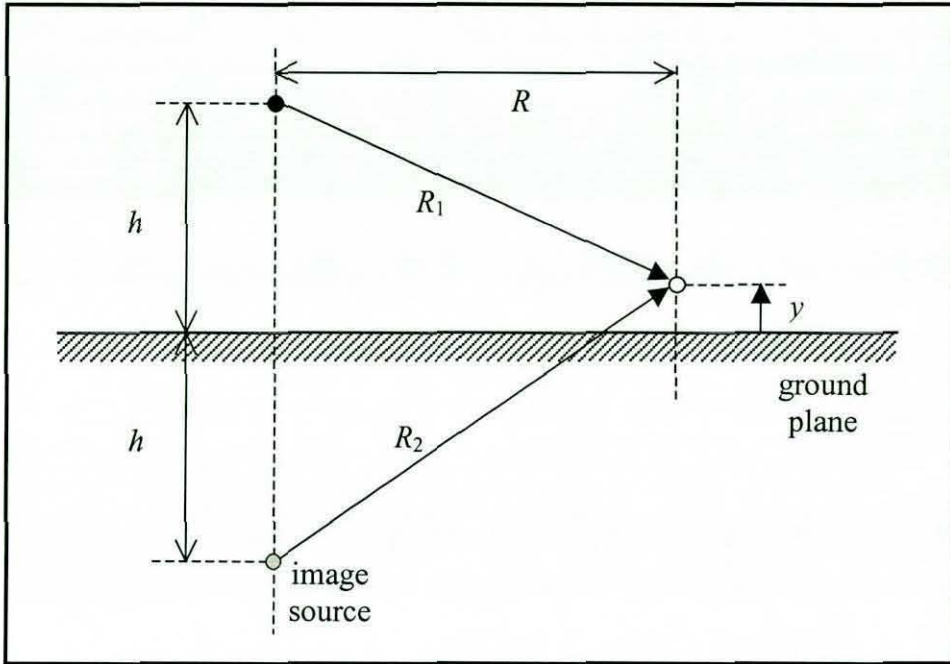
145

Fig. 8.10   Geometry for analysis of antenna above a ground plane

Under the condition $R \geq h+y$, the square roots may be approximated using appropriate binomial expansions, and neglecting the higher order terms (ie. assuming $R>h+y$) allows the following approximate form to be derived:

$$E_z(R,h,y,\lambda) \cong \frac{e^{\left\{-j\frac{\pi}{\lambda R}\left[2R^2+y^2+h^2\right]\right\}}}{R^3}\left\{\left[2R^2-(y+h)^2\right]\cos\left(\frac{2\pi h y}{\lambda R}\right)+2hye^{j\frac{2\pi h y}{\lambda R}}\right\} \qquad (8.12)$$

Furthermore, if hy/R is sufficiently small (8.12) can be further approximated to:

$$E_z(R,h,y,\lambda) \approx \frac{\left[2R^2-y^2-h^2\right]}{R^3}\cos\left\{\frac{2\pi h y}{\lambda R}\right\}e^{\left\{-j\frac{\pi}{\lambda R}\left[2R^2+y^2+h^2\right]\right\}} \qquad (8.13)$$

The approximation of (8.13) is more convenient than (8.9) for assessing the implications for the ampltiude and phase errors arrising for various measurement configurations.

Phase error

If the phase is assumed to vary monotonically between points on the receiving "aperture" corresponding to y_1 and y_2, then the phase error can be extracted from (8.13) as:

$$\delta\phi(R, y_1, y_2, \lambda) \approx \frac{\pi}{\lambda R}\left[y_1^2 - y_2^2\right]$$ (8.14)

Applying a phase error criterion of no more than π/k radians to obtain the corresponding range requirement Rp_k then gives the result:

$$Rp_k(y_1, y_2, \lambda, n) \geq \frac{k}{\lambda}\left[y_2^2 - y_1^2\right]$$ (8.15)

Thus, for a maximum phase error of $\pi/8$ radians between the middle (at $y=h$) and upper end (at $y=h+D_R/2$) of a receiver aligned with a transmitter at height h, (8.15) gives a range requirement:

$$Rpg_8\left(h, \frac{D_R}{2}, \lambda\right) \geq \frac{2D_R^2}{\lambda} + \frac{8hD_R}{\lambda}$$ (8.16)

This result yields the widely quoted value of $2D_R^2/\lambda$ when h is reduced to zero. It also shows that that the antenna separation that is required at finite height above a ground plane is considerably larger than is the case in free-space, and is influenced by the transmitter height as well as the receiver extent.

From (8.15), the separation required to obtain a maximum phase error of π/k radians over a length $D_R/2$ normal to the axis of a two-element array (such as a dipole at resonance) is:

$$Rpf_k\left(0, \frac{D_R}{2}, \lambda, n\right) \geq \frac{kD_R^2}{4\lambda}$$ (8.17)

The separation required for $k=8$ is therefore $2D_R^2/\lambda$, but the results of section 8.2 indicate that $k=24$ more accurately describes the phase errors that can be tolerated for a dipole, suggesting a separation of $6D_R^2/\lambda$. For a receiver placed at height H the range requirement is dependent on the phase error across the full length of the receiver, which for a maximum of π/k radians is:

$$Rpg_k\left(H - \frac{D_R}{2}, H + \frac{D_R}{2}, \lambda, n\right) \geq 2k\frac{HD_R}{\lambda}$$ (8.18)

Amplitude error

If the amplitude is assumed to vary monotonically between points on the receiving "aperture" corresponding to y_1 and y_2, then the amplitude error can expressed in terms of the ratio of the field magnitudes from (8.13) for the two points:

$$\delta\psi(R,y_2,y_1,\lambda)=\left[\frac{2R^2-y_2^2-h^2}{2R^2-y_1^2-h^2}\right]\frac{\cos\{2\pi h y_2/\lambda R\}}{\cos\{2\pi h y_1/\lambda R\}} \tag{8.19}$$

Writing y_2 as $y_2=y_1+\Delta$ and expanding the cosine in the numerator using Taylor's series gives:

$$\delta\psi(R,y_1,\Delta,\lambda)\cong\left[1-\frac{2y_1\Delta+\Delta^2}{2R^2-y_1^2-h^2}\right]\left[1-\frac{2\pi h\Delta}{\lambda R}\tan\left\{\frac{2\pi h y}{\lambda R}\right\}-\frac{1}{2!}\left\{\frac{2\pi h\Delta}{\lambda R}\right\}^2+...\right] \tag{8.20}$$

Assuming that $hy\ll\lambda R$ and $h\Delta\ll\lambda R$ this approximates to:

$$\delta\psi(R,y_1,\Delta,\lambda)\approx1-\left[\frac{2\pi h}{\lambda R}\right]^2\left[y_1\Delta+\frac{\Delta^2}{2}\right] \tag{8.21}$$

Thus, for an amplitude variation that is no worse than a factor u the required separation is:

$$Ra_u(y,\Delta,\lambda)\geq\frac{2\pi h}{\lambda}\sqrt{\left[\frac{\Delta}{1-u}\right]\left[\frac{\Delta}{2}+y\right]} \tag{8.22}$$

Over a length $D_R/2$ from the axis of a two-element array, the separation that is needed to ensure that the power difference is no more than 10% (ie. 0.457 dB, $u=\sqrt{0.9}=0.949$), is given by:

$$Raf_{0.949}\left(0,\frac{D_R}{2},\lambda\right)\geq\frac{D_R D_T}{\lambda}\sqrt{\frac{\pi^2}{8[1-u]}}\approx4.9\frac{D_R D_T}{\lambda} \tag{8.23}$$

This is rather larger than the $2D_R D_T/\lambda$ requirement for isolated antennas with significant directivity, and indicates a similar distance to that obtained from equation (8.18), which is based on phase error considerations for a dipole antenna in free-space.

For a receiver placed at height H the range requirement is dependent on the phase error across the full length of the receiver:

$$Rag_u\left(h-\frac{D_R}{2},D_R,\lambda\right)\geq\frac{2\pi h}{\lambda}\sqrt{\frac{HD_R}{1-u}} \tag{8.24}$$

which depends on the transmitter and receiver heights, as well as the receiver extent. Thus, for a maximum amplitude error of 0.5 dB, $u=0.944$ and equation (8.24) becomes:

$$Rag_{0.944}\left(h-\frac{D_R}{2},D_R,\lambda\right)\geq\frac{26.55h}{\lambda}\sqrt{HD_R} \tag{8.25}$$

Numerical validation

For the dipole antenna used in section 8.2 (ie. $D_R = D_T = 1.5$ m), equation (8.17) suggests that the separation needed for gain measurements between an identical pair of such antennas is at least $2D_R^2/\lambda$ (ie. 1.44 m at resonance) for a maximum phase error of $\pi/8$ radians, while equation (8.23) suggests a separation of at least $4.9D_R^2/\lambda$ (ie. 3.53 m) for a maximum amplitude error of 0.457 dB. The latter value corresponds fairly well with the value of 4 m that was obtained from numerical simulations of gain measurements, but the $6D_R^2/\lambda$ that is required to limit the phase error to no more than $\pi/24$ radians, which appears to be the requirement at other frequencies, provides a closer value of 4.32 m. Thus, for a dipole in free space, the commonly used criteria of $\pi/8$ radians for phase error is found to be insufficient to provide acceptable accuracy in gain measurements using a similar sized antenna, although the 0.457 dB amplitude error criterion (which occurs at resonance) is sufficient to obtain an adequate approximation to a plane wave at the receive antenna position. The phase error criterion for dipoles near to a ground plane is found to be less stringent ($\sim\pi/20$ radians) than in free space, although the presence of the ground plane results in a requirement for even greater separations than in free space in order to satisfy the necessary phase and amplitude error criteria.

The success of the approximations for a dipole above a ground plane is illustrated in Fig. 8.11, which compares the separation requirements predicted from equation (8.16) for a phase error of $\pi/16$ radians and from equation (8.25) for an amplitude error of 0.5 dB with exact values for a 1.5 m dipole antenna at a height of 1.725 m above a ground plane. The latter were obtained by evaluating equation (8.7) over a range of points over the aperture and searching for the maximum amplitude and phase errors. The phase error estimate that is obtained from (8.19) is found to provide a very good indication of the distances predicted from the exact results, with differences ranging from 4% at resonance to 1.5% at 250 MHz. The estimate for the amplitude error is not as good as that obtained for phase error, with differences ranging from about 10% at resonance to about 5% at 250 MHz. At 50 MHz the errors are around 24% for estimates based on both amplitude and phase considerations. However, the exact results indicate that phase error is the dominant influence on the separation requirement above resonance, although the amplitude error represents the more significant limitation below resonance. The larger error associated with range estimates based on the amplitude error criterion is due to the assumption that the error varies monotonically over the receiver aperture. While this is the case for points close to the axis of the array, for receive apertures that are displaced from the axis the amplitudes at the end-points of the receiver aperture will not necessarily give the maximum deviation, with the result that the values obtained from the estimate are underestimated (as shown in Fig. 8.11).
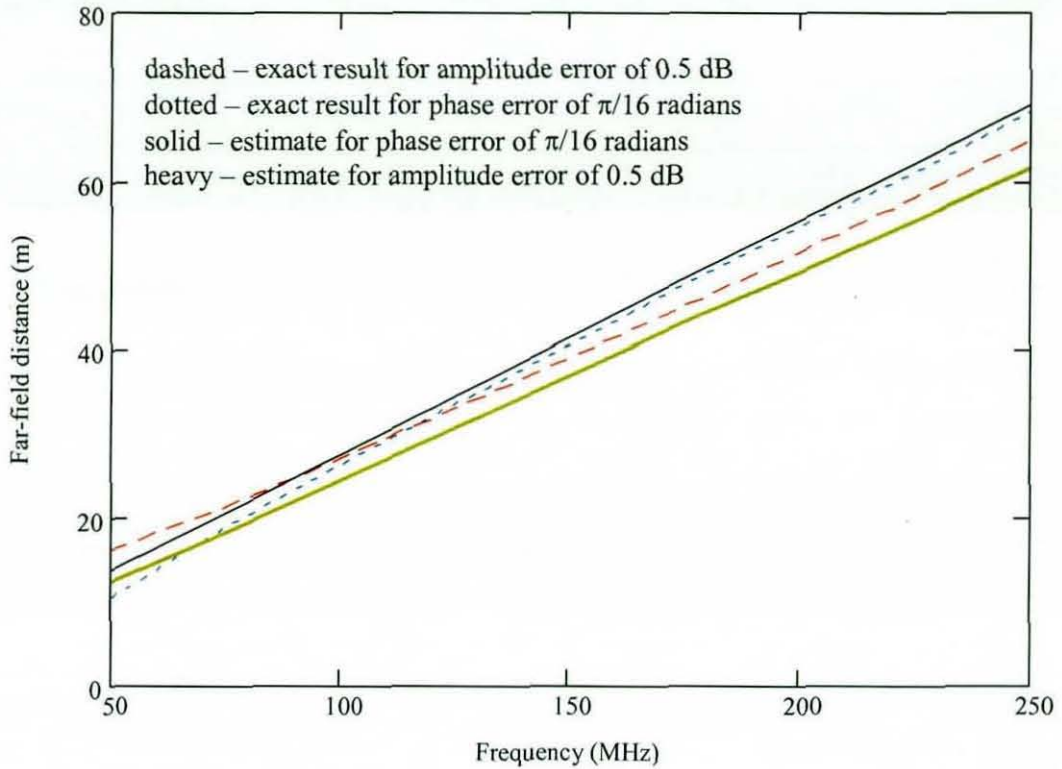
dashed – exact result for amplitude error of 0.5 dB
dotted – exact result for phase error of $\pi/16$ radians
solid – estimate for phase error of $\pi/16$ radians
heavy – estimate for amplitude error of 0.5 dB

Fig. 8.11 **Computed and estimated ranges based on phase and amplitude error criteria for a pair of 1.5 m dipoles at 1.725 m above an infinite, perfectly conducting ground plane**

8.5   Vehicle-mounted monopole

A model comprising a vehicle-like object, augmented with a 0.6 m vertical wire representing a monopole antenna at the centre of the roof (see Fig. 8.12), was used to investigate the radiation characteristics of vehicle mounted antennas and their measurement.
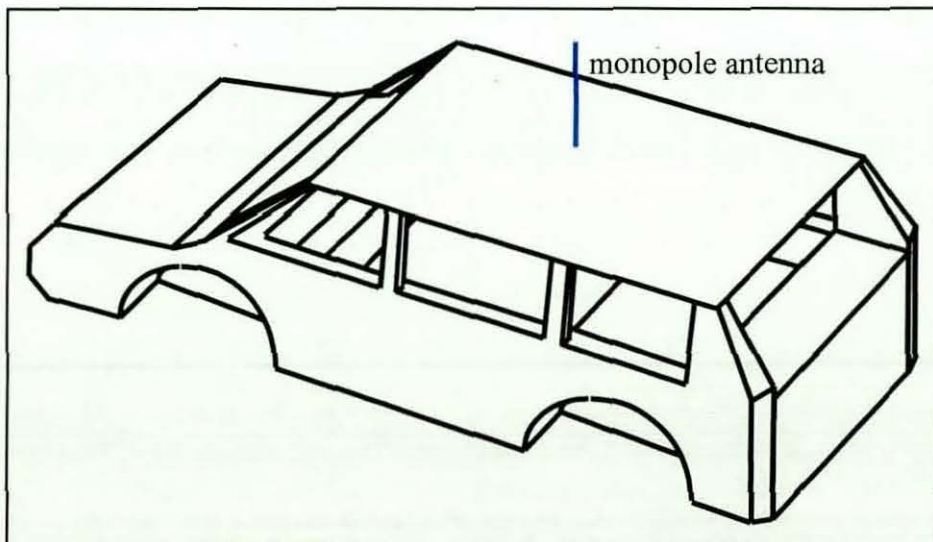

Fig. 8.12   **View of simulated vehicle geometry and monopole on roof**

Far-field characteristics

The monopole antennas that have traditionally been fitted to vehicles for radio reception are essentially distorted dipoles, with the vehicle body acting as the lower element of the antenna. The radiation patterns and maximum far-field gain of this system have been computed at selected frequencies, so that the gain in the direction of the reference antenna (which is placed to the side of the vehicle) could be determined.

The peak gain of the vehicle antenna and the peak gain of the reference dipole were also computed, and these results are summarized in Fig.8.13, for frequencies around the first resonance of the two antennas. It can be seen that while the gain of the reference dipole varies little around its resonant frequency (at 95 MHz), the gain of the vehicle mounted antenna changes very radically around its first resonance (ie. 120 MHz).

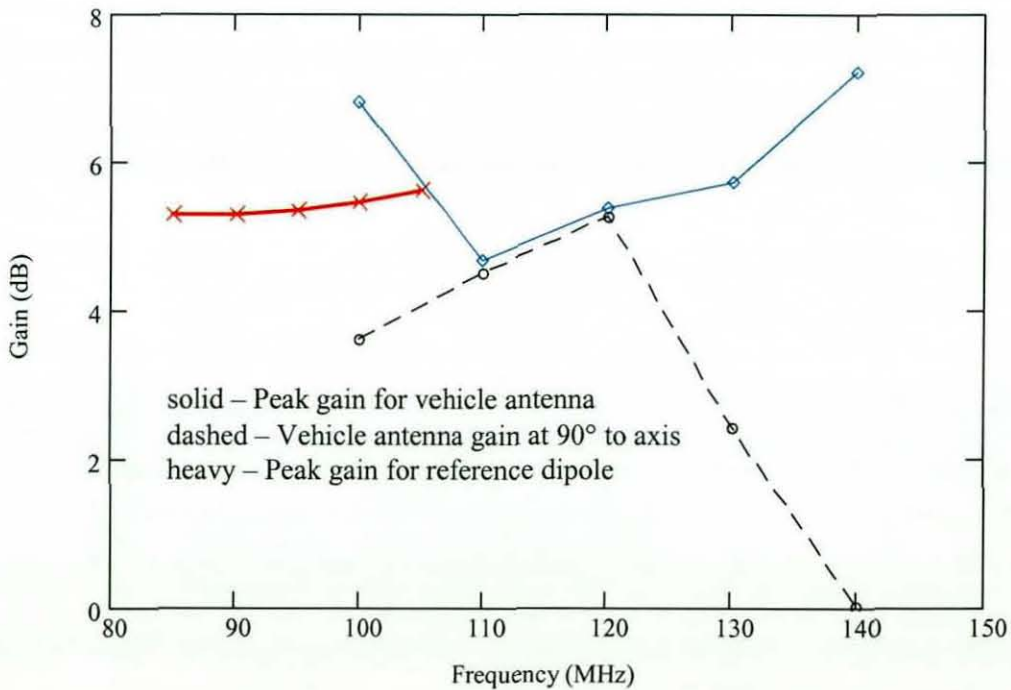**Fig. 8.13   Computed far-field gains for vehicle mounted antenna and reference dipole used for simulated gain measurements**

This is further illustrated by the results of Figs. 8.14-8.18, which show the far-field patterns for the vehicle-mounted antenna. In these views, the vehicle is pointing towards the lower right-hand corner in these plots. The height of the roof was 1.725 m, while the length of the monopole element was 0.6 m.

The patterns for the vehicle-mounted antenna are similar in form to the simple dipole, particularly at lower frequencies. However significant pattern asymmetries can be seen in the vehicle results, and the disturbances become more marked as the frequency increases. For the sample geometry that was investigated, the peak gain in the azimuthal plane is in a single lobe directed towards the front of the vehicle at 100MHz (see Fig. 8.14). As the frequency approaches 120 MHz, the pattern becomes dominated by two lobes to the sides of the vehicle (see Figs. 8.15-8.16). The form of the elevation lobes also appears to reflect the rectangular nature of the roof panel at the resonant frequency of the monopole (120 MHz).

Fig. 8.14   Far-field pattern at 100 MHz for 0.6 m monopole at centre of car roof

Fig. 8.15   Far-field pattern at 110 MHz for 0.6 m monopole at centre of car roof

Fig. 8.16   Far-field pattern at 120 MHz for 0.6 m monopole at centre of car roof

As the frequency approaches 140 MHz, the pattern becomes dominated by lobes that are directed both forwards and backwards at 45° to the axis of the vehicle (see Figs. 8.17-8.18). The form of the elevation lobes also becomes much more complicated.
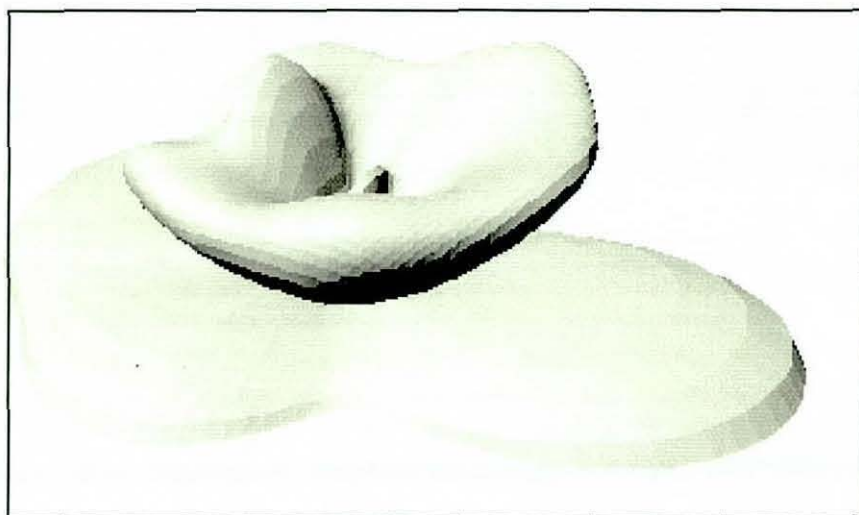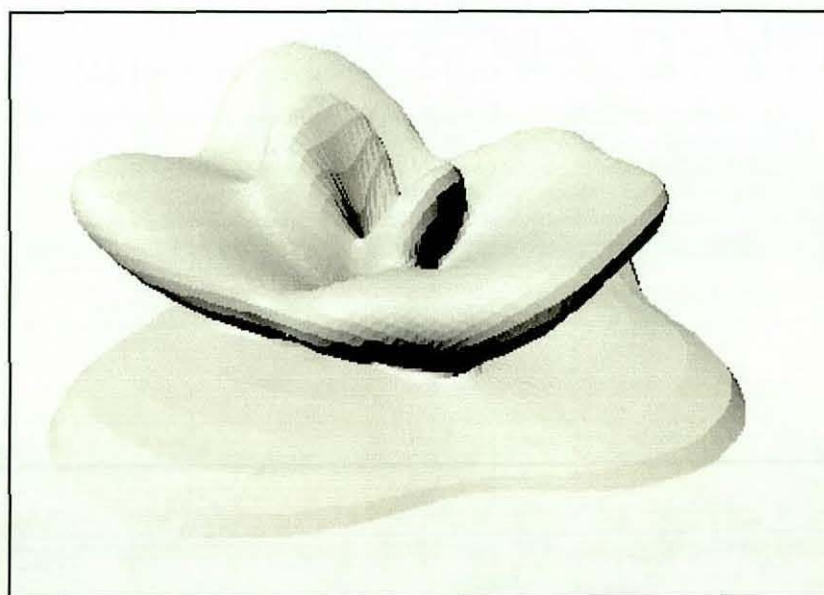

Fig. 8.17   Far-field pattern at 130 MHz for 0.6 m monopole at centre of car roof

Fig. 8.18   Far-field pattern at 140 MHz for 0.6 m monopole at centre of car roof
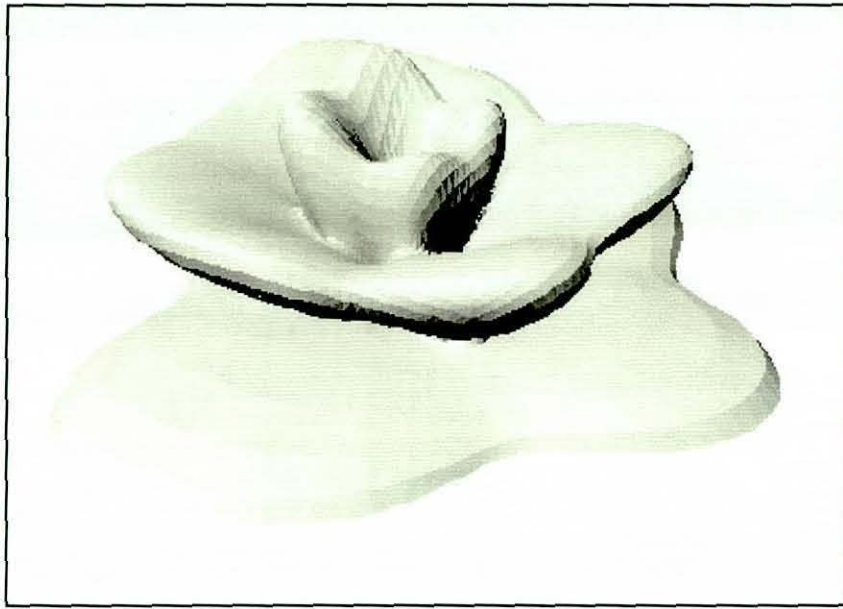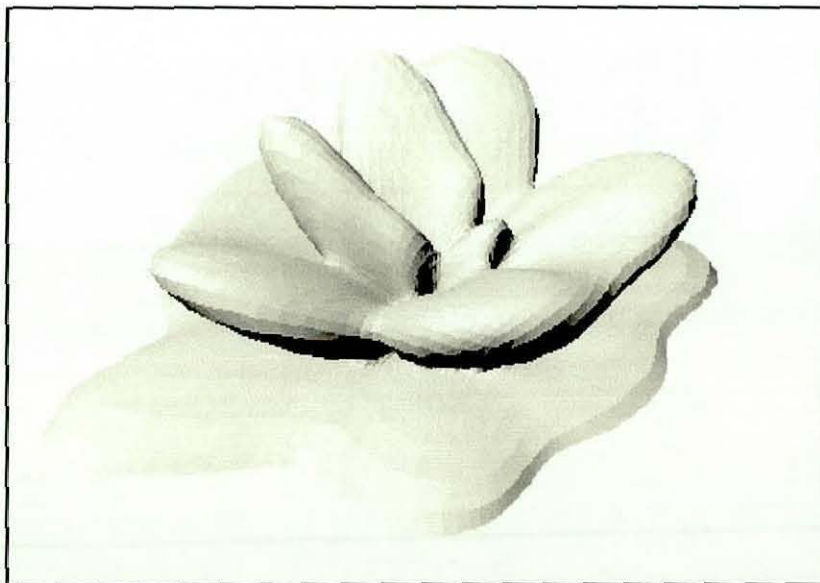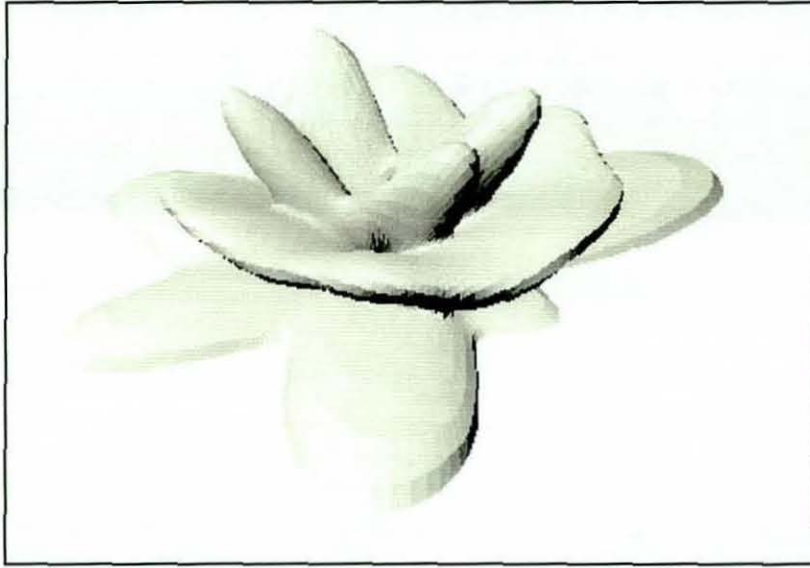
Simulated vehicle gain measurements

Gain measurements were simulated using a simple 1.5 m dipole as a reference antenna, with the measurement range varied from 12 m to 28 m. The computer memory required for these models was already so large that the investigation of very large ranges was not possible. Nonetheless, the results obtained for simple antennas suggested that extrapolation of the gain error plots would perhaps be feasible.

The inability to accommodate very large ranges in the TLM models precluded direct calibration of the TLM dipole model to obtain its far-field gain. The results obtained using MoM were therefore used to provide the gain of the reference antenna for the simulated vehicle antenna gain measurement. Nonetheless, a direct comparison between TLM and MoM dipole models at 18 m range (see Fig. 8.19) shows a fairly good correspondence. The additional ripple in the TLM result is probably due to finite reflections from the workspace boundaries.

The computed input reflection coefficient for the test antenna indicates that the resonant frequency is 95 MHz, while that for the vehicle-mounted monopole is around 120 MHz (see Fig. 8.20). Thus, the resonant frequency of the monopole is not significantly affected by the vehicle structure, although the bandwidth of the null in the input reflection coefficient around resonance is broader than would be expected for the ideal monopole or dipole with these dimensions.
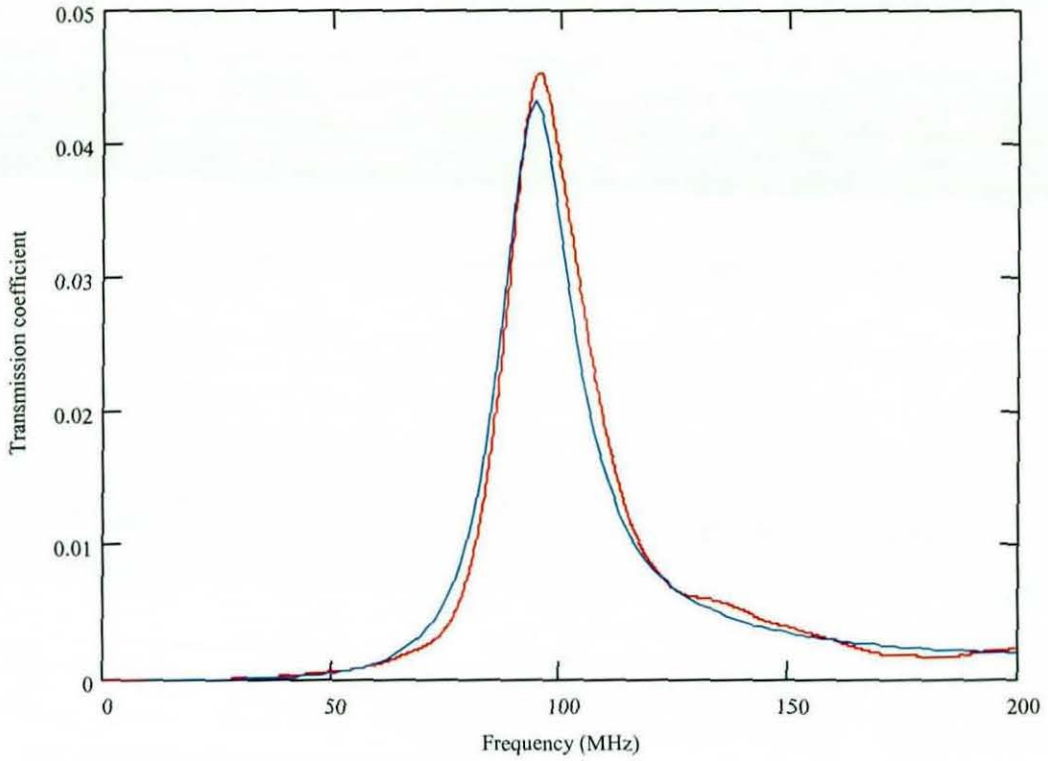
**Fig. 8.19   Computed transmission between dipoles over ground:
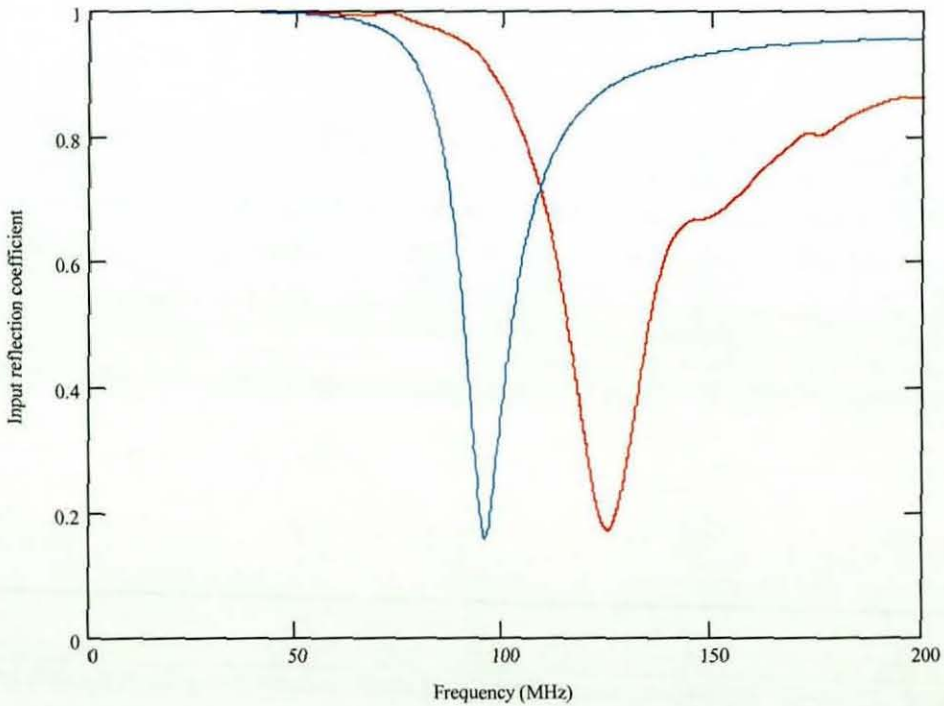TLM (red) and MoM (blue) results**

**Fig. 8.20   Input reflection coefficients for TLM models of test dipole (blue)
and vehicle mounted antenna (red)**

The resonant frequency of the vehicle-mounted antenna also differs from that of the test antenna. However, in practice it is unlikely that measurements would be made using a reference antenna that is tuned to match the antenna under test. Thus, this configuration represents a realistic practical test condition. The resulting coupling between the vehicle antenna and the test antenna, which is illustrated for a separation of 20 m in Fig. 8.21, reflects the different resonant frequencies of the two devices.
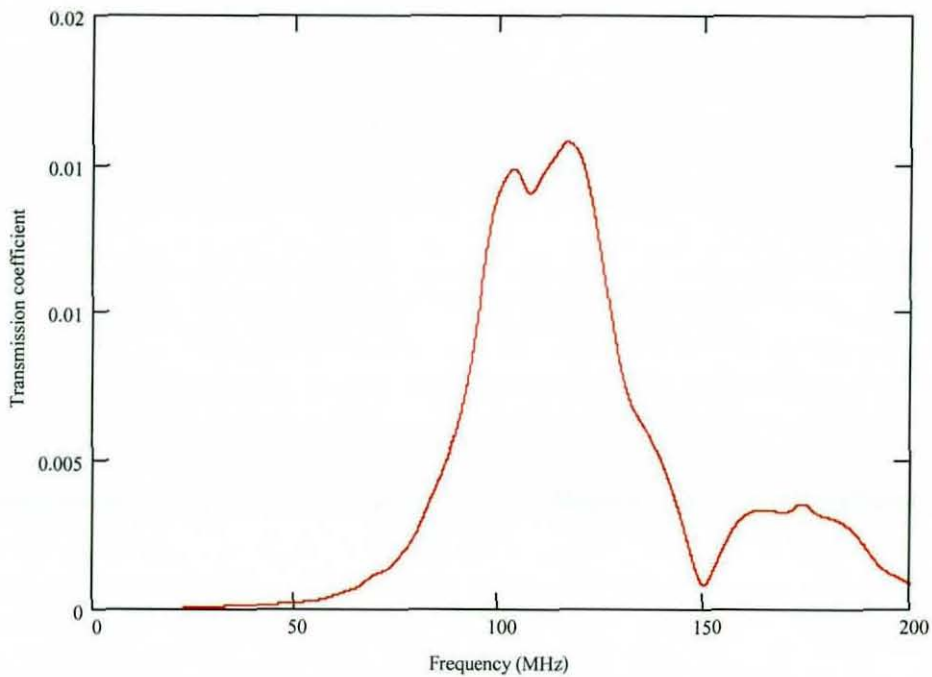
**Fig. 8.21   Coupling between test dipole and vehicle mounted antenna
for 20 m separation**

Results for the vehicle antenna gain estimates are shown in Figs. 22-23, showing the error with range and frequency. The computed far-field directivity has been augmented with the effects of finite impedance mismatch, so that the resulting gain values are comparable with those obtained from the simulated measurements. This then allows the errors due to finite range effects to be determined, including possible contributions from multiple reflections and re-radiation.

These results obtained show some very large errors, and behaviour that is quite different to that of the simple dipole antenna. These errors almost certainly indicate that the far-field condition has not been achieved, which was expected for ranges of <30 m. However, the unexpectedly erratic variations in the gain error also preclude the possibility of estimating the separation that is required to obtain accurate results using this data.

Fig. 8.22   Error in estimated vehicle antenna gain with separation at various frequencies
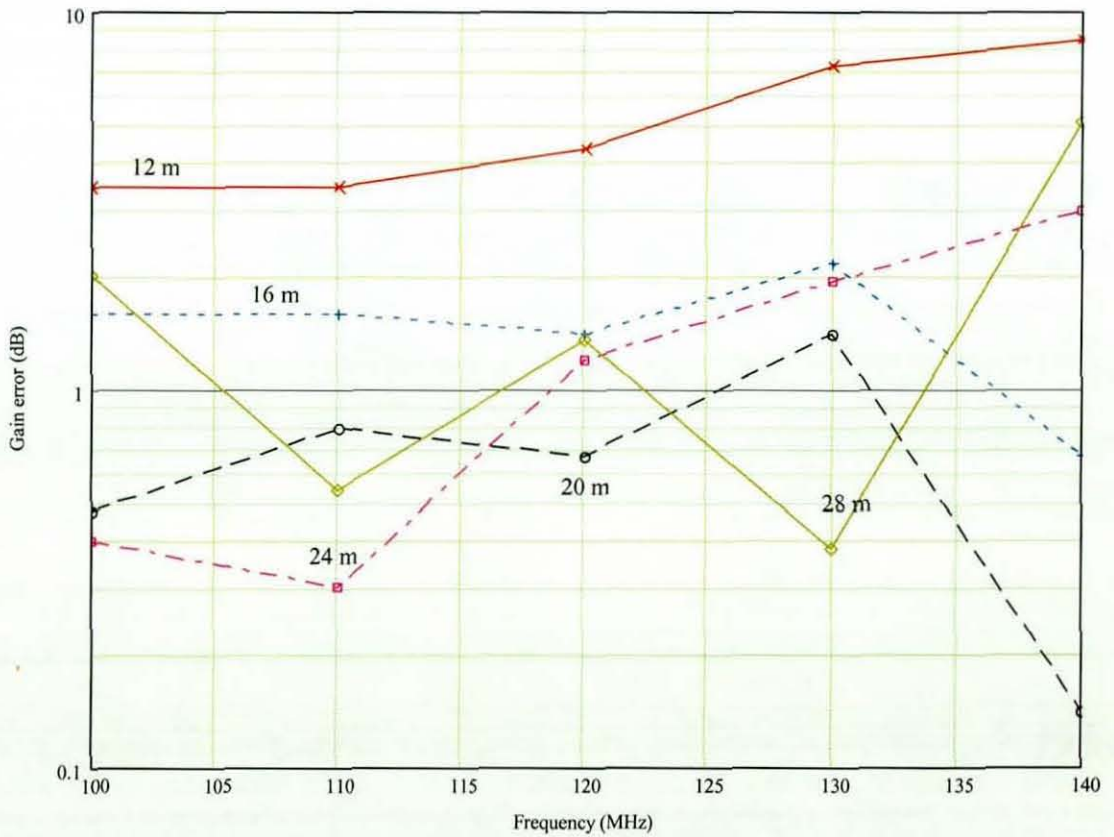
Fig. 8.23   Error in estimated vehicle antenna gain with frequency at various separations

Experimental validation

The results above suggest that the measurement of far-field antenna properties for vehicles on a conducting ground may require access to a very large ground plane. This therefore limits the opportunities for experimental validation to evaluating the coupling to nearby antennas. Nonetheless, the far-field properties predicted for the vehicle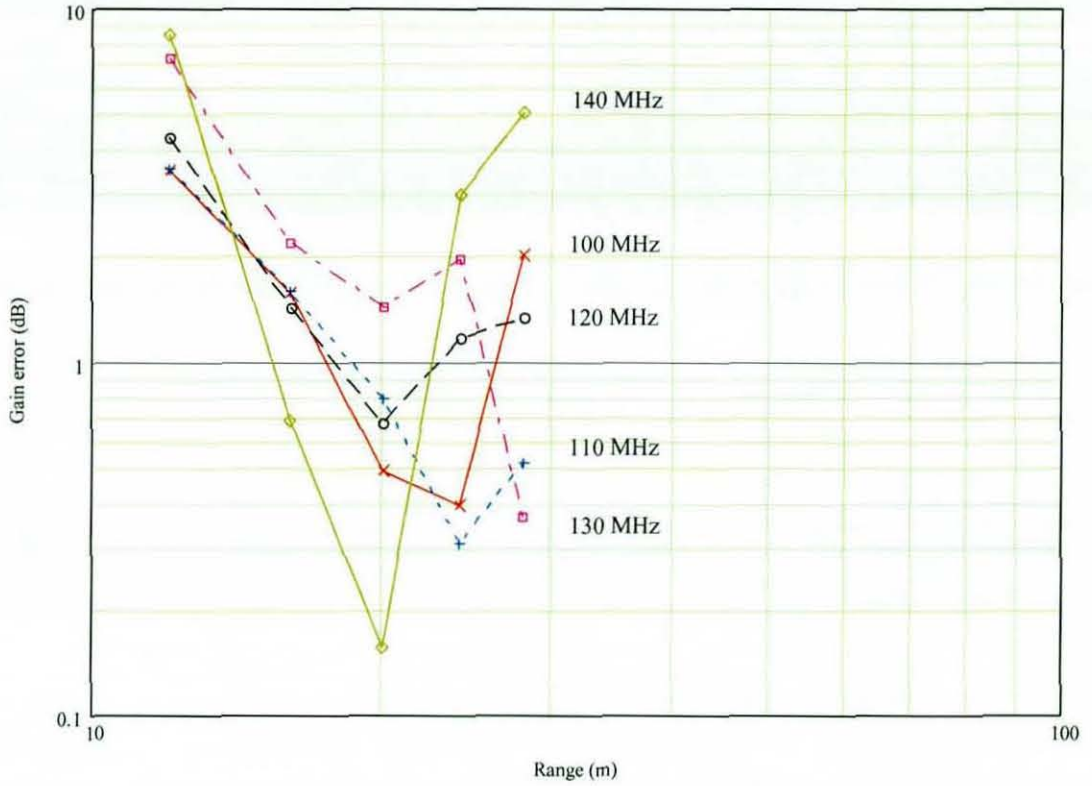 antenna are based on computed near-field quantities, so the experimental validation of near-field predictions should provide an indication of the quality of the far-field predictions. Moreover, calculating the coupling to a nearby antenna is possible and the corresponding measurements much more reliable than can be achieved for far-field gain measurements using the test sites that were available.

The coupling between a monopole mounted on the roof of a vehicle body shell using a magnetic mount and a nearby dipole was derived from a TLM model of the vehicle and antennas. These results are compared with similar measurements in Fig. 8.24 below. In this case the monopole was 0.5 m long, while the dipole was 1.2 m long and the distance between them was 5 m (with the dipole at the side of the vehicle). The balun used with the dipole was separately characterized, using network analyser measurements to determine the scattering matrices for these parts of the system, so that the coupling between the antenna terminals could be de-embedded from the measurements for comparison with the model (using a similar method to that described in section 6.5 of this thesis).

Fig. 8.24   Measured and computed coupling at 90° to vehicle axis

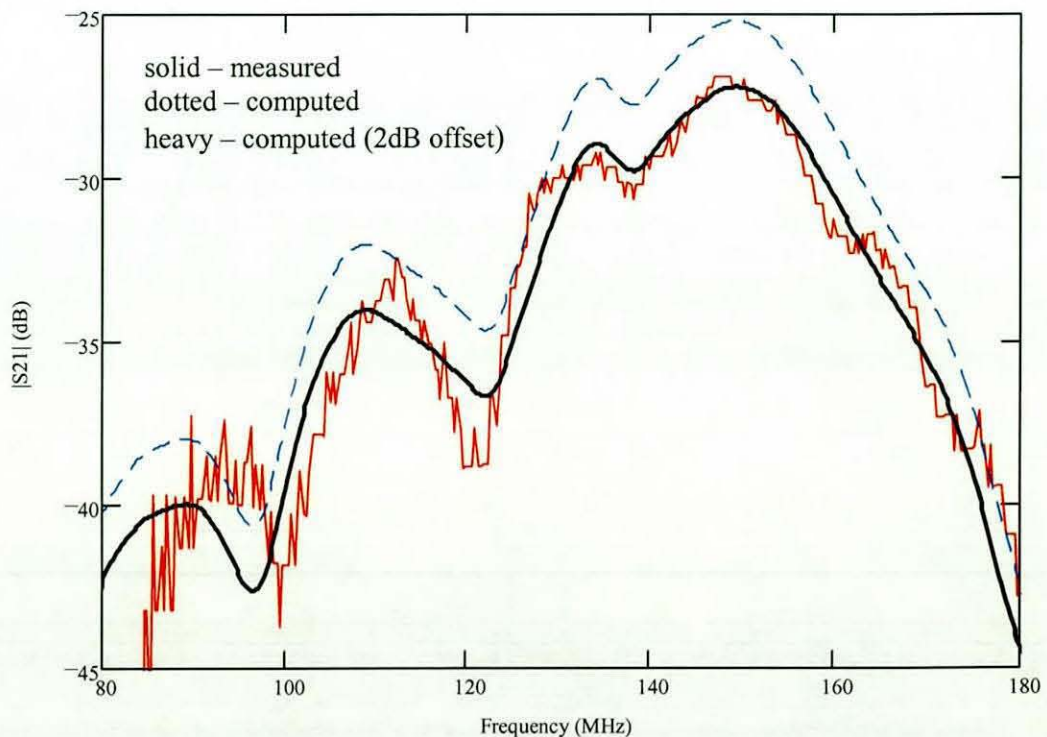Given the level of approximation to the real vehicle structure that is present in the model, which employed a 2.5 cm cubic mesh, the correlation between the model and measurement should not be expected to be perfect. There are differences in both the amplitude and position of the features in the frequency response. Nonetheless, the topological characteristics of the computed and measured results are very similar. The model results overestimate the coupling by around 2 dB, which is of similar magnitude to that seen in earlier validation studies [4.10] based on the coupling between a pair of the dipoles used in this validation experiment. This may result from construction features of the real dipole antenna that are not represented in the simple models used here.

The dipole antennas used in these measurements were based on those described by FitzGerrell [8.9], which include a cylindrical dielectric support around the antenna terminals, as well as lengths of cable and associated dielectric supports that form part of a balun based on a quad-hybrid coupler. It was not possible to accommodate these details in such large models without exceeding the computing resources that were available.

8.6   Conclusions

Simulations of simple gain measurement methods based on the Friis transmission formula indicate that the phase error that can be tolerated using low gain antennas is much smaller than that which is normally found to be sufficient for high gain devices. For a pair of dipoles separated by a distance $2D_R^2/\lambda$ in free space (corresponding to a phase error of $\pi/8$ radians) the range related gain error is around 1 dB while the gain is only around 2 dB. These models indicate that separation requirements corresponding to a phase error of $\pi/24$ radians are required to obtain a more acceptable error of 0.1 dB. Antennas that are operated close to a ground plane have higher far-field gains, due to the formation of an array. Simulated gain measurements between a pair of vertical dipoles above a ground plane indicate that less stringent phase error requirements, but much greater separations, are needed to obtain the target accuracy of 0.1 dB.

Analysis of the amplitude and phase errors that result for such systems shows that a separation of $6D_R^2/\lambda$ (for a phase error of $\pi/24$ radians) is necessary in order to obtain a more acceptable error of 0.1 dB for dipoles in free space. Above a ground plane, it is shown that a distance of $2nHD_R/\lambda$ (to limit phase errors to π/n radians) is required for a receiver at height H. Even for a phase error of $\pi/8$ radians and the minimum possible height ($D_R/2$) this would imply a range of at least $8D_R^2/\lambda$, but the more stringent phase error limits that are found to be necessary for dipole antennas result in a multiplier in the region of 30-40, requiring much greater distances. The impact of amplitude errors is generally smaller than that due to the phase errors.

Numerical models and theoretical analysis of simple gain measurements for vertical dipoles at similar heights to the roof of a vehicle suggest that ranges of ~40 m would be required to limit range related errors to around 0.1 dB. However, numerical models of such measurements for the roof-mounted monopole antenna show no indication of convergence at ranges up to ~30 m, suggesting that much larger distances are required to obtain an adequate approximation to far-field conditions for this case. For vehicle mounted antennas, therefore, range requirements of ~100 m seem more likely in order for successful gain measurements based on simple transmission measurements to be achieved.

Numerical models of a simple vertical monopole mounted at the centre of the roof of a representative vehicle indicate that the far-field gain and radiation patterns for vehicle-mounted antennas can differ significantly from that of the "ideal" antenna. Since direct validation of these predications was not possible because of measurement range requirements, the coupling to a dipole at 5 m distance was used as a more readily measured and computed quantity which can be used to assess the quality of the far-field predictions (which are based on near-field calculations). Considering the limitations of the model, in terms of vehicle geometry and the fidelity of the antenna models, the measured and computed results are remarkably similar.

The results obtained from the simulated dipole gain measurements suggested that, despite the large distances required to obtain far-field conditions, a simple extrapolation method could perhaps be used to obtain results from a number of measurements at more practicable distances using a small number of simple measurements. However, the results obtained from models of the vehicle-mounted monopole suggest that more sophisticated (and costly) extrapolation methods (such as that outlined in [8.12], based on the plane wave scattering matrix description of antenna interactions [8.13]) would probably be required in order to achieve reliable measurements. Alternatively, a hemispherical scanning near-field measurement facility [8.14] may represent a more cost effective solution to this problem.

8.7   References

[8.1]   T.J. Talty, D. Yingcheng and L. Lanctot, *Automotive antennas: trends and future requirements*, Proceedings of IEEE Antennas and Propagation Symposium, Boston, USA, July 2001, Vol. 1, pp. 430-433

[8.2]   E.K. Walton, *Automotive conformal antenna research at the Ohio State University*, Proceedings of IEEE Antennas and Propagation Symposium, Boston, USA, July 2001, Vol. 4, pp. 586-587

[8.3]   M.L. Djordjevic and B.M. Notaros, *Highly efficient large-domain moment-method analysis and CAD of radio-frequency antennas mounted on or situated in vehicles*, Proceedings of IEEE Vehicular Technology Conference, Boston, USA, September 2000, Vol. 5, pp. 2373-2377

[8.4]   R. Ehmann, B. Wagner and T. Weiland, *Farfield calculations for car antennas at different locations*, IEEE Transactions on Magnetics, Vol. 33, No. 2 (Part 2), March 1997, pp. 1508-1511

[8.5]   S.A. Schelkunoff and H.T. Friis, *Antennas: theory and practice,* Wiley, 1952, §6.7

[8.6]   C.H. Walter, *Travelling wave antennas*, McGraw-Hill, 1965, p.38

[8.7]   D.C. Hawkins and T. Milligan, *Exact derivation of aperture errors in antenna measurements*, IEEE Antennas and Propagation Magazine, Vol. 38, No. 4, August 1996, pp. 56-60

[8.8]   J.D. Kraus, *Electromagnetics*, McGraw-Hill, 1985, §14.9

[8.9]   R.S. Elliott, *Antenna theory and design*, Prentice-Hall, 1981, §7.14

[8.10] S.A. Schelkunoff and H.T. Friis, *Antennas: theory and practice,* Wiley, 1952, §6.10

[8.11] R.G. FitzGerrell, *Standard linear antennas, 30 to 1000 MHz*, IEEE Transactions on Antennas and Propagation, Vol. 34, December 1986, pp. 1425-1429

[8.12] A.C. Newell, R.C. Baird and P.W. Wacker, *Accurate measurement of antenna gain and polarization at reduced distances by an extrapolation technique*, IEEE Transactions on Antennas and Propagation, Vol. 21, No. 4, July 1973, pp. 418-431

[8.13] D.M. Kerns, *Plane wave scattering matrix theory of antennas and antenna-antenna interactions*, NBS Monograph 162, National Bureau of Standards, Washington, 1981

[8.14] R. Kronberger, A. Stephan and M. Daginnus, *3D antenna measurement and electromagnetic simulation for advanced vehicle antenna development*, Proceedings of IEEE Antennas and Propagation Symposium, Boston, USA, July 2001, Vol. 3, pp. 342-345

CHAPTER 9: CONCLUSIONS AND FURTHER WORK

Historically, physical measurements have been the only viable approach for the investigation of electromagnetic performance for complex systems such as vehicles. The earliest TLM models of vehicles were built initially from assemblies of primitive bodies, and later derived from finite element meshes that were hand-built for noise and vibration analysis. The frequency range that could be addressed also fell short of the 1 GHz upper frequency of the relevant standards. Within the last five years, however, vehicle CAD data has become routinely available and the computing resources required for whole vehicle simulation to frequencies in excess of 1 GHz have now become affordable, and fast enough, to make engineering applications practicable.

Although numerical modelling is now becoming a more feasible alternative to physical testing, the credibility of simulation results must be demonstrated against measured results in order to promote wider acceptance of modelling. Validation exercises also have an essential role in establishing strategies for developing numerical models of complex structures such as vehicles. The work presented in this thesis therefore aims to improve the convergence between measurements and simulations. Elements of much the work described in this thesis have been presented in a number of publications, which are listed in Appendix A.

9.1 Model validation approach

The initial premise in validating numerical models against experiment is that the measurements must be correct, almost by definition, particularly if they comply with widely accepted standards (and can therefore be reproduced by another laboratory). It is argued here, however, that this approach is flawed in that almost all measurements of any complexity are subject to some form of interpretation. Simply comparing measurements based on the same flawed interpretation tells us very little about their absolute accuracy, only their precision. Since experiments inevitably rely on a theoretical model to support their interpretation the results do not necessarily reflect absolute measurements, but in fact reflect the expectations of the designer of the experiment. Thus, it seems more appropriate to consider a measurement as an "experimental model", providing yet another imperfect representation of the parameter of interest. Consequently, the validity of the reference measurements also needs to be established.

Mathematical modelling of the key elements of the measurement processes is proposed in this thesis as the only reliable approach for addressing these issues. Such analysis provides a mechanism for establishing the credibility of the measurement, and quantifying potential limitations that may need to be considered when numerical results are compared with it. Numerical models, unlike measurements, are able to provide both absolute field quantities and the results of simulated measurements (typically antennas), thus allowing the interpretational errors to be investigated and quantified. The results presented here regarding the measurement of wire currents, radiated emissions and antenna gain demonstrate that experimental results are no less in need of validation than the numerical results that are, more conventionally, judged against them.

A balanced approach to model validation provides the opportunity to refine both the modelling techniques and the measurement methods that are used, bringing benefits to both methods of investigation. These objectives support the overall goal of improving the quality of model validation results. The use of modelling techniques to investigate measurement methods is also shown to lead to improvements in the accuracy of physical measurements.

9.2   Vehicle modelling strategies

In addition to presenting a more realistic approach to model validation, the results of a number practical model validation exercises have been outlined. The latter range from very simple configurations, such as simple wire networks and a rectangular test object, through to models of vehicles illuminated by typical EMC test antennas for frequencies up to 1 GHz. The results of these studies demonstrate that it is possible to achieve good agreement between numerical models and measurements, provided that the models reflect the key elements of the measurement process and that the two results are presented in a manner that is directly comparable.

For electric field analysis, for example, normalizing the field at a point to that computed at a specific reference point without the test object present is shown to be very successful. This presentation approach effectively mirrors the correct interpretation of measured results (where the "threat" is related to the field a specified point without the vehicle present), but also avoids the need to replicate the physical source characteristics in detail. Nonetheless, the model must represent the antenna used in the test, since typical measurement conditions (where the spacing between the antenna and the vehicle is only ~1 m, and the vehicle is commonly mounted on a ground plane) cannot be adequately represented by a simple plane wave.

Successfully predicting cable coupling was found to be much more difficult, even for relatively simple networks. However, an approximate analytical model that was developed for a symmetrical four-port network with finite termination mismatch is shown to compare well with 3D field simulations of such systems. This suggests that the discrepancies that are found between model and measurement results are more likely to be due to difficulties in obtaining the desired wire configuration in the physical system than to weaknesses in the numerical methods.

Strategies for developing computationally efficient whole vehicle electromagnetic models have also been considered, including proposals for identifying and classifying geometrical requirements for different modelling applications. Furthermore, the essential content of whole vehicle models has also been investigated, using both experimental and numerical approaches to establish the significance of major vehicle components such as window glazing, seat cushions, seat frames, window heater arrays and sunroofs. Results of this nature have not been previously reported.

Microwave network theory provides a convenient mechanism for describing EMC phenomena, and it is shown that the renormalization properties of the scattering matrix provide an efficient method to accommodate the high levels of uncertainty regarding the termination impedances of vehicle wiring harnesses (which are expected to vary with frequency as well as with operating mode) without the need to repeat time consuming 3D simulations. An approximate method for populating the vehicle scattering matrix is also proposed, based on the combination of a few 3D simulations with many network simulations.

This approach represents an extension from the separated methods, which have proved satisfactory for calculating field coupling to cables, and was suggested by reported measurements of the scattering parameters for a harness in a vehicle, which suggest that the coupling between most cable bundles is likely to be negligible. This would allow the number of 3D simulations required to be minimized to as few as the number of "antennas" (intentional or unintentional) that are present in the system. The use of network simulations to populate the remaining regions of the scattering matrix would allow the uncertainties regarding harness construction and location to be accommodated much more efficiently than would be the case if 3D simulations were required for this purpose. Uncertainty regarding the termination impedances of the network could then be accommodated by renormalizing the scattering matrix, rather than by resorting to more simulations at either 3D or network level. However, this approach has yet to be demonstrated using a practical example.

9.3   Measurement methods

A significant proportion of this work has been concerned with the application of numerical models to the investigation of a number of practical measurement issues. This work has resulted in proposals for improvements in a number of measurement practices.

In a model validation study it was found that measured and computed currents on a wire inside a test object differed in amplitude but had very similar features, while the electric field results matched in both amplitude and features. This observation prompted an analysis of the calibration of current measurement transducers at high frequencies, by taking account of reflections that occur in the calibration fixture due to impedance mismatch and the presence of the transducer in the calibration fixture. Improved estimates for the transfer impedance were derived from the scattering matrix of the calibration fixture using a 1D transmission line model, and numerical models were used to demonstrate that the current at the centre of the wire in the calibration fixture can be accurately estimated from the scattering matrix. Results of this nature have not previously been reported.

The relationship between emissions levels at different distances is of importance for physical measurements, since it may be desirable to make use of measurements at closer ranges (eg. in a chamber rather than on an OATS). Furthermore, for simulations using volume meshing techniques (such as TLM, FDTD and FEM), a "measurement" point that is closer to the vehicle results in a smaller model. An investigation of these issues, which was based on analysis of raw field predications and simulated measurements using a representative model of a broadband antenna with a synthetic "vehicle-like" geometry as the source, indicated subtle differences in the interpretation of automotive emissions measurements at 3 m and 10 m distances. Experimental studies also supported these theoretical findings.

The desire to validate predicted far-field gain and radiation patterns of vehicle-mounted antennas using simple gain measurement methods in a semi-anechoic environment prompted an analysis of the separation requirements for antenna gain measurements based on the far-field assumptions for low-gain antennas and for antennas operated above a ground plane. These results do not appear to be available in the published literature. Both the analytical studies and simulated measurements indicated that the range requirements exceeded the dimensions of the available ground planes, with the result that an "indirect" validation approach (based on the predicted near-field, which is used to compute the far-field characteristics) was adopted as a more practicable alternative.

9.4   Further research

Whilst whole vehicle electromagnetic models are now becoming increasingly practicable, the information that can be obtained from such models is often not directly useful for automotive EMC engineering. Consequently, approaches for analysing and presenting the available data in ways that can support the assessment of EMC risk need to be investigated. Detailed modelling of the wiring harness, for example, is currently of doubtful practical benefit since details of the termination impedances are largely unavailable at present, and both the construction and location of the harness elements are subject to considerable uncertainty. However, analysis of the statistics of the field distribution along a harness path could perhaps be used to assess the EMC risk for these parts, or to rank the relative merits of alternative routes if options are available.

Although electromagnetic models can already provide useful inputs to the vehicle development process, the ultimate goal of predicting functional EMC performance has yet to be achieved. Technical and practical strategies for carrying out this wider system modelling in an efficient and equitable manner will need to be developed in order to achieve these aims. Such models will need to include both electronic and software system performance in addition to the purely electromagnetic characteristics of the vehicle.

The work reported here includes preliminary investigations of the features that must be included or could be neglected in automotive electromagnetic models. However, vehicles are increasingly complex systems, and considerable further work remains to be done in this area in order to ensure that the capabilities and limitations of such models are better understood. This understanding will be essential in order to allow numerical results to be used with confidence in the design process, where measured data is unavailable to compare with simulations. This is a rather different situation to that found in the aerospace industry, where the nature and duration of the product development lifecycle is such that it is possible to use a combination of modelled and measured results.

The use of antennas on vehicles is rising rapidly, and emissions measurements at 3 m from the vehicle are increasingly desirable for commercial and technical reasons (eg. rising ambient levels on OATS). Consequently, a more comprehensive theoretical and experimental investigation of the near field structure around radiating vehicles could be beneficial for improving both the interpretation of vehicle emissions measurements at different distances and low-cost measurement techniques that are suitable for automotive antennas.

Although electromagnetic models can provide information that is of direct relevance for vehicle antenna engineering, the inclusion of models of complex antenna designs in vehicle level simulations currently presents very significant practical difficulties. Strategies for approximating the behaviour of such devices, in a manner that contains the computational requirements within acceptable levels whilst representing the behaviour of the device to an adequate degree, will be needed to allow prediction of the installed performance characteristics of automotive antennas.

Despite the falling costs of high performance computing resources, they are more than matched by increasing end-user expectations (and upper frequency limits in particular). However, vehicle manufacturers will only adopt numerical methods if the results can be made available within the timing constraints of vehicle development programmes, which are subject to increasing pressure for savings in both development time and costs. Thus, the computing requirements associated with vehicle level models remain so large that there is a continuing need for faster, more efficient and more accurate 3D field modelling tools.

Hybrid methods, which take advantage of the computational benefits of different numerical techniques for specific parts of the model, have been the subject of increasing research for this purpose, but numerous practical and theoretical problems remain to be resolved before they can be deployed within industrial processes. High performance boundary conditions for finite methods have also been the subject of considerable research effort, but such schemes are not universally successful and the computational overheads associated with these techniques can sometimes negate the benefits of reduced model size. Further development of efficient numerical techniques and modelling strategies are therefore essential for the future.

Further investigation of experimental methods using numerical models, which have the potential to provide wider and more detailed information than can be obtained from measurements alone, is essential to improve the quality and understanding of experimental results. In particular, current injection and measurement transducers are commonly employed in EMC testing, and their calibration and interpretation will require more careful consideration as future test requirements will need to be extended into the microwave band in order to accommodate technological advances in automotive electronics. Other areas of concern include radiated emissions and immunity test methods for vehicles at frequencies in excess of 1 GHz, which are not addressed by current automotive standards. Simulated measurements of this type will be invaluable in guiding the development of existing test methods for higher frequency applications.

9.5   Overall conclusion

In practice, a measurement essentially provides an answer to a "question" that is often not well defined, while a model provides an answer to a question that is generally very well defined (because the model content and environment are controlled by the analyst), but is probably not quite the question that is of interest (because of computing limitations and incomplete information about the real system).   Successful model validation therefore requires the establishment of a sufficient degree of convergence between the model and the measurement to ensure that both approaches address the same question, or at least questions that are sufficiently similar for the results to be comparable. The results of model validation studies and numerical modelling of experimental test and calibration methods are both essential to achieve this goal.

Building confidence through the successful comparison of results from a number of differing experimental and numerical methods is probably the best approach the validation of both measured and computed results for complex systems. However, practical constraints generally limit the availability of data for validation purposes, so numerical models that are intended for experimental validation must reflect the key features of the physical measurement process in order to maximize the chances of a successful outcome.

The development and deployment of electromagnetic modelling techniques in automotive applications is now beginning to mature, and it seems likely that within the next ten years the prediction of functional EMC performance will be achievable over the current test frequency band (up to 1 GHz). Nonetheless, vehicle measurements are already being carried out by vehicle manufacturers at frequencies up to 3 GHz, to take account of Bluetooth and GSM, and adaptive cruise control systems based on 77 GHz radar technology are about to reach the luxury car market. Furthermore, there are already plans for vehicle-vehicle and vehicle-roadside communications operating at low microwave frequencies. Consequently, the struggle to cope with vehicle models at the frequencies of interest shows little sign of becoming any easier for the foreseeable future.

APPENDIX A: RELATED PUBLICATIONS

A number of publications that relate to the work described in this thesis are listed below.

[A.1]   A.R. Ruddle, D.A. Topham, D.D. Ward and P.J. Page, *Theoretical investigation of automotive emissions measurements at 3 m and 10 m ranges*, Proceedings of 13th Zurich EMC Symposium, February 1999, pp. 285-289

[A.2]   D.D. Ward, A.R. Ruddle, P.A. Phillips and P.J. Page, *Correlation of automotive electromagnetic emissions measurements*, SAE International Congress and Exposition, Detroit, Michigan, USA, March 1999, Paper 1999-01-1096

[A.3]   A.R. Ruddle, A.J.M. Martin, D.D. Ward and A.P. Duffy, *Objective validation techniques for automotive EMC engineering*, IEE Colloquium on "EMC for automotive electronics", Birmingham, 28th September 1999, Digest No. 1999/134, Paper No. 7

[A.4]   A.R. Ruddle, A. Sarantidis and D.D. Ward, *Modelling the installed performance of vehicle mounted antennas*, Proceedings of IEE National Conference on Antennas and Propagation, York, UK, April 1999, pp. 3-5

[A.5]   A.R. Ruddle, *Simulation of far-field characteristics and measurement techniques for vehicle mounted antennas*, IEE Colloquium on "Antennas for automotive applications", London, 10th March 2000, Digest No. 2000/02, Paper No. 7

[A.6]   A.R. Ruddle and D.D. Ward, *Numerical modelling as a cost effective tool for the design and optimisation of EMC test chambers*, Proceedings of the 4th European EMC Conference, Brugge, Belgium, September 2000, Volume 1, pp. 137-142

[A.7]   A.R. Ruddle, S.C. Pomeroy and D.D. Ward, *Comparison of analytical, numerical and measured results for simple networks near a ground plane*, Proceedings of 14th Zurich EMC Symposium, February 2001, pp. 413-418

[A.8]   A.R. Ruddle, S.C. Pomeroy and D.D. Ward, *Calibration of current transducers at high frequencies*, IEEE Transactions on EMC, Vol. 43, No. 1, February 2001, pp. 100-104

[A.9]   A.R. Ruddle, S.C. Pomeroy and D.D. Ward, *Modelling the installed performance of automotive antennas integrated with vehicle glazing*, Proceedings of 11th International Conference on Antennas and Propagation, Manchester, April 2001, Vol. 2, pp. 732-735

[A.10] J.A. Flint and A.R. Ruddle, *The GEMCAR project – generic guidelines for the modelling of automotive EMC*, Proceedings of ARMMS 2001 RF and Microwave Conference, Loughborough, UK, 30th April- 1st May 2001

[A.11] A.R. Ruddle, S.C. Pomeroy and D.D. Ward, *Numerical modeling of a stripline antenna in a large semi-anechoic chamber,* Proceedings of IEEE EMC Symposium, Montreal, August 2001, Vol. 1, pp. 298-301

[A.12] A. Rubinstein, F. Rachidi, J.-P. Parmantier, X. Ferrières, S. Alestra, R. Perraud, A.R. Ruddle and B. Reusser, *Modélisation de la penetration d'un champ électromagnétique à l'intérieur d'une automobile: simulation et validation expérimentale*, Actes du Colloque CEM, Grenoble, France, March 2002

[A.13] A.R. Ruddle, *Numerical modelling of the impact of automotive screen heaters on vehicle EMC characteristics*, Proceedings of 5th European EMC Conference, Sorrento, Italy, September 2002, Vol. 2, pp. 721-725

[A.14] A.R. Ruddle, *Measured impact of seats and glazing on the coupling of electromagnetic fields into vehicles and their wiring harnesses*, Proceedings of 15th Zurich EMC Symposium, February 2003, pp. 487-492

[A.15] A.R. Ruddle, *Computed impact of optional vehicle features (sunroof and windscreen heater) on automotive EMC characteristics*, Proceedings of 15th Zurich EMC Symposium, February 2003, pp. 475-480

[A.16] X. Ferrières, J.-P. Parmantier, S. Bertuol and A.R. Ruddle, *Modelling EM coupling onto vehicle wiring based on the combination of a hybrid FV/FDTD method and a cable network method*, Proceedings of 15th Zurich EMC Symposium, February 2003, pp. 465-470

[A.17] A.R. Ruddle, A.J.M. Martin and D.D. Ward, *Quantitative data comparisons: applications and experiences in automotive EMC*, Proceedings of 15th Zurich EMC Symposium, February 2003, Supplement, pp. 111-116

[A.18] A.R. Ruddle, *EU Framework V Project "GEMCAR": Guidelines for Electromagnetic Compatibility Modelling for Automotive Requirements*, Proceedings of 15th Zurich EMC Symposium, February 2003, Supplement, pp. 199-204

[A.19] A.R. Ruddle and I. Hendrikx, *EU Framework V Project "GEMCAR": User requirements analysis*, Proceedings of 15th Zurich EMC Symposium, February 2003, Supplement, pp. 199-204

[A.20] S. Alestra, X. Ferrières, J.-P. Parmantier, R. Perraud, F. Rachidi, A. Rubinstein, A.R. Ruddle and N. Whyman, *EU Framework V Project "GEMCAR": CEM techniques investigated,* Proceedings of 15th Zurich EMC Symposium, February 2003, Supplement, pp. 205-210

[A.21] J.-P. Parmantier, X. Ferrières and A.R. Ruddle, *EU Framework V Project "GEMCAR": Efficient simulation strategies*, Proceedings of 15th Zurich EMC Symposium, February 2003, Supplement, pp. 211-217

[A.22] A.R. Ruddle, *EU Framework V Project "GEMCAR": Practical aspects of the development of whole vehicle electromagnetic models*, Proceedings of 15th Zurich EMC Symposium, February 2003, Supplement, pp. 219-224

[A.23] A.R. Ruddle, S. Alestra, X. Ferrières, I. Hendrikx, J.-P. Parmantier, R. Perraud, F. Rachidi, A. Rubinstein, F. Sobaru, C. Thomas and N. Whyman, *EU Framework V Project "GEMCAR": Model validation activities*, Proceedings of 15th Zurich EMC Symposium, February 2003, Supplement, pp. 225-233

[A.24] A.R. Ruddle, S.C. Pomeroy and D.D. Ward, *Estimation of far-field distances for antennas close to ground and implications for simple gain measurement methods*, to be published in Proceedings of 12th International Conference on Antennas and Propagation, Exeter, UK, April 2003, pp. 699-702